

DISSERTATION

A STUDY OF LOW CLOUD CLIMATE FEEDBACKS USING A GENERALIZED
HIGHER-ORDER CLOSURE SUBGRID MODEL

Submitted by

Grant J. Firl

Department of Atmospheric Science

In partial fulfillment of the requirements

For the Degree of Doctor of Philosophy

Colorado State University

Fort Collins, Colorado

Summer 2013

Doctoral Committee:

Advisor: David A. Randall

Scott Denning
Richard Johnson
Paul Evangelista

Copyright by Grant J. Firl 2013

All Rights Reserved

ABSTRACT

A STUDY OF LOW CLOUD CLIMATE FEEDBACKS USING A GENERALIZED HIGHER-ORDER CLOSURE SUBGRID MODEL

One of the biggest uncertainties in projections of future climate is whether and how low cloudiness will change and whether that change will feed back on the climate system. Much of the uncertainty revolves around the difference in scales between the processes that govern low cloudiness and the processes that can be resolved in climate models, a fact that relegates shallow convection to the parameterization realm with varying levels of success. A new subgrid-scale parameterization, named THOR, has been developed in an effort to improve the representation of low cloudiness via parameterization in climate models. THOR uses the higher-order closure approach to determine the statistics describing subgrid-scale processes. These statistics are used to determine a trivariate double-Gaussian PDF among w , θ_{il} , and q_t . With this information, one can diagnose what portion of the grid cell is cloudy, subgrid-scale cloud water content, and subgrid-scale vertical cloud water flux. In addition, samples are drawn from the trivariate PDF in order to drive the microphysics and radiation schemes. Although schemes similar to THOR have been developed over the past decade, THOR includes several novel concepts, like the generalization of the saturation curve to include condensation over both ice and liquid substrates, the determination of the PDF parameters from the given turbulence statistics, the introduction of a stochastic parcel entrainment process for the turbulence length scale, and a sub-column approach for calculating radiative transfer using the PDF.

The new model is evaluated by simulating five test cases spanning a wide range of boundary layer cloud types, from stratocumulus to cumulus and the transition between the two.

The results are compared to an ensemble of LES models running the same cases, with particular attention paid to turbulence statistics and cloud structure. For all cloud types tested, THOR produces results that are generally within the range of LES results, indicating that the single-column THOR is able to reproduce the gross characteristics of boundary layer clouds nearly as well as three-dimensional LES. Sensitivity to vertical grid spacing, diagnostic/prognostic third-order moments, choice of turbulence length scale entrainment process, and whether or not PDF sampling is used to drive the microphysics and radiation schemes is assessed for all test cases. Simulation of the cumulus regime was degraded when vertical grid spacing exceeded 200 m, when more third-order moments were predicted, when higher parcel entrainment rates were assumed, and when PDF sampling for the microphysics scheme was omitted. Simulation of stratocumulus was degraded with grid spacing larger than 100 m, when PDF sampling for microphysics was omitted, and when PDF sampling for radiation was included.

Lastly, THOR is used to study low cloud climate feedbacks in the northeastern Pacific Ocean in the context of the CGILS project. Initial conditions and forcings are supplied at 13 points along the GPCI cross-section that spans from the ITCZ northeast to the coast of California transecting regions of shallow cumuli and stratocumuli, for both the current climate and a climate with a +2K SST perturbation. A change in net cloud radiative forcing of $0-8 \text{ W m}^{-2}$ was simulated along the cross-section for the perturbed climate, representing neutral to weak positive feedback. The responsible mechanism appeared to be increased boundary layer entrainment and stratocumulus decoupling leading to reduced maximum cloud cover in the cumulus regime and reduced liquid water path in the stratocumulus regime.

ACKNOWLEDGEMENTS

A special thanks is owed to my graduate advisor, Dr. David A. Randall, for his patience, guidance, and support throughout my graduate studies. This work would not have been possible without his skillful teaching and constant supply of interesting ideas. I would also like to thank Drs. Scott Denning, Richard Johnson, and Paul Evangelista for their input and guidance provided as members of my graduate advisory committee. In addition, I'm grateful for the thorough and thought-provoking instruction provided by the world-class faculty of this department and for the tremendous example set by students and research scientists in the Randall research group. I especially would like to thank my wife, Julia, and my young son, Wesley, for daily reminders of why I strive for excellence and the vital importance of scientific progress.

This work has been supported by the National Science Foundation Science and Technology Center for Multi-Scale Modeling of Atmospheric Processes, managed by Colorado State University under cooperative agreement No. ATM-0425247 and by the Department of Energy, Contract no. DE-SC0008459.

TABLE OF CONTENTS

ABSTRACT	ii
ACKNOWLEDGEMENTS	iv
Chapter 1. Background	1
Chapter 2. Model Description	12
2.1. Higher-Order Closure Model	14
2.2. Turbulence Scales	26
2.3. Trivariate Double-Gaussian PDF Parameter Estimation	33
2.4. Mixed-Phase Subgrid-Scale Condensation	42
2.5. Microphysics Driver and Scheme	54
2.6. Radiation Driver and Scheme	63
2.7. Surface Layer Scheme	68
2.8. Implementation Notes	76
Chapter 3. Model Evaluation and Sensitivities	83
3.1. Shallow Cumulus Cases	86
3.2. Stratocumulus Cases	127
3.3. Transitional Case	154
Chapter 4. Low Cloud Feedback Experiments	180
4.1. CGILS	182
4.2. Location S6	188
4.3. Location S11	194

4.4. Location S12.....	199
4.5. Cross Section Results	204
Chapter 5. Conclusion	215
BIBLIOGRAPHY	227
Appendix A. Estimated Inversion Strength Calculation	234
Appendix B. Parcel Condensation	236
Appendix C. Notes on Solving the Nonlinear System.....	238
Appendix D. Microphysics Scheme.....	242
List of Acronyms.....	244

CHAPTER 1

BACKGROUND

For a casual observer of the tropical atmosphere, perhaps it is easy to overlook the seemingly passive and numerous shallow cumulus clouds or even the persistent shields of stratocumulus that form in subsidence regions in favor of the impressive masses of deep, heavily-precipitating cumulonimbi that form along the intertropical convergence zone (ITCZ), within convectively-coupled equatorial waves, or tropical disturbances. After all, deep convection actively transports mass, heat, moisture, momentum, and chemical constituents vertically, significantly alters the local radiation budget, and produces latent heating that helps to drive the Hadley circulation and determine the mean temperature profile for much of the tropics. The ascending branch of deep convection has a very powerful effect, but its areal extent is small compared to the accompanying descending branch, so that the area covered by active deep convective cores is a very small percentage of the tropics at any one time. Shallow convection, on the other hand, participates in transport, radiation, and latent heating, but with much reduced magnitudes and with compressed vertical profiles. While the local effect of shallow convection may be comparatively subtle, its global effect is magnified by its frequency of occurrence and its vast areal extent. In addition, shallow convection is controlled by many intricate processes, the balance of which is potentially easily disturbed in a changing climate. Therefore, the importance of shallow convection for the climate system is profound.

As with all clouds, shallow clouds interact with incoming and outgoing radiation and have a significant impact on the local radiative balance. Incoming shortwave radiation is reflected very effectively by cloud droplets, reducing the radiation that reaches the surface

and creating a surface cooling effect. Outgoing longwave radiation is absorbed and reemitted by the same cloud droplets according to their temperature. Some of the longwave radiation that would have escaped into space had a cloud not been present is reemitted back toward the surface, creating a warming effect. The net radiative forcing of a cloud is the sum of these two effects. For low, shallow clouds, since the temperature at cloud top is only slightly cooler than the surface, the longwave warming effect is small compared to the shortwave cooling effect during the day. As a result, shallow clouds exert a net cooling effect locally. Shallow clouds cover a significant portion of the world in the annual mean. Observations of shallow cloud fraction have been made using passive satellite sensors (International Satellite Cloud Climatology Project (ISCCP), Rossow and Schiffer (1999)), active satellite sensors (Cloud-Aerosol Lidar and Infrared Pathfinder Satellite Observations (CALIPSO), Medeiros et al. (2010)), and from the surface (Norris 1998). These studies estimate annual mean low cloud amount to be in the range 23 - 30%. Given the extensive low cloud coverage and the associated relatively strong surface cooling, the impact of low clouds on Earth's radiation budget is substantial. Hartmann et al. (1992) estimated using Earth Radiation Budget Experiment (ERBE) data that low clouds contribute 16 W m^{-2} of cooling in the annual mean, roughly 60% of the total net cloud radiative forcing determined in that study.

Shallow convection, particular shallow cumulus, may play an important role in the initiation and development of many larger-scale phenomena. The shallow diabatic heating profile associated with shallow cumulus creates a shallow circulation with low-level convergence and mid-level divergence (Zhang and Hagos 2009). Since the mean moist static energy profile features high values at the surface and lower values in the middle troposphere, the circulation induced by shallow cumulus is a net importer of moist static energy in a vertically-integrated

sense. The import of moist static energy into the column and the redistribution of moisture from the boundary layer to the middle troposphere is thought to precondition the atmosphere for deeper convective events. Peters and Bretherton (2006) examined composite mesoscale precipitation events and convectively-coupled Kelvin waves in the tropics and found that the shallow diabatic heating mode associated with shallow cumulus precedes the larger events by a few days, gradually moistening the middle troposphere and creating an environment where moist, buoyant updrafts are less diluted by the entrainment of dry air. Benedict and Randall (2007) identified a similar mechanism in advance of the onset of the Madden-Julian Oscillation. Neggers et al. (2007) studied a mechanism called the “shallow cumulus humidity throttle” whereby the intensity of shallow convection in the subsiding subtropical regions determines the amount of moisture fluxed into the free troposphere to fuel deep convection in the ITCZ, ultimately modulating its width and strength.

Due to their role in the physical mechanisms described above, shallow clouds exert considerable influence on the current climate and how the climate system responds to imposed changes via feedbacks. While cloud feedbacks have long been recognized as a leading source of uncertainty in climate projections (Cess et al. 1990), they remain so to this day (Bony et al. (2006); Randall et al. (2007); Soden and Vecchi (2011)). Of the climate feedbacks examined by Bony et al. (2006) (water vapor, lapse rate, albedo, and cloud feedbacks), cloud feedbacks exhibited the largest variance among the feedbacks diagnosed from the participating climate models of the Fourth Assessment Report (AR4) of the Inter-governmental Panel on Climate Change (IPCC). Further, the uncertainty associated with cloud feedbacks in general is mostly attributable to uncertainty of feedbacks from low clouds (Webb et al. (2006); Bony and Dufresne (2005); Soden and Vecchi (2011)). Cloud feedbacks can be divided into two

terms: one term that is a function of the change in the cloud area and one term that is a function of the change in cloud optical depth or albedo (Stephens 2010). Proposed positive and negative feedbacks are associated with both terms. Whether the proposed feedbacks operate in nature, how much they contribute to the climate sensitivity, and to what extent they are represented by current climate models remain unclear.

Of the two terms contributing to the low cloud feedback, the term involving the change in cloud area has garnered more attention in the literature. One negative feedback mechanism is based on the observed positive correlation relationship between lower tropospheric stability and low clouds. Klein and Hartmann (1993) and Miller (1997) argue that subtropical marine low cloud cover is not only a function of local sea surface temperature (SST), but also of the larger dynamical regime in which it resides. Given only an increase in SST, the lower tropospheric stability in the vicinity of low clouds would decrease, indicating a decrease in total low cloud cover. However, an increase in SST across the tropics leads to more latent heat release in regions of deep convection. Since the tropical troposphere is unable to support strong temperature gradients, the increased temperatures found in the free troposphere in deep convective regions is translated throughout the tropics and subtropics. The change in temperature in the free atmosphere is greater than the change in local SST in regions of low clouds, causing the lower tropospheric stability to increase, leading to an increase in low cloud cover. This mechanism represents a negative low cloud feedback since an increase in low cloud cover opposes the original warming. Wood and Bretherton (2006) clarified the apparent relationship between lower tropospheric stability and low clouds by focusing on the strength of the trade inversion. They argue that the strength of the trade inversion is the physical control on low clouds and that the reason the lower tropospheric stability measurement

(defined as the potential temperature difference between 700 hPa and the the surface) has any predictive power is that it is a bulk measure of the strength of the inversion. Using this more precise relationship and its associated measurement, “estimated inversion strength” (EIS), has a different implication for the strength of the feedback mechanism. Most of the gain in lower tropospheric stability in a warming climate is likely due to the change in the temperature profile above the inversion, with estimated inversion strength (EIS) remaining mostly unchanged. As a result, this implies that the magnitude of the negative feedback associated with this mechanism may have been overestimated.

One positive feedback mechanism associated with the change in low cloud amount has been identified using observations. Clement et al. (2009) argue that high SSTs are correlated with a weakening of the subtropical high. This weakening is consistent with reduced subsidence and reduced EIS, allowing a transition from stratocumulus to cumulus, reducing cloud fraction. A reduction in low cloud amount reduces the shortwave cooling produced and leads to further increases in SST. Eitzen et al. (2011) argue that a similar process occurs, but they say that it does not necessarily rely on a weakening subtropical high or reduced subsidence. Instead, all that is needed is a local increase in SSTs to decrease EIS and aid the transition from stratocumulus to cumulus, creating a positive feedback using the mechanism above. Soden and Vecchi (2011) indicate that some climate models that predict a positive low cloud feedback have a feedback mechanism different than the one described using observations, whereby subtropical subsidence is increased and leads to a reduction in lower tropospheric relative humidity. Apparently, for the models used in this study, the drying of the lower troposphere by subsidence trumps the effect of increasing EIS on low level clouds, contradicting observations of increasing low cloud amount with EIS. Further, Soden and Vecchi (2011)

show that the climate models that exhibit a higher climate sensitivity have a very active and positive low cloud feedback and a large reduction in marine low level clouds. This suggests that the highly sensitive climate models may be erroneously so, since the positive low cloud feedback operating in them is not consistent with the positive low cloud feedback identified from observations.

Although cloud feedbacks due to the change in cloud amount have received more attention, cloud feedbacks due to the change in cloud optical depth may be relevant as well. One of the first low cloud feedbacks proposed in the literature is the negative feedback associated with the Clausius-Clapeyron relationship. As temperature rises, assuming a constant boundary layer relative humidity, the amount of moisture available for boundary layer clouds increases, making them optically thicker and more reflective (Betts and Harshvardhan 1987). More recent observational data from ISCCP and ERBE suggest that this proposed feedback may not be operating in nature since the observed low cloud optical depth actually decreases as temperature rises, creating a positive feedback (Tselioudis and Rossow (1994); Bony et al. (1997)). The physical mechanism responsible for such a decrease in optical thickness with temperature is unclear, but it is hypothesized that increases in precipitation efficiency or dry air entrainment with temperature or perhaps changes in the character of aerosols may be responsible (Tselioudis et al. (1998); Stevens and Feingold (2009)). Stephens (2010) compared low cloud optical depth in two atmospheric models with observations and determined that the models overestimate the optical depth of low clouds by a factor of two, causing an overestimate in shortwave cooling due to low clouds. Further, the modeled low cloud optical depths are so thick that they are in a regime where a change in optical depth produces little change in albedo, whereas clouds in the real world operate in a regime where a small change

in optical depth creates a large change in albedo. For this reason, Stephens (2010) asserts that the low cloud optical depth feedback in models is not nearly sensitive enough and an important negative feedback may be missing.

Given the importance of low clouds through their modulation of the climate system, it is critical that they are properly represented in climate models. Unfortunately, the representation of low clouds and their effects in climate models has been a longstanding issue. Findings from numerous studies suggest that low clouds are misrepresented in at least three ways. The first and perhaps most obvious misrepresentation is their areal extent. Not only is the low cloud amount underestimated in the subsiding regimes of tropical and subtropical oceans (Zhang et al. (2005); Tselioudis and Jakob (2002); Lin and Zhang (2004); Ringer and Allan (2004); Webb et al. (2001); Marchand et al. (2009); Marchand and Ackerman (2010)), but also in the midlatitude extratropics (Zhang et al. (2005); Klein and Jakob (1999); Norris and Weaver (2001)), and even over calm subsiding regions over land (Tselioudis and Jakob 2002). The second misrepresentation of low clouds is their optical thickness. Most of the same models that underestimate the low cloud areal extent also overestimate the optical thickness of the low clouds that are produced (Zhang et al. (2005); Lin and Zhang (2004); Klein and Jakob (1999); Tselioudis and Jakob (2002); Weare (2004)). Such a combination of errors can mask model deficiencies since they tend to compensate for each other in the computation of shortwave cloud forcing (Zhang et al. (2005); Tselioudis and Jakob (2002); Lin and Zhang (2004); Webb et al. (2001)). The third misrepresentation of low clouds is the underestimation of low cloud top heights. This error is especially prevalent in the trade-wind cumulus regions of the tropical oceans (Norris and Weaver (2001); Tselioudis and Jakob (2002); Webb et al. (2001); Marchand et al. (2009)).

The misrepresentation of low clouds has important implications for climate models feedbacks and overall climate sensitivity. Norris and Weaver (2001) found that low clouds in the National Center for Atmospheric Research (NCAR) Community Climate Model (CCM3) are more sensitive to changes in sea level pressure changes than sea surface temperature changes, indicating that the low clouds in the model are controlled more by large-scale dynamics and subsidence than by local SST, counter to observational studies Eitzen et al. (2011). The overestimate of low cloud optical thickness in many climate models leads to an insensitivity to cloud optical depth feedbacks since the low clouds are so thick that they are seen as black in the infrared (Weare 2004). Such an insensitivity has been documented in the Community Atmosphere Model (CAM) (Stephens 2010), European Centre for Medium-Range Weather Forecasts (ECMWF) and Goddard Institute for Space Studies (GISS) climate models (Tselioudis and Jakob 2002), Hadley Centre climate model (Ringer and Allan 2004), Super-parameterized Community Atmosphere Model (SPCAM) (Marchand and Ackerman 2010), and others (Weare 2004). Models with such a misrepresentation are also implied to be insensitive to direct and indirect aerosol effects and their associated feedbacks since small variations in cloud optical properties created by these effects are insignificant when cloud optical depths are high (Weare 2004). Further, Weare (2004) shows that some Atmospheric Model Intercomparison Project (AMIP) II models have a negative correlation between low cloud amount and low cloud optical depth, opposite of what is observed. A positive correlation in the natural world implies that a change in either cloud amount or cloud optical depth by some physical mechanism causes the other metric to change in the same sense, amplifying the original response in terms of cloud radiative forcing. A negative correlation

in the models implies that a change in either variable is opposed by the change in the other, unrealistically muting any model feedbacks.

Many authors have offered reasons as to why specific climate models represent low clouds poorly and others have demonstrated improvements in their representation using a variety of methods. It has long been recognized that the horizontal and vertical resolution of climate models is inadequate to simulate most shallow convection processes (Zhang et al. (2005); Ringer and Allan (2004)), and that sub-10 m resolution might be required for proper simulation of updrafts and downdrafts and entrainment in stratocumulus (Stevens et al. 2005). Nevertheless, grid-spacing sensitivity tests have shown that some improvement in the representation of low clouds can be obtained by increasing vertical resolution modestly in climate models (Tselioudis and Jakob (2002); Marchand and Ackerman (2010)). In much of the tropics and subtropics, shallow convection is limited by the strength of subsidence and the height of the trade inversion – thus it is part of a larger circulation that is at least partially controlled remotely. For this reason, it is necessary (but not sufficient) for climate models to properly calculate the large-scale conditions and the strength of the tropical circulation in order to properly simulate low clouds in this region. Webb et al. (2001) list errors in the large-scale subsidence as one reason why the Hadley and Laboratoire de Météorologie Dynamique (LMD) climate models misrepresent shallow convection. Medeiros and Stevens (2011) point out, however, that even if several aquaplanet atmospheric general circulation models (AGCMs) produce similar and reasonably correct large-scale conditions, the models still seem to have a wide range of representations of low clouds and exhibit large magnitude errors, suggesting that subgrid scale (SGS) parameterizations may be to blame. The boundary layer turbulence scheme has been singled out by many authors as a potential source of

low cloud misrepresentation (Ringer and Allan (2004); Lin and Zhang (2004); Zhang et al. (2005); Tao et al. (2009)). Others have shown that improving the boundary layer turbulence scheme can lead to improvements in the representation of low clouds (Zhang et al. (2005); Noda et al. (2010); Cheng and Xu (2011); Bogenschutz et al. (2012)).

The picture that has emerged from the last several decades of research is that low, shallow clouds are very important for the climate system. They cool the surface with a strongly negative cloud radiative effect, are instrumental in preconditioning the middle troposphere for deeper convection, and represent an important cog in the cloud-climate feedback machinery. Less clear is the precise role they play in those feedbacks. Both positive and negative feedback mechanisms have been proposed for the low cloud amount and the low cloud optical depth. Whether low clouds amplify warming from anthropogenic sources or dampen it is an active and sometimes polemical topic of research. The current generation of climate models could potentially shed some much-needed light on the debate, but unfortunately, they suffer from a varied misrepresentation of low clouds. Errors in low cloud amount are often radiatively compensated for by errors of the opposite sign in low cloud optical depth, complicating interpretations of modeled feedbacks and sensitivity. Improving the representation of low clouds in climate models should therefore be a high priority.

The research presented in this study is intended to make progress toward that goal. Based on the encouraging work of others who have demonstrated improvement in boundary layer cloud representation by improving boundary layer turbulence schemes, the main thrust of this research is to develop a new state-of-the-art SGS parameterization that more accurately represents the processes important for the prediction of boundary layer clouds. Chapter 2 presents this new model in great detail, from the underlying higher-order closure

turbulence scheme to the determination of SGS cloudiness and its interaction with SGS motion, precipitation generation, and radiative transfer. Next, the new model is evaluated by running many standard test cases and comparing its output to the detailed evolution of clouds predicted by an ensemble of large eddy simulations (LESs). In addition, tests are run in order to determine model sensitivities to various configurations and model algorithms. Evaluation of the model and its sensitivities are discussed in chapter 3. An application of the newly created model is demonstrated in chapter 4 where it is run at multiple points along a strategic cross-section in the northeastern Pacific Ocean in order to study low cloud feedbacks and to provide potential insights into the new model's performance if used as a SGS parameterization in a global climate model. Finally, the study is tied together with concluding remarks in chapter 5.

CHAPTER 2

MODEL DESCRIPTION

Traditionally, SGS models have been called “boundary layer” or “turbulence” schemes, but perhaps neither are appropriate titles for a new, **Two-and-a-Half OR**der closure scheme called THOR presented in this work. THOR attempts to bridge the spatial scale gap between processes that can adequately be represented on a very large scale grid in an AGCM and processes that occur on a very fine scale that cannot be adequately represented on such a grid. At its core, THOR uses a higher-order closure scheme that calculates quantities that can be interpreted as the *statistical* state of SGS processes: variances of variables like temperature, humidity, and momentum and covariances among the same variables. Chief among the quantities needed by AGCMs and provided by such a scheme are the “turbulent” fluxes of heat, moisture, and momentum, which are themselves covariances. These “turbulent” fluxes are not only the product of what one may consider classical turbulence, but also processes more akin to ordinary advection (on scales between the classical turbulence scale and the resolved), and physical processes like condensation/evaporation, precipitation, and radiation that occur on scales closer to the molecular level than the grid scale. So, what many may call “turbulence” terms are not really representing turbulence alone, but all processes occurring under the umbrella of subgrid scale. In addition, these SGS processes are not merely confined to the boundary layer, and presumably take place throughout the depth of the atmosphere.

Given the variances and covariances calculated by a higher-order closure scheme that describe the statistical state of SGS processes, improvements may be made to other traditional parameterizations which have heretofore used AGCM grid scale mean variables as

their input. THOR uses the so-called “assumed probability density function (PDF)” approach to accomplish these improvements. This technique uses the grid-scale mean values of temperature, humidity, and vertical velocity from the AGCM together with their variances, covariances, and skewnesses calculated from the higher-order closure model to define a specific trivariate PDF that describes how the variables interact with each other in each grid cell. This PDF provides the probability of finding a particular temperature, humidity, and vertical velocity triplet in each grid cell. One could imagine that the highest probability triplet would be found around the grid-scale mean triplet, and that there is a spread of values around the triplet whose width in each variate direction (and the tilt between variables) is controlled by the SGS processes occurring in that particular grid cell. With this probability information, one can inform the condensation, microphysics, and radiation schemes. For example, one may call many instances of a traditional radiation scheme with varying values of temperature and cloud water based on their probability of occurrence in the column to get a more accurate representation of radiative transfer than using the AGCM grid cell mean values alone.

In the following sections of this chapter, a detailed description of how THOR is formulated and implemented is provided. First, the core higher-order closure model and length scale algorithms are discussed. Next, the new assumed PDF parameter estimation algorithm is included, followed by a discussion of a new SGS condensation scheme that natively includes ice. The next two sections involve using the diagnosed PDF to drive interchangeable microphysics and radiation parameterizations. Next, a new surface layer scheme is explained. The chapter concludes with a short discussion about model implementation and efficiency.

2.1. HIGHER-ORDER CLOSURE MODEL

In an atmospheric model, whether or not it is explicitly stated, it is implicitly assumed that variables being calculated at grid centers are values representing the mean state of the entire grid cell. As a consequence of this relationship, the predictive equations for all variables of interest must be Reynolds averaged so that the evolution of the grid cell mean quantities are predicted. For example, the momentum equation with the Boussinesq approximation valid at each infinitesimal point may be written in Einstein notation as

$$\frac{\partial u_i}{\partial t} = -u_j \frac{\partial u_i}{\partial x_j} + \frac{\theta'_v}{\theta_{v0}} g + f \epsilon_{ij3} u_j - \frac{1}{\rho_0} \frac{\partial p}{\partial x_i} + \nu \frac{\partial^2 u_i}{\partial x_j^2} \quad (1)$$

where the terms on the right-hand side of (1) represent advection, the gravitational acceleration, the Coriolis force, the pressure gradient force, and the frictional drag due to molecular viscosity, respectively. To derive an analogous equation for the grid cell mean value of momentum, Reynolds decomposition is used, whereby the momentum variable, u_i , is divided into its grid-cell mean value and its fluctuation about the grid-cell mean value. The momentum equation is then Reynolds averaged, yielding the following

$$\frac{\partial \overline{u_i}}{\partial t} = -\overline{u_j} \frac{\partial \overline{u_i}}{\partial x_j} - g + f \epsilon_{ij3} \overline{u_j} - \frac{1}{\rho_0} \frac{\partial \overline{p}}{\partial x_i} + \nu \frac{\partial^2 \overline{u_i}}{\partial x_j^2} - \frac{\partial \overline{u'_i u'_j}}{\partial x_j} \quad (2)$$

where every term in equation (2) has an analogous term in equation (1) except for the last term of (2). This term is known as the “turbulence” term and represents the effects of SGS processes on the evolution of the mean momentum field. Such a term is present in the Reynolds averaged thermodynamic and moisture equations too. If one prefers to think in statistical terms, these terms may be thought of as the gradients of variances and covariances.

The term “higher-order closure” model has to do with how the turbulence terms are calculated. A first-order closure model assumes that the turbulence terms act as diffusion, smoothing out gradients in the mean quantities. Such a closure only requires the gradients of the mean quantities themselves and a diffusion coefficient, often signified by the letter K (hence the term “ K -theory”). Higher-order closure models (a general term for any closure higher than first) are based on the idea that one can derive predictive equations from first principles in order to calculate the turbulence terms. These higher-order equations, however, contain terms that cannot be explicitly calculated from quantities known by the host model. For example, the second-order equation for the momentum turbulence term (known as the Reynolds stress equation) contains third-order moments, terms involving the correlation between subgrid pressure perturbations and momentum perturbations, and terms involving the destruction of momentum variance, or turbulence dissipation. Assumptions must be made about each of these terms in order to close the equation set. It should be noted that each order of equations has terms of the next highest order; e.g. second-order equations contain third-order moments, third-order equations contain fourth-order moments, etc. The order of the closure is determined by the order where one makes a simplifying assumption about the nature of the next highest order. It is assumed (but not necessarily true) that errors introduced by simplifying assumptions at higher orders are less offensive than those at lower orders.

The THOR model uses a so-called “two-and-a-half” order closure scheme. Predictive equations are derived for the second- and third-order moments from first principles. Next, closure assumptions are made about the pressure correlation and dissipation terms in both the second- and third-order moment equations and about the fourth-order moments in the

third-order moment equations. Finally, the tendency terms in the third-order moment equations are assumed to be small and are set to zero. Such an assumption is equivalent to stating that the third-order moments change very slowly in time. This allows the third-order moment equations to be manipulated into simple algebraic relations, reducing the computational complexity of the model without sacrificing the underlying physics. This last assumption is what distinguishes this model from a fully third-order closure model, and why it is deemed a two-and-a-half order closure. A detailed derivation of the scheme can be found in Firl (2009), and is based on the dry higher-order closure model of Cheng et al. (2005), although the scheme has been greatly extended for a mixed-phase moist atmosphere. Changes since the work of Firl (2009) include using ice-liquid water potential temperature, θ_{il} , as the thermodynamic energy variable to easier facilitate mixed-phase clouds (instead of θ_l), changing the dissipation terms of the turbulence kinetic energy (TKE) component equations, altering constants used in the various closure assumptions, and a few changes in the calculation of the diagnostic third-order moments. The latter two are discussed further below.

The predictive second-order moment equations in Einstein notation with parameterizations for the pressure correlation and dissipation terms are as follows.

$$\begin{aligned} \frac{\partial \overline{u'_i u'_j}}{\partial t} = & -\overline{w' u'_i} \frac{\partial \overline{u_j}}{\partial z} - \overline{w' u'_j} \frac{\partial \overline{u_i}}{\partial z} - \frac{\partial \overline{w' u'_i u'_j}}{\partial z} - \frac{2c_4}{\tau_p} \left(\overline{u'_i u'_j} - \frac{2}{3} \delta_{ij} \bar{e} \right) \\ & + \delta_{ij} \frac{g}{\theta_v} \overline{w' \theta'_v} \left[2\delta_{3i} + c_5 \left(\frac{2}{3} - 2\delta_{3i} \right) \right] - \frac{4}{3} \delta_{ij} \frac{\bar{e}}{\tau} \end{aligned} \quad (3)$$

$$\frac{\partial \overline{w' \theta'_{il}}}{\partial t} = -\overline{w'^2} \frac{\partial \overline{\theta_{il}}}{\partial z} - \frac{\partial \overline{w'^2 \theta'_{il}}}{\partial z} + (1 - c_7) \frac{g}{\theta_v} \overline{\theta'_{il} \theta'_v} - \frac{2c_6}{\tau_p} \overline{w' \theta'_{il}} \quad (4)$$

$$\frac{\partial \overline{w' q'_t}}{\partial t} = -\overline{w'^2} \frac{\partial \overline{q_t}}{\partial z} - \frac{\partial \overline{w'^2 q'_t}}{\partial z} + (1 - c_7) \frac{g}{\theta_v} \overline{q'_t \theta'_v} - \frac{2c_6}{\tau_p} \overline{w' q'_t} \quad (5)$$

$$\frac{\partial \overline{\theta'_{il}{}^2}}{\partial t} = -2\overline{w'\theta'_{il}} \frac{\partial \overline{\theta_{il}}}{\partial z} - \frac{\partial \overline{w'\theta'_{il}{}^2}}{\partial z} - \frac{4c_2}{\tau} \overline{\theta'_{il}{}^2} \quad (6)$$

$$\frac{\partial \overline{\theta'_{il}q'_t}}{\partial t} = -\overline{w'\theta'_{il}} \frac{\partial \overline{q_t}}{\partial z} - \overline{w'q'_t} \frac{\partial \overline{\theta_{il}}}{\partial z} - \frac{\partial \overline{w'\theta'_{il}q'_t}}{\partial z} - \frac{4c_2}{\tau} \overline{\theta'_{il}q'_t} \quad (7)$$

$$\frac{\partial \overline{q_t^2}}{\partial t} = -2\overline{w'q'_t} \frac{\partial \overline{q_t}}{\partial z} - \frac{\partial \overline{w'q_t^2}}{\partial z} - \frac{4c_2}{\tau} \overline{q_t^2} \quad (8)$$

where $i = 1, 2, 3$ and $\bar{e} = 1/2 (\overline{u'^2} + \overline{v'^2} + \overline{w'^2})$ is the TKE and all buoyancy terms (those that involve θ_v) are given by the relation

$$\overline{\chi'\theta'_v} = \overline{\chi'\theta'_{il}} + \varepsilon_1 \theta_{v0} \overline{\chi'q'_t} + \left(\frac{L_v}{c_p \pi} - \varepsilon_2 \theta_{v0} \right) \overline{\chi'q'_l} + \left(\frac{L_s}{c_p \pi} - \varepsilon_2 \theta_{v0} \right) \overline{\chi'q'_i} \quad (9)$$

In equation (9), χ denotes any of the variables w , θ_{il} , or q_t , $\varepsilon_1 = \frac{1-\varepsilon}{\varepsilon}$, $\varepsilon_2 = \frac{1}{\varepsilon}$, $\varepsilon = \frac{R_d}{R_v}$, R_d is the gas constant for dry air, R_v is the gas constant for water vapor, L_v and L_s are the latent heats of vaporization and fusion, c_p is the specific heat of dry air at constant pressure, and $\pi = \left(\frac{p}{p_0} \right)^{\frac{R_d}{c_p}}$ is the Exner function. The last two terms of (9) contain correlations involving cloud water, and must be calculated with the SGS condensation scheme discussed in section 2.4. Note that equations (3) - (8) assume that turbulence in the horizontal orientation is small compared to the vertical orientation (an assumption based on the asymmetry of atmospheric model grids). Therefore, only vertical derivatives are kept, and horizontal fluxes are ignored. Due to this assumption, this equation set expanded from Einstein notation represents 10 total predictive equations (equation (3) describes the evolution of $\overline{u'^2}$, $\overline{v'^2}$, $\overline{w'^2}$, $\overline{w'u'}$, and $\overline{w'v'}$). It should be noted that only four of the second-order moments are needed directly by the host model predicting grid-cell mean quantities: $\overline{w'\theta'_{il}}$, $\overline{w'q'_t}$, $\overline{w'u'}$, and $\overline{w'v'}$. The other 6 variances and covariances calculated in this set are needed to close the set of equations through the buoyancy, pressure correlation, or dissipation terms. In addition, $\overline{\theta'_{il}{}^2}$, $\overline{\theta'_{il}q'_t}$, and

$\overline{q_t'^2}$ are instrumental for calculating SGS condensation and other parameterizations included in THOR. The quantities $\overline{u'v'}$, $\overline{u'\theta'_{il}}$, $\overline{u'q'_t}$, $\overline{v'\theta'_{il}}$, and $\overline{v'q'_t}$ are neglected.

The variances and covariances predicted in THOR are subject to some realizability constraints. For example, since all variances are positive-definite quantities, if the model predicts a negative variance, the offending quantity is simply set to a very small positive number. Since variances are not conserved, this correction is sufficient. In addition, the covariances $\overline{w'\theta'_{il}}$, $\overline{w'q'_t}$, and $\overline{\theta'_{il}q'_t}$ must be checked to ensure that their associated correlations are realistic, i.e.

$$\begin{aligned}
-1 &\leq \frac{\overline{w'\theta'_{il}}}{\sqrt{\overline{w'^2\theta'_{il}{}^2}}} \leq 1 \\
-1 &\leq \frac{\overline{w'q'_t}}{\sqrt{\overline{w'^2q_t'^2}}} \leq 1 \\
-1 &\leq \frac{\overline{\theta'_{il}q'_t}}{\sqrt{\overline{\theta'_{il}{}^2q_t'^2}}} \leq 1
\end{aligned} \tag{10}$$

The two types of closure assumptions included in equations (3) - (8) are pressure correlations and turbulence dissipation. The parameterizations are listed in tables 2.1 and 2.2 and are exactly as described in Cheng et al. (2005). The pressure correlation closure contains two terms: a so-called “return-to-isotropy” term and a buoyancy-related term. The return-to-isotropy term is formulated to act slowly to destroy anisotropic fluxes and the buoyancy-related term is formulated to act quickly and counteracts the buoyancy production term of the TKE components and scalar fluxes. The dissipation closure simply damps the TKE components and scalar variances and covariance according to a turbulence time scale, τ .

TABLE 2.1. Pressure correlation parameterizations for the second-order moment equations

Moment	Parameterization
$\overline{u'_i u'_j}$	$\frac{2c_4}{\tau_p} \left(\overline{u'_i u'_j} - \frac{2}{3} \delta_{ij} \bar{e} \right) + c_5 \frac{g}{\theta_v} \overline{w' \theta'_v} \delta_{ij} \left(\frac{2}{3} - 2\delta_{3i} \right)$
$\overline{w' \theta'_{il}}$	$\frac{2c_6}{\tau_p} \overline{w' \theta'_{il}} + c_7 \frac{g}{\theta_v} \overline{\theta'_{il} \theta'_v}$
$\overline{w' q'_t}$	$\frac{2c_6}{\tau_p} \overline{w' q'_t} + c_7 \frac{g}{\theta_v} \overline{q'_t \theta'_v}$

TABLE 2.2. Dissipation parameterizations for the second-order moment equations

Moment	Parameterization
$\overline{u'_i u'_j}$	$-\frac{4}{3} \delta_{ij} \frac{\bar{e}}{\tau}$
$\overline{\theta'^2_{il}}$	$-\frac{4c_2}{\tau} \overline{\theta'^2_{il}}$
$\overline{\theta'_{il} q'_t}$	$-\frac{4c_2}{\tau} \overline{\theta'_{il} q'_t}$
$\overline{q'^2_t}$	$-\frac{4c_2}{\tau} \overline{q'^2_t}$

The dissipation time scale is defined as

$$\tau = \frac{L}{\bar{e}} \quad (11)$$

where L is the turbulence length scale that provides a measure of the largest energy-containing eddies (discussed in section 2.2). It can therefore be interpreted as an average residence time in an energy-containing turbulent eddy. The return-to-isotropy timescale, τ_p , is defined as

$$\tau_p = \begin{cases} \frac{\tau}{1 + 0.04N^2\tau^2} & \text{if } N^2 > 0 \\ \tau & \text{if } N^2 \leq 0 \end{cases} \quad (12)$$

where N^2 is the Brunt-Väisälä frequency. This timescale is identical to the dissipation time scale under neutral or unstable conditions, but is smaller than the dissipation timescale for conditions of greater stability. This formulation leads to increased destruction of anisotropic fluxes in stable environments. Use of a return-to-isotropy timescale has not been universal for these types of models in the literature, but was used in the higher-order closure models of Cheng et al. (2005) and its precursor Canuto et al. (1994). The latter work claims that use of (12) improves the behavior of the higher-order closure model near inversions.

The closure constants are tunable parameters and have taken on a range of values in the literature. The constant c_2 controls the rate of dissipation of scalar covariances and is set to 0.2. The constants c_4 and c_6 come from the return-to-isotropy terms of the pressure correlation closure. These are set at 2.0 and 2.5, respectively. The constants c_5 and c_7 come from the buoyancy-related terms of the pressure correlation closure. While c_5 is set to 0, it was found that a single value for c_7 was an inappropriate choice. A higher value of c_7 leads to better simulations in cumulus regimes, whereas a lower value leads to better simulations in stratocumulus and stratus regimes. A physical explanation for this is unknown, but it seems that the pressure correlation term more effectively balances out the production of turbulent fluxes due to buoyancy in cumulus regimes versus more stratified cloud regimes. Perhaps the lack of an appropriate single value to use speaks to the inadequacy of the pressure correlation closure for cloudy boundary layers, as it was devised assuming a dry atmosphere. Nevertheless, a procedure has been implemented to provide an appropriate value of c_7 to use in THOR depending on the state of the mean thermodynamic profiles.

Work by Wood and Bretherton (2006) has shown that there is a very good correlation between a quantity known as estimated inversion strength (EIS) and low cloud cover. This

work has built on the well-known relationship between lower tropospheric stability (LTS) and low cloud cover, but provides an even more robust relationship and is thought to be more applicable even in a changed climate. The EIS-low cloud cover relationship is useful in this context because EIS is a very simple quantity to calculate in a model and it provides a good indication of whether the model is operating in an environment more conducive to stratified cloud cover or cumulus-like cloud cover, and therefore what value of c_7 is appropriate to use. The relationship is used in the following way to determine c_7 . First, the EIS is calculated according to appendix A. Then, the following linear relationship from Wood and Bretherton (2006) is used to determine an EIS cloud fraction:

$$\text{EIS cloud fraction} = 0.14 + 0.06 * \text{EIS} \quad (13)$$

Finally, the value of c_7 is equal to its cumulus-like value under a certain EIS cloud fraction threshold and equal to its stratiform-like value over a certain EIS cloud fraction threshold.

In between, the value of c_7 is interpolated:

$$c_7 = \begin{cases} 0.9 & \text{EIS cloud fraction} < 0.32 \\ 0.9 + \frac{\text{EIS cloud fraction} - 0.32}{0.60 - 0.32} (0.6 - 0.9) & 0.32 \leq \text{EIS cloud fraction} < 0.60 \\ 0.6 & \text{EIS cloud fraction} \geq 0.6 \end{cases} \quad (14)$$

Such a formulation provides an adequate value of c_7 to use under any regime and facilitates good simulation of all boundary layer cloud types. It should be noted that there is precedent for attempting to fine-tune higher-order closure constants. Golaz et al. (2007) found that varying model constants according to the skewness of the vertical velocity could improve a higher-order closure model's simulation.

The last pieces of information required to close equations (3) - (8) are the variance and covariance transport terms made up of third-order moments. A list of the necessary third-order moments are shown in table 2.3. As mentioned previously, the third-order moments are diagnostic and are adapted from the work of Cheng et al. (2005). The relations for calculating them are given by equations (15)-(26).

TABLE 2.3. Third-order moments calculated in THOR

Moments from Equations (3)-(8)	$\overline{w'w'u'}, \overline{w'w'v'}, \overline{w'u'u'},$ $\overline{w'v'v'}, \overline{w'w'w'}, \overline{w'w'\theta'_{il}}, \overline{w'w'q'_t},$ $\overline{w'\theta'_{il}\theta'_{il}}, \overline{w'\theta'_{il}q'_t}, \overline{w'q'_tq'_t}$
Add'l Moments for PDF Diagnosis	$\overline{\theta'_{il}\theta'_{il}\theta'_{il}}, \overline{q'_tq'_tq'_t}$

$$\overline{w'^3} = \frac{3\tau}{2c_8 + p_1 + 3(1 - d_1)\tau \frac{\partial \overline{w}}{\partial z}} \left(-\overline{w'^2} \frac{\partial \overline{w'^2}}{\partial z} + \lambda \overline{w'^2 \theta'_v} \right) \quad (15)$$

$$\overline{w'w'\theta'_{il}} = \frac{1}{\frac{2c_8 + p_2}{\tau} + 2(1 - d_3) \frac{\partial \overline{w}}{\partial z}} \left(-\overline{w'\theta'_{il}} \frac{\partial \overline{w'^2}}{\partial z} - 2\overline{w'^2} \frac{\partial \overline{w'\theta'_{il}}}{\partial z} + 2\lambda \overline{w'\theta'_{il}\theta'_v} \right. \\ \left. - (1 - d_2) \frac{\partial \overline{\theta'_{il}}}{\partial z} \overline{w'w'w'} \right) \quad (16)$$

$$\overline{w'w'q'_t} = \frac{1}{\frac{2c_8 + p_4}{\tau} + 2(1 - d_7) \frac{\partial \overline{w}}{\partial z}} \left(-\overline{w'q'_t} \frac{\partial \overline{w'^2}}{\partial z} - 2\overline{w'^2} \frac{\partial \overline{w'q'_t}}{\partial z} + 2\lambda \overline{w'q'_t\theta'_v} \right. \\ \left. - (1 - d_6) \frac{\partial \overline{q'_t}}{\partial z} \overline{w'w'w'} \right) \quad (17)$$

$$\overline{w'w'u'} = \frac{\tau}{(2c_8 + p_{17}) + \tau(1 - d_{31}) \frac{\partial \bar{w}}{\partial z}} \left(-\overline{w'u'} \frac{\partial \bar{w}^2}{\partial z} - 2\overline{w'^2} \frac{\partial \bar{w}u}{\partial z} + 2\lambda \overline{w'u'\theta'_v} \right. \\ \left. - 2(1 - d_{32}) \frac{\partial \bar{u}}{\partial z} \overline{w'w'w'} \right) \quad (18)$$

$$\overline{w'w'v'} = \frac{\tau}{(2c_8 + p_{23}) + \tau(1 - d_{46}) \frac{\partial \bar{w}}{\partial z}} \left(-\overline{w'v'} \frac{\partial \bar{w}^2}{\partial z} - 2\overline{w'^2} \frac{\partial \bar{w}v}{\partial z} + 2\lambda \overline{w'v'\theta'_v} \right. \\ \left. - 2(1 - d_{47}) \frac{\partial \bar{v}}{\partial z} \overline{w'w'w'} \right) \quad (19)$$

$$\overline{w'\theta'_{il}\theta'_{il}} = \frac{1}{\frac{2c_8 + p_3}{\tau} + (1 - d_5) \frac{\partial \bar{w}}{\partial z}} \left(-2\overline{w'\theta'_{il}} \frac{\partial \bar{w}\theta'_{il}}{\partial z} - \overline{w'^2} \frac{\partial \bar{\theta}_{il}^2}{\partial z} + \lambda \overline{\theta'_{il}\theta'_{il}\theta'_v} \right. \\ \left. - (2 - d_4) \frac{\partial \bar{\theta}_{il}}{\partial z} \overline{w'w'\theta'_{il}} \right) \quad (20)$$

$$\overline{w'\theta'_{il}q'_t} = \frac{1}{\frac{2c_8 + p_6}{\tau} + (1 - d_{12}) \frac{\partial \bar{w}}{\partial z}} \left(-\overline{w'q'_t} \frac{\partial \bar{w}\theta'_{il}}{\partial z} - \overline{w'\theta'_{il}} \frac{\partial \bar{w}q'_t}{\partial z} - \overline{w'^2} \frac{\partial \bar{\theta}'_{il}q'_t}{\partial z} \right. \\ \left. + \lambda \overline{\theta'_{il}q'_t\theta'_v} - (1 - d_{10}) \frac{\partial \bar{\theta}_{il}}{\partial z} \overline{w'w'q'_t} - (1 - d_{11}) \frac{\partial \bar{q}_t}{\partial z} \overline{w'w'\theta'_{il}} \right) \quad (21)$$

$$\overline{w'q'_tq'_t} = \frac{1}{\frac{2c_8 + p_5}{\tau} + (1 - d_9) \frac{\partial \bar{w}}{\partial z}} \left(-2\overline{w'q'_t} \frac{\partial \bar{w}q'_t}{\partial z} - \overline{w'^2} \frac{\partial \bar{q}_t^2}{\partial z} + \lambda \overline{q'_tq'_t\theta'_v} \right. \\ \left. - (2 - d_8) \frac{\partial \bar{q}_t}{\partial z} \overline{w'w'q'_t} \right) \quad (22)$$

$$\overline{w'u'u'} = \frac{1}{\frac{2c_8+p_{11}}{\tau} + (1-d_{20})\frac{\partial\bar{w}}{\partial z}} \left(-2\overline{w'u'}\frac{\partial\overline{w'u'}}{\partial z} - \overline{w'^2}\frac{\partial\overline{u'^2}}{\partial z} + \lambda\overline{u'u'\theta'_v} - 2(1-d_{19})\frac{\partial\bar{u}}{\partial z}\overline{w'u'u'} \right) \quad (23)$$

$$\overline{w'v'v'} = \frac{1}{\frac{2c_8+p_{14}}{\tau} + (1-d_{26})\frac{\partial\bar{w}}{\partial z}} \left(-2\overline{w'v'}\frac{\partial\overline{w'v'}}{\partial z} - \overline{w'^2}\frac{\partial\overline{v'^2}}{\partial z} + \lambda\overline{v'v'\theta'_v} - 2(1-d_{25})\frac{\partial\bar{v}}{\partial z}\overline{w'v'v'} \right) \quad (24)$$

$$\overline{\theta'_{il}\theta'_{il}\theta'_{il}} = \frac{\tau}{2c_{10} + p_7} \left(-3\overline{w'\theta'_{il}}\frac{\partial\overline{\theta'^2_{il}}}{\partial z} - (3-d_{13})\frac{\partial\bar{\theta}_{il}}{\partial z}\overline{w'\theta'_{il}\theta'_{il}} \right) \quad (25)$$

$$\overline{q'_t q'_t q'_t} = \frac{\tau}{2c_{10} + p_{10}} \left(-3\overline{w'q'_t}\frac{\partial\overline{q'^2_t}}{\partial z} - (3-d_{18})\frac{\partial\bar{q}_t}{\partial z}\overline{w'q'_t q'_t} \right) \quad (26)$$

where $\lambda = \frac{\tau_l}{\tau} (1 - c_{11}) \frac{g}{\theta_v}$ and $\tau_l = \text{MIN}(600 \text{ s}, \tau)$. Such a capping of τ_l was necessary to prevent the third-order moments from growing too large when there is little turbulence or when the length scale is long (when τ is large).

As with the second-order moments, equations (15)-(26) include closures for the pressure correlation and dissipation terms, but also for the fourth-order moments. They were derived in the same manner as the second-order moment equations (see Firl (2009) for details). The full prognostic third-order moment equations were derived from first principles and the closure assumptions from Cheng et al. (2005) were substituted for the unknown terms. Finally, the time rate-of-change terms were assumed to be zero. The terms in the pressure correlation closure are analogs to the same terms in the second-order moments. There is a

slow-acting return-to-isotropy term that damps the third-order moments, governed by the constant c_8 , and a fast-acting buoyancy term that counteracts the buoyancy production term, governed by the constant c_{11} . These constants are set equal to 3.25 and 0.4, respectively. The dissipation closure term is a simple damping, governed by the turbulence time scale, τ , and modified by the constant c_{10} , set at 2.0. The fourth-order moment closure is effectively an extension of the typical one used in third-order closure models that is based on the idea that fourth-order moments may be parameterized using the so-called “quasi-normal assumption”, i.e. $\overline{a'b'c'd'} = \overline{a'b'} * \overline{c'd'} + \overline{a'c'} * \overline{b'd'} + \overline{a'd'} * \overline{b'c'}$. Cheng et al. (2005) extend this closure by including an additional damping term, governed by the constants p_n using the τ timescale, and a term that partially negates the so-called mechanical production terms, governed by the constants d_n . The authors claim that these additional terms help to account for the non-Gaussian portion of the fourth-order moments that is neglected with the classic quasi-normal assumption. Using LES data, they determine that the best values of the constants d_n to use *completely* negates the mechanical production terms. Initial tests with THOR, however, indicate that using the values for the d_n constants suggested by Cheng et al. (2005) damps the values of $\overline{\theta'_{il}\theta'_{il}\theta'_{il}}$ and $\overline{q'_tq'_tq'_t}$ too much. Therefore, values of d_n in THOR follow those used in Cheng et al. (2005), except for those associated with $\overline{\theta'_{il}\theta'_{il}\theta'_{il}}$ and $\overline{q'_tq'_tq'_t}$, d_{13} and d_{18} , which are set to 0. Such a modification improves the magnitudes of these particular third-order moments and leads to better performance of the SGS condensation scheme, which uses these moments to estimate the assumed PDF parameters.

The third-order buoyancy terms are given by a similar equation to (9):

$$\overline{\chi'_1\chi'_2\theta'_v} = \overline{\chi'_1\chi'_2\theta'_{il}} + \varepsilon_1\theta_{v_0}\overline{\chi'_1\chi'_2q'_t} + \left(\frac{L_v}{c_p\pi} - \varepsilon_2\theta_{v_0}\right)\overline{\chi'_1\chi'_2q'_l} + \left(\frac{L_s}{c_p\pi} - \varepsilon_2\theta_{v_0}\right)\overline{\chi'_1\chi'_2q'_i} \quad (27)$$

where the symbols χ_1 and χ_2 correspond to any of the variables u, v, w, θ_{il} , or q_t . If one were to use equation (27) in its entirety, it would require an additional 16 third-order moments to close the system, a significant increase in complexity and computational burden. In THOR, however, it is assumed that the cloud water terms (the last two terms in (27)) dominate the buoyancy terms and that there is significant cancelation between the first two terms, making their sum small, and allowing their neglect. In initial tests with THOR using the additional 16 third-order moments and equation (27) in its entirety, two undesirable effects were noted. First, significant noise was introduced into the solution, affecting the model's stability. Second, transport of TKE and heat and moisture fluxes were underestimated, especially in cumulus regimes, due to the buoyancy terms having the wrong sign at the top of the cloud layer. Perhaps further research is warranted to understand why the inclusion of the proper terms leads to undesirable effects in this model.

2.2. TURBULENCE SCALES

The turbulence length scale used in THOR is mostly the same as that used in Firl (2009) with the addition of an option to use an updated parcel entrainment algorithm. The overarching concept remains – the length scale is based on the mean free path of a parcel as in Bougeault and André (1986). Parcels are initialized with the environmental values of liquid-ice potential temperature and moisture content and given an initial kinetic energy equal to the environmental TKE. They are allowed to ascend and descend, losing or gaining kinetic energy due to the buoyancy accelerations of the environment. As a parcel ascends or descends, it may undergo condensation, generating parcel cloud water or ice. Further, as parcels move through the environment, they entrain environmental air into them. The standard formulation of THOR uses a constant fractional entrainment rate of $6.0 \times 10^{-4} \text{ m}^{-1}$,

as done in Golaz et al. (2002). An option has been added in THOR to relax the assumption of constant entrainment and to use a more physically realistic entrainment parameterization instead. The new parameterization treats entrainment as a stochastic Poisson process, incorporating discrete entrainment events following the LES study of Roms and Kuang (2010). THOR's sensitivity to this new entrainment option is tested and discussed in chapter 3.

For both entrainment options, the master length scale is defined as

$$L = \sqrt{L_{up}L_{down}} \quad (28)$$

where L_{up} and L_{down} are the upward and downward mean free path distances for a parcel originating at any level and are themselves defined by

$$\int_{z_0}^{z_0+L_{up}} \frac{g}{\theta_v} [\theta_{v_{parcel}}(z) - \bar{\theta}_v(z)] dz = -\bar{e}(z_0) \quad (29)$$

and

$$\int_{z_0-L_{down}}^{z_0} \frac{g}{\theta_v} [\theta_{v_{parcel}}(z) - \bar{\theta}_v(z)] dz = \bar{e}(z_0) \quad (30)$$

For a discretized model, the algorithm for determining L_{up} is as follows. For each level in the model with height of z_0 , initialize a parcel with the environmental values at that level

$$\begin{aligned} \theta_{il_{parcel}} &= \bar{\theta}_{il}(z_0) \\ q_{t_{parcel}} &= \bar{q}_t(z_0) \\ \text{energy}_{parcel} &= \bar{e}(z_0) \end{aligned} \quad (31)$$

While the parcel energy is greater than zero, attempt to lift the parcel one grid level upward, to height $z_1 = z_0 + \Delta z$.

As the parcel ascends, it may undergo entrainment. Assuming a constant entrainment rate, the thermodynamic properties of the parcel at height z_1 would be

$$\begin{aligned}\theta_{il_{parcel}(z_1)} &= \theta_{il_{parcel}(z_0)} + \Delta z \left\{ -\mu \left[\theta_{il_{parcel}(z_0)} - 1/2 (\overline{\theta_{il}}(z_0) + \overline{\theta_{il}}(z_1)) \right] \right\} \\ q_{t_{parcel}(z_1)} &= q_{t_{parcel}(z_0)} + \Delta z \left\{ -\mu \left[q_{t_{parcel}(z_0)} - 1/2 (\overline{q_t}(z_0) + \overline{q_t}(z_1)) \right] \right\}\end{aligned}\tag{32}$$

where μ is the fractional entrainment rate. If the assumption of constant entrainment is relaxed, it is recognized that as the parcel ascends, it has a certain probability of undergoing an entrainment event, and the process for determining entrainment is as follows. According to the stochastic parcel model of Romps and Kuang (2010), the probability that a parcel undergoes an entrainment event over a distance Δz is given by $\frac{\Delta z}{\lambda}$ where λ is the mean distance between entrainment events in meters. To determine whether an entrainment event has occurred as the parcel ascended one level, draw a uniform random number on the interval $(0, 1]$. If the random number is less than $\frac{\Delta z}{\lambda}$, then an entrainment event has occurred. Otherwise, $\theta_{il_{parcel}}$ and $q_{t_{parcel}}$ remain the same. If an entrainment event has occurred, one still needs to determine the proportion of the parcel's mass that is replaced by the entrained environmental air. Romps and Kuang (2010) assume that the fractional mass of entrained air follows an exponential distribution. Using this assumption, one may obtain a value for σ , the ratio of entrained mass to parcel mass, if one knows $\overline{\sigma}$, the mean value of the exponential distribution. A random value of σ is generated from the exponential distribution using the formula

$$\sigma = -\frac{\overline{\sigma}}{\ln(x)}\tag{33}$$

where x is a uniform random number on $(0, 1]$. Finally, the new parcel values of θ_{il} and q_t are calculated with

$$\begin{aligned}\theta_{il_{parcel}(z_1)} &= \frac{1}{1 + \sigma} \theta_{il_{parcel}(z_0)} + \frac{\sigma}{1 + \sigma}^{1/2} (\overline{\theta_{il}}(z_0) + \overline{\theta_{il}}(z_1)) \\ q_{t_{parcel}(z_1)} &= \frac{1}{1 + \sigma} q_{t_{parcel}(z_0)} + \frac{\sigma}{1 + \sigma}^{1/2} (\overline{q_t}(z_0) + \overline{q_t}(z_1))\end{aligned}\tag{34}$$

Romps and Kuang (2010) determined that the best fit values for λ and σ for shallow cumulus using LES and a parcel model are $\lambda = 226$ m and $\bar{\sigma} = 0.91$. This corresponds to a fractional entrainment rate of about $4.0 \times 10^{-3} \text{ m}^{-1}$. Note that this is considerably stronger entrainment than is assumed by the similar length scale parameterization of Golaz et al. (2002) where the fractional entrainment rate is assumed to be a constant value of $6.0 \times 10^{-4} \text{ m}^{-1}$. For the sensitivity test, the value of $\bar{\sigma}$ is reduced to 0.1356, which corresponds to the lower fractional entrainment rate of Golaz et al. (2002), so that the stochastic entrainment algorithm is more easily compared to the the constant entrainment rate case.

Regardless of the entrainment process chosen, as the parcel ascends, its temperature and pressure decrease, and it is possible that the initially dry parcel may reach saturation and form a cloud. Since condensation releases latent heat, the formation of a cloud in the parcel would boost its buoyancy relative to the environment, so potential condensation should be accounted for in the parcel model. The parcel θ_v is given by

$$\theta_{v_{parcel}} = \theta_{il_{parcel}} + \varepsilon_1 \theta_{v_0} q_{t_{parcel}} + \left(\frac{L_v}{c_p \pi} - \varepsilon_2 \theta_{v_0} \right) q_{l_{parcel}} + \left(\frac{L_s}{c_p \pi} - \varepsilon_2 \theta_{v_0} \right) q_{i_{parcel}}\tag{35}$$

After entrainment has been taken care of, $\theta_{il_{parcel}}$ and $q_{t_{parcel}}$ are known and only liquid and ice water contents are needed to determine the parcel θ_v . One can determine $q_{l_{parcel}}$ and

$q_{i_{parcel}}$ using a procedure similar to that found in the SGS condensation scheme (see section 2.4), minus the SGS variability aspect. The simplified procedure is included in appendix B.

At this point, $\theta_{v_{parcel}}$ is known and one can determine whether it has enough energy to have ascended the distance Δz . To do this, the convective available potential energy (CAPE) over Δz needs to be calculated. Since $\theta_{v_{parcel}}$ and $\bar{\theta}_v$ are known at z_0 and z_1 , the CAPE is calculated as

$$\int_{z_0}^{z_1} \frac{g}{\theta_v} [\theta_{v_{parcel}}(z) - \bar{\theta}_v(z)] dz = 1/2 \left\{ \left[\frac{g}{\bar{\theta}_v(z_1)} (\theta_{v_{parcel}}(z_1) - \bar{\theta}_v(z_1)) \right] + \left[\frac{g}{\bar{\theta}_v(z_0)} (\theta_{v_{parcel}}(z_0) - \bar{\theta}_v(z_0)) \right] \right\} (z_1 - z_0) \quad (36)$$

This quantity represents the CAPE (or convective inhibition (CIN)) between the levels z_0 and z_1 . If positive, the parcel is accelerated upward, and, if negative, the parcel energy is decreased by the CIN and it decelerates. Further, if

$$\text{energy}_{parcel}(z_0) + \text{RHS}(36) > 0 \quad (37)$$

then the parcel has sufficient energy to ascend by Δz , and L_{up} for the parcel originating at z_0 increases by Δz . The parcel energy is then updated for the level z_1

$$\text{energy}_{parcel}(z_1) = \text{energy}_{parcel}(z_0) + \text{RHS}(36) \quad (38)$$

and the process is repeated for the parcel over the next vertical grid space, including potential entrainment and condensation.

If, on the other hand,

$$\text{energy}_{parcel}(z_0) + \text{RHS}(36) \leq 0 \quad (39)$$

then the parcel does not have sufficient energy to ascend the entire Δz distance and the precise level of neutral buoyancy between z_0 and z_1 needs to be determined. Consider equation (29) modified so that the upper limit reflects the height of neutral buoyancy

$$\int_{z_0}^{z_{nb}} \underbrace{\frac{g}{\theta_v} [\theta_{v_{parcel}}(z) - \bar{\theta}_v(z)]}_B dz = -\bar{e}(z_0) \quad (40)$$

The B term, while it only has values at discrete levels in a model, can be determined at any height between z_0 and z_1 , z , using linear interpolation

$$B(z) = \frac{B(z_1) - B(z_0)}{z_1 - z_0} (z - z_0) + B(z_0) \quad (41)$$

Substituting equation (41) into equation (40) yields the integral

$$\int_{z_0}^{z_{nb}} \frac{B(z_1) - B(z_0)}{z_1 - z_0} (z - z_0) + B(z_0) dz = -\bar{e}(z_0) \quad (42)$$

Integration yields

$$\frac{B(z_1) - B(z_0)}{z_1 - z_0} \left(\frac{z_{nb}^2}{2} - \frac{z_0^2}{2} - z_{nb}z_0 + z_0^2 \right) + B(z_0) (z_{nb} - z_0) + \bar{e}(z_0) = 0 \quad (43)$$

Solving for z_{nb} yields the following quadratic equation in z_{nb}

$$\frac{B(z_1) - B(z_0)}{2(z_1 - z_0)} z_{nb}^2 + \left(B(z_0) - \frac{B(z_1) - B(z_0)}{z_1 - z_0} z_0 \right) z_{nb} + \frac{B(z_1) - B(z_0)}{2(z_1 - z_0)} z_0^2 - B(z_0)z_0 + \bar{e}(z_0) = 0 \quad (44)$$

If $B(z_1) = B(z_0)$ then z_{nb} reduces to

$$z_{nb} = z_0 - \frac{\bar{e}(z_0)}{B(z_0)} \quad (45)$$

Note that the second term must be positive since $B(z_0)$ must be negative if a parcel's energy is to be "consumed" by the buoyancy force. If $B(z_1) \neq B(z_0)$ then

$$z_{nb} = z_0 - \frac{(z_1 - z_0)}{B(z_1) - B(z_0)} \left(B(z_0) + \sqrt{B^2(z_0) - \frac{2\bar{e}(z_0)(B(z_1) - B(z_0))}{z_1 - z_0}} \right) \quad (46)$$

where the negative root of equation (44) is the physical solution. Every parcel reaches its neutral buoyancy level at some point, so equation (45) or equation (46) is the last step for determining L_{up} for every parcel after it has ascended any number of grid levels. A similar procedure is used for determining L_{down} .

As in Firl (2009) and Golaz et al. (2002), both L_{up} and L_{down} are "nonlocalized" by considering parcels originating at other levels. For L_{up} , if a parcel originating below a given level, say, from the surface, reaches a height higher than a parcel originating at that level, then L_{up} is calculated using the height reached by the higher-ending parcel. Similarly, for L_{down} , parcels originating above a given level may descend further than parcels originating at the given level. In this case, L_{down} is calculated using the lower-ending parcel. This procedure significantly improves continuity in the calculation of the length scale and reduces computational noise.

The procedure for calculating the turbulence length scale is called at a longer time step than the prognostic variables (on the order of 1 minute) since it is assumed that this quantity changes more slowly than the second-order moments. This speeds up the computation while affecting the solution very little. In addition, a minimum value of the master length scale, L is assumed to be related to the grid spacing ($L_{min} = \frac{1}{4}\Delta z$), a minimum value of TKE is assumed to be $0.01 \text{ m}^2\text{s}^{-2}$, and the maximum value of τ is assumed to be 2000 s.

2.3. TRIVARIATE DOUBLE-GAUSSIAN PDF PARAMETER ESTIMATION

Between a host model providing grid-cell mean quantities and the higher-order closure model discussed above providing information about the SGS variability within each grid cell, there is *almost* enough information to diagnose a trivariate PDF among vertical velocity, ice-liquid water potential temperature, and total water specific humidity so that one has a good estimate of the probability of finding a particular (w, θ_{il}, q_t) triplet in each grid cell. The remaining requirement is that one assumes a particular PDF family, i.e. single Gaussian, beta, double Gaussian, etc. The choice of PDF family should depend on how well it can describe the SGS variability of the atmospheric conditions of interest.

A single joint Gaussian distribution would be appropriate if one expected very similar or homogeneous conditions throughout the grid box, with only a simple spread around the mean values. Indeed, early versions of SGS condensation schemes assumed a simple single joint Gaussian PDF between θ_l and q_t (Sommeria and Deardorff (1977), Mellor (1977)). Such a scheme has the practical advantage of not needing any third-order moments to calculate its parameters. In practice, however, a grid box may often contain two or more distinct areas with very different properties. For example, a grid box may contain both cloudy and clear portions and contain both updrafts and downdrafts. A bimodal distribution such as a double joint Gaussian PDF would be able to describe such a situation more accurately since it can represent two “populations” of air parcels within one box. It also has the benefit of being able to reduce to a single Gaussian in more homogeneous environments. In addition, a double Gaussian PDF is capable of representing skewed variability, a property thought to be especially important in a more actively convective environment and one which

a single Gaussian cannot represent. For these reasons, it is prudent to assume that the SGS variability is represented by a joint double Gaussian PDF.

To calculate the parameters of a joint double Gaussian PDF, one needs several third-order moments. Since predicting more third-order moments has traditionally been seen as too computationally expensive, several authors have developed schemes to work with fewer third-order moments. Lewellen and Yoh (1993) created a scheme that needs $\overline{\theta_l'^3}$, $\overline{q_t'^3}$, and $\overline{w'^3}$ and Larson et al. (2002) developed a scheme that uses $\overline{w'^3}$ as the only third-order moment. Bogenschutz et al. (2010) compared schemes based on double joint Gaussian PDFs with those based on a single joint Gaussian PDF and a double delta PDF. They found that one scheme of Larson et al. (2002) that only requires $\overline{w'^3}$ performed the best of those tested when compared with LES output. It is interesting to note that the double joint Gaussian scheme that uses fewer third-order moments actually performed better than a scheme that uses more, suggesting that additional third-order moments may not be necessary to accurately represent the SGS variability. Despite the success of the joint double Gaussian scheme found in Larson et al. (2002) that only uses one third-order moment, a different scheme is employed in THOR – one that attempts to relax some hard-to-justify assumptions. The new scheme is described below.

A double Gaussian PDF for a single variable is defined as the weighted sum of two single Gaussian PDFs as in Randall (2012):

$$f(x; \overline{x}_1, \sigma_{x_1}, \overline{x}_2, \sigma_{x_2}, a) = \frac{(1-a)}{\sigma_{x_1} \sqrt{2\pi}} e^{-1/2 \left(\frac{x-\overline{x}_1}{\sigma_{x_1}} \right)^2} + \frac{a}{\sigma_{x_2} \sqrt{2\pi}} e^{-1/2 \left(\frac{x-\overline{x}_2}{\sigma_{x_2}} \right)^2} \quad (47)$$

To define such a double Gaussian requires five parameters listed as arguments in (47): the relative weight of one of the single Gaussians, a , the means of each single Gaussian, x_1 and

x_2 , and the standard deviations for each single Gaussian, σ_{x_1} and σ_{x_2} . It is assumed that the first three moments of x are known, \bar{x} , $\overline{x'^2}$, and $\overline{x'^3}$. It can be shown (as in Randall (2012)) that

$$\bar{x} = (1 - a) \bar{x}_1 + a \bar{x}_2 \quad (48)$$

$$\overline{x'^2} = [(1 - a) \sigma_{x_1}^2 + a \sigma_{x_2}^2] + a(1 - a) (\bar{x}_2 - \bar{x}_1)^2 \quad (49)$$

$$\overline{x'^3} = a(1 - a) (\bar{x}_2 - \bar{x}_1) [3(\sigma_{x_2}^2 - \sigma_{x_1}^2) + (\bar{x}_2 - \bar{x}_1)^2 (1 - 2a)] \quad (50)$$

so that the higher-order moments are expressed in terms of the bias, $(\bar{x}_2 - \bar{x}_1)$, and the “sub-plume” variances, $\sigma_{x_1}^2$ and $\sigma_{x_2}^2$.

We wish to define the complete set of parameters for the double Gaussian using only the first three moments of x , although the problem in its current state contains five unknowns with only three equations. In order to solve this problem, some simplifying assumptions must be made. Perhaps the simplest assumption is to assume $\sigma_{x_2} = \sigma_{x_1} = 0$ to reduce the double Gaussian PDF into a double delta PDF as is done in Randall et al. (1992). Then, the system can be solved for a , \bar{x}_1 , and \bar{x}_2 using equations (48) - (50). Another simplifying assumption is to assume $\sigma_{x_2} = \sigma_{x_1} = c \overline{x'^2}$ where c is some constant, as was done by Larson et al. (2001a). With this assumption, it is also straightforward to solve for the remaining three parameters given equations (48) - (50). Lewellen and Yoh (1993) solve this problem in a different way, using a transcendental equation for a and other nontrivial assumptions. The validity of the sub-plume variance assumptions mentioned above is drawn into question when considering the variables of interest in the atmosphere, namely w , θ_{il} , and q_t . Given the dimensions of grids used in most atmospheric models, the assumption of zero sub-plume variance, although conceptually useful, is obviously suspect. Further, assuming that each of the two Gaussian

plumes have equal variances is also problematic. Observations and intuition suggest that the Gaussian plume with the smaller weight, that which represents convective updrafts, for example, should have a higher sub-plume variance than the Gaussian with the larger weight, which represents the surrounding environment.

Given the limitations imposed by the assumptions mentioned above, we seek an alternate parameterization that relaxes the assumptions, or at least incorporates assumptions more in-line with physical principles. Recalling also that we seek a trivariate double Gaussian in the variables w , θ_{il} , and q_t , it is apparent that solving for the Gaussian weight, a , is not a trivial endeavor, and it should depend not only on the moments of one variable, but all of them if it is to represent the weight of one of the trivariate Gaussian plumes. Given this reality, the first assumption to be made is that a is known a priori, and its parameterization will be discussed following the determination of the biases and sub-plume variances for each variable.

After eliminating a from the list of needed parameters, one more assumption is required to reduce the parameter number to three, where the system is solvable. The final assumption constitutes a parameterization of the sub-plume variances. Consider the following relationships:

$$\begin{aligned}\sigma_{x_1}^2 &= \overline{x'^2}_{thresh} + \frac{\sigma_x^2}{1-a} \\ \sigma_{x_2}^2 &= \overline{x'^2}_{thresh} + \frac{\sigma_x^2}{a}\end{aligned}\tag{51}$$

where $\overline{x'^2}_{thresh}$ is a threshold value near zero, whose value sets a floor for the host model's variance. Such a nonzero threshold is important to avoid divisions by zero in a numerical model. This parameterization is based on the physical principle that the sub-plume variance

of the minor Gaussian plume should be greater than the sub-plume variance of the major, or “environmental,” plume. This parameterization reduces the two sub-plume variance parameters to one parameter, namely σ_x , and brings the problem into balance in terms of equations and unknowns.

Consider the new solvable system, equations (48) - (50) rewritten with the substitution of the parameterization in equation (51).

$$\bar{x}_1 = \bar{x} + a(\bar{x}_2 - \bar{x}_1) \quad (52)$$

$$\bar{x}_2 = \bar{x} - (1 - a)(\bar{x}_2 - \bar{x}_1)$$

$$\begin{aligned} \overline{x'^2} = & \left[(1 - a) \left(\overline{x'^2}_{thresh} + \frac{\sigma_x}{1 - a} \right) + a \left(\overline{x'^2}_{thresh} + \frac{\sigma_x^2}{a} \right) \right] \\ & + a(1 - a)(\bar{x}_2 - \bar{x}_1)^2 \end{aligned} \quad (53)$$

$$\begin{aligned} \overline{x'^3} = & a(1 - a)(\bar{x}_2 - \bar{x}_1) \\ & \left\{ 3 \left[\overline{x'^2}_{thresh} + \frac{\sigma_x^2}{a} - \left(\overline{x'^2}_{thresh} + \frac{\sigma_x^2}{1 - a} \right) \right] + (\bar{x}_2 - \bar{x}_1)^2 (1 - 2a) \right\} \end{aligned} \quad (54)$$

Equation (52) is used only to calculate the means of the two Gaussian plumes from the bias using \bar{x} , and can be utilized after equations (53) and (54) are used to solve for the bias, $(\bar{x}_2 - \bar{x}_1)$, and σ_x^2 . Equations (53) and (54) can be simplified considerably to yield

$$\overline{x'^2} = \overline{x'^2}_{thresh} + 2\sigma_x^2 + a(1 - a)(\bar{x}_2 - \bar{x}_1)^2 \quad (55)$$

$$\overline{x'^3} = 3(1 - 2a)(\bar{x}_2 - \bar{x}_1)\sigma_x^2 + a(1 - a)(1 - 2a)(\bar{x}_2 - \bar{x}_1)^3 \quad (56)$$

The cubic in equation (56) can be further simplified using (55):

$$\overline{x'^3} = (1 - 2a)(\overline{x_2} - \overline{x_1}) \left[\sigma_x^2 + \left(\overline{x'^2} - \overline{x'^2}_{thresh} \right) \right] \quad (57)$$

Of course, the system (55), (57) must be solved for the three variables of interest, replacing x in equations (47) - (57) with w , θ_{il} , and q_t . Appendix C outlines one method of solving the nonlinear system that relies on a look-up table rather than going through the considerable computational expense of solving a nonlinear system at every grid point at every time step.

We return now to the determination of the Gaussian weight, a . As mentioned previously, for a trivariate double Gaussian, the weight should really be a function of all of the variables of interest, instead of just one variable, as has been assumed by previous authors (Larson et al. 2002). The parameterization of a combines ideas from Larson et al. (2002) and Lewellen and Yoh (1993) and is a function of the skewnesses of the variables of interest. From the former, we'll incorporate the assumption that $\sigma_{x_1}^2 = \sigma_{x_2}^2 = \sigma_{constant}^2$ (only for the calculation of a), and from the latter, we'll incorporate the idea that the value of skewness used in the formula will be the maximum value of skewness among w , θ_{il} , and q_t . The formula for a is therefore

$$a = 1/2 \left[1 - skew \left(\frac{1}{4(1 - \sigma_{constant}^2)^3 + skew^2} \right) \right] \quad (58)$$

where $skew = \text{MAX}(|skew_w|, |skew_{\theta_{il}}|, |skew_{q_t}|)$ and $\sigma_{constant}^2 \leq 0.5$. The value of $\sigma_{constant}^2$ moderates how quickly a becomes small as $skew$ increases. Values closer to 0.5 cause a to be small for lower values of $skew$ than values closer to 0. Larson et al. (2002) used $\sigma_{constant}^2 = 0.4$ and this value is retained in THOR. In the future, it may become desirable to relax the constant $\sigma_{constant}^2$ assumption and instead parameterize it as a function of skewness as well.

Since a is calculated independently of the nonlinear system, it is possible that the parameterization in equation (58) might produce values of a where no solution exists for the system for one of the variables of interest. We would like to determine the maximum value of a for which there is a solution to the nonlinear system (55), (57). From equations (55) and (57), the bias can be written as

$$(\bar{x}_2 - \bar{x}_1) = \sqrt{\frac{(\overline{x'^2} - \overline{x'^2}_{thresh}) - 2\sigma_x^2}{a(1-a)}} \quad (59)$$

and

$$(\bar{x}_2 - \bar{x}_1) = \frac{\overline{x'^3}}{(1-2a) \left[(\overline{x'^2} - \overline{x'^2}_{thresh}) + \sigma_x^2 \right]} \quad (60)$$

The maximum value of the bias calculated from (59) occurs when $\sigma_x^2 = 0$. There can be no solution to the system if the maximum value of the bias from (59) is less than the value of the bias calculated from (60) when $\sigma_x^2 = 0$. This provides a constraint on a , and its maximum value can be calculated by equating equations (59) and (60) when $\sigma_x^2 = 0$ and solving for a .

$$\sqrt{\frac{(\overline{x'^2} - \overline{x'^2}_{thresh})}{a(1-a)}} = \frac{\overline{x'^3}}{(1-2a) \left[(\overline{x'^2} - \overline{x'^2}_{thresh}) \right]} \quad (61)$$

Solving for a yields

$$a = 1/2 \left(1 - \frac{1}{\sqrt{1 + \frac{4}{skew^2}}} \right) \quad (62)$$

This is the maximum value for a for which a solution to the system exists. In practice, for each variable of interest, the maximum value of a is calculated using (62). If a calculated from (58) exceeds the maximum allowable value for a given variable, the skewness of the offending variable is truncated to its maximum possible value to guarantee a solution to the

system can be found. The maximum allowable skewness is found by solving (62) for *skew*:

$$skew = \sqrt{\frac{4}{\frac{1}{(1-2a)^2} - 1}} \quad (63)$$

Another constraint on a is that it cannot be equal to 0.5 since it would lead to a singularity from equation (60). In practice a is constrained by $a_{min} < a \leq 0.49$ where a_{min} is calculated from (58) with a maximum value of skewness in the model, currently set to 4. It should also be noted that since a is constrained to be less than 0.5, the solution generated by the system (55), (57) will always have a positive bias. Therefore, the sign of the bias is modified according to the sign of the skewness of the variable of interest. Negative skewness translates to negative bias. In addition, when the magnitudes of skewness are high, leading to values of a near zero, this scheme can produce large values of third-order moments. To combat this issue, values of the turbulence time scale, τ , are adjusted for the third-order moments when $a < 0.1$ according to

$$\tau = \frac{\tau}{1 + (1 - 10a)} \quad (64)$$

Equation (64) reduces τ and the magnitudes of third-order moments by up to a factor of two for low values of a . A similar adjustment is made in Golaz et al. (2002) for values of a less than 0.05, although in that paper, τ is reduced by up to a factor of 4.

Although all of the parameters for the individual single variate double Gaussians have been calculated, there are still six correlations between the single variate PDFs that must be specified. As done in previous works, it will be assumed that $r_{w,q_{t1}} = r_{w,q_{t2}} = r_{w,q_t}$, $r_{w,\theta_{i1}} = r_{w,\theta_{i2}} = r_{w,\theta_{il}}$ and $r_{\theta_{il},q_{t1}} = r_{\theta_{il},q_{t2}} = r_{\theta_{il},q_t}$. However, unlike Larson et al. (2002), it will not be assumed that $r_{w,q_t} = r_{w,\theta_{il}} = 0$. Using only the covariance second-order moments

and already-calculated parameters, the correlations are given by the formulas

$$\begin{aligned}
r_{\theta_{il}, q_t} &= \frac{\overline{\theta'_{il} q'_t} - (1-a)(q_{t_1} - \overline{q_t})(\theta_{il_1} - \overline{\theta_{il}}) - a(q_{t_2} - \overline{q_t})(\theta_{il_2} - \overline{\theta_{il}})}{(1-a)\sqrt{\sigma_{q_{t_1}}^2 \sigma_{\theta_{il_1}}^2} + a\sqrt{\sigma_{q_{t_2}}^2 \sigma_{\theta_{il_2}}^2}} \\
r_{w, \theta_{il}} &= \frac{\overline{w' \theta'_{il}} - (1-a)(w_1 - \overline{w})(\theta_{il_1} - \overline{\theta_{il}}) - a(w_2 - \overline{w})(\theta_{il_2} - \overline{\theta_{il}})}{(1-a)\sqrt{\sigma_{w_1}^2 \sigma_{\theta_{il_1}}^2} + a\sqrt{\sigma_{w_2}^2 \sigma_{\theta_{il_2}}^2}} \\
r_{w, q_t} &= \frac{\overline{w' q'_t} - (1-a)(w_1 - \overline{w})(q_{t_1} - \overline{q_t}) - a(w_2 - \overline{w})(q_{t_2} - \overline{q_t})}{(1-a)\sqrt{\sigma_{w_1}^2 \sigma_{q_{t_1}}^2} + a\sqrt{\sigma_{w_2}^2 \sigma_{q_{t_2}}^2}}
\end{aligned} \tag{65}$$

Finally, a few notes on some implementation details are in order to handle computational singularities and to reduce noise. First, since skewness requires both second- and third-order moments to calculate (skewness = $\frac{\overline{x^3}}{x^2^{1.5}}$) and since second- and third-order moments are defined on different grid levels (see section 2.8 for grid placement), some interpolation is necessary. In THOR, the PDF parameters are calculated on grid interfaces, so the skewness of a variable, x , is calculated on grid interface, $k + 1/2$, using the following formula

$$\text{skewness}_{x_{k+1/2}} = \frac{1}{2} \left(\frac{\overline{x^3}_{k+1}}{\text{MAX}(\overline{x^2}_{k+3/2}, \overline{x^2}_{k+1/2})^{1.5}} + \frac{\overline{x^3}_k}{\text{MAX}(\overline{x^2}_{k+1/2}, \overline{x^2}_{k-1/2})^{1.5}} \right) \tag{66}$$

The value of a calculated with the skewness is smoothed in both space and time in order to help control unphysical oscillations. The value of a is smoothed in space with

$$a_{k+1/2} = \frac{1}{3} (a_{k-1/2} + a_{k+1/2} + a_{k+3/2}) \tag{67}$$

and a_k not allowed to change more than $\frac{1}{2} \frac{\Delta t}{7200s}$ in one time step. Lastly, the denominators in equation (65) lead to computational noise when they are close to 0. A minimum threshold is set to prevent such noise.

2.4. MIXED-PHASE SUBGRID-SCALE CONDENSATION

With the joint double Gaussian PDF determined, one can use the PDF to calculate many cloud-related properties in each grid cell, such as the cloud fraction, cloud liquid water, cloud ice, and second- and third-order correlations involving cloud water, which are critical for determining buoyancy terms of the higher-order closure model. One important difference between THOR and its predecessor models is how it directly accounts for ice. Previous models assume cloud formation only happens in a liquid state, and only *ex post facto* convert a portion of the cloud liquid to ice. An approach that includes liquid, ice, and mixed-phase cloud formation should be used to improve the generality of the host model so that it may confidently be used in higher latitudes and altitudes where freezing temperatures are commonplace. A description of the mixed-phase cloud permitting SGS condensation scheme included in THOR is discussed next.

First, consider the arbitrary joint Gaussian PDF found in figure 2.1¹. It shows a typical spread of θ_{il} and q_t values in a grid cell at 900 hPa. The contours represent deciles of the likelihood of finding a particular (θ_{il}, q_t) pair in that grid cell. Black solid and dashed lines denote the actual saturation curve and linearized saturation over liquid, respectively, while red solid and dashed lines denote the actual saturation curve and linearized approximation over ice, respectively. The final black dash-dotted line represents the freezing point of water. Assuming liquid clouds only (and no supersaturation), one could integrate over the portion of the PDF that lies above the black saturation curve to obtain the cloud fraction and cloud water content. Of course, when one considers a mixed-phase cloud, the situation is muddled. Some condensation occurs over liquid water and some occurs over ice. Which

¹Although a *double* joint Gaussian PDF is used in THOR, a single joint PDF is used in this discussion for clarity.

saturation curve would be appropriate to use in order to estimate cloud fraction and cloud water content?

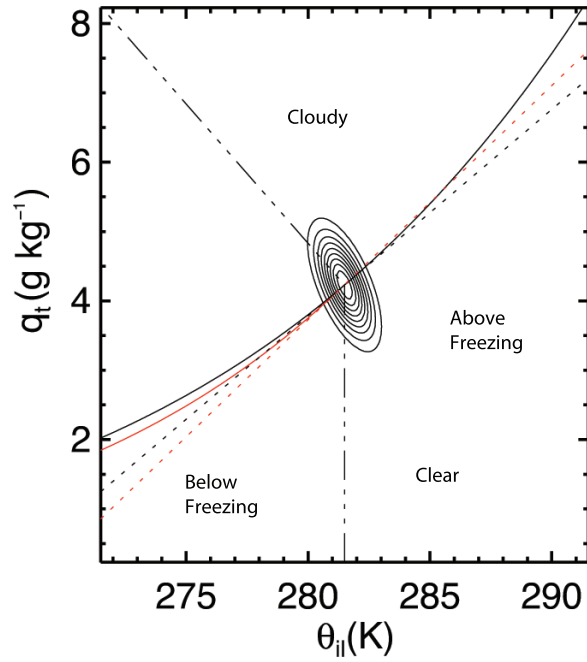


FIGURE 2.1. Typical joint-Gaussian PDF of θ_{il} and q_t in a grid cell. The lines are q_s over liquid (black solid), q_s over ice (red solid), linear approximation to q_s over liquid (black dotted), linear approximation to q_s over ice (red dotted), θ_{il} of freezing point (black dash-dotted).

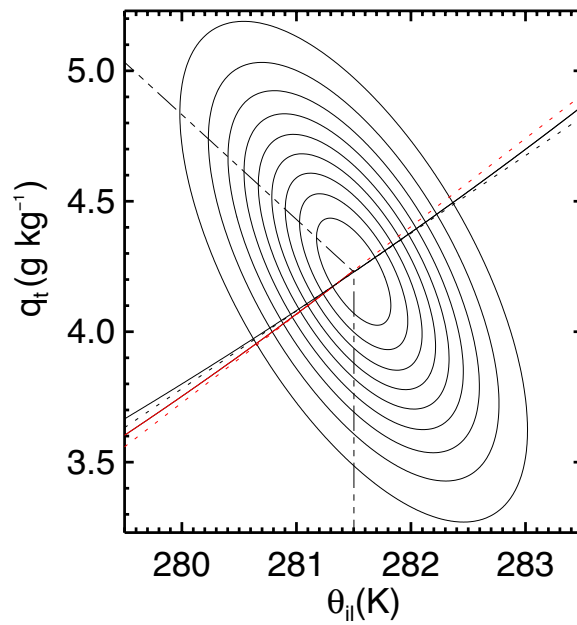


FIGURE 2.2. As in figure 2.1, but “zoomed in.”

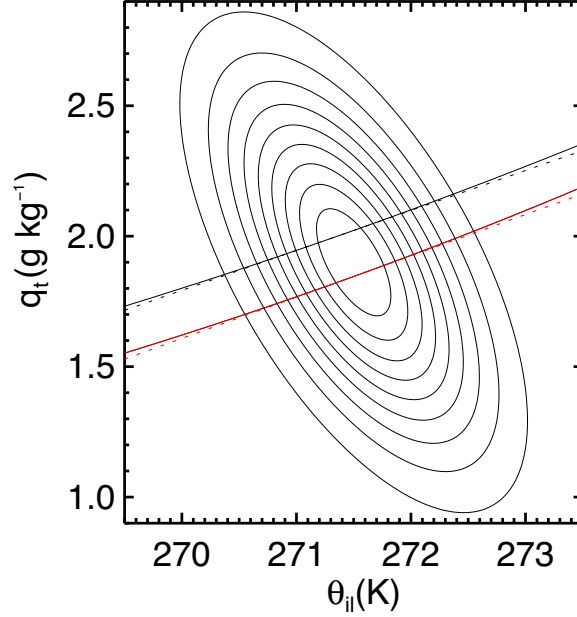


FIGURE 2.3. As in figure 2.2, but the mean θ_{il} is 10 K colder.

In addition, performing the integration of the portion of the joint Gaussian PDF that lies on one side of a nonlinear curve is impossible analytically and time-consuming numerically. The problem becomes tractable if one approximates the saturation curve as a line, as has been done by many authors, including Sommeria and Deardorff (1977) and Mellor (1977). The black and red dotted lines in figure 2.1 represent the linear approximations of the saturation curves over liquid and ice, respectively, using a Taylor series approximation evaluated at the mean value of the joint Gaussian PDF as done in Sommeria and Deardorff (1977) and Mellor (1977). From the zoomed-in perspective in figure 2.2, it becomes obvious that the linear saturation approximation over ice (red dotted) is a better approximation to the actual saturation curve in the freezing portion of the PDF, but diverges from the actual saturation curve in the warm portion. Likewise, the linear saturation approximation over liquid is a better approximation on the warm side and diverges from the saturation over ice on the frozen side of the PDF. Although the difference in the magnitude of the errors between the

two linear approximations may seem small in this example, as the mean temperature drops well below freezing, the increasing discrepancy between the actual saturation curves over ice and liquid causes their linear approximations to diverge further as well (see, e.g. figure 2.3).

An appropriate linearized saturation curve for warm, mixed-phase, and ice clouds can be obtained by combining the linearizations over liquid and ice in the following way. Define θ_{il} and T_{il} as

$$\begin{aligned}\theta_{il} &= \theta - \left(\frac{p_0}{p}\right)^\kappa \left(\frac{L_v}{c_p} q_l + \frac{L_s}{c_p} q_i\right) \\ T_{il} &= \left(\frac{p}{p_0}\right)^\kappa \theta_{il}\end{aligned}\tag{68}$$

As in Sommeria and Deardorff (1977), the linearization of the saturation curve over liquid is given by the following first-order Taylor polynomial

$$q_{s_l} = \overline{q_{s_{li}}} + \left(\frac{\partial q_{s_l}}{\partial T}\right)_{T=\overline{T_{il}}} (T - \overline{T_{il}})\tag{69}$$

where $\overline{q_{s_{li}}}$ is the saturation specific humidity over liquid evaluated at $\overline{T_{il}}$ and

$$\left(\frac{\partial q_{s_l}}{\partial T}\right)_{T=\overline{T_{il}}} = \frac{\varepsilon \overline{q_{s_{li}}} L_v}{R_d \overline{T_{il}}^2}\tag{70}$$

is the Clausius-Clapeyron relationship over liquid, also evaluated at $\overline{T_{il}}$. Similarly, the linearization of the saturation curve over ice is given by

$$q_{s_i} = \overline{q_{s_{ii}}} + \left(\frac{\partial q_{s_i}}{\partial T}\right)_{T=\overline{T_{il}}} (T - \overline{T_{il}})\tag{71}$$

where $\overline{q_{s_{il}}}$ is the saturation specific humidity over ice evaluated at $\overline{T_{il}}$ and

$$\left(\frac{\partial q_{s_i}}{\partial T}\right)_{T=\overline{T_{il}}} = \frac{\varepsilon \overline{q_{s_{il}}} L_s}{R_d \overline{T_{il}}^2} \quad (72)$$

is the Clausius-Clapeyron relationship over ice. Equations (69) and (71) can be combined using a simple weighting system

$$q_s = w_n q_{s_l} + (1 - w_n) q_{s_i} \quad (73)$$

where w_n is a weight that should be equal to unity for temperatures above freezing and transition to zero as supercooled liquid is completely taken over by ice. The weight could conceivably be a function of many variables (e.g., temperature, ice condensation nuclei, etc.) although for THOR's implementation, it is only a function of temperature.

Before expanding equation (73) with equations (69) and (71), it is useful to write the term $(T - \overline{T_{il}})$ in terms of the variables θ_{il} , q_l , and q_i as is done in Mellor (1977):

$$\begin{aligned} (T - \overline{T_{il}}) &= \left(T - \frac{\overline{T}}{\overline{\theta}} \theta_{il}\right) \\ &= \left[T - \frac{\overline{T}}{\overline{\theta}} \left(\overline{\theta} - \frac{\overline{\theta}}{\overline{T}} \frac{L_v}{c_p} \overline{q_l} - \frac{\overline{\theta}}{\overline{T}} \frac{L_s}{c_p} \overline{q_i}\right)\right] \\ &= \left(T - \overline{T} + \frac{L_v}{c_p} \overline{q_l} + \frac{L_s}{c_p} \overline{q_i}\right) \\ &= \left(T' - \frac{L_v}{c_p} q_l' - \frac{L_s}{c_p} q_i' + \frac{L_v}{c_p} q_l + \frac{L_s}{c_p} q_i\right) \\ &= \left(\frac{\overline{T}}{\overline{\theta}} \theta_{il}' + \frac{L_v}{c_p} q_l + \frac{L_s}{c_p} q_i\right) \end{aligned} \quad (74)$$

Substituting equations (69) - (72) and (74) into equation (73) gives the generalized saturation curve linearization as

$$q_s = w_n \left[\frac{\overline{q_{s_{il}}}}{\overline{q_{s_{il}}}} + \frac{\varepsilon \overline{q_{s_{il}}} L_v}{R_d \overline{T_{il}}^2} \left(\frac{\overline{T}}{\overline{\theta}} \theta'_{il} + \frac{L_v}{c_p} q_l + \frac{L_s}{c_p} q_i \right) \right] + (1 - w_n) \left[\frac{\overline{q_{s_{il}}}}{\overline{q_{s_{il}}}} + \frac{\varepsilon \overline{q_{s_{il}}} L_s}{R_d \overline{T_{il}}^2} \left(\frac{\overline{T}}{\overline{\theta}} \theta'_{il} + \frac{L_v}{c_p} q_l + \frac{L_s}{c_p} q_i \right) \right] \quad (75)$$

This linearization is equivalent to the black linear approximation in figures 2.1 - 2.3 for temperatures above freezing and to the red linear approximation below some threshold temperature where presumably only ice exists. For temperatures in between, equation (75) provides a linear approximation between the two extremes.

Having obtained a suitable saturation curve linear approximation, the next step is to determine the portion of the PDF that is saturated. In order to do so, a useful variable transformation is performed. Following Mellor (1977), Larson et al. (2002), and Chen (1991) define a quantity, s as

$$s \equiv q_t - q_s \quad (76)$$

It is equal to the total cloud condensate, $q_c = q_l + q_i$, when positive and is a measure of subsaturation when negative. Combining equations (75) and (76) yields

$$s = (\overline{q_t} + q'_t) - w_n \left[\frac{\overline{q_{s_{il}}}}{\overline{q_{s_{il}}}} + \frac{\varepsilon \overline{q_{s_{il}}} L_v}{R_d \overline{T_{il}}^2} \left(\frac{\overline{T}}{\overline{\theta}} \theta'_{il} + \frac{L_v}{c_p} q_l + \frac{L_s}{c_p} q_i \right) \right] - (1 - w_n) \left[\frac{\overline{q_{s_{il}}}}{\overline{q_{s_{il}}}} + \frac{\varepsilon \overline{q_{s_{il}}} L_s}{R_d \overline{T_{il}}^2} \left(\frac{\overline{T}}{\overline{\theta}} \theta'_{il} + \frac{L_v}{c_p} q_l + \frac{L_s}{c_p} q_i \right) \right] \quad (77)$$

Although q_l and q_i are unknown at this point, the assumption is made that they are related to the total cloud condensate by the same weighting used to determine the general linearized

saturation:

$$\begin{aligned}
 q_l &= w_n q_c \\
 q_i &= (1 - w_n) q_c
 \end{aligned}
 \tag{78}$$

Since it is the goal to determine the cloud properties of the grid cell, it is only of interest when $s > 0$, or when $s = q_c$. Using this fact, the substitution of equation (78) into equation (77) after solving for s yields

$$s = c_{qt} \left\{ \bar{q}_t - \left[w_n \bar{q}_{s_{il}} + (1 - w_n) \bar{q}_{s_{il}} \right] \right\} + c_{qt} q'_t - c_{\theta_{il}} \theta'_{il}
 \tag{79}$$

where

$$c_{qt} = \frac{1}{1 + \frac{\varepsilon}{c_p R_d \bar{T}_{il}^2} \left\{ \left[w_n L_v + (1 - w_n) L_s \right] \left[w_n L_v \bar{q}_{s_{il}} + (1 - w_n) L_s \bar{q}_{s_{il}} \right] \right\}}
 \tag{80}$$

and

$$c_{\theta_{il}} = \frac{\bar{T}}{\bar{\theta}} \frac{\varepsilon}{R_d \bar{T}_{il}^2} \left[w_n L_v \bar{q}_{s_{il}} + (1 - w_n) L_s \bar{q}_{s_{il}} \right] c_{qt}
 \tag{81}$$

The formulation of s in equation (79) is very similar to that found in Mellor (1977), Larson et al. (2002), and Chen (1991) except for the substitution of weighted linear combinations for the saturation specific humidities, latent heats, and Clausius-Clapeyron relationships. The quantity s can be split into a mean and a deviation

$$\begin{aligned}
 \bar{s} &= c_{qt} \left\{ \bar{q}_t - \left[w_n \bar{q}_{s_{il}} + (1 - w_n) \bar{q}_{s_{il}} \right] \right\} \\
 s' &= c_{qt} q'_t - c_{\theta_{il}} \theta'_{il}
 \end{aligned}
 \tag{82}$$

with a variance of

$$\overline{s'^2} = c_{q_t}^2 \overline{q_t'^2} - 2c_{q_t}c_{\theta_{il}}\overline{\theta'_{il}q'_t} + c_{\theta_{il}}\overline{\theta_{il}'^2}$$

or

(83)

$$\sigma_s^2 = c_{q_t}^2 \sigma_{q_t}^2 - 2c_{q_t}c_{\theta_{il}}r_{\theta_{il}q_t}\sigma_{q_t}\sigma_{\theta_{il}} + c_{\theta_{il}}\sigma_{\theta_{il}}^2$$

With the new definition of s and its variance, the integrals over the joint Gaussian PDF are performed exactly the same as in the other previously mentioned studies:

$$R = 1/2 \left[1 + \operatorname{erf} \left(\frac{Q_1}{\sqrt{2}} \right) \right]$$

$$q_c = R\bar{s} + \frac{\sigma_s}{\sqrt{2\pi}} \exp \left(\frac{-Q_1^2}{2} \right)$$
(84)

where R is the cloud fraction and $Q_1 = \frac{\bar{s}}{\sigma_s}$.

All that remains to close the SGS condensation parameterization is the weight, w_n . As stated previously, it is assumed in THOR that it is only a function of temperature, and it is taken to be the same weighting formula used in the System for Atmospheric Modeling (SAM) microphysics parameterization (Khairoutdinov and Randall 2003)

$$w_n = \max \left[0, \min \left(\frac{T - T_{00}}{T_0 - T_{00}} \right) \right]$$
(85)

where $T_{00} = 253.16$ K and $T_0 = 273.16$ K.

Since the temperature itself is a function of the cloud condensate, an iterative procedure is needed to calculate it. The following algorithm is used:

- (1) If $\overline{T_{il}} > 273.16$ K then $w_n = 1$, and no iteration is needed.
- (2) Otherwise, calculate the first guess w_n assuming no cloud condensate ($T = T_{il}$).

- (3) Calculate c_{q_t} and $c_{\theta_{il}}$ according to (80) and (81), s according to (82), and σ_s according to (83).
- (4) Using values calculated in step 3, calculate the values of SGS cloud fraction and cloud condensate using (84).
- (5) Partition cloud condensate into liquid and ice using (78) and calculate a new estimate of temperature using the definition of T_{il} (68).
- (6) Calculate a new estimate for w_n using (85).
- (7) Repeat steps 2 - 6 until the change in temperature estimates is below some threshold, currently 0.001 K.

As mentioned previously, this discussion has been carried out for only one of the two Gaussian plumes. In practice, the preceding algorithm must be performed for the first Gaussian plume using w_1 , θ_{il_1} , q_{t_1} , $\sigma_{q_{t_1}}$, $\sigma_{\theta_{il_1}}$, and $r_{\theta_{il}q_{t_1}}$ to determine R_1 , q_{l_1} , and q_{i_1} , and then for the second Gaussian plume using the same parameters with a 2 subscript. The values for the two plumes are then combined using the Gaussian mixture parameter, a :

$$\begin{aligned}\bar{q}_l &= (1 - a) q_{l_1} + a q_{l_2} \\ \bar{q}_i &= (1 - a) q_{i_1} + a q_{i_2} \\ \bar{R} &= (1 - a) R_1 + a R_2\end{aligned}\tag{86}$$

In addition to cloud fraction and mean values of cloud liquid and ice, second- and third-order cloud liquid and ice correlations are needed from the parameterization to close the buoyancy terms in the higher-order moment equations (see, e.g. equation (27)). They can be calculated from the PDF parameters and calculated cloud properties using the following

formulas. For second-order liquid:

$$\begin{aligned}
\overline{w'q'_l} &= (1 - a) [(w_1 - \bar{w}) q_{l_1} + \overline{w'q'_{l_1}}] + a [(w_2 - \bar{w}) q_{l_2} + \overline{w'q'_{l_2}}] \\
\overline{\theta'_{il}q'_l} &= (1 - a) [(\theta_{il_1} - \bar{\theta}_{il}) q_{l_1} + \overline{\theta'_{il}q'_{l_1}}] + a [(\theta_{il_2} - \bar{\theta}_{il}) q_{l_2} + \overline{\theta'_{il}q'_{l_2}}] \\
\overline{q'_tq'_l} &= (1 - a) [(q_{t_1} - \bar{q}_t) q_{l_1} + \overline{q'_tq'_{l_1}}] + a [(q_{t_2} - \bar{q}_t) q_{l_2} + \overline{q'_tq'_{l_2}}]
\end{aligned} \tag{87}$$

where

$$\begin{aligned}
\overline{w'q'_{l_n}} &= w_n R_n (c_{q_t} \sigma_{w_n} \sigma_{q_{t_n}} r_{w,q_t} - c_{\theta_{il}} \sigma_{w_n} \sigma_{\theta_{il_n}} r_{w,\theta_{il}}) \\
\overline{\theta'_{il}q'_{l_n}} &= w_n R_n (c_{q_t} \sigma_{\theta_{il_n}} \sigma_{q_{t_n}} r_{\theta_{il},q_t} - c_{\theta_{il}} \sigma_{\theta_{il_n}}^2) \\
\overline{q'_tq'_{l_n}} &= w_n R_n (c_{q_t} \sigma_{q_{t_n}}^2 - c_{\theta_{il}} \sigma_{\theta_{il_n}} \sigma_{q_{t_n}} r_{\theta_{il},q_t})
\end{aligned} \tag{88}$$

and $n = 1, 2$. For third-order liquid:

$$\begin{aligned}
\overline{w'^2 q'_l} &= (1 - a) \left\{ [(w_1 - \bar{w})^2 + \sigma_{w_1}^2] (q_{l_1} - \bar{q}_l) + 2 (w_1 - \bar{w}) \overline{w' q'_{l_1}} + \overline{w' w' q'_{l_1}} \right\} \\
&+ a \left\{ [(w_2 - \bar{w})^2 + \sigma_{w_2}^2] (q_{l_2} - \bar{q}_l) + 2 (w_2 - \bar{w}) \overline{w' q'_{l_2}} + \overline{w' w' q'_{l_2}} \right\} \\
\overline{w' \theta'_{il} q'_l} &= (1 - a) \left\{ [(w_1 - \bar{w}) (\theta_{il_1} - \bar{\theta}_{il}) + r_{w, \theta_{il}} \sigma_{w_1} \sigma_{\theta_{il_1}}] (q_{l_1} - \bar{q}_l) \right. \\
&+ (w_1 - \bar{w}) \overline{\theta_{il} q_{l_1}} + (\theta_{il_1} - \bar{\theta}_{il}) \overline{w' q'_{l_1}} + \overline{w' \theta'_{il} q'_{l_1}} \left. \right\} \\
&+ a \left\{ [(w_2 - \bar{w}) (\theta_{il_2} - \bar{\theta}_{il}) + r_{w, \theta_{il}} \sigma_{w_2} \sigma_{\theta_{il_2}}] (q_{l_2} - \bar{q}_l) \right. \\
&+ (w_2 - \bar{w}) \overline{\theta_{il} q_{l_2}} + (\theta_{il_2} - \bar{\theta}_{il}) \overline{w' q'_{l_2}} + \overline{w' \theta'_{il} q'_{l_2}} \left. \right\} \\
\overline{w' q'_t q'_l} &= (1 - a) \left\{ [(w_1 - \bar{w}) (q_{t_1} - \bar{q}_t) + r_{w, q_t} \sigma_{w_1} \sigma_{q_{t_1}}] (q_{l_1} - \bar{q}_l) \right. \\
&+ (w_1 - \bar{w}) \overline{q_t q_{l_1}} + (q_{t_1} - \bar{q}_t) \overline{w' q'_{l_1}} + \overline{w' q'_t q'_{l_1}} \left. \right\} \\
&+ a \left\{ [(w_2 - \bar{w}) (q_{t_2} - \bar{q}_t) + r_{w, q_t} \sigma_{w_2} \sigma_{q_{t_2}}] (q_{l_2} - \bar{q}_l) \right. \\
&+ (w_2 - \bar{w}) \overline{q_t q_{l_2}} + (q_{t_2} - \bar{q}_t) \overline{w' q'_{l_2}} + \overline{w' q'_t q'_{l_2}} \left. \right\} \\
\overline{\theta'^2_{il} q'_l} &= (1 - a) \left\{ [(\theta_{il_1} - \bar{\theta}_{il})^2 + \sigma_{\theta_{il_1}}^2] (q_{l_1} - \bar{q}_l) + 2 (\theta_{il_1} - \bar{\theta}_{il}) \overline{\theta'_{il} q'_{l_1}} + \overline{\theta'_{il} \theta'_{il} q'_{l_1}} \right\} \\
&+ a \left\{ [(\theta_{il_2} - \bar{\theta}_{il})^2 + \sigma_{\theta_{il_2}}^2] (q_{l_2} - \bar{q}_l) + 2 (\theta_{il_2} - \bar{\theta}_{il}) \overline{\theta'_{il} q'_{l_2}} + \overline{\theta'_{il} \theta'_{il} q'_{l_2}} \right\} \\
\overline{\theta'_{il} q'_t q'_l} &= (1 - a) \left\{ [(\theta_{il_1} - \bar{\theta}_{il}) (q_{t_1} - \bar{q}_t) + r_{\theta_{il} q_{t_1}} \sigma_{\theta_{il_1}} \sigma_{q_{t_1}}] (q_{l_1} - \bar{q}_l) \right. \\
&+ (\theta_{il_1} - \bar{\theta}_{il}) \overline{q'_t q'_{l_1}} + (q_{t_1} - \bar{q}_t) \overline{\theta'_{il} q'_{l_1}} + \overline{\theta'_{il} q'_t q'_{l_1}} \left. \right\} \\
&+ a \left\{ [(\theta_{il_2} - \bar{\theta}_{il}) (q_{t_2} - \bar{q}_t) + r_{\theta_{il} q_{t_2}} \sigma_{\theta_{il_2}} \sigma_{q_{t_2}}] (q_{l_2} - \bar{q}_l) \right. \\
&+ (\theta_{il_2} - \bar{\theta}_{il}) \overline{q'_t q'_{l_2}} + (q_{t_2} - \bar{q}_t) \overline{\theta'_{il} q'_{l_2}} + \overline{\theta'_{il} q'_t q'_{l_2}} \left. \right\} \\
\overline{q_t'^2 q'_l} &= (1 - a) \left\{ [(q_{t_1} - \bar{q}_t)^2 + \sigma_{q_{t_1}}^2] (q_{l_1} - \bar{q}_l) + 2 (q_{t_1} - \bar{q}_t) \overline{q'_t q'_{l_1}} + \overline{q'_t q'_t q'_{l_1}} \right\} \\
&+ a \left\{ [(q_{t_2} - \bar{q}_t)^2 + \sigma_{q_{t_2}}^2] (q_{l_2} - \bar{q}_l) + 2 (q_{t_2} - \bar{q}_t) \overline{q'_t q'_{l_2}} + \overline{q'_t q'_t q'_{l_2}} \right\}
\end{aligned} \tag{89}$$

where

$$\begin{aligned}
\overline{w'w'q'_{ln}} &= w_n \frac{1}{\sqrt{2\pi}\sigma_{s_n}} \left(\frac{\overline{w'q'_{ln}}}{w_n R_n} \right)^2 e^{-1/2\left(\frac{s_n}{\sigma_{s_n}}\right)} \\
\overline{w'\theta'_{il}q'_{ln}} &= w_n \frac{1}{\sqrt{2\pi}\sigma_{s_n}} \left(\frac{\overline{w'q'_{ln}}}{w_n R_n} \right) \left(\frac{\overline{\theta'_{il}q'_{ln}}}{w_n R_n} \right) e^{-1/2\left(\frac{s_n}{\sigma_{s_n}}\right)} \\
\overline{w'q'_t q'_{ln}} &= w_n \frac{1}{\sqrt{2\pi}\sigma_{s_n}} \left(\frac{\overline{w'q'_{ln}}}{w_n R_n} \right) \left(\frac{\overline{q'_t q'_{ln}}}{w_n R_n} \right) e^{-1/2\left(\frac{s_n}{\sigma_{s_n}}\right)} \\
\overline{\theta'_{il}\theta'_{il}q'_{ln}} &= 0 \\
\overline{\theta'_{il}q'_t q'_{ln}} &= 0 \\
\overline{q'_t q'_t q'_{ln}} &= 0
\end{aligned} \tag{90}$$

For the second- and third-order ice correlations, the formulas are exactly the same as (87)-(90) except for q_l being replaced by q_i everywhere and w_n being replaced by $(1 - w_n)$.

Furthermore, another variable, t , is introduced. It is orthogonal to s in the same way that θ_{il} is orthogonal to q_t so that transformations can be made between a (θ_{il}, q_t) pair and a (s, t) pair. Such a transformation is needed for the PDF sampling scheme discussed in section 2.5. This facilitates a straightforward method to draw from the cloudy or clear portion of the diagnosed PDF since the line $s = 0$ divides the two portions. It is defined as

$$t = \bar{t} + t'$$

where

$$\bar{t} = 0$$

$$t' = c_{q_t} q'_t + c_{\theta_{il}} \theta'_{il}$$

(91)

and its associated second-order moments are

$$\overline{t'^2} = c_{q_t}^2 \overline{q_t'^2} + 2c_{\theta_{il}} c_{q_t} \overline{\theta_{il}' q_t'} + c_{\theta_{il}}^2 \overline{\theta_{il}'^2}$$

$$\overline{s' t'} = c_{q_t}^2 \overline{q_t'^2} - c_{\theta_{il}}^2 \overline{\theta_{il}'^2}$$

or

(92)

$$\sigma_t^2 = c_{q_t}^2 \sigma_{q_t}^2 + 2c_{q_t} c_{\theta_{il}} r_{\theta_{il} q_t} \sigma_{q_t} \sigma_{\theta_{il}} + c_{\theta_{il}}^2 \sigma_{\theta_{il}}^2$$

$$r_{s,t} \sigma_s \sigma_t = c_{q_t}^2 \sigma_{q_t}^2 - c_{\theta_{il}}^2 \sigma_{\theta_{il}}^2$$

2.5. MICROPHYSICS DRIVER AND SCHEME

Although precipitation processes occur on a scale closer to molecular level than climate model grid scale, it is often implicitly assumed that microphysical processes can be parameterized using climate model grid scale variables alone. Ignoring SGS variability has been shown to lead to underestimation biases for processes such as precipitation generation, collection, coalescence, and aggregation (Larson et al. 2001b). Use of a SGS condensation parameterization provides a wealth of information about variability within a grid cell that may be used to more accurately simulate microphysical processes. Indeed, Larson et al. (2005) have shown that such underestimation biases can be improved by utilizing information about SGS variability to drive a microphysics parameterization. They developed a PDF sampling system that can be used to drive any microphysics parameterization. It uses the so-called “latin hypercube” sampling method that is similar to a Monte Carlo method but includes additional steps to ensure samples are sufficiently spread out over a given PDF. This method was shown to reduce the noise introduced by random sampling by preventing

the samples from aggregating together in sample space as much as in the standard Monte Carlo approach.

The latin hypercube PDF sampling approach of Larson et al. (2005) is used in THOR as a microphysics package driver. This allows potentially any microphysics parameterization to be substituted for the current included scheme. Although the authors give an example of using this approach with a microphysics scheme that needs w , θ_l , q_t , the cloud droplet number mixing ratio, and the drizzle mixing ratio, THOR's implementation uses a microphysics scheme that only requires θ_{il} and q_t as input. In addition, the procedure outlined in Larson et al. (2005) only includes samples from the cloudy portion of the PDF. THOR's implementation includes samples from the clear portion of the PDF as well. While much of THOR's implementation follows from the mentioned work, its precise algorithm is presented in detail in this document for reference and to point out any differences that exist.

The best possible estimate of microphysical processes given a joint PDF of temperature and humidity would require a large number of samples (infinite?) so that all portions of the PDF are sampled equally. Since a microphysics routine is called for each sample, the more samples taken from the PDF, the more computationally expensive it is. If one assumes that the joint PDF varies slowly in time, taking a few samples each time step would create a good estimate of microphysics processes over a sufficiently long period of time as all portions of the PDF are sampled eventually. The introduced variability is highest if one sample is taken each time step, and is reduced with more samples.

The first step for implementation of the latin hypercube sampling method consists of generating a number of latin hypercube samples from a *uniform* distribution. This must be performed $d+1$ times where d is the number of variables needed as input for the microphysics

parameterization. The number of samples for each variable, n_t , is somewhat of an arbitrary parameter, but must be equal to the number of samples taken in one time step, n , times some integer, i . Since there is “overhead” computational expense associated with producing the uniform latin hypercube samples, it makes sense to calculate enough samples at one time to last several time steps. For example, if one desired two samples per time step, one could use $n_t = 12$ so that enough samples are generated at a time to last 6 time steps.

To generate the uniform latin hypercube samples, two $n_t \times (d + 1)$ matrices are created, Π and U , shown as equations (93) and (94). For THOR, $d = 2$, corresponding to θ_{il} and q_t . The additional column is needed to choose which Gaussian plume of the double joint Gaussian PDF is sampled, as will be described soon. Each column in Π consists of a permutation of integers of the interval $[0, n_t - 1]$, whereas each member of U is an independent random number on the interval $(0, 1)$. The matrices Π and U are combined using (95) to form the matrix V which holds the actual latin hypercube samples for a uniform distribution. Each row in V holds one sample that will be converted to a (θ_{il}, q_t) pair and each column in V contains values on the range $(0, 1)$ that are guaranteed to span that range without “clumping” together. Since the SGS condensation parameterization allows for partial cloudiness and since different microphysical processes happen within clouds (autoconversion, aggregation, etc.) and outside of clouds (evaporation), two sets of samples are needed – V_{cl} and V_{clr} . It should be pointed out that THOR differs from Larson et al. (2005) with the treatment of clear samples – THOR handles clear samples separately, whereas Larson et al. (2005)

neglects them.

$$\Pi = \left(\begin{array}{c} \overbrace{\left(\begin{array}{c} \text{random permutation of } [0, n_t - 1] \\ \dots \\ \text{random permutation of } [0, n_t - 1] \end{array} \right)}^{d+1} \\ \left. \vphantom{\left(\begin{array}{c} \text{random permutation of } [0, n_t - 1] \\ \dots \\ \text{random permutation of } [0, n_t - 1] \end{array} \right)} \right\} n_t \end{array} \right) \quad (93)$$

$$U = \left(\begin{array}{c} \overbrace{\left(\begin{array}{ccc} \text{RND}(0, 1) & \dots & \text{RND}(0, 1) \\ \vdots & \ddots & \vdots \\ \text{RND}(0, 1) & \dots & \text{RND}(0, 1) \end{array} \right)}^{d+1} \\ \left. \vphantom{\left(\begin{array}{ccc} \text{RND}(0, 1) & \dots & \text{RND}(0, 1) \\ \vdots & \ddots & \vdots \\ \text{RND}(0, 1) & \dots & \text{RND}(0, 1) \end{array} \right)} \right\} n_t \end{array} \right) \quad (94)$$

$$V_{ij} = \frac{1}{n_t} \Pi_{ij} + \frac{1}{n_t} U_{ij} \quad (95)$$

Next, the samples from the uniform distribution need to be converted to samples from the actual diagnosed joint Gaussian PDF. Since there are two Gaussian plumes from which to draw a sample, it first must be decided from which plume to draw. This is accomplished using the last columns in V_{cld} and V_{ctr} . For each cloudy sample in V_{cld} (each row), the sample should be drawn from the first Gaussian plume if the value from the last column of V_{cld} is less than the probability of a point being in the cloudy portion of the first Gaussian plume.

Namely, the Gaussian plume chosen is given by

$$\text{Gaussian plume chosen} = \begin{cases} 1 & V_{cld3,j} < \frac{(1-a)R_1}{(1-a)R_1 + aR_2} \\ 2 & \text{otherwise} \end{cases} \quad (96)$$

where a is the Gaussian mixture parameter, and R_1 and R_2 are plume cloud fractions from section 2.4. For each clear sample, the first Gaussian plume should be chosen if the value from the last column of V_{clr} is less than the probability of a point being in the clear portion of the first Gaussian plume. Namely,

$$\text{Gaussian plume chosen} = \begin{cases} 1 & V_{clr3,j} < \frac{(1-a)(1-R_1)}{1 - [(1-a)R_1 + aR_2]} \\ 2 & \text{otherwise} \end{cases} \quad (97)$$

With the Gaussian plume chosen for each sample in V_{cld} and V_{clr} , the next task is to use the diagnosed PDF parameters to find a specific (s, t) pair for each sample. The procedure that is detailed in Larson et al. (2005) follows the conditional distribution approach whereby one finds the s value using the marginal distribution of s followed by the calculation of the t value from the conditional distribution of t , given the value of s . Their procedure relates the sample values from the uniform PDF to a Gaussian PDF that has been truncated at $s = 0$. They found the the s value for a cloudy sample is related to the samples in V_{cld} by

$$s_{sample} = \sigma_{s_i} F_G^{-1} [V_{cld1,j} R_i + (1 - R_i)] + \bar{s}_i \quad (98)$$

where i denotes the Gaussian plume chosen and F_G^{-1} is the inverse of the standard normal cumulative distribution function. It should be noted that equation (98) is slightly different

than equation (28) in Larson et al. (2005) since they derived the formula for a standard normal distribution, whereas (98) is valid for a Gaussian distribution with mean s_i and standard deviation σ_{s_i} . Although not included in Larson et al. (2005), the same procedure produces the following relation for the clear samples in V_{clr}

$$s_{sample} = \sigma_{s_i} F_G^{-1} [V_{clr_{1,j}} (1 - R_i)] + \bar{s}_i \quad (99)$$

A t value corresponding to each s sample is calculated using the following method. According to Larson et al. (2005), the conditional PDF of t given the samples's value of s is a Gaussian PDF with mean and variance given by

$$\begin{aligned} \mu &= \bar{t}_i + \frac{\overline{s't'_i}}{s'^2_i} (s_{sample} - \bar{s}_i) \\ \Sigma &= \overline{t'^2_i} - \frac{\overline{s't'^2_i}}{s'^2_i} \end{aligned} \quad (100)$$

For both cloudy and clear samples, the uniform PDF samples in V_{cld} and V_{clr} are related to the Gaussian PDF with mean and variance given in (100) by

$$t_{sample} = \sqrt{\overline{t'^2_i} - \frac{\overline{s't'^2_i}}{s'^2_i}} F_G^{-1} (V_{2,j}) + \frac{\overline{s't'_i}}{s'^2_i} (s_{sample} - \bar{s}_i) \quad (101)$$

Finally, θ_{il} and q_t values can be retrieved from the (s, t) sample using the definitions (82) and (91). Combining equations for s' and t' yield

$$\begin{aligned} \theta'_{il} &= \frac{t'_{sample} - s'_{sample}}{2C_{\theta_{il}}} \\ q'_t &= \frac{t'_{sample} - s'_{sample}}{2C_{q_t}} \end{aligned} \quad (102)$$

where $s'_{sample} = s_{sample} - \bar{s}_i$ and $t'_{sample} = t_{sample}$ (since $\bar{t} = 0$). Retrieving the whole values of θ_{il} and q_t (mean plus perturbation) yields

$$\begin{aligned}\theta_{il_{sample}} &= \bar{\theta}_{il_i} + \frac{t'_{sample} - (s_{sample} - \bar{s}_i)}{2c_{\theta_{il}}} \\ q_{t_{sample}} &= \bar{q}_{t_i} + \frac{t'_{sample} - (s_{sample} - \bar{s}_i)}{2c_{q_t}}\end{aligned}\tag{103}$$

where i once again denotes from which Gaussian plume the sample is drawn from.

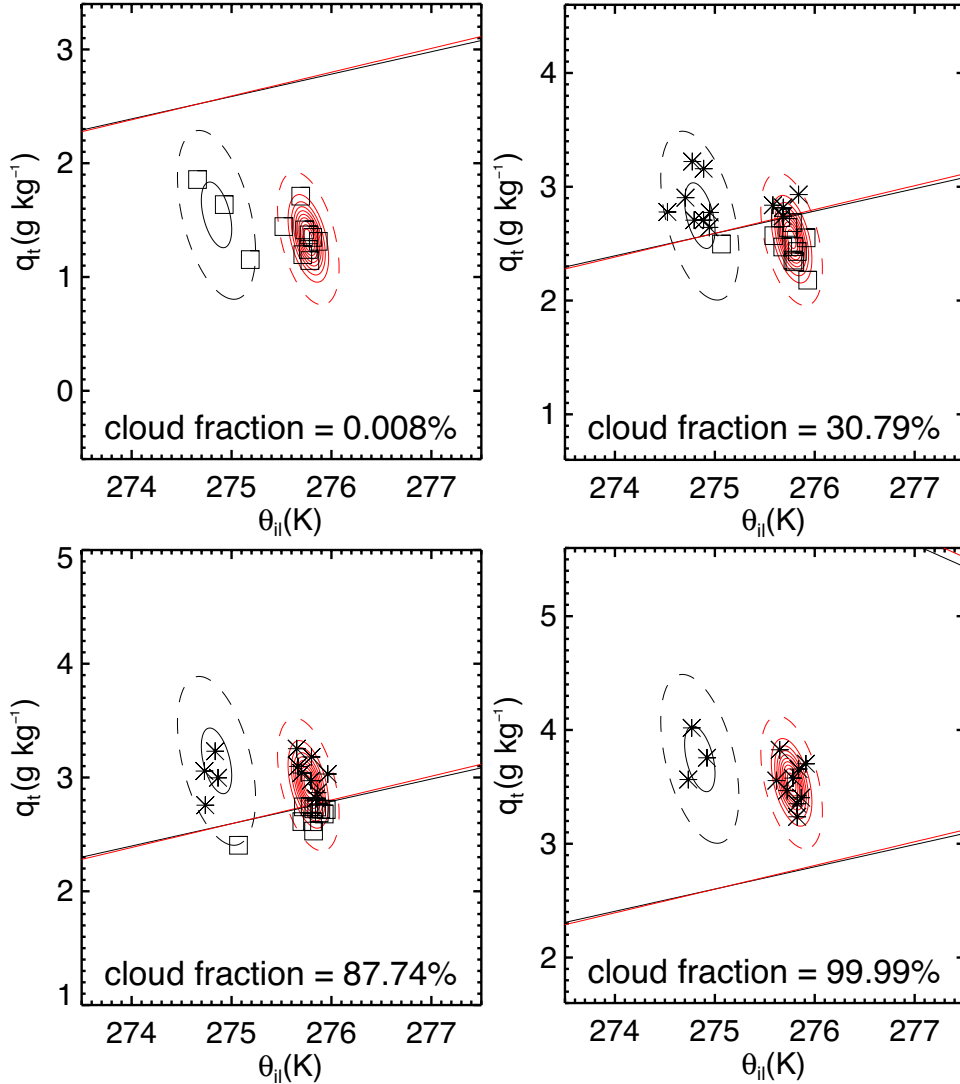


FIGURE 2.4. Shown are latin hypercube samples for different levels of saturation. Asterisks denote cloudy samples and boxes denote clear samples. The solid lines denote saturation. Black contours and lines are for the less dominant Gaussian plume; red lines are for the dominant Gaussian plume.

Figure 2.4 shows an example of the latin hypercube sampling process for a typical double Gaussian PDF at different levels of saturation. For each panel, notice how the samples are more likely to be drawn from the vicinity of the mean of each plume yet the samples are adequately spread out to cover the PDF. For a more efficient algorithm, only clear samples are drawn from a PDF with a cloud fraction below a threshold (top left panel) and only cloudy samples are drawn from a PDF that is saturated above a threshold (bottom right). For partial cloudiness (top right and bottom left), both sets of samples are drawn.

From the samples of θ_{il} and q_t , the microphysics parameterization needs the actual temperature, cloud liquid and ice water contents, and water vapor specific humidity. These are calculated in the following way. For clear samples, the procedure is quite straightforward. Assuming no cloud liquid water or ice ($q_{l_{sample}} = 0$ and $q_{i_{sample}} = 0$), the temperature of the sample is

$$T_{sample} = \left(\frac{p}{p_0}\right)^\kappa \theta_{il_{sample}} + \frac{L_v}{c_p} \bar{q}_r + \frac{L_s}{c_p} (\bar{q}_g + \bar{q}_s) \quad (104)$$

where subscripts r , s , and g denote rain, snow, and graupel, respectively. Also, trivially for clear samples, $q_{v_{sample}} = q_{t_{sample}}$. For cloudy samples, however, the temperature depends on the sample cloud liquid and water contents, all of which are unknown. As before, a simple iterative procedure is used.

- (1) If $\overline{T_{il_{sample}}} > 273.16$ K then $q_{l_{sample}} = s_{sample}$, and no iteration is needed.

$$T_{sample} = \left(\frac{p}{p_0}\right)^\kappa \theta_{il_{sample}} + \frac{L_v}{c_p} (q_{l_{sample}} + \bar{q}_r) + \frac{L_s}{c_p} (\bar{q}_g + \bar{q}_s) \quad (105)$$

- (2) Otherwise, calculate the first guess w_n assuming no condensate ($T_{sample} = T_{il_{sample}}$).

$$w_n = \max \left[0, \min \left(1, \frac{T_{sample} - T_{00}}{T_0 - T_{00}} \right) \right] \quad (106)$$

(3) Using the weight from step 2, calculate the sample's cloud liquid and ice content.

$$q_{l_{sample}} = w_n s_{sample} \quad (107)$$

$$q_{i_{sample}} = (1 - w_n) s_{sample}$$

(4) Calculate a new sample temperature using

$$T_{sample} = \left(\frac{p}{p_0}\right)^\kappa \theta_{il_{sample}} + \frac{L_v}{c_p} (q_{l_{sample}} + \bar{q}_r) + \frac{L_s}{c_p} (q_{i_{sample}} + \bar{q}_g + \bar{q}_s) \quad (108)$$

(5) Calculate a new estimate for w_n using (106).

(6) Repeat steps 3 - 5 until the change in temperature estimates is below some threshold, currently 0.001 K.

Finally, for the cloudy sample, $q_{v_{sample}} = q_{t_{sample}} - q_{l_{sample}} - q_{i_{sample}}$.

The microphysics scheme used in THOR is the simple bulk scheme of Khairoutdinov and Randall (2003) from the SAM model. It requires one to predict q_p , the precipitating water mixing ratio, and to partition it amongst rain, snow, and graupel using the mean temperature of a grid cell. The physical processes included in this scheme are rain autoconversion, ice aggregation into snow, collection of cloud water by all precipitation species, collection of cloud ice by all precipitation species, and evaporation of all precipitation species. Formulas, constants, and thresholds for these processes are exactly as described in Khairoutdinov and Randall (2003) except that the inputs to the scheme are samples and not grid-cell mean values and the threshold for rain autoconversion has been reduced from 1.0 g/kg to 0.65 g/kg to better match results with observations. The formulas implemented are recreated in appendix D, where it is shown how the samples generated in this section are used. Since it is possible that any number of samples are used in any timestep with the sampling method

described, multiple estimates of the microphysical processes may be generated. Ultimately, all of the estimates of the process rates are averaged using the arithmetic mean over the samples so that only one rate is generated at each time step for each process.

2.6. RADIATION DRIVER AND SCHEME

Clouds and radiation strongly affect each other. Clouds are effective “trappers” of long-wave radiation and reflectors and scatterers of shortwave radiation. Radiative cooling can drive circulations that perpetuate clouds, like stratocumulus fields, and shortwave heating at cloud top can thin or dissipate clouds. A parameterization designed to better simulate clouds and their effects should therefore include an accurate representation of radiative transfer. Typically in large-scale models, the radiative transfer scheme utilizes one-dimensional columns and neglects 3D radiative transfer. In addition, accounting for SGS cloudiness with such a scheme can be difficult. In the popular Rapid Radiative Transfer Model for GCMs (RRTMG) radiation scheme, the default behavior of the parameterization is to assume 100% cloud cover if any cloud water is found in a grid cell. An elegant solution to the problem of solving radiative transfer in heterogeneous cloud fields has been proposed by Pincus et al. (2003), called the Monte Carlo Independent Column Approximation (McICA). This approach hinges on the generation of “sub-columns” that each contain a random sample of the SGS cloud field. Each sub-column is then used for one band of a broadband radiative transfer calculation. The individual band calculations from the random sub-columns are then combined to form a single profile of radiative heating rate. This approach is nearly as efficient as a normal broadband radiative transfer calculation, except for the overhead associated with generating the random sub-columns since each band is only calculated once. To use the McICA approach, one needs to be able to modify the actual radiation code in

order to calculate each individual band with a different sub-column input. For THOR, it is desirable to create a radiation driver that uses aspects of the McICA approach but leaves the radiation code unmodified so that different radiation schemes may be substituted. Therefore, THOR's radiation driver is designed to create the random sub-columns with cloud properties according to the diagnosed PDF, and to call a chosen broadband radiative transfer calculation for each sub-column. This approach is not as efficient as the McICA approach since all bands are used for each sub-column rather than one band per sub-column.

The sub-column generator follows the approach of Räisänen et al. (2004). Although the radiation scheme requires profiles of the input variables from the entire domain, the sub-column generator only provides binary cloud values and random cloud water samples drawn from the PDF for levels between the cloud top and the cloud base. Starting from the cloud top, the generator draws a random number from $[0,1]$. If the random number is less than the cloud fraction at that layer, then the sub-column is deemed cloudy, otherwise it is deemed clear. If the sub-column is cloudy, an additional random number from $[0,1]$ is drawn to determine the cloud water. The second random number is considered the cumulative frequency distribution of cloud water, and the actual value of cloud water is found by taking the inverse of the cumulative frequency distribution for the assumed cloud water distribution, in THOR's case a Gaussian distribution. For subsequent levels below the cloud top height, one needs to determine the cloud overlap. The Räisänen et al. (2004) method uses a generalized overlap assumption that assumes the actual cloud overlap falls between maximum and random. It is based on the idea that cloud layers close together are more likely to overlap in a maximal way, whereas cloud layers separated by a vertical distance have a greater probability of overlapping in a random way. Precisely how the overlap relationship

is determined is controlled by an exponential function based on the distance between layers and a so-called “decorrelation depth.” There are separate decorrelation depths for cloud fraction and cloud water, and their values are estimated according to observational data. The algorithm is described in detail below.

Since the radiative transfer scheme is usually called at a longer time step than other quantities, the following algorithm is used with time-mean profiles calculated since the last radiation time step. The first step is to determine the lowest and highest levels of cloud fraction in the domain, denoted by z_{top} and z_{bot} . Above z_{top} and below z_{bot} , the sub-column profiles are identical and equal to the time-mean profiles. Where cloud fraction exists in the domain, between z_{bot} and z_{top} , the following algorithm is used to construct the cloud property sub-columns.

For each sub-column, at z_{top} , determine which Gaussian plume to draw a sample from.

$$\text{Gaussian plume chosen} = \begin{cases} 2 & \text{RND}_1 \leq a_{z_{top}} \\ 1 & \text{otherwise} \end{cases} \quad (109)$$

where RND_1 (and all random numbers in this algorithm) is a random number on $[0,1]$ and $a_{z_{top}}$ is the Gaussian weight from section 2.3 at the cloud top level. Let n be the Gaussian plume chosen. Next, determine whether there is cloud at the current level for the Gaussian plume chosen in (109). Let $x_{z_{top}} = \text{RND}_2$. Then

$$\text{cloud fraction}_{top} = \begin{cases} 0 & x_{z_{top}} \leq 1 - R_{n_{z_{top}}} \\ 1 & \text{otherwise} \end{cases} \quad (110)$$

where $R_{n_{z_{top}}}$ is the cloud fraction for plume n at cloud top. If cloud fraction $_{top} = 1$, then determine the cloud water at this level. Let $y_{z_{top}} = \text{RND}_3$ which is the value of the cumulative distribution function. To retrieve the cloud water sample, use the following formula that uses the inverse of the cumulative distribution function using the diagnosed PDF at this level (same as the formula for the microphysics sampling algorithm).

$$q_{c_{top}} = \sigma_{s_n} F_G^{-1} [y_{z_{top}} R_n + (1 - R_n)] + \overline{s_n} \quad (111)$$

where all values on the RHS of this equation are at the cloud top level.

For levels between z_{top} and z_{bot} , the cloud properties depend on the cloud overlap and an additional step is added to determine whether the overlap is maximum or random. An “overlap parameter” between two levels is calculated according to

$$\begin{aligned} o_{cld} &= e^{-\frac{(z_{k+1}-z_k)}{L_{cf}}} \\ o_{qc} &= e^{-\frac{(z_{k+1}-z_k)}{L_{qc}}} \end{aligned} \quad (112)$$

where k is the index of the current level, $k + 1$ is the index for the level above, L_{cf} is the decorrelation depth for cloud fraction, and L_{qc} is the decorrelation depth for cloud water. Discussions about appropriate values of the decorrelation lengths can be found in Pincus et al. (2005) and Barker (2008). For THOR, constant values of $L_{cf} = 2000\text{m}$ and $L_{qc} = 1/2 L_{cf}$ were used. As in the top cloud layer, the Gaussian plume is chosen with an additional random number using

$$\text{Gaussian plume chosen} = \begin{cases} 2 & \text{RND}_4 \leq a_k \\ 1 & \text{otherwise} \end{cases} \quad (113)$$

Next, the value of x_k is determined according to

$$x_k = \begin{cases} x_{k+1} & \text{RND}_5 \leq o_{cld} \\ \text{RND}_6 & \text{otherwise} \end{cases} \quad (114)$$

This determines whether maximum overlap (x_{k+1}) or random overlap (RND_6) is chosen.

Once again, it must be determined if this level is cloudy or not:

$$\text{cloud fraction}_k = \begin{cases} 0 & x_k \leq 1 - R_{n_k} \\ 1 & \text{otherwise} \end{cases} \quad (115)$$

If cloudy, it must be determined whether to use maximum or random overlap for cloud water:

$$y_k = \begin{cases} y_{k+1} & \text{RND}_7 \leq o_{qc} \\ \text{RND}_8 & \text{otherwise} \end{cases} \quad (116)$$

Finally, the cloud water sample value is chosen given the cumulative distribution function,

y_k :

$$q_{c_k} = \sigma_{s_n} F_G^{-1} [y_k R_n + (1 - R_n)] + \bar{s}_n \quad (117)$$

For all levels, the cloud liquid and ice are partitioned according to

$$\begin{aligned} q_l &= w q_{c_k} \\ q_i &= (1 - w) q_{c_k} \end{aligned} \quad (118)$$

where $w = \frac{q_l}{q_l + q_i}$. For each sub-column, the profiles of water vapor, cloud liquid water, cloud ice water, and absolute temperature are calculated and used as input into the broadband

radiative transfer scheme RRTMG. The longwave and shortwave fluxes are averaged over all sub-columns, and the heating rates are calculated using the averaged radiative fluxes. Any number of sub-columns may be used, although an additional radiation calculation is required for each sub-column, so it may significantly slow down the integration. For the results presented in this work, the number of sub-columns used was 10.

2.7. SURFACE LAYER SCHEME

The portion of the Earth’s boundary layer closest to the surface is often called the “surface layer” or “constant flux layer,” and it is often treated differently than the remainder of the boundary layer. It is in this layer that Monin-Obukhov similarity theory is often applied to provide surface fluxes, variances, and covariances and even to provide diagnostic values of state variables at given heights within the layer. The central idea of the theory is that the variables of interest in the surface layer (fluxes, variances, mean state variables, height) can be combined into nondimensional groups and that the empirical relationships derived from observations between the nondimensional groups are universal. If the relationships are universal, it follows that the empirical relationships derived from a particular dataset are applicable for conditions much different than those used to derive the original relations. For example, the so-called “Businger-Dyer” relationships relate fluxes of momentum and heat to their mean profiles as a function of height and stability (Businger et al. 1971). Their relationships were calculated using data from a field experiment in southwestern Kansas, and yet their relationships based on Monin-Obukhov similarity theory have been used successfully to represent surface layers around the world with vastly different geographies and meteorological conditions.

Although questions have been raised regarding the applicability of the original Businger-Dyer relationships to more extreme static stabilities (both positive and negative), many recent “state-of-the-art” surface layer schemes still use formulas very close to the original ones. The surface layer scheme used in THOR was recently developed for use in the Weather Research & Forecasting model by Jimenez et al. (2012), but it can be thought of as using the same ideas and relationships as Businger et al. (1971) fine-tuned to be more applicable for very stable and very unstable conditions. What follows is a description of the surface scheme used in THOR, including any deviations from the Jimenez et al. (2012) formulation.

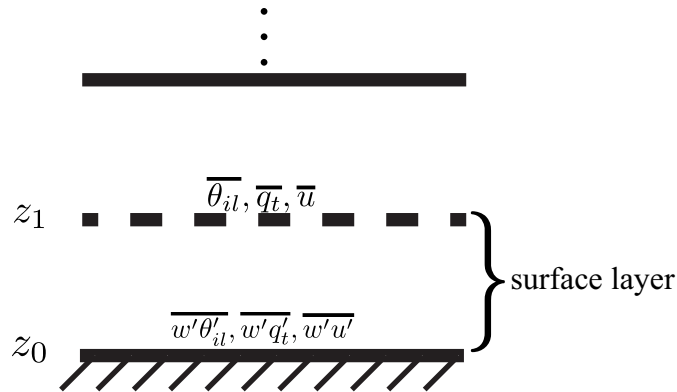


FIGURE 2.5. Surface Layer Grid

THOR’s grid near the surface is shown in figure 2.5. Mean state variables reside in the cell centers and second-order moments reside on cell interfaces, with the bottom interface representing the roughness length, z_0 . It is assumed that second-order moments are constant in the surface layer so that the calculation of the fluxes at z_1 is sufficient to know the surface

fluxes. The surface fluxes are given by the following bulk aerodynamic formulas

$$\begin{aligned}
\tau &= \rho u_*^2 = \rho C_d U_1^2 \\
H &= -\rho c_p u_* \theta_* = -\rho c_p C_h U_1 (\theta_a - \theta_g) \\
LH &= L_v \rho u_* q_* = L_v \rho M C_q U_1 (q_g - q_a)
\end{aligned} \tag{119}$$

where τ , H , and LH represent the surface momentum, sensible heat, and latent heat flux, C_d , C_h , and C_q are the bulk transfer coefficients for momentum, heat, and moisture, U_1 is the wind speed, subscript a denotes values at z_1 , subscript g denotes values at or just above the physical surface, M is a measure of soil moisture availability (supplied by a land surface parameterization in the future), u_* is the friction velocity, θ_* is the temperature scale, and q_* is the moisture scale. The bulk transfer coefficients from Jimenez et al. (2012) can be written

$$\begin{aligned}
C_d &= \frac{k^2}{A^2} \\
C_h &= \frac{k^2}{A \left[\ln \left(\frac{z + z_{0h}}{z_{0h}} \right) - \psi_h \left[\zeta \left(1 + \frac{z_{0h}}{z} \right) \right] + \psi_h \left(\zeta \frac{z_{0h}}{z} \right) \right]} \\
C_q &= \frac{k^2}{A \left[\ln \left(\frac{ku_* z}{K_a} + \frac{z}{z_l} \right) - \psi_h(\zeta) + \psi_h \left(\zeta \frac{z_l}{z} \right) \right]}
\end{aligned} \tag{120}$$

where

$$A = \ln \left(\frac{z + z_0}{z_0} \right) - \psi_m \left[\zeta \left(1 + \frac{z_0}{z} \right) \right] + \psi_m \left(\zeta \frac{z_0}{z} \right),$$

k is the von Kármán constant (taken as $k = 0.4$), z_0 is the roughness length for momentum, z_{0h} is the roughness length for scalars, and K_a is described as the the “background molecular diffusivity” in Grell et al. (1994). Its value is taken to be $K_a = 2.4 \times 10^{-5} \text{ m}^2\text{s}^{-1}$. The symbol

z_l is the depth of the viscous sublayer (0.01 m) over land and equal to z_{0h} over the ocean. Note that while Jimenez et al. (2012) assume that z_0 and z_{0h} are equal, that assumption is relaxed here.

The symbols ψ_m and ψ_h are integrated forms of the Monin-Obukhov similarity functions with their inputs following. The symbol ζ is known as the nondimensional Monin-Obukhov stability parameter and is defined as $\zeta = \frac{z}{L}$ where L is the Obukhov length defined by (Stull 1988)

$$L = \frac{-\overline{\theta}_v u_*^3}{gk\overline{w'\theta'_{vs}}} \quad (121)$$

Since ζ depends on values of the surface fluxes which themselves depend on ζ , iteration is often used to solve the system. However, ζ can be approximated as a function of the bulk Richardson number, Ri_b , alone. The bulk Richardson number is calculated as

$$Ri_b = \frac{gz_1}{\theta_a} \left(\frac{\theta_{va} - \theta_{vg}}{U_1^2} \right) \quad (122)$$

where the windspeed U_1 is enhanced by w_* to account for gustiness in a convective boundary layer following Beljaars (1995):

$$U_1 = \sqrt{u_1^2 + v_1^2 + w_*^2} \quad (123)$$

The 1 subscripts denote that they are values from the lowest model level and the convective velocity w_* is given by

$$w_* = \sqrt[3]{\frac{gz_i \overline{w'\theta'_{vs}}}{\theta_{va}}} \quad (124)$$

The boundary layer height, z_i , is approximated to 1000 m for this calculation and the buoyancy flux $\overline{w'\theta'_{vs}}$ is taken from the previous time step since the addition of w_* in equation

(123) is itself an approximation. To calculate the Monin-Obukhov stability parameter, ζ , as a function of Ri_b , THOR uses the method of Li et al. (2010). Their method has been tested using a wide range of roughness lengths and atmospheric stabilities and was found to be superior to previous non-iterative methods for determining ζ and can be summarized with

$$\zeta = \begin{cases} (a_{s_{11}}\alpha + a_{s_{21}}) Ri_b + b_{s_{11}}\alpha + b_{s_{21}}\beta + b_{s_{22}} & Ri_b > 0.2 \\ [(a_{w_{11}}\beta + a_{w_{12}})\alpha + (a_{w_{21}}\beta + a_{w_{22}})] Ri_b^2 + \\ \quad [(b_{w_{11}}\beta + b_{w_{12}})\alpha + (b_{w_{21}}\beta + b_{w_{22}})] Ri_b & 0 < Ri_b \leq 0.2 \\ 0 & Ri_b = 0 \\ a_{u_{11}}\alpha Ri_b^2 + [(b_{u_{11}}\beta + b_{u_{12}})\alpha^2 + (b_{u_{21}}\beta + b_{u_{22}})\alpha + \\ \quad (b_{u_{31}}\beta^2 + b_{u_{32}}\beta + b_{u_{33}})] Ri_b & Ri_b < 0 \end{cases} \quad (125)$$

where $\alpha = \ln\left(\frac{z}{z_0}\right)$, $\beta = \ln\left(\frac{z_0}{z_{0h}}\right)$, z_{0h} is the roughness length for heat and the constants are given in table 2.4.

TABLE 2.4. Constant values for the ζ function of Li et al. (2010)

Constant	Value	Constant	Value	Constant	Value
$a_{s_{11}}$	0.7529	$a_{w_{11}}$	0.5738	$a_{u_{11}}$	0.0450
$a_{s_{21}}$	14.9400	$a_{w_{12}}$	-0.4399	$b_{u_{11}}$	0.0030
$b_{s_{11}}$	0.1569	$a_{w_{21}}$	-4.9010	$b_{u_{12}}$	0.0059
$b_{s_{21}}$	-0.3091	$a_{w_{22}}$	52.5000	$b_{u_{21}}$	-0.0828
$b_{s_{22}}$	-1.3030	$b_{w_{11}}$	-0.0539	$b_{u_{22}}$	0.8845
		$b_{w_{12}}$	1.5400	$b_{u_{31}}$	0.1739
		$b_{w_{21}}$	-0.6690	$b_{u_{32}}$	-0.9213
		$b_{w_{22}}$	-3.2820	$b_{u_{33}}$	-0.1057

With ζ calculated, one can determine the integrated universal functions needed for the bulk transfer coefficients using the following from Jimenez et al. (2012):

$$\psi_m(\zeta') = \begin{cases} -a \ln \left[\zeta' + (1 + \zeta'^b)^{1/b} \right] & Ri_b > 0 \\ 0 & Ri_b = 0 \\ \frac{\psi_{K_m}(\zeta') + \zeta'^2 \psi_{C_m}(\zeta')}{1 + \zeta'^2} & Ri_b < 0 \end{cases} \quad (126)$$

$$\psi_h(\zeta') = \begin{cases} -c \ln \left[\zeta' + (1 + \zeta'^d)^{1/d} \right] & Ri_b > 0 \\ 0 & Ri_b = 0 \\ \frac{\psi_{K_h}(\zeta') + \zeta'^2 \psi_{C_h}(\zeta')}{1 + \zeta'^2} & Ri_b < 0 \end{cases} \quad (127)$$

where ζ' are the input values listed in the bulk aerodynamic coefficient formulas (equation (120)). The $\psi_{K_{h,m}}$ and $\psi_{C_{h,m}}$ in the formulas for the unstable Richardson numbers come from the fact that Jimenez et al. (2012) used the Monin-Obukhov similarity functions from the Kansas experiments (the Businger-Dyer relationships) for near-neutral stability values and different similarity functions for more unstable conditions. These integrated universal

functions are

$$\begin{aligned}
\psi_{K_m}(\zeta') &= 2 \ln\left(\frac{1+x}{2}\right) + \ln\left(\frac{1+x^2}{2}\right) - 2 \tan^{-1}x + \frac{\pi}{2} \\
\psi_{K_h}(\zeta') &= 2 \ln\left(\frac{1+x^2}{2}\right) \\
\psi_{C_{h,m}}(\zeta') &= \frac{3}{2} \ln(y^2 + y + 1/3) - \sqrt{3} \tan^{-1}\left(2y + \frac{1}{\sqrt{3}}\right) + \frac{\pi}{\sqrt{3}}
\end{aligned} \tag{128}$$

where

$$\begin{aligned}
x &= (1 - 16\zeta')^{1/4} \\
y &= (1 - \alpha_{m,h}\zeta')^{1/3}
\end{aligned}$$

and $\alpha_m = 10$ and $\alpha_h = 34$. The constants a, b, c , and d in equations (126) and (127) are $a = 6.1$, $b = 2.5$, $c = 5.3$, and $d = 1.1$.

At this point, there is enough information to calculate the total momentum flux, τ , from equation (119) using C_d from equation (120). To calculate the remaining fluxes, one needs to first calculate the friction velocity, u_* from

$$u_* = \text{MAX}\left(0.001, \sqrt{C_d U_1^2}\right) \tag{129}$$

With u_* , the remaining sensible and latent heat fluxes may be calculated with equations (119) and (120). The component momentum fluxes, $\overline{w'u'}$ and $\overline{w'v'}$ are calculated from u_* using

$$\begin{aligned}
\overline{w'u'} &= \left(\frac{u_1}{U_1}\right) u_*^2 \\
\overline{w'v'} &= \left(\frac{v_1}{U_1}\right) u_*^2
\end{aligned} \tag{130}$$

The surface fluxes of θ_{il} and q_t can be trivially calculated from H and LH in equation (119) with

$$\begin{aligned}\overline{w'\theta'_{il}} &= \frac{H}{\rho c_p} \\ \overline{w'q'_t} &= \frac{LH}{L_v c_p}\end{aligned}\tag{131}$$

In addition to the fluxes of momentum, heat, and moisture in the surface layer, one needs values of the other second-order moments in the surface layer as boundary conditions. The relationships listed in Stull (1988) based on the surface layer static stability are used in this case. For stable conditions, $Ri_b \geq 0$, the following relationships are used

$$\begin{aligned}\overline{u'^2} &= \overline{v'^2} = 4.25u_*^2 \\ \overline{w'^2} &= 2.5u_*^2 \\ \overline{\theta'^2_{il}} &= 4\theta_*^2 \\ \overline{q'^2_t} &= 4q_*^2 \\ \overline{\theta'_{il}q'_t} &= 4\theta_*q_*\end{aligned}\tag{132}$$

where $\theta_* = \frac{\overline{w'\theta'_{il}}}{u_*}$ and $q_* = \frac{\overline{w'q'_t}}{u_*}$. For unstable conditions, $Ri_b < 0$, the following relationships are used instead.

$$\begin{aligned}
\overline{u'^2} &= \overline{v'^2} = 4.25u_*^2 \\
\overline{w'^2} &= 3.6(-\zeta)^{2/3}u_*^2 \\
\overline{\theta'^2_{il}} &= 0.9(-\zeta)^{-2/3}\theta_*^2 \\
\overline{q'^2_t} &= 0.9(-\zeta)^{-2/3}\theta_*q_* \\
\overline{\theta'_{il}q'_t} &= 0.9(-\zeta)^{-2/3}q_*^2
\end{aligned} \tag{133}$$

Finally, although a host model for the THOR parameterization is expected to provide values for the roughness lengths over land from a land surface model or from a land surface categorization technique, a simple parameterization for the roughness lengths over the ocean is provided in THOR. For the momentum roughness length over the ocean, Charnock's relation (Charnock 1955) is used: $z_0 = 0.015\frac{u_*^2}{g}$. For the scalar roughness length, the formulas for the roughness lengths for heat and water vapor found in Brutsaert (1982) are averaged together: $z_{0_h} = \frac{0.51\nu}{u_*}$ where $\nu = 1.4 \times 10^{-5} \text{ m}^2\text{s}^{-1}$ is the kinematic viscosity of air.

2.8. IMPLEMENTATION NOTES

The continuous predictive equations presented in this chapter must be discretized in order to be useful in a numerical model. The choice of grid construction and derivative discretization follows Firl (2009), and the model grid is shown in figure 2.6. THOR uses a staggered grid approach with mean quantities and third-order moments at grid centers (dashed lines) and second-order moments and PDF samples at grid interfaces (solid lines). This grid allows a simple two-point centered spatial derivative discretization that is second-order accurate in

space. The time-stepping scheme chosen for THOR is the simple forward Euler scheme for the same reasons given in Firl (2009), namely simplicity, continuity with past schemes, and the scheme is reasonably stable for diffusion problems (the closest simple analog to THOR). The predictive equation for precipitating water and the calculation of subsidence forcing are the only exceptions. These processes are discretized using the upstream scheme.

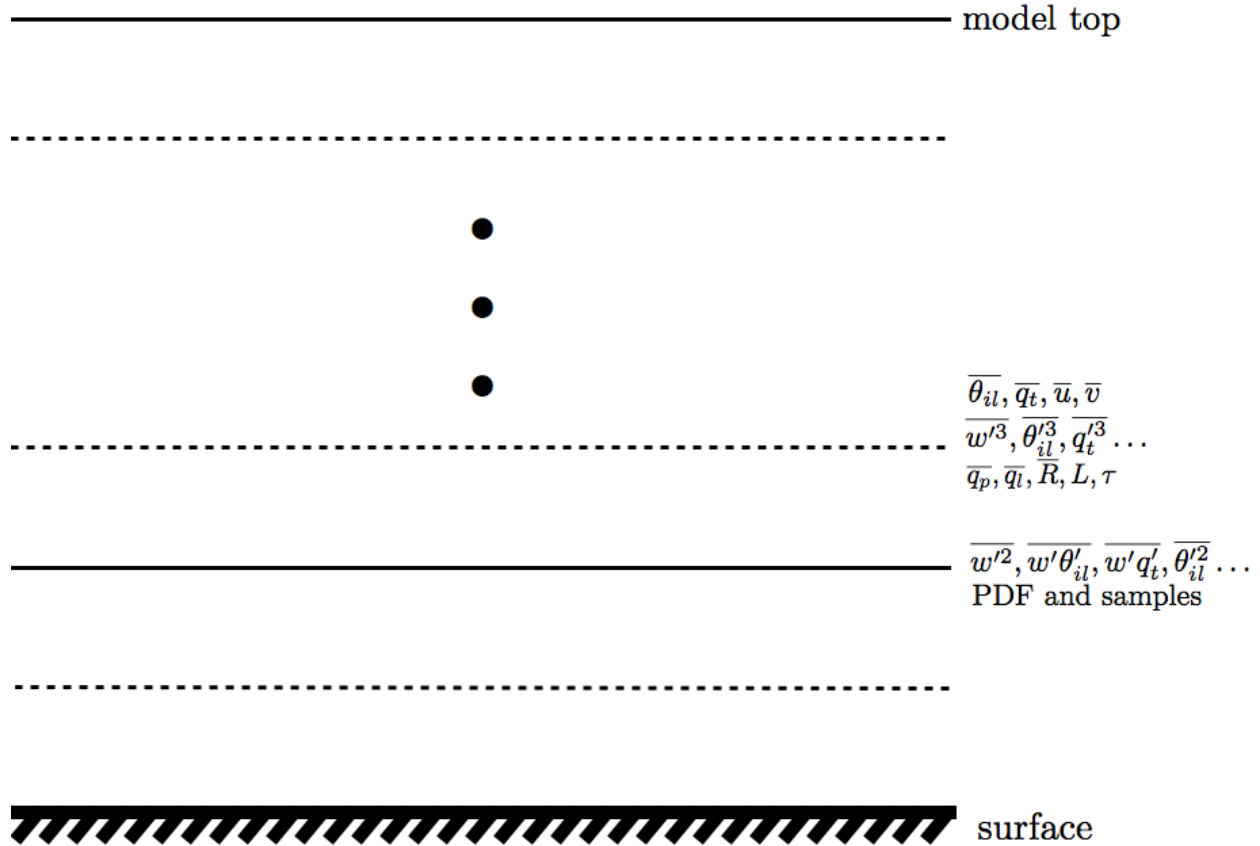


FIGURE 2.6. A depiction of THOR’s staggered grid and the placement of variables.

Due to the many different types of parameterizations in THOR and the complexity of the higher-order closure model, it is difficult to obtain a precise stability criterion. Firl (2009) determined that a useful guide for determining computational stability can be gleaned by considering the discretization of the transport terms of the second-order moments. For example, consider the discretized form of the predictive equation for $\overline{w'^2}$ in equation (3)

with only the transport term kept and neglecting the third-order moment buoyancy term in equation (15):

$$\begin{aligned} \frac{\overline{w'^2}_{k+1/2}^{t+1} - \overline{w'^2}_{k+1/2}^t}{\Delta t} = & -\frac{1}{\Delta z} \left(\right. \\ & \frac{-3\tau}{2c_8 + p_1 + 3(1 - d_1)\tau \frac{\partial \overline{w}}{\partial z}} \frac{1}{2} \left(\overline{w'^2}_{k+1/2}^t + \overline{w'^2}_{k+3/2}^t \right) \frac{\overline{w'^2}_{k+3/2}^t - \overline{w'^2}_{k+1/2}^t}{\Delta z} - \\ & \left. \frac{-3\tau}{2c_8 + p_1 + 3(1 - d_1)\tau \frac{\partial \overline{w}}{\partial z}} \frac{1}{2} \left(\overline{w'^2}_{k+1/2}^t + \overline{w'^2}_{k-1/2}^t \right) \frac{\overline{w'^2}_{k+1/2}^t - \overline{w'^2}_{k-1/2}^t}{\Delta z} \right) \end{aligned} \quad (134)$$

One can recognize equation (134) as the discretized form of the diffusion equation for $\overline{w'^2}_{k+1/2}$ with the diffusion constant, K , equal to:

$$K = \frac{3\tau \overline{w'^2}}{2c_8 + p_1 + 3(1 - d_1)\tau \frac{\partial \overline{w}}{\partial z}} \quad (135)$$

For centered spatial derivatives and the forward Euler time-stepping scheme, the stability criterion for the diffusion equation is given by

$$\frac{K\Delta t}{(\Delta z)^2} \leq \frac{1}{2} \quad (136)$$

Using this relationship, one can get a good estimate of the maximum usable time step for a given grid spacing if K is known. Of course, the same analysis is valid for all of the other second-order moments calculated in THOR, but, in practice, the K value for $\overline{w'^2}$ has the greatest magnitude. Table 2.5 gives the maximum values of K for four of the simulations used in this study, together with the grid spacing used, the maximum theoretical time step from equation (136), and the actual maximum time step determined from test runs.

The theoretical maximum time steps are within 10-20% of the actual maximum time steps determined from test runs.

TABLE 2.5. Theoretical and actual maximum time steps for four test cases.

Case	max K [m ² s ⁻¹]	Δz [m]	theoretical Δt [s]	actual Δt [s]
BOMEX	100	100	50	60
DYCOMS	100	25	3.125	3.85
RICO	300	40	2.67	2.9
ASTEX	75	25	4.17	4.5

To get an idea of algorithm efficiency, runtimes were recorded for four test cases run on an Apple Macbook Pro built in late 2011 with a 2.5 GHz Intel Core i7 processor. The statistics of the four runs are recorded in table 2.6. The runtimes range from 43 milliseconds for the 6 hour BOMEX run with 30 grid levels to 17.06 seconds for the 40 hour ASTEX run with 120 levels. The BOMEX run is most efficient, taking 0.006 seconds per simulated grid level per simulated day, and the RICO case is least efficient taking 0.112 seconds per grid level per simulated day.

TABLE 2.6. Runtimes for four test cases

Case	Δt [s]	# of levels	simulated time [day]	runtime [s]	efficiency [s level ⁻¹ day ⁻¹]
BOMEX	50.0	30	0.25	0.043	0.006
RICO	2.8	100	1.0	11.237	0.112
DYCOMS	3.8	60	0.25	1.31	0.087
ASTEX	4.5	120	1.67	17.06	0.085

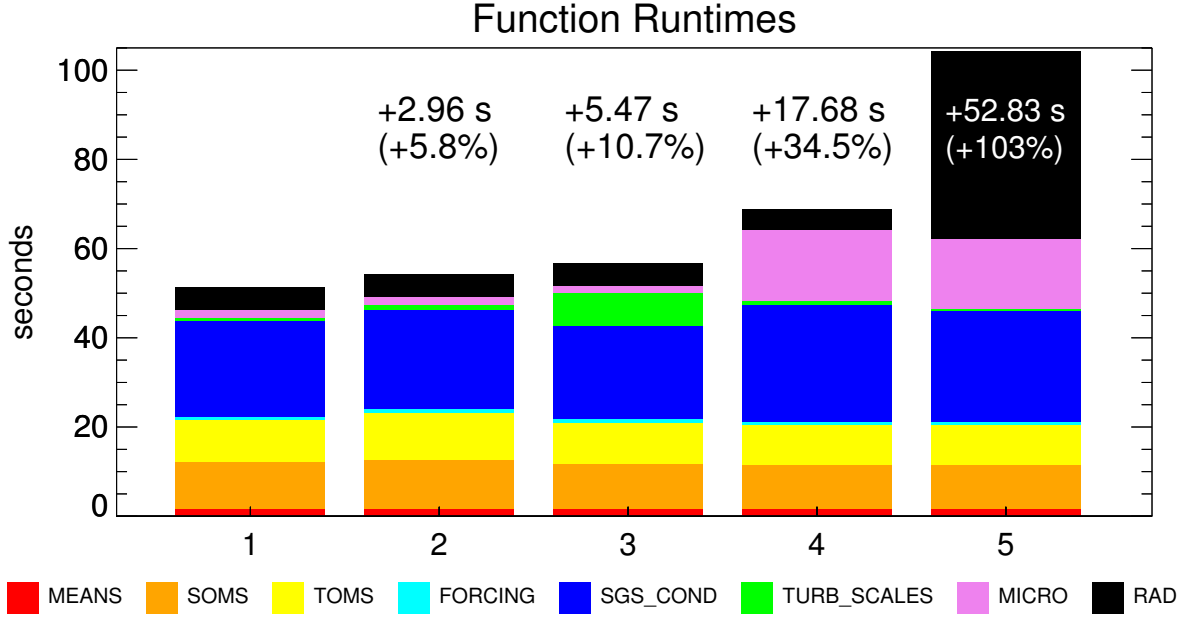


FIGURE 2.7. Runtimes divided into model functions for the five experiments listed in the text. The functions are divided into “MEANS” (prediction of mean quantities), “SOMS” (prediction of the second-order moments), “TOMS” (calculation of the third-order moments), “FORCING” (calculation of large-scale forcing), “SGS_COND” (all calculation related to SGS condensation), “TURB_SCALES” (all calculation involved with turbulence length and time scales), “MICRO” (all calculation involved with microphysics), and “RAD” (all calculation involved in calculating radiative transfer). The interior labels denote the increase in computation time from experiment 1.

In figure 2.7, the runtimes of the individual model components are shown for five different model configurations, all using the ASTEX case. Experiment 1 uses the most efficient algorithms including diagnostic third-order moments, a constant turbulence length scale entrainment rate, and no PDF sampling for either the microphysics or radiation schemes. Experiment 2 is run to determine the expense of using prognostic third-order moments and is set up exactly like experiment 1 except for the third-order moment algorithm. Experiment 3 is designed to determine the added expense of using the stochastic turbulence length scale algorithm and is set up exactly like experiment 1 except for that algorithm. Experiment 4 is run to determine the added expense of using latin hypercube PDF sampling for the microphysics scheme, and it is exactly like experiment 1 except for the microphysics PDF

sampling. Experiment 5 is designed to determine the added cost of using PDF sampling for both microphysics and radiation, and it is exactly like experiment 1 except for the addition of both PDF sampling algorithms. First, it is apparent that the prediction of grid-cell mean quantities and the calculation of the large-scale forcing are the least computationally expensive components of THOR. The core higher-order closure model consists of the second- and third-order moment calculations, and takes up about 40% of the computational load for the simplest run (experiment 1). The time required to run these components stays consistent throughout the experiments as well, although the proportion of the total runtime changes depending on the complexity of the other model components. The calculation of the SGS condensation scheme (including diagnosis of the PDF) accounts for about 40% of experiment 1 as well, with the radiation, microphysics, and turbulence length and time scale calculations taking up the remaining roughly 15% of the time. Experiment 2 shows that there is relatively little added computational expense of using full predictive equations for the third-order moments, a roughly 6% time penalty. Experiment 3 shows that using the stochastic algorithm for calculating the turbulence length scale increases the cost associated with calculating this quantity by roughly eight-fold, although the impact on the model as a whole is still somewhat minor at about an 11% penalty. Experiment 4 shows that sampling the PDF for the microphysics scheme (using 2 samples per time step) increases the cost associated with microphysics by another eight-fold or so over the non-sampling run and increases the overall runtime by over 34%. Once again, experiment 5 demonstrates an approximate eight-fold increase in computation time when sampling is added for the radiation scheme (with 10 subcolumns generated per radiation time step), leading to a combined

increase of over 100% in execution time for using both sampling processes compared to the most efficient run without sampling.

CHAPTER 3

MODEL EVALUATION AND SENSITIVITIES

THOR was designed to be a “general” SGS model in the sense that the goal was to be able to adequately parameterize SGS processes under any type of cloud regime, from clear sky to cumulus regimes with cloud fractions significantly less than one to stratocumulus and stratus regimes with cloud fractions close to one. In addition, should the parameterization be used throughout the model domain in a AGCM, it should be able to handle deep convection. In order to test THOR’s ability, several test cases were chosen spanning a range of atmospheric conditions and cloud types including non-precipitating shallow cumulus (BOMEX), slightly more active and precipitating shallow cumulus (RICO), nocturnal drizzling stratocumulus (DYCOMS), mixed-phase arctic precipitating stratocumulus (MPACE), and transitional stratocumulus-to-cumulus clouds (ASTEX). All test cases are idealized to some extent and have been previously utilized for LES intercomparison studies, whereby many LES models from different institutions simulate the same case, compare their results to each other and to observations. The LES models provide a detailed three-dimensional evolution of the cloud field and their conglomerate results will be used as a standard to which THOR’s results are compared.

Since THOR includes many novel components, several sensitivity tests were performed for each case to determine what effect various parameterization algorithms have on the simulated atmosphere. Perhaps the simplest and most obvious sensitivity test is to determine how THOR behaves with different vertical grid spacing, especially considering that THOR may be run at a coarse resolution in a AGCM for computational economy. One would expect the simulation of stratocumulus clouds to be quite sensitive to changes in vertical grid spacing

given their finely balanced nature and their dependence on sharp temperature inversions to regulate entrainment and to trap moisture close to the surface. The simulation of cumulus would seem to be less sensitive to grid spacing, although subtle gradients important for defining cloud base and cloud top could easily be “smoothed out” at coarser resolutions. The sensitivity to grid spacing is tested for all cases.

Another sensitivity test is performed to determine what effect there is from using diagnostic third-order moments versus fully or partially prognostic third-order moments. Although André et al. (1976) and Krueger (1988) determined that third-order closure is required to adequately represent a convective boundary layer, it is less clear whether all of the third-order moments must be calculated with full predictive equations as was done by these two authors. Other modelers have opted for the so-called “intermediately prognostic” approach whereby only some of the third-order moments are predicted, as in Lappen and Randall (2001), Golaz et al. (2002), and Cheng and Xu (2006). Only the third-order moment of vertical velocity is predicted in the first two references, while the latter predicts the third-order moments of vertical velocity, liquid-water potential temperature, and total water mixing ratio. Using an even more simplified approach, Zeman and Lumley (1976), Canuto et al. (1994), and Cheng et al. (2005) have shown that fully diagnostic third-order moments are sufficient for modeling buoyancy-driven boundary layers. In this study, a sensitivity test will be performed for each case to determine the effects of a fully prognostic, partially prognostic, and fully diagnostic third-order closure on the simulated atmosphere.

A third sensitivity test involves the entrainment process in the calculation of the turbulence length scale. Recall from the definition of the turbulence dissipation time scale (equation (11)), that the turbulence length scale, L , determines the rate at which turbulence

is dissipated in THOR. The length scale, L , and the dissipation time scale, τ , are directly proportional so that a long length scale equates to a greater time scale. When the turbulence length scale and dissipation time scale are high, it takes longer for turbulence to be dissipated and the second- and third-order moments will have a larger magnitude. When they are low, turbulence is dissipated quickly and the second- and third-order moments will be reduced. Also recall that the turbulence length scale is calculated using a parcel model. As a parcel ascends or descends, it entrains environmental air. The rate at which it entrains affects the distance a parcel travels, and therefore the length scale. All things being equal, a high entrainment rate leads to a lower turbulence length scale, faster turbulence dissipation, and reduced second- and third-order moments. The stochastic entrainment process adds a realistic randomness to the calculation of the length scale that can potentially alter the behavior of THOR's simulated cloud fields. The stochastic entrainment operating on released parcels generates parcels of both high and low relative buoyancy, and the higher buoyancy parcels can penetrate a cloud-top inversion more easily, potentially smoothing out gradients there and allowing deeper convective elements. Sensitivities to mean entrainment rate and whether the parcel entrainment is stochastic are investigated for all cases.

The fourth sensitivity test included in this study is whether the ice phase is considered in the SGS condensation scheme. Recall from section 2.4 that the SGS condensation schemes of Mellor (1977) and Larson et al. (2002) were extended in THOR to account for mixed-phase and ice clouds via the generalization of the linearized saturation curve. In addition, covariances and third-order moments involving cloud water and ice are modified to account for such clouds. By taking saturation over ice into account, THOR's SGS condensation scheme should calculate more cloud ice and liquid in mixed-phase or ice cloud regimes compared to

the alternative liquid-only schemes. In addition, buoyancy-related terms in the second- and third-order moment equations will be increased slightly due to the inclusion of the latent heat of fusion in the cloud water correlation terms where ice is present. The effect of including the ice phase will be examined for the MPACE case, the only one in this study where an appreciable amount of ice was present in the clouds.

The last two sensitivity tests both have to do with how the use of the assumed PDF approach can improve existing external parameterizations, namely the microphysics and radiation parameterizations. Larson et al. (2005) have shown that using a technique whereby samples are drawn from the assumed PDF to drive a standard microphysics parameterization can be successful in reducing systematic biases produced by driving the microphysics scheme with grid-cell mean variables, as is typically done. The approach is mirrored with THOR and the effects of including this technique are quantified for the cases that involve precipitation, RICO, DYCOMS, MPACE, and ASTEX. The sampling approach used to drive the radiation scheme is similar in many respects, but uses a straight Monte Carlo technique rather than the latin hypercube sampling in the microphysics driver. The effects of using the assumed PDF to generate sub-columns to calculate radiative transfer are assessed using two cases that call for an active radiation scheme, MPACE and ASTEX.

3.1. SHALLOW CUMULUS CASES

Seemingly quiescent, it might be somewhat surprising to learn that accurately parameterizing shallow cumulus on the SGS is actually a greater challenge than doing so for active and dynamic stratocumulus. The key difficulty lies in the spatial distribution and spatial and temporal scale of these clouds in nature. For an atmosphere conducive to cumulus

convection, the majority of the spatial extent of the cloud layer is occupied by slowly descending, clear air, which by its vertical movement, gradually dries and warms the cloud layer. The remainder of the spatial extent of this layer contains the clouds that define the layer. The clouds are created by relatively small scale and ephemeral buoyant thermals, whose thermodynamic and dynamic properties differ greatly from the majority surrounding environment. The rising thermals reach the lifted condensation level, condense some of their water vapor releasing latent heat, and gain kinetic energy due to their buoyant advantage over the surrounding environment. Throughout their lifetimes, turbulence eddies on the edges of the clouds mix relatively dry and cool air from the surrounding environment, diluting the original thermals and robbing them of their kinetic energy and buoyancy, eventually leading to their demise. By this physical arrangement, that the greatest extent of the cloud layer consists of slowly warming and drying clear and nearly stationary air and only a small portion contains the active heat-, momentum-, and moisture-transporting elements, the statistics of such a layer are more difficult to describe by a subgrid model than a stratocumulus layer that can be considered more homogeneous in comparison. In statistical parlance, the thermodynamic and dynamic properties of a cumulus cloud layer can therefore be highly skewed – the probability density function that describes the distribution of vertical velocity, for example, has a component that has a small spread around a small negative value and a component that has a large spread around a larger positive value. Properly representing such skewness requires a good handle on the third-order moments in such a layer, and as discussed previously, higher-order moments can be more difficult and costly to accurately estimate and are more poorly constrained by observations.

In order to determine how well THOR can parameterize shallow cumulus convection, two cases from the GASS¹ boundary layer cloud working group have been simulated. One case is based on the Barbados Oceanographic and Meteorological Experiment (BOMEX) measurement campaign and the other is based on the Rain In Cumulus over the Ocean (RICO) field program. For both cases, the results will focus on the simulated cloud structure and the turbulence statistics, and where possible, the results are compared to the published results from the LES intercomparisons for each case. Along with results from the control simulation, results from the various sensitivity test are discussed as well.

3.1.1. BOMEX CASE. The BOMEX case is based on an undisturbed and steady period of shallow cumulus convection that was observed during the field campaign. The case coordinators provided profiles of the initial mean potential temperature, water vapor content, and horizontal winds. The surface heat and momentum fluxes are all prescribed, and the modeled atmosphere is subjected to weak subsidence, a large-scale pressure gradient, and weak horizontal advection of moisture. The radiative heating rate is prescribed and assumes only longwave cooling. For complete details of the case specifications and LES results, the interested reader is directed to the paper by Siebesma et al. (2003). The LES models produced a cloud field with a maximum cloud fraction near 6%, a cloud base around 500 m and a cloud depth of between 1 and 1.5 km.

Using the initial profiles and forcings as specified in Siebesma et al. (2003), for the control simulation, THOR used a grid spacing of 100 m and a time step of 1 s. The domain size was 3 km and the simulation was run for 6 hours of simulated time. For all profiles produced for this case, the output was averaged over the last 3 hours of the simulation. Each set of plots

¹GASS is an acronym that stands for Global Atmospheric Systems Study and is part of Global Energy and Water Exchanges Project (GEWEX). GEWEX is a core project of the World Climate Research Programme (WCRP). GASS has been previously known as GEWEX Cloud Systems Study (GCSS).

shows many pieces of information. First, the initial profiles are denoted by a dotted black line. The results from the LES intercomparison are displayed using the following convention: the mean of the LES results is plotted with a thick black dashed line, and the range of LES values are denoted by thinner black dashed lines. Output from THOR is displayed with thick solid lines; black will always denote the control simulation. Thick solid colored lines will denote specific sensitivity experiment values from THOR.

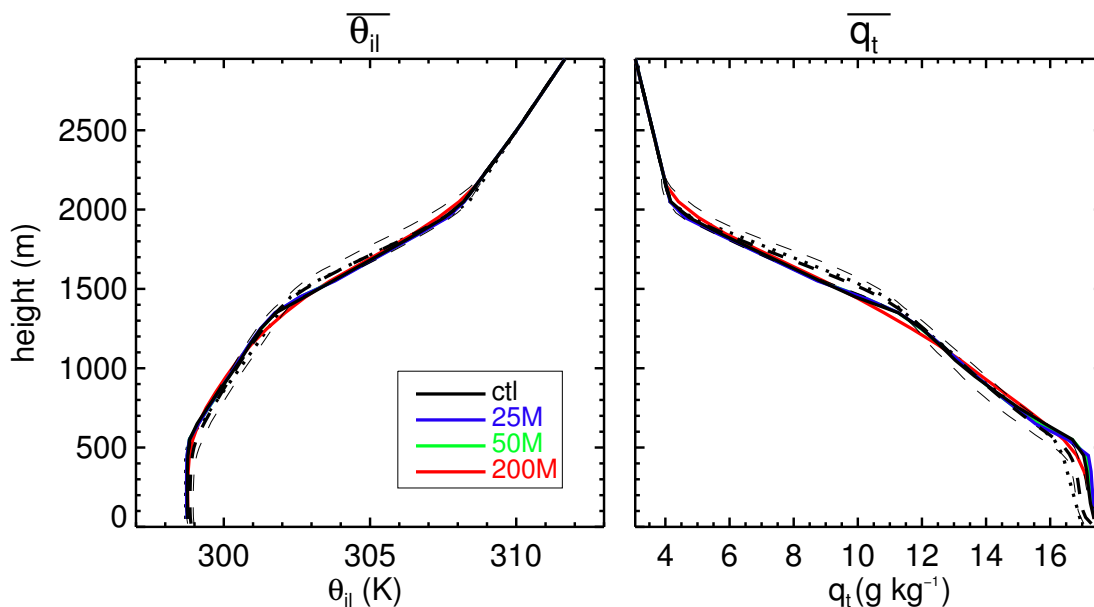


FIGURE 3.1. Profiles of $\overline{\theta_{il}}$ (left) and $\overline{q_t}$ (right) for the grid spacing sensitivity test. Solid lines denote THOR output. The black solid line denotes the control THOR simulation. Colored solid lines denote output from sensitivity tests. The black dotted line denotes the initial profile. The black dashed lines denote output from the LES intercomparison; the thickest dashed line is the LES mean, while the thinner dashed lines denote the minimum and maximum values from the LES intercomparison.

Figure 3.1 shows the mean thermodynamic profiles for the BOMEX case. Four distinct stability zones are evident: a shallow neutral sub-cloud layer up to about 500 m, a conditionally unstable cloud layer from 500 m to about 1400 m, a stable inversion layer from 1400 m to about 2000 m and the near pseudo-adiabatic free troposphere above about 2000 m.

Moisture decreases from the sub-cloud layer up to the free troposphere as the distance from the ocean source increases. Of note is the very tight packing of lines in both plots. There is very little difference among the control, the three sensitivity tests, the LES simulations, and the initial conditions. Of course, one might expect the mean profiles to change little given weak forcing, but there are a few minor differences worth noting. The first is that the inversion layer is slightly warmer and drier in the THOR profiles than the LES simulations. The reason for this, as will be shown in subsequent plots, is slightly underestimated convective transport due to clouds. To keep the mean profiles in steady-state, the SGS transport of θ_i and q_i must balance the warming and drying due to subsidence. In the inversion layer in the THOR simulations, the subsidence forcing overcomes the turbulent convective transport. In addition, the sub-cloud layer is slightly too moist in the THOR simulations compared to the LES simulations. This too can be attributed to turbulent transport out of the sub-cloud layer that is slightly too weak. Nevertheless, it seems encouraging that the THOR simulations match the LES simulations pretty closely, with the THOR profiles nearly universally staying within the range of the LES results. In addition, there seems to be little difference among the different grid-spacing choices, signaling that THOR is relatively insensitive to the choice of grid-spacing for this cloud regime.

The cloud structure simulated by THOR is shown in figures 3.2 and 3.3. For all grid-spacings less than 200 m, THOR produces a cloud field that has a maximum near 500 m with a cloud fraction between 6 and 9%. The cloud fraction decreases to a minimum near 1000 m and a secondary maximum appears below the cloud top of around 1500 m. THOR's results mirror the LES simulations nicely, although the cloud base is perhaps 100 m too low and the cloud top is a couple hundred meters too low. Both of these biases are consistent

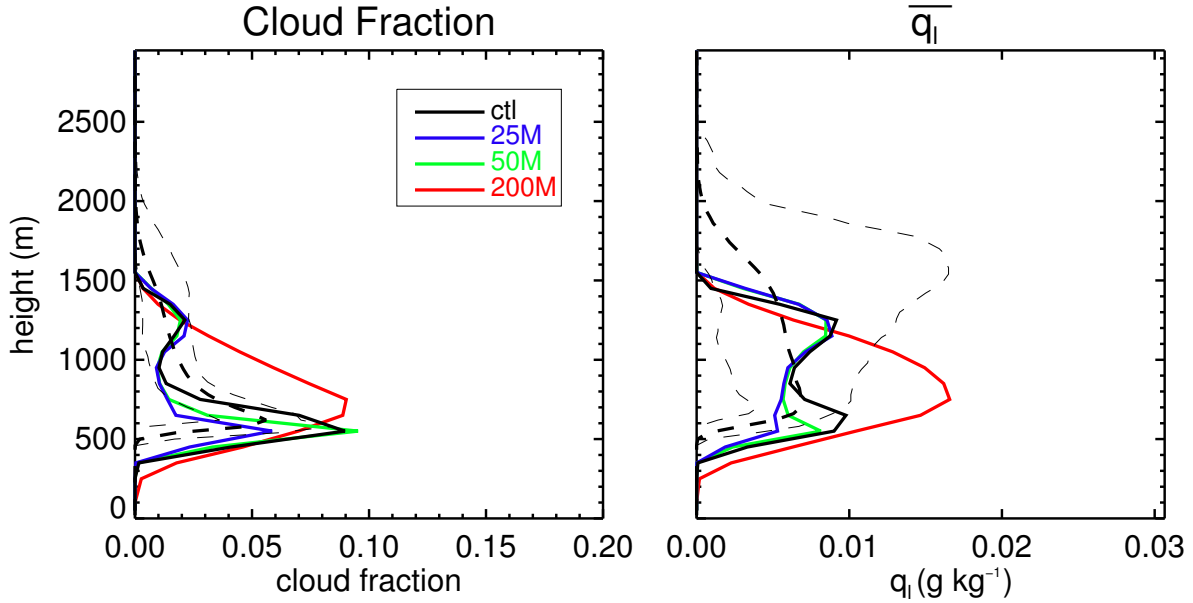


FIGURE 3.2. Profiles of cloud fraction (left) and $\overline{q_l}$ (right) for the grid spacing sensitivity test. Lines are as in figure 3.1

with the mean profiles discussed above, that the convective turbulent transport produced by the cloud field is a bit too weak in THOR, causing a cloud base and top that are a bit too low. The cloud water profile is consistent with the cloud fraction profile, and the cloud water predicted by THOR is within the range of LES results for all grid spacings except for 200 m. For the coarsest grid spacing tested, 200 m, both the cloud fraction and water content diverge slightly from the finer grid spacing and LES results, as the gradients in the flux profiles are somewhat smoothed out, and the maximum of the turbulent transport is found slightly lower in the column (see figure 3.4).

The time evolution of the cloud field is shown in figure 3.3 with a time-height cross-section from the control simulation and a time-series of cloud liquid water path. From the time series of cloud liquid water path, it is evident that a quasi-steady state was reached in the simulations for all grid-spacings (except for perhaps the 200 m test) by about 3 hours into the simulation. The liquid water path from the THOR simulations compares quite favorably

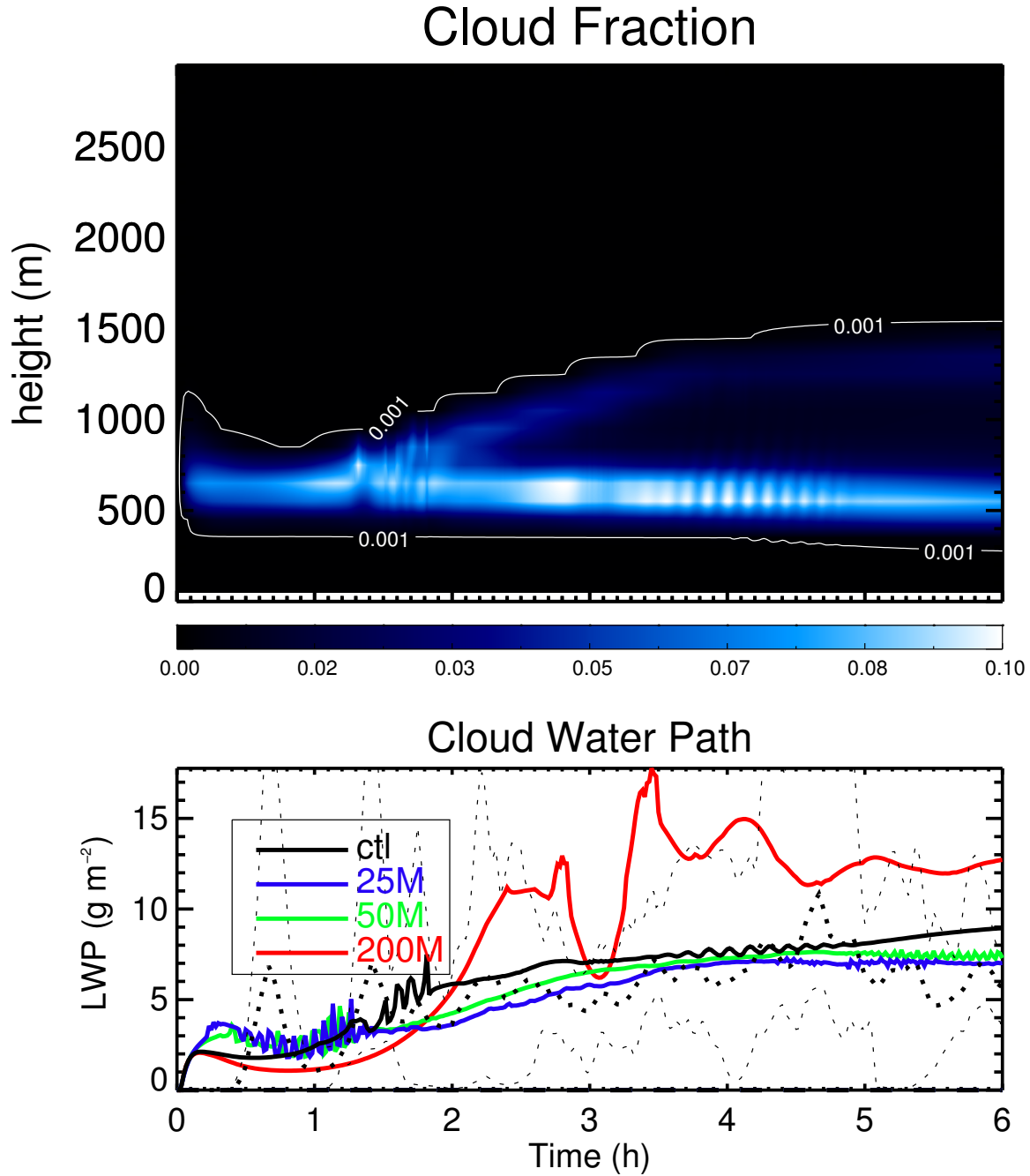


FIGURE 3.3. Time-height cross section of cloud fraction from the control case (top) and time series of liquid water path for all runs of the grid spacing sensitivity test (bottom). Lines are as in figure 3.1

to the LES results, generally falling within their simulated range. Small oscillations with a period of a few minutes appear in the three THOR runs with grid spacing less than 200 m. Inspection of the cloud fraction time-height cross section reveals that the oscillation

is confined to the levels near cloud base. It appears that the oscillation develops as the cloud base transition from the 650 m level to the 550 m level. It is interesting to note the development of the the two levels of maximum cloud fraction. Initially, cloud is only diagnosed near cloud base, but as the atmosphere evolves to its steady state, two distinct maxima emerge: the cloud base and the cloud top, where the cumulus clouds tend to reach neutral buoyancy and the cloud properties are mixed or “detrained” into the environment. The two maxima are somewhat more distinct in THOR than in the LES results according to figure 3.2, but a cloud fraction maximum near the detrainment zone is a feature that is often observed in nature. The differences apparent in the THOR 200 m simulation are perhaps indicative of under-resolving the cumulus clouds. The liquid water path time series for the 200 m test shows an initial underestimation and subsequent “bursts” of convective activity, contributing to the increased variance of the liquid water path in time.

Profiles of selected second-order moments are shown in figure 3.4. For turbulent moments, comparison of THOR’s results with LES is a little complicated since the LES results encompass both resolved and SGS contributions. For the LES models, since they are designed to resolve most of the “energy-containing” eddies, the majority of the turbulent moments come from the resolved component, and the remainder SGS component is usually calculated with a simple first-order scheme. For THOR, all of the turbulent moments are from the subgrid scale, as there are no explicitly resolved eddies in the one-dimensional model. In addition, since THOR is being used as a single-column model, there is no calculation of a mean vertical velocity and so the advection terms of all turbulent moments have been assumed to be zero. When THOR is used as a parameterization for a three-dimensional host

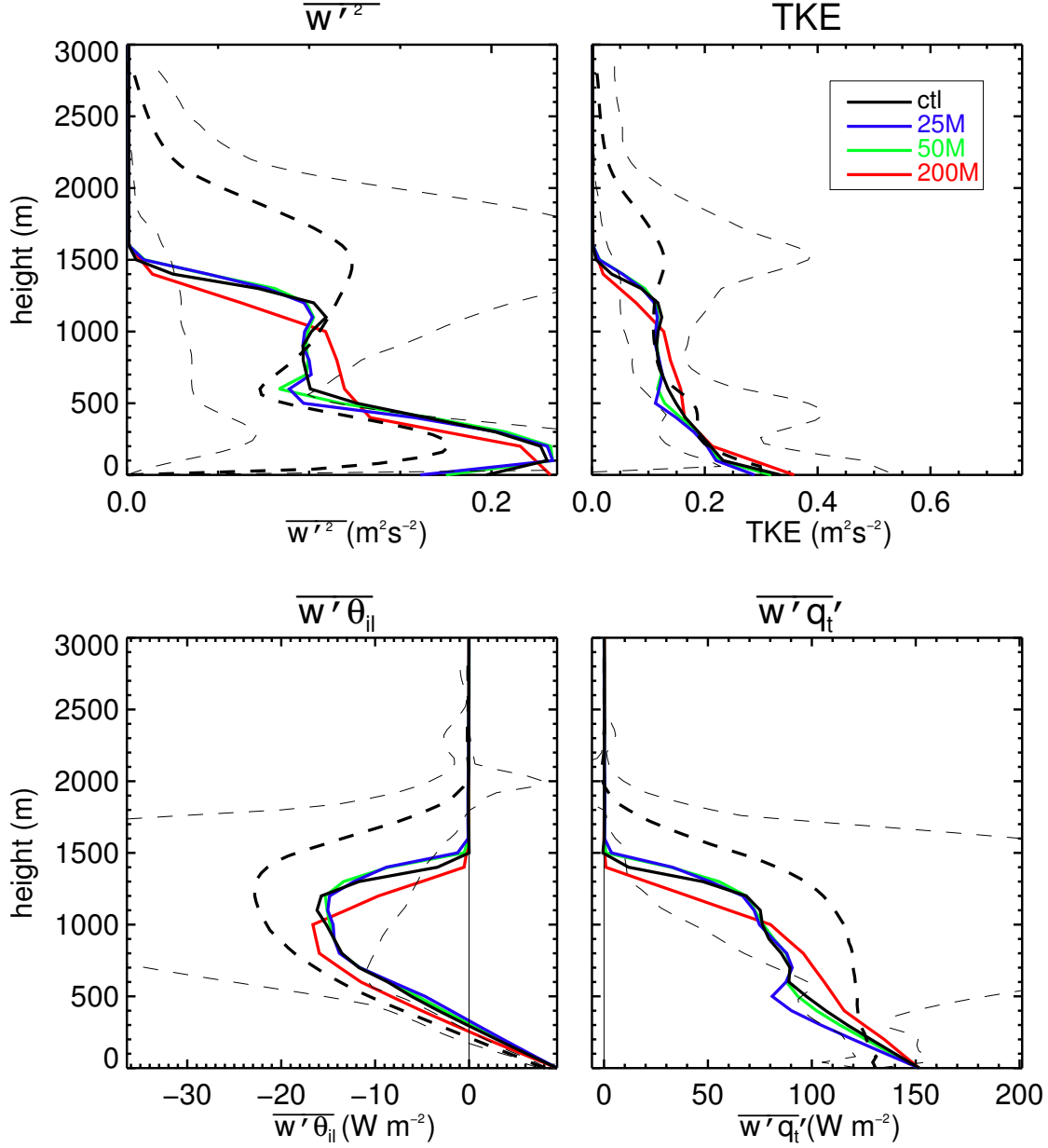


FIGURE 3.4. Profiles of vertical velocity variance (top left), TKE (top right), and sensible (bottom left) and latent heat fluxes (bottom right) for the grid spacing sensitivity test. Lines are as in figure 3.1

model where vertical velocity is calculated, the advective terms should be properly calculated. With these caveats, a comparison of THOR’s second- and third-order moments to LES results can still be instructive. For all second-order moments shown, the profiles from THOR are much “shorter” than their LES counterparts, i.e. the second-order moments go to

zero near 1500 m (coinciding with cloud top in THOR), whereas turbulent fluxes of heat and moisture extend perhaps another 500 m in LES and TKE extends nearly up to the domain top. Few differences can be found among the different grid spacing tests except for the 200 m test. The results from this test show that the cloud layer depth has been further decreased and the maximum values of the second-order moments are found lower in the column. This can be explained by examining the third-order moments responsible for transporting the moisture and heat fluxes and TKE components upward in the column, namely the moments $\overline{w'^2 q'_t}$, $\overline{w'^2 \theta'_{il}}$ and $\overline{w'^3}$, respectively, in figure 3.6. The magnitude of these moments has been reduced since the mechanical production terms contain gradients that have been smoothed over by use of the higher grid spacing. In addition, buoyancy terms calculated from the SGS condensation scheme are a function of skewness. When skewness values are decreased, the buoyancy production terms decrease with them.

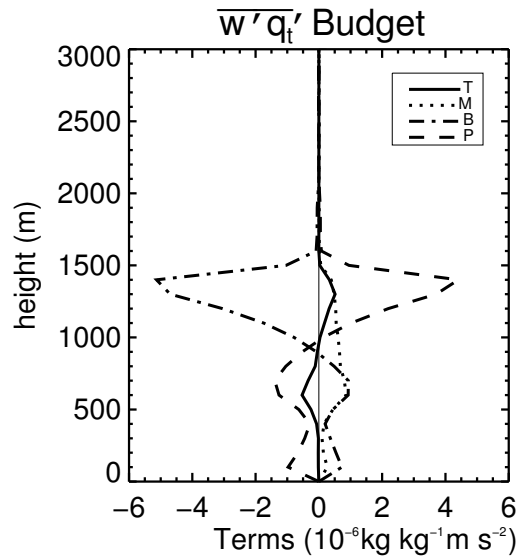


FIGURE 3.5. Profiles of the terms in the moisture flux equation for the control BOMEX simulation. T stands for the transport (third-order moment) term, M is for the mechanical production term, B is for the buoyancy production term, and P is for the pressure correlation term. Refer to equation 5 for the specification of the terms.

Some of the discrepancy between THOR’s results and LES can be explained by the lack of advection from resolved eddies as discussed above, but one can also examine second-order moment budgets to determine if perhaps errors in specific terms create a bias. Figure 3.5 shows the moisture flux budget, or the individual terms in the moisture flux equation. Although the budget terms are not available for the LES results, one can still get a good idea as to which terms may lead to THOR’s underestimation of the moisture flux (and by extension the heat flux) in the cloud layer. From about the middle of the cloud field and below (about 1000 m), an upward moisture flux is generated by the mechanical and buoyancy terms and is opposed by pressure correlation term. The transport term transports the upward moisture flux from the bottom half of the cloud to the top half. Above about 1000 m, the buoyancy and pressure correlation terms reverse their roles. The buoyancy term contributes to a downward flux of moisture and is opposed by the mechanical, transport and pressure terms. Since the buoyancy term is the only negative term in the top half of the cloud, and this appears to be where the moisture flux diverges most from the LES profiles, this indicates either that the buoyancy term is too strongly negative in this region or that some combination of the transport, mechanical and pressure terms are too weakly positive in this region. Given that the magnitude of TKE is more in line with LES results, the mechanical term is probably not to blame.

Further, mean profiles of several third order moments are shown in figure 3.6. Although only $\overline{w^3}$ was available from the LES results in Siebesma et al. (2003), figures 3 and 4 from a paper by Larson and Golaz (2005) show the other third-order moments included in figure 3.6 for both the Regional Atmospheric Modeling System (RAMS) LES and the Cloud Layers Unified By Binormals (CLUBB) model for a general idea as to how THOR compares. The

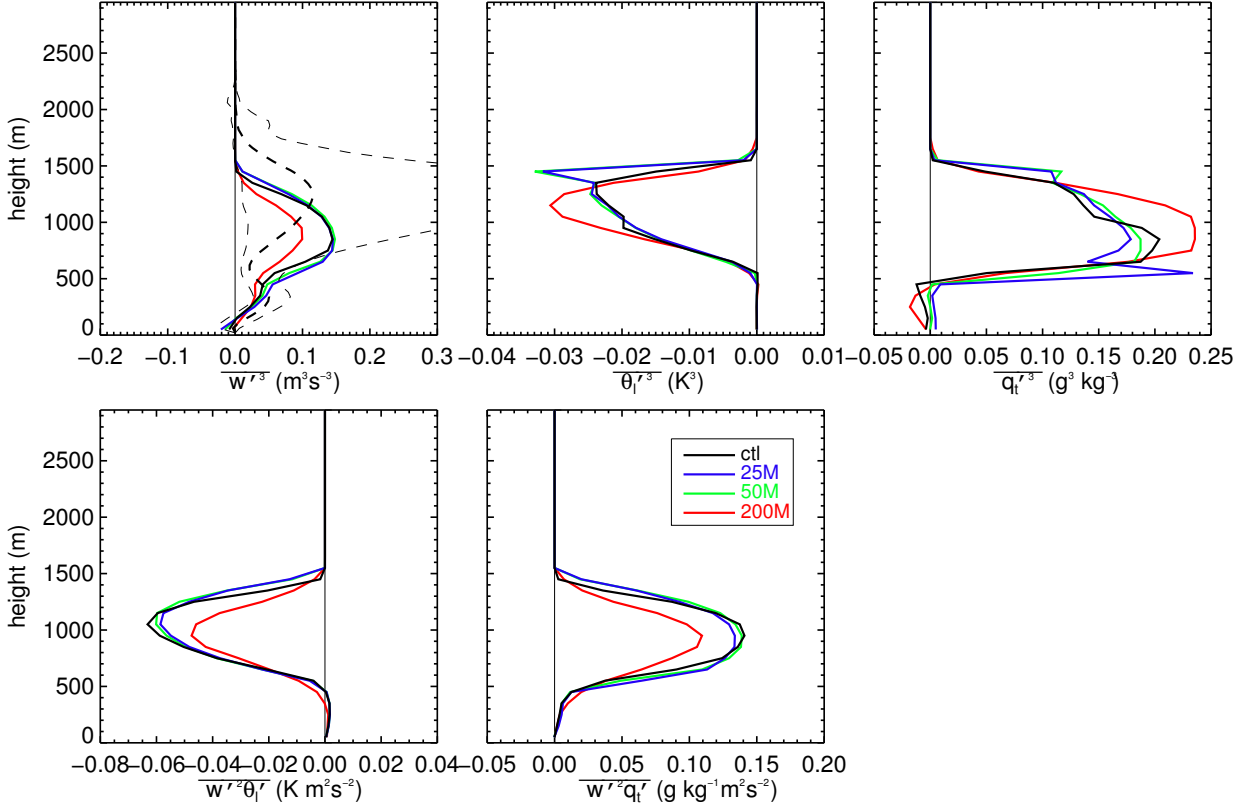


FIGURE 3.6. Profiles of selected third-order moments for the grid spacing sensitivity test. Lines are as in figure 3.1

magnitude of $\overline{w'^3}$ compares well with the LES models, but, as with the second-order moments, the maximum occurs too low in the column. As for the other third-order moments included in figure 3.6, compared with the models tested in Larson and Golaz (2005), THOR produces magnitudes of the third-order moments that agree better with LES than CLUBB, although they still suffer from the underestimation of the cloud top height. Given the relatively good agreement of the third-order moments with LES, the underestimation of the moisture and heat fluxes discussed previously probably boils down to the interplay between the buoyancy and pressure correlation terms in those equations.

As mentioned in the chapter introduction, two additional sensitivity tests were conducted using the BOMEX case. The next sensitivity test to be discussed explores the effect of using

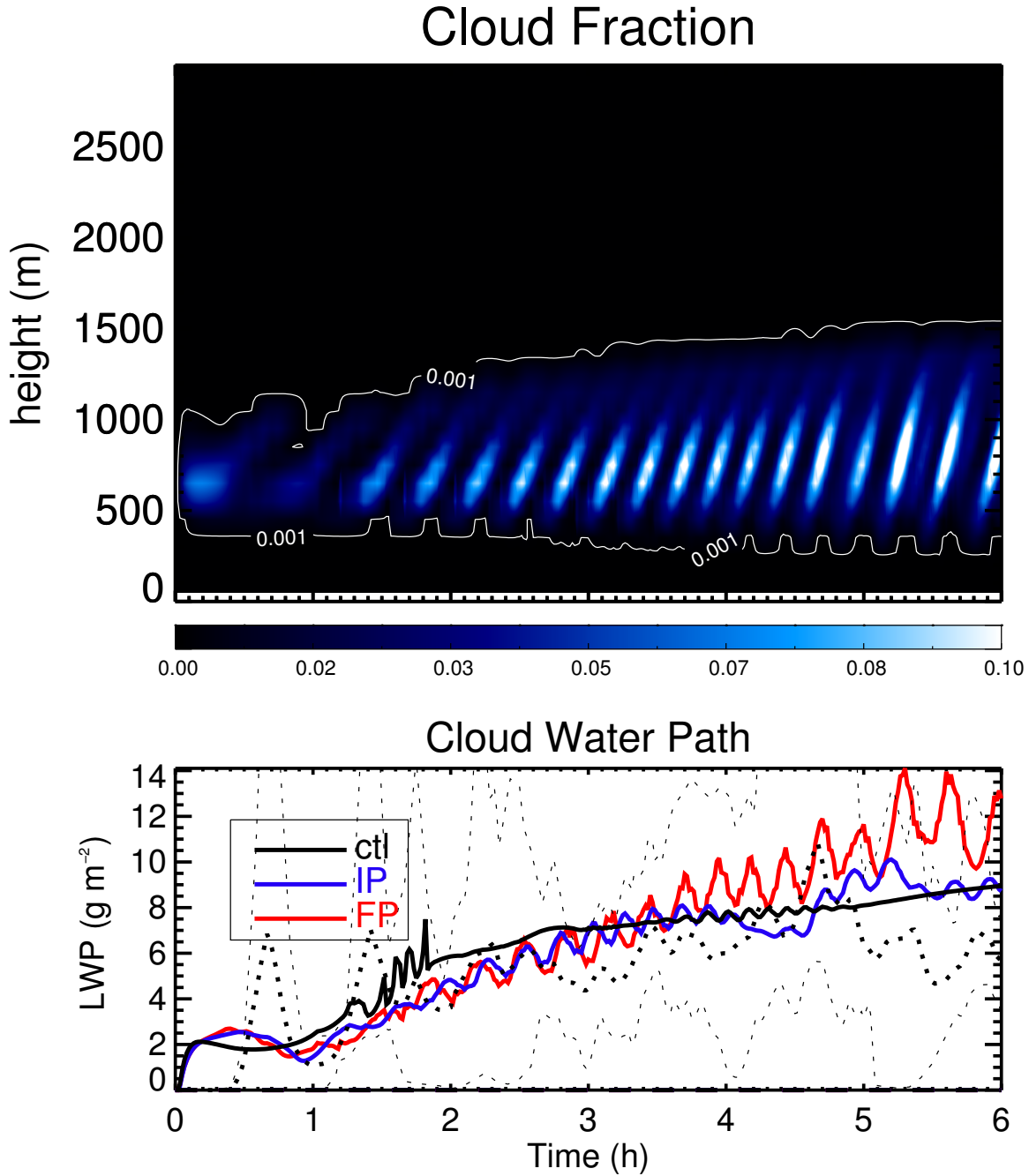


FIGURE 3.7. As in figure 3.3 but for the third-order moment sensitivity test.

diagnostic versus intermediately prognostic versus fully prognostic third-order moments. The time-height cross-section of cloud fraction for the fully prognostic test and time-series for all tests in shown in figure 3.7. Upon inspection and comparison with figure 3.3, the immediately obvious difference is the existence of an oscillation in the cloud field. Such an oscillation has

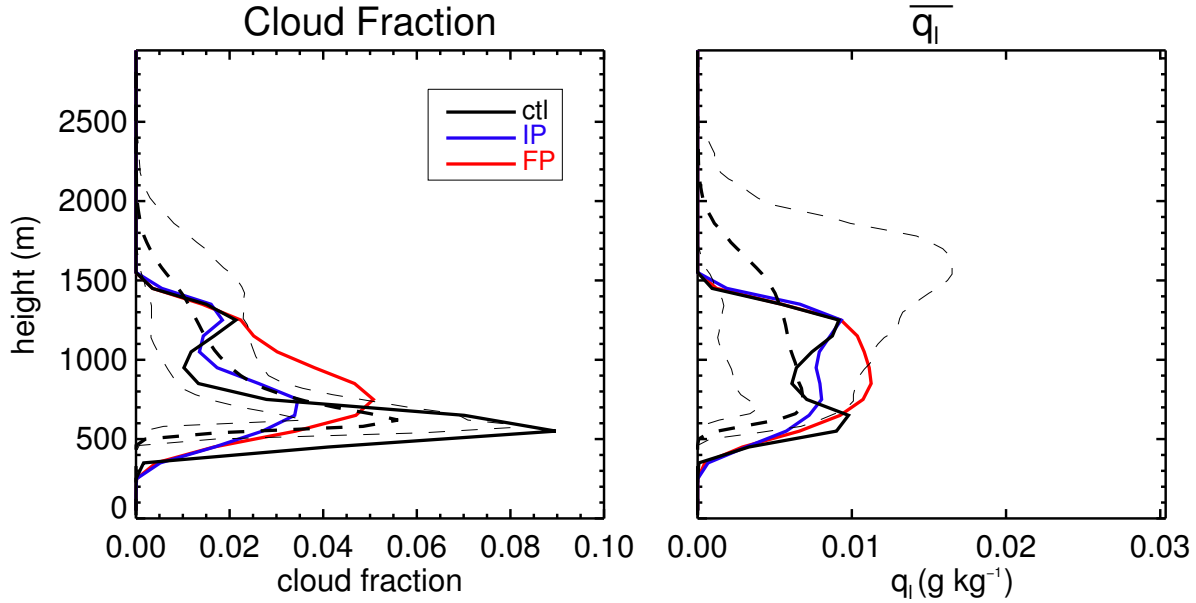


FIGURE 3.8. As in figure 3.2, but for the third-order moment sensitivity test.

been simulated before with similar models (see Firl (2009) and Cheng et al. (2004)). In fact, the results from THOR reproduce the findings of Cheng et al. (2004), that the oscillation in the cloud field is worst for a fully prognostic model and can be reduced by switching to an intermediately prognostic approach. A fully diagnostic approach almost completely eliminates the oscillation. It is interesting to note that the period of the oscillation changes depending on how many third-order moments are prognosed. For a fully prognostic approach, the period seems to be on the order of 15 minutes, but for the intermediately prognostic approach, the period is closer to 10 minutes.

In addition to the oscillation, using fully or partially prognostic third-order moments changes the vertical structure of the cloud cover. The fully diagnostic approach has the most pronounced cloud base and the intermediately prognostic approach has the thinnest cloud base. The fully prognostic version features a cloud water maximum near mid-cloud instead of near cloud base. The additional cloud water near the middle of the cloud deck

causes the liquid water path to be highest for the fully prognostic test case as well, yet even the worst case still has reasonable agreement with the LES results. It is interesting to note that despite the significant difference in the time-evolution of the cloud field, the cloud depth is identical for all methods.

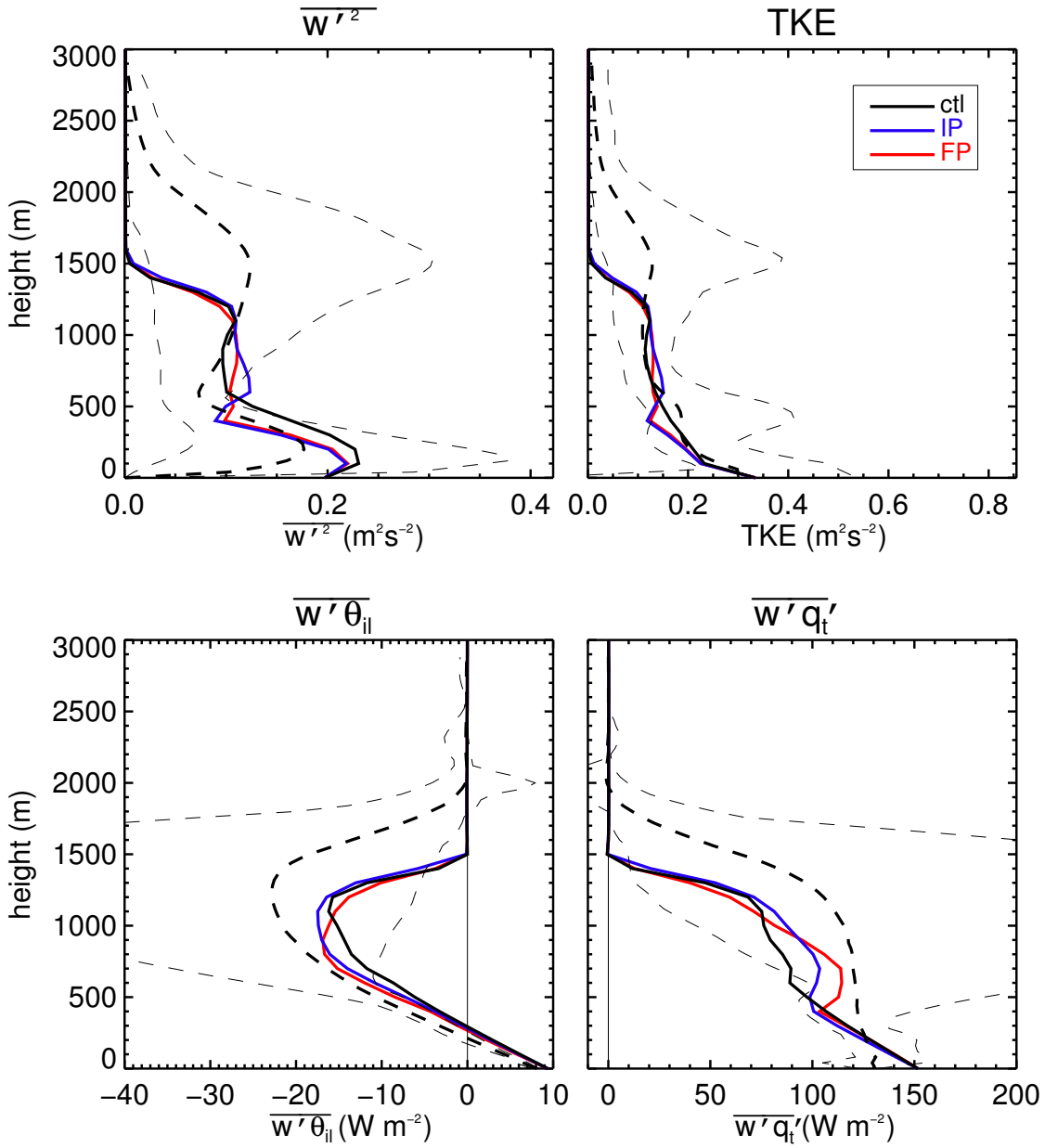


FIGURE 3.9. As in figure 3.4, but for the third-order moment sensitivity test.

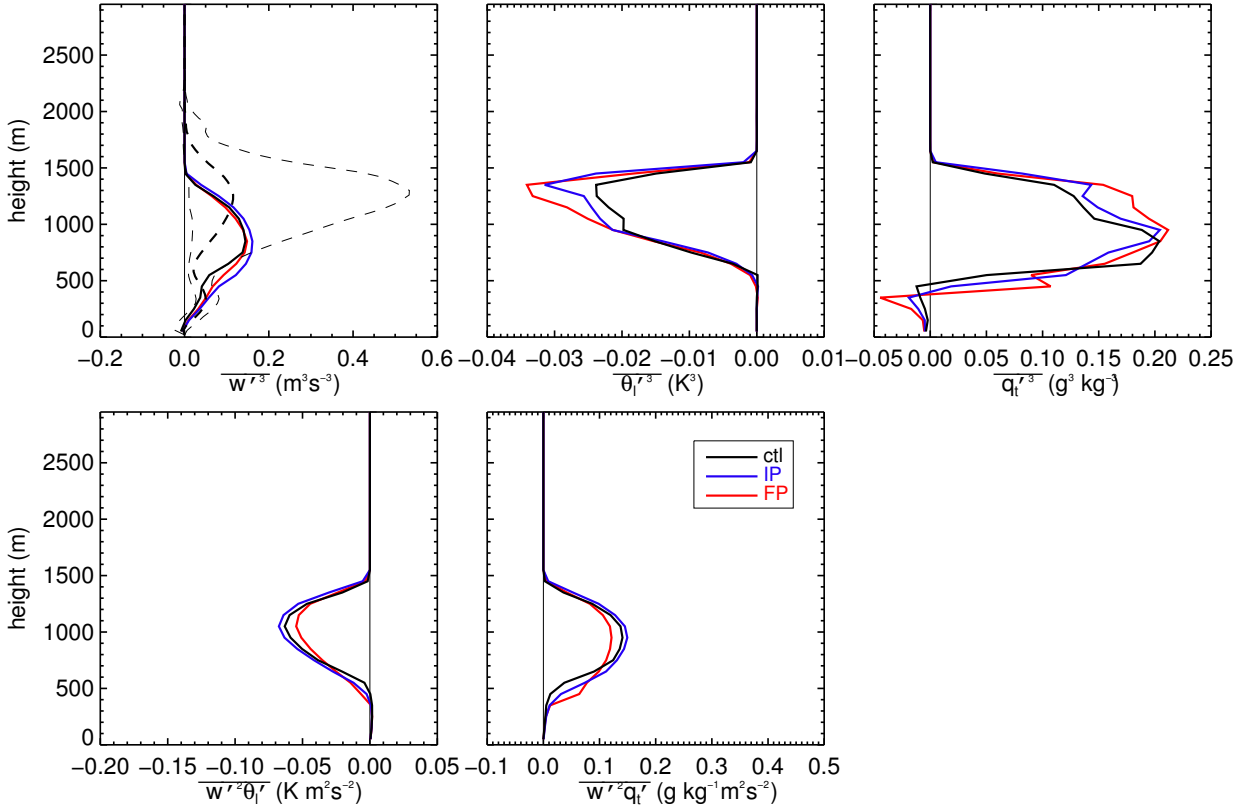


FIGURE 3.10. As in figure 3.6, but for the third-order moment sensitivity test.

Despite the oscillation, the mean profiles of the second- and third-order moments for the last three hours of all the third-order moment sensitivity simulations are quite similar as shown in figures 3.9 and 3.10. Although not shown, the oscillation is also present in quantities such as the moisture flux, but the minimums and maximums appear to cancel each other out to create mean profiles that very nearly resemble the more steady-state solution of the control diagnostic simulation. Minor differences exist among the test simulations, including a slight increase in magnitude and a minor decrease in elevation of the maximum of the heat and moisture fluxes. Remarkably, even the third-order moment profiles are nearly the same. There are slight increases in the magnitudes of the skewness of θ_{il} and q_t as the number of third-order moments prognosed is increased, but the differences seem minor. Since the magnitudes and shapes of the third-order moment profiles are nearly the same regardless

of the method of calculation, and since the fully diagnostic approach provides the steadiest solution and weakest oscillation, this sensitivity test seems to provide further encouragement that the fully diagnostic approach to solving for the third-order moments is a fine choice for a higher-order closure model.

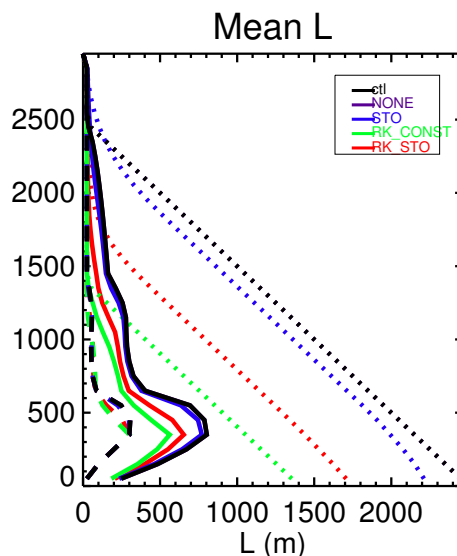


FIGURE 3.11. Shown are the mean turbulence length scales calculated for the different sensitivity test runs. Dotted lines denote the upward length scale, dashed lines denote the downward length scale, and the solid lines denote the “master” turbulence length scale, the geometric mean of the downward and upward length scales. The control simulation (black lines) uses a constant low entrainment rate. The NONE (purple) simulation uses no parcel entrainment. The lines labeled STO (blue and red) use the stochastic parcel entrainment algorithm, and the lines labeled RK (green and red) use a higher parcel entrainment rate.

The last sensitivity test performed in conjunction with the BOMEX case examines the affects of using different methods and rates of parcel entrainment for the calculation of the turbulence length scale. Recall from the chapter introduction that higher entrainment rates tend to reduce the turbulence length scale, increase turbulence dissipation, and generally reduce the strength of the parameterized SGS convective overturning. The stochastic entrainment algorithm being tested generates pseudo-random entrainment rates centered around a

mean rate and calculates a mean length scale from the release of many independent parcels. Also recall from section 2.2 that the two mean entrainment rates being used are a lower rate from Golaz et al. (2002) and a higher rate from the Romps and Kuang (2010) paper (hence RK). The length scales calculated from the various sensitivity test runs are shown in figure 3.11. The greatest difference among the test runs is with the upward length scale. Since the “master” turbulence length scale is the geometric mean of the downward and upward length scales, the differences in the master length scale are not as pronounced as with the upward length scale. The two tests using the higher entrainment rate have the smallest length scales. It is interesting to note that the control simulation that uses a low, constant parcel entrainment rate and the test that assumes no parcel entrainment produce the same length scale, signaling that it might be possible to save computational expense and assume that no parcel entrainment takes place when simulating a cumulus cloud regime. When using the low entrainment rate with the stochastic algorithm, there is a slight reduction in the upward length scale in general, although the profile is smoothed out near the top and bottom of the domain.

What effect do the different length scales have on the simulated cloud field? According to figures 3.12 - 3.14, for all cases that assume a low entrainment rate or no entrainment, there is virtually no difference in the simulations, regardless of whether the stochastic algorithm was used or not. When the higher entrainment rate is introduced, however, differences begin to emerge. The run using a constant, high entrainment rate produces a cloud that is shallower and thicker, leading to the highest cloud liquid water path of those tested. When the stochastic algorithm is combined with the higher entrainment rate, there is a little noise introduced into the solution (upon inspection of the liquid water path), but the

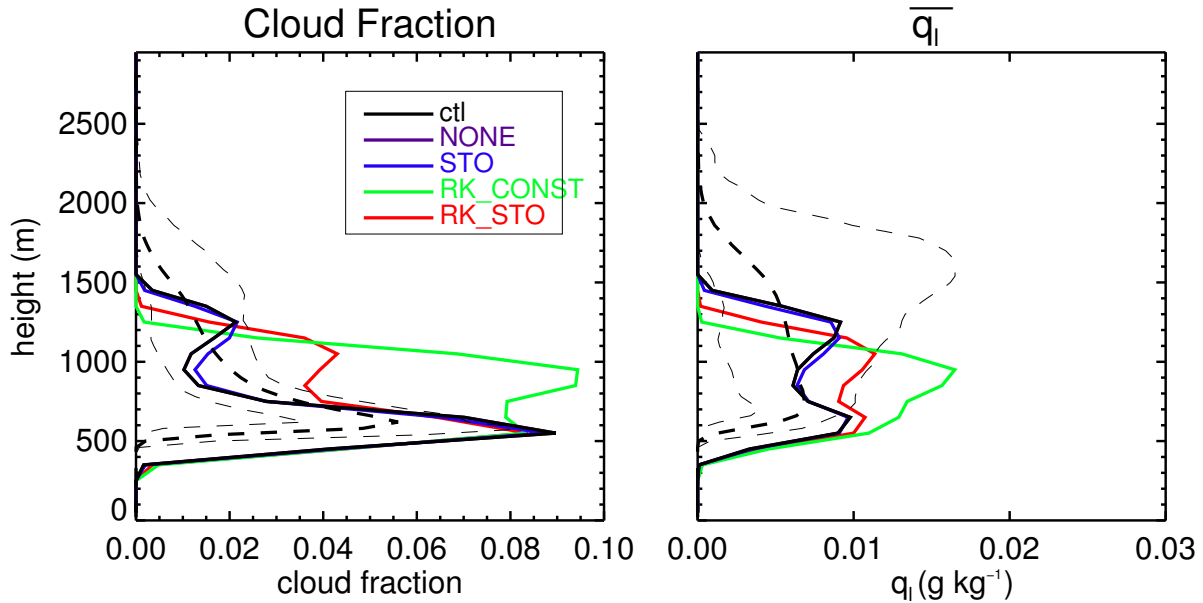


FIGURE 3.12. As in figure 3.2, but for the length scale entrainment sensitivity test.

solution produces a taller and slightly optically thinner cloud than for the high, constant entrainment case. The stochastic algorithm doesn't completely negate the effects of using a high entrainment rate, but it does seem to improve the simulation if a higher entrainment rate is used. The second-order moment profiles shown in figure 3.14 confirm the hypothesis that using a higher entrainment rate leads to decreased turbulence length scales and more turbulence dissipation. The runs using a higher entrainment rate show reduced vertical velocity variance and TKE and the maxima of the vertical heat and moisture fluxes are found lower in the column, signifying reduced convective overturning.

3.1.2. RICO CASE. The RICO case shares many characteristics with the BOMEX case. The initial profiles and large-scale forcings describe a state of the atmosphere conducive to shallow cumulus and the case specifications were created from observations during a several-week relatively undisturbed period that featured shallow, lightly precipitating cumulus. As

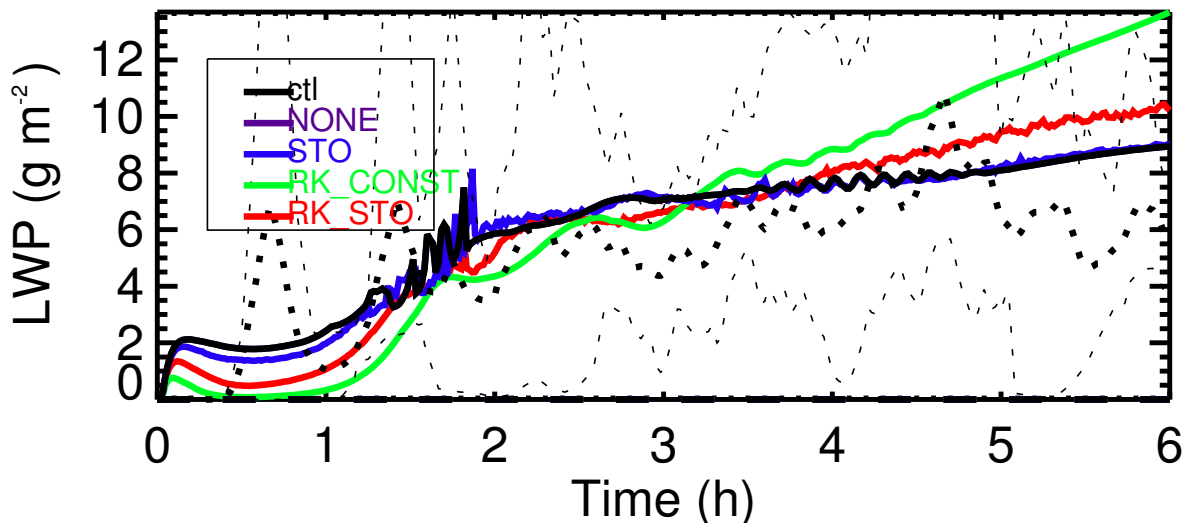


FIGURE 3.13. Time-series of liquid water path for the length scale entrainment sensitivity test. Lines are as in figure 3.1

with BOMEX, this case can be considered a “composite” case, where the atmospheric conditions are based on an averages over a sufficiently long time period, and therefore the model results should not be compared with observations from a specific time period within the observational campaign. A key difference between the two cases are that the RICO field campaign featured slightly more robust cumuli with appreciable precipitation. One of the goals of the LES intercomparison featuring this case was to examine the impact of different microphysical parameterizations on the precipitation generated by shallow cumuli and to determine what affect differences in precipitation might have on the cumulus cloud field (vanZanten et al. 2011).

Interested readers are directed to vanZanten et al. (2011) for a complete description of the case simulated here, although pertinent details are included below. As with the BOMEX case, initial profiles are provided for potential temperature, water vapor specific humidity, and the horizontal components of momentum. Throughout the simulation, these mean variables are modified by prescribed surface fluxes, prescribed large-scale horizontal

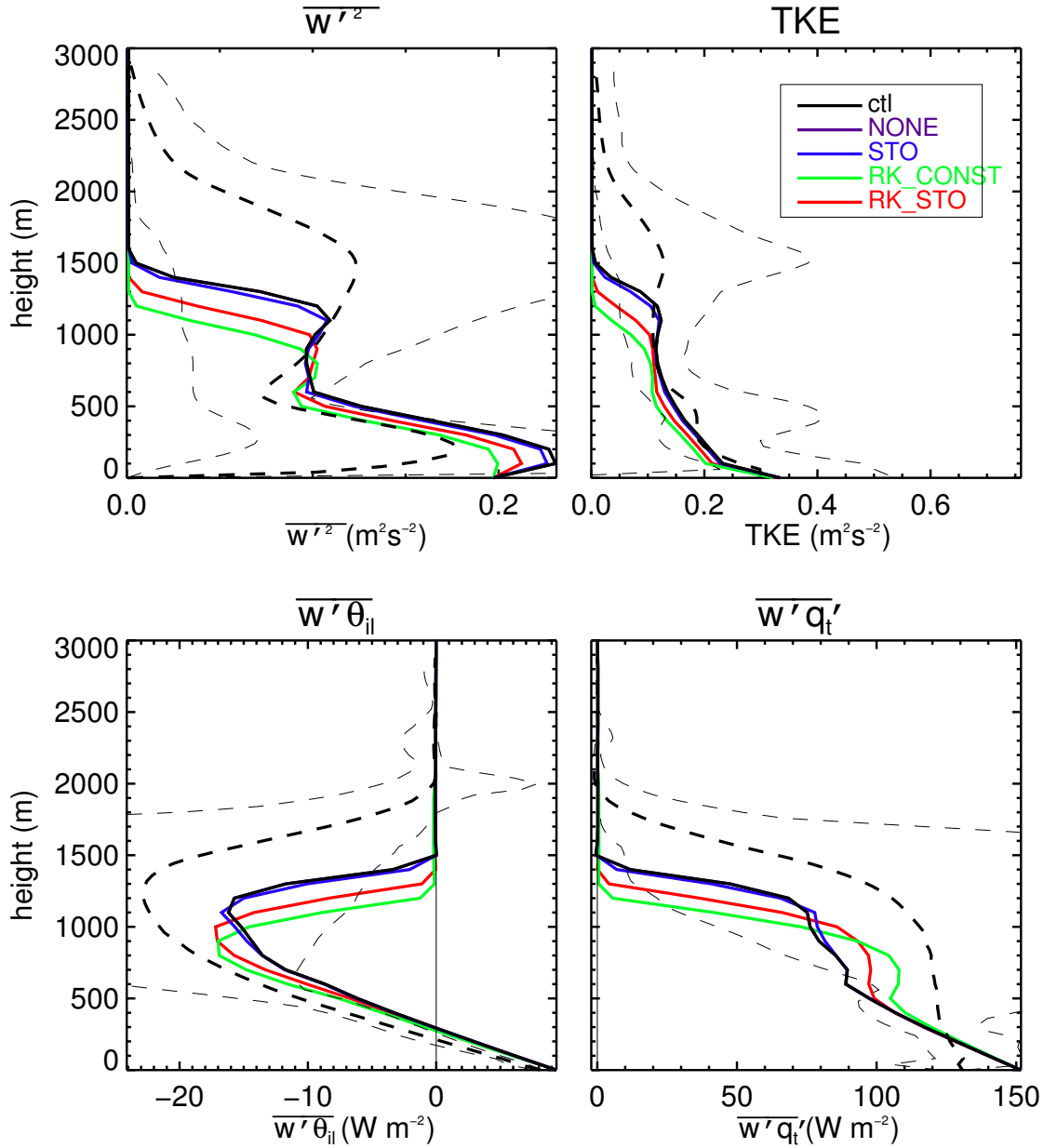


FIGURE 3.14. As in figure 3.4, but for the length scale entrainment sensitivity test.

advection of temperature and moisture, prescribed subsidence, prescribed geostrophic winds, and a prescribed radiative heating rate. The resultant cloud field produced by the LES participants was an approximately 2000 m deep field of shallow cumulus with a maximum cloud fraction at cloud base (~ 500 m) of around 6%. THOR was run for 24 hours of simulated time with a grid spacing of 40 m (for the control) and a time step of 1 s over a

4000 m domain. The results presented in this section feature profiles averaged over the last 4 hours of the simulation, and the convention for plot lines and colors follows section 3.1.1.

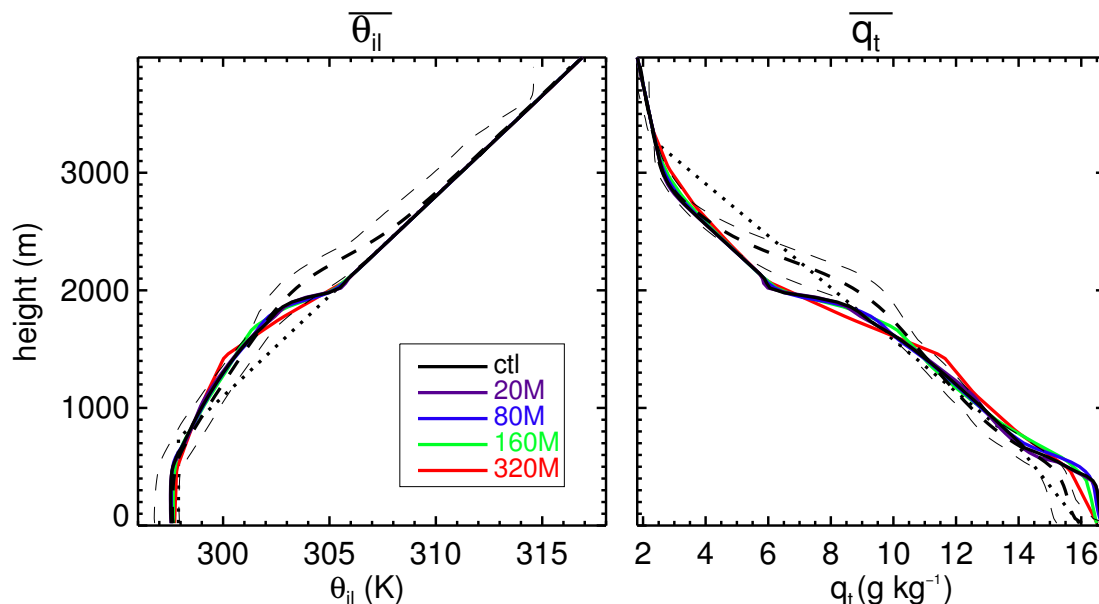


FIGURE 3.15. Mean profiles of θ_{il} (left) and q_t (right) for the last four hours of the control and grid spacing sensitivity test runs. Solid lines denote THOR output, with the black representing the control run and colors indicating sensitivity test runs. Black dashed lines denote LES ensemble results, with the thickest dashed line denoting the LES ensemble mean and the thinner dashed lines denoting the LES ensemble range. The black dotted lines denote initial conditions.

The mean profiles for the ice-liquid-water potential temperature and total water specific humidity are shown in figure 3.15 for the control grid spacing and for tests using 20 m, 80 m, 160 m, and 320 m. Overlaid are the LES intercomparison results in black dashed lines, with the heaviest dashed line being the mean and the lighter dashed lines denoting the range of LES results. Although the profiles are initialized with only two layers (a subcloud layer with a neutral profile and a free atmosphere layer near pseudoadiabatic), four distinct layers develop during the simulation due to the imposed forcing (just like BOMEX): a subcloud layer, a cloud layer, an inversion layer, and a free tropospheric layer. In general, the agreement between THOR and the LES models is good, although there are some notable differences.

As with the BOMEX case, the subcloud layer (below about 500 m) is considerably too moist, with all THOR runs producing profiles outside of the range of LES results. In addition, the inversion layer in THOR is too low by several hundred meters, signifying that the convective flux underestimation problem noted in section 3.1.1 is again present in the RICO case. Notable differences among the grid spacing tests do not begin to show up in the mean thermodynamic profiles until the 320 m test. For this test, the inversion layer is even lower than for the other runs.

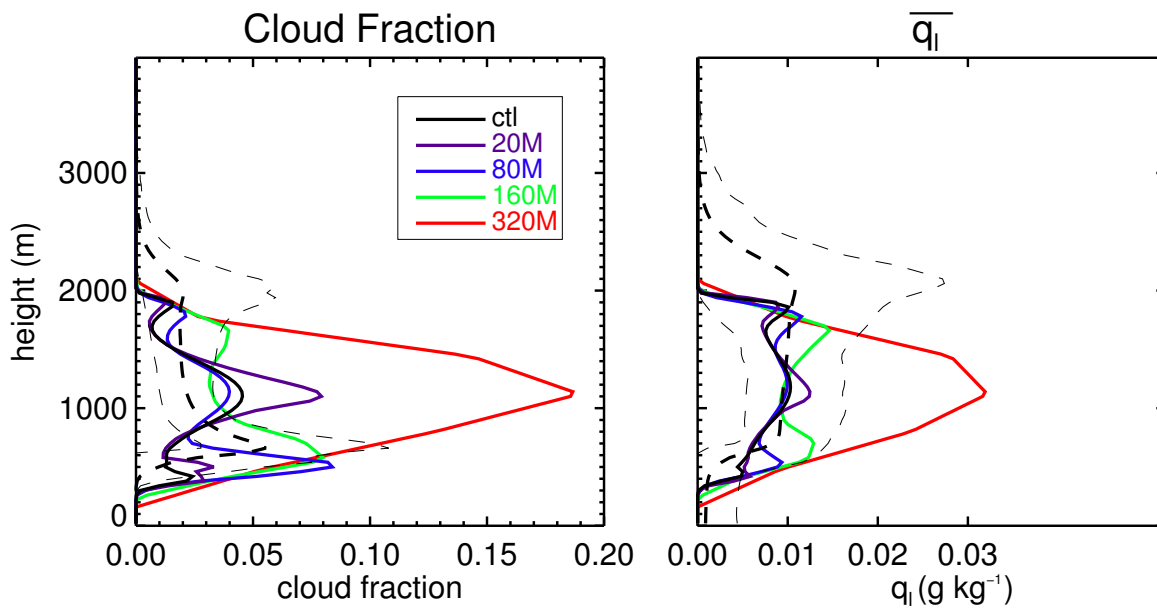


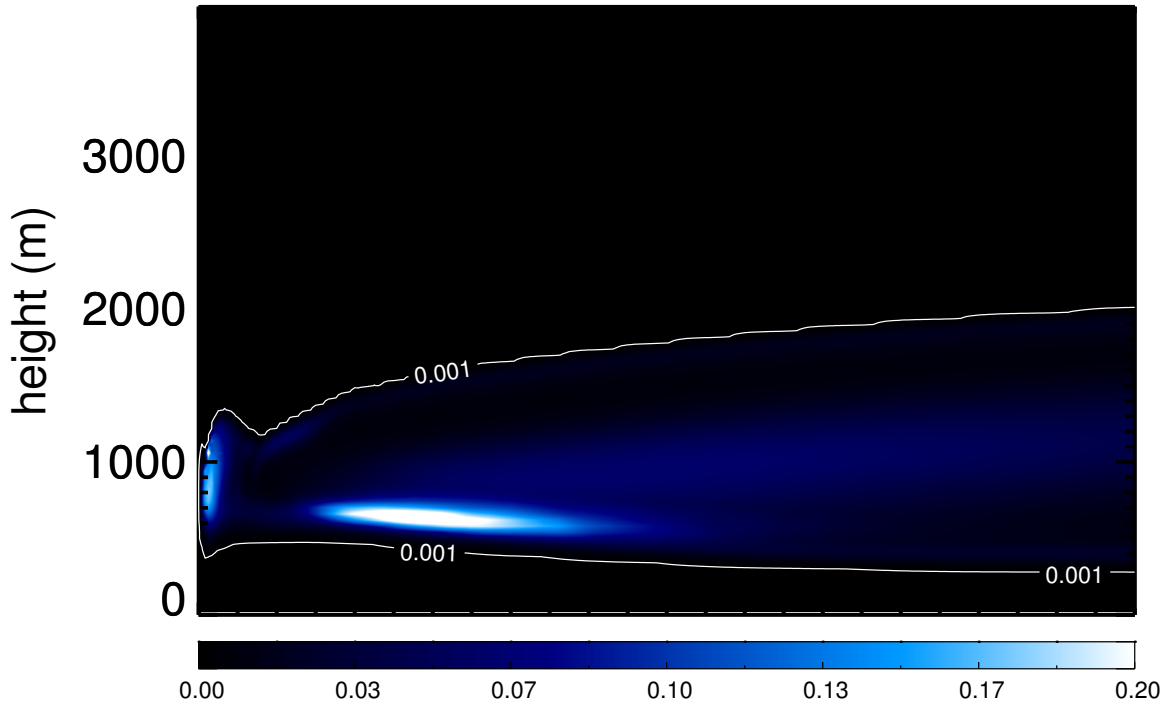
FIGURE 3.16. Mean profiles of cloud fraction (left) and q_l (right) for the grid spacing sensitivity test runs. Lines are as in figure 3.15.

The simulated cloud structure is shown in figure 3.16. All THOR runs certainly produce cumulus-like profiles with the maximum cloud fraction approaching 19% in the worst simulation (the 320 m run). Both cloud fraction and cloud liquid water content magnitudes are generally in line with the LES results for all grid spacings below 320 m, although cloud height is underestimated in all simulations compared to LES. An interesting difference is exposed when examining the cloud structure produced by THOR with different grid spacings. For fine

grid spacings, 80 m or below, a tri-modal structure is evident with local maxima near cloud base, near the middle of the cloud field, and at cloud top. For the 160 m grid spacing test, a familiar bi-modal structure develops with maxima at cloud base and in the detrainment zone at cloud top. For the coarsest grid spacing, 320 m, there is only a single, overestimated cloud fraction maximum near the middle of the cloud field. To dig a little deeper into the tri-modal structure simulated with finer grid spacing runs, it is useful to recall how the mean cloud fraction is calculated at each level, in equation (86). The mean cloud fraction is the sum of the cloud fraction diagnosed from each Gaussian plume multiplied by the weight of each Gaussian plume. It turns out that the middle maximum is a product of cloud being diagnosed in the “environmental” plume (plume 1), which can be interpreted as non-core or non-dynamically active cloud. So, while the tri-modal structure may be erroneous, it is diagnosed from a portion of the PDF that is much less active in determining the buoyancy terms that influence the turbulence calculated by the higher-order closure model.

Figure 3.17 displays the time evolution of the cloud field. The cloud fraction time-height cross-section shows that after an initial burst of cloud activity during the spin-up period, a smooth evolution of the cloud field ensues, as the cloud base slowly lowers to about 400 m and the cloud top slowly rises to about 2000 m. The erroneous middle-cloud maximum is evident and seems to rise at the same rate as the cloud top. The liquid water path for grid spacings below 80 m are consistent with each other and is slightly underestimated compared to the LES mean although well within the range of LES results. Since the magnitude of the cloud water content is very similar for THOR and the LES models, the underestimation of cloud liquid water path is attributable to the underestimation of cloud top height. For grid spacings of 160 and 320 m, the liquid water path increases, although it is not until

Cloud Fraction



Cloud Water Path

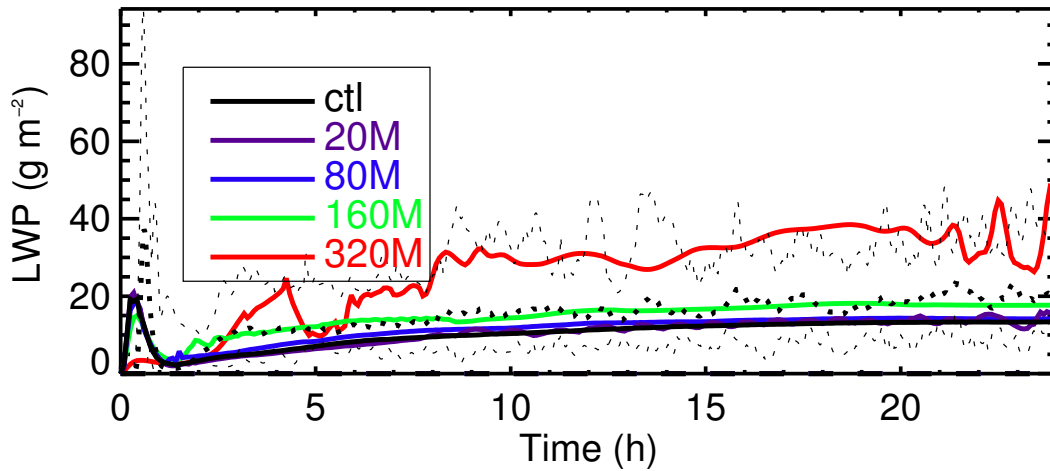


FIGURE 3.17. Time-height cross-section of cloud fraction for the control run (top) and liquid water path time-series for the control run and grid spacing sensitivity runs. Lines are as in figure 3.15.

320 m until the liquid water path predicted by THOR begins to reach the maximum values obtained by LES.

To gain a better understanding of the cloud field produced by THOR, it is interesting to look at trivariate double-Gaussian PDFs that are diagnosed from the predicted higher-order moments. Figures 3.18 - 3.20 depict the actual PDFs diagnosed in THOR for three regions in the atmospheric column: sub-cloud (figure 3.18), cloud base (figure 3.19) and mid-cloud (figure 3.20). For each of these figures, the cloud fraction time-height cross-section is displayed in the bottom right corner with a red X to denote the point in time and space where the PDF is taken from. Overlaid green contours in this plot show lines of constant TKE. The two plots on top and the one furthest right are single-variate PDFs for w , θ_{il} and q_t , with the solid lines denoting the total (weighted sum of both Gaussian plumes) PDF, the dashed lines denoting plume 1 (the “environmental” plume), and the dotted lines denoting plume 2 (the active or “updraft” plume). The three remaining plots show the bivariate joint PDFs between w and q_t (center left), θ_{il} and q_t (center right), and w and θ_{il} (bottom left). The solid contours in each of these plots show deciles of probability while the dashed contour shows 0.01% of the maximum probability. Points plotted with symbols in the w - q_t bivariate PDF denote mean values of the individual Gaussian plumes, a + symbol for plume 1 and a * symbol for plume 2. The solid line in the θ_{il} - q_t joint PDF represents the generalized and linearized saturation curve. Points above this line are saturated while points below are unsaturated. Finally, the blue and red asterisks in the θ_{il} - q_t joint PDF plot show the actual (θ_{il}, q_t) samples chosen from the latin-hypercube sampling algorithm to drive the microphysics parameterization, where the blue symbols are in-cloud and the red symbols are extra-cloud.

The sub-cloud PDF plot (figure 3.18) shows that there is considerable variability in w and q_t , but little in θ_{il} . Plumes 1 and 2 are relatively equally weighted (since the dashed

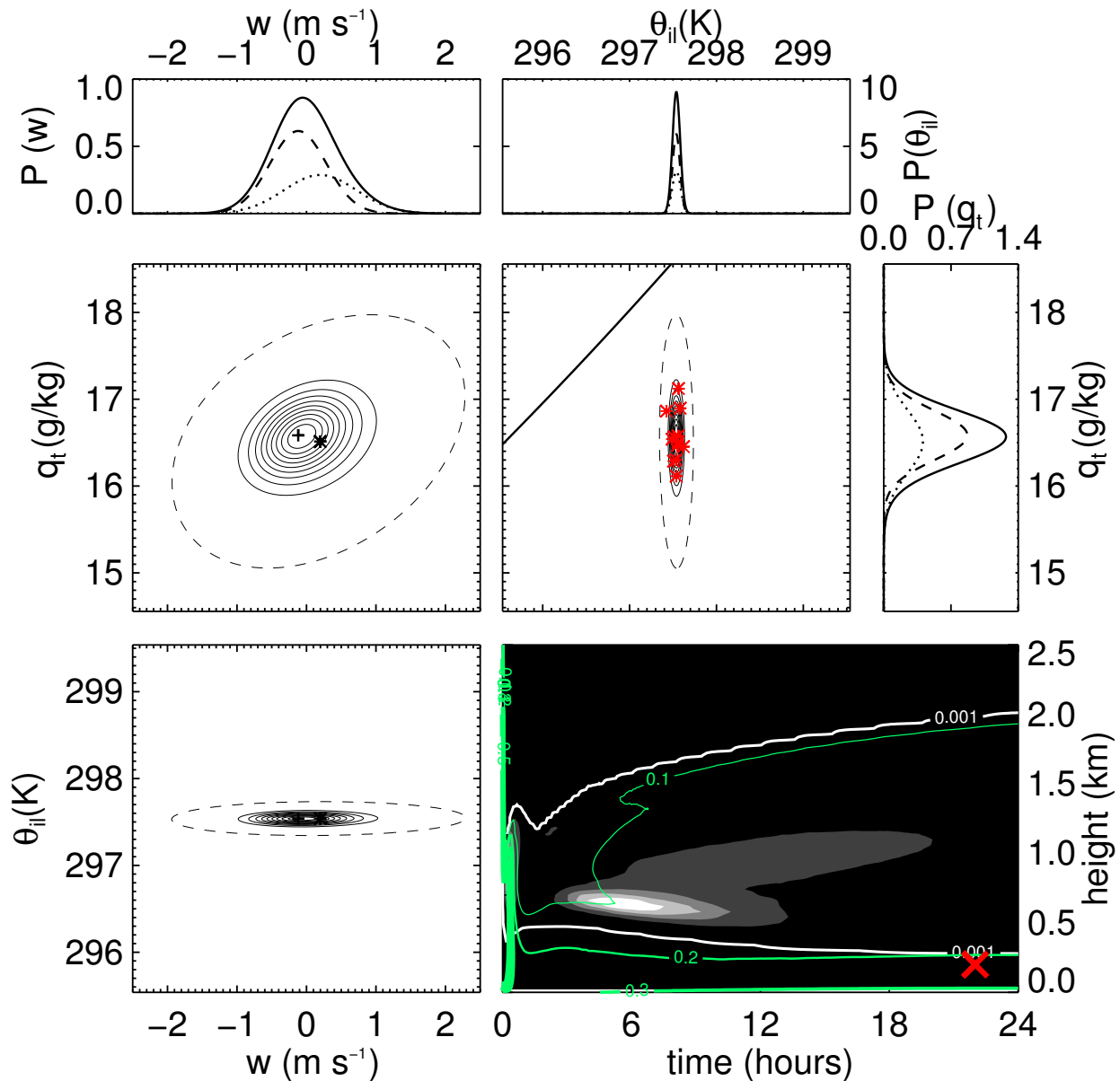


FIGURE 3.18. Graphical representation of the trivariate double-Gaussian PDF for the sub-cloud layer of the RICO control simulation. The bottom right plot is for orientation purposes and shows the cloud fraction in white contours and the TKE in green contours, with the red X denoting the particular point in time and space for the PDFs shown in the rest of the plots. The top and right plots show single-variate PDFs whereas the middle and bottom-left plots show bivariate PDFs. The axes labeled on the exterior of the plots are valid for the interior plots as well. Symbols and contours for the PDF plots are explained in the text.

and dotted lines in the single-variate PDFs are roughly the same magnitude), signifying that turbulence is somewhat isotropic in this layer and upward- and downward-fluxing eddies are in rough balance. There is little skewness in any of the variables, and the mean values for each plume are close to the grid-cell mean values. This particular grid cell is completely clear with none of the θ_{il} - q_t bivariate PDF above the saturation line. The only bivariate PDF that shows much correlation is the w - q_t bivariate PDF which is positively correlated (due to its tilt), although you might expect this since $\overline{w'\theta'_{il}}$ and $\overline{\theta'_{il}q'_t}$ are both small below cloud base (see figures 3.21 and 3.22).

At cloud base (figure 3.19), the PDF changes significantly. First, from looking at the univariate PDFs, it is apparent that the environmental plume dominates in terms of weight. The PDFs from plume 2 are barely visible in any of these plots since the value of a , the Gaussian weight of plume 2, is very small (on the order of $1/100$). One can get an idea for how the plume 2 PDF affects the total PDF by examining the bivariate PDFs. The dashed contours show that while the total PDFs are dominated by the lower-variance environmental plume, the higher-variance plume 2 adds significant variance to the “tails” of the total PDF. On which side of the mean value the tail is weighted is governed by the skewnesses of the variables. Skewnesses for w and q_t are strongly positive since their PDF tails are strongly weighted toward the positive side. In fact, the mean values of w and q_t for plume 2 are about 1 m s^{-1} and 1 g kg^{-1} higher than for plume 1. In addition, some of plume 2 is above the condensation line, signifying the presence of cloud. Finally, while the latin hypercube samples for the clear portion (red) are tightly packed in the low-variance environmental plume, the cloudy samples (blue) are spread out more, reflecting the higher variance of the updraft-containing plume 2.

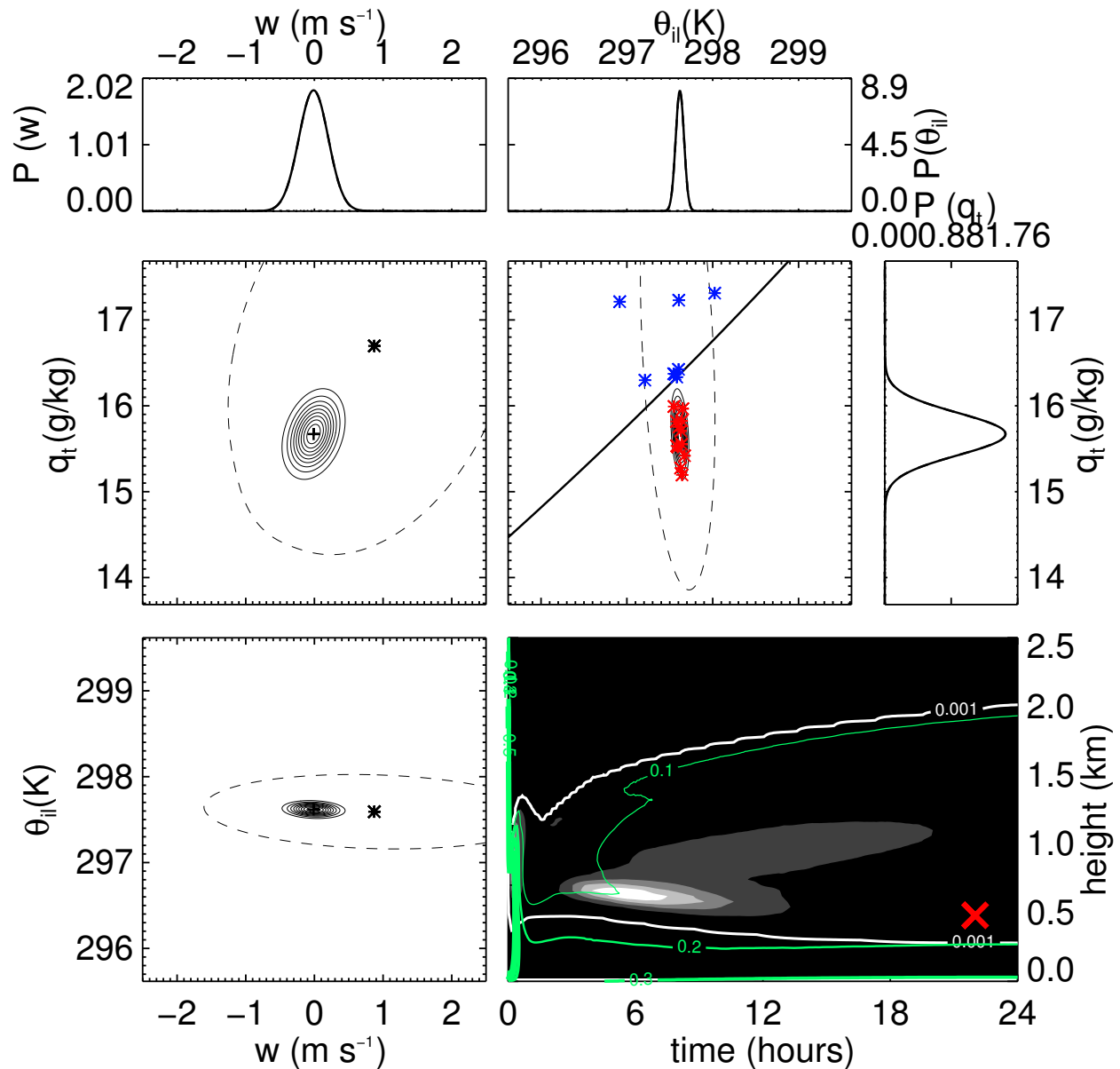


FIGURE 3.19. As in figure 3.18, but for a representative cloud base location.

In the middle of the cloud, the PDF changes more subtly. The variances of θ_{il} and q_t in the environmental plume increase as one gets closer to the subsidence inversion. In addition, the w - θ_{il} and θ_{il} - q_t bivariate PDFs show significant negative correlation as the correlation in the w - q_t bivariate decreases, which is again consistent with the profiles of $\overline{w'\theta'_{il}}$, $\overline{w'q'_t}$, and $\overline{\theta'_{il}q'_t}$ closer to the inversion. The increasingly negative correlation in the θ_{il} - q_t bivariate PDF,

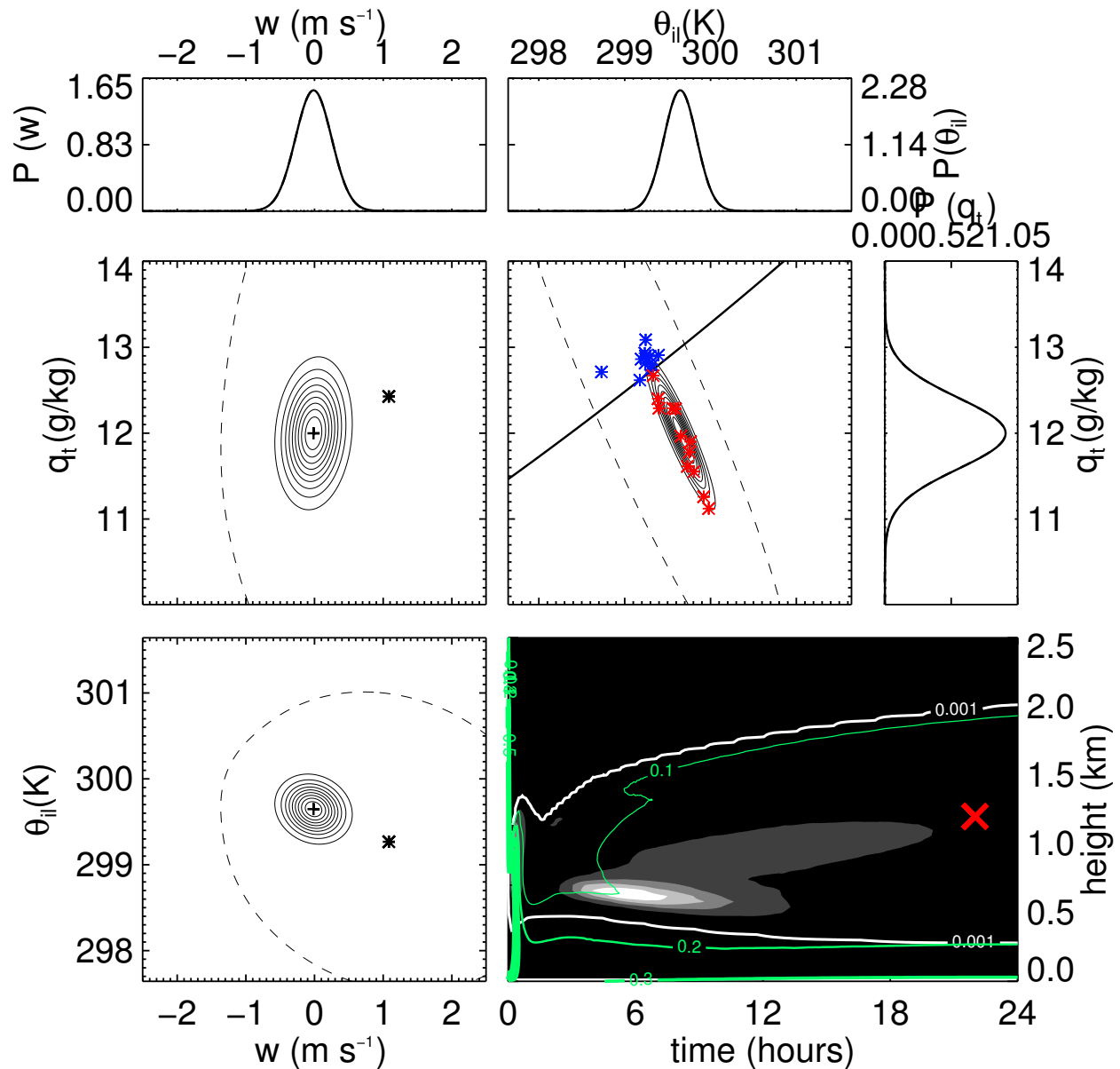


FIGURE 3.20. As in figure 3.18, but for a representative mid-cloud location.

together with increasing environmental variances of these variables, tilts this bivariate PDF to a more favorable position for the SGS condensation scheme to diagnose condensation in the environmental plume, which might help to explain the tri-model structure discussed in conjunction with figure 3.16. Lastly, there is significant skewness for all variables since the PDFs are weighted toward one side of the mean values for each variable. The mean values

of plume 2 are over 1 m s^{-1} higher for w , about 0.4 g kg^{-1} higher for q_t and about 0.5 K lower for θ_{il} than plume 1 at this time and height.

For the RICO case, the profiles of the vertical fluxes of θ_{il} and q_t and the variance of w look pretty similar in comparison to LES than they do for the BOMEX case. The vertical velocity variance is too high in the sub-cloud layer and in the cloud layer, although the shape of the profile is what one would expect. The magnitude of TKE in the cloud layer is very close to what is calculated for the LES models, but is underestimated in the subcloud layer. This suggests that the horizontal components of TKE must be significantly underestimated, but this is not that surprising of a result since the LES models are probably capturing a lot of lateral movement due to cold pools at the surface and detrainment and entrainment activity in the cloud layer that is missing in THOR. The underestimation of the vertical thermodynamic fluxes continue to be an issue as well, although they generally fall within the range of LES results. For all profiles in figure 3.21, all grid spacing tests yield similar results with the exception of the 320 m test, which tends to place maxima even lower in the column than the others.

The thermodynamic variances and covariance are shown in figure 3.22. As with other second- and third-order moments, the profiles are too short, maxing out near the cloud top simulated by THOR around 2000 m. The inversion maxima for these quantities are greater than LES for several reasons. First, the subsidence inversion in the THOR runs ends up being sharper than the one created by LES. In an LES, presumably there are many convective elements as in nature, where some are more buoyant and dynamically active than others and ultimately reach higher heights. Perhaps some of these elements reach above the inversion layer, providing a type of “diffusion” that helps to smooth out the profiles near the inversion.

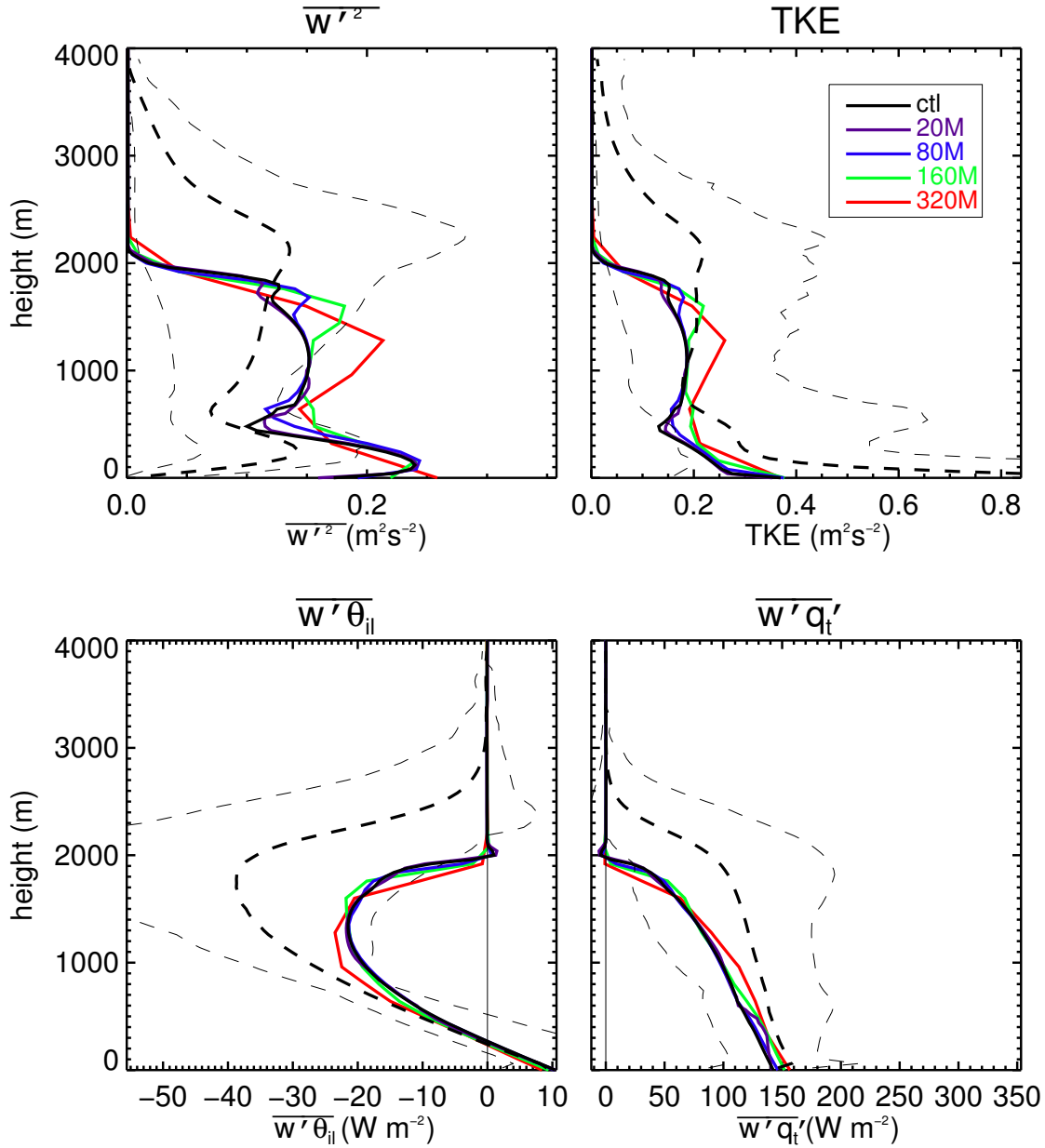


FIGURE 3.21. Mean profiles of the vertical velocity variance (top left), TKE (top right), sensible heat flux (bottom left), and latent heat flux (bottom right) for the control and grid spacing sensitivity runs. Lines are as in figure 3.15.

THOR seems to have trouble representing this process with a higher-order closure statistical approach. Nevertheless, a sharper inversion leads to higher thermodynamic variances in the inversion layer through the mechanical production term. Second, turbulent transport due to the third-order moments could be too strong, transporting too much variance to the

inversion layer. This seems unlikely, as the the magnitude of the third-order moments seems to be well in-line with LES results for the shallow cumulus regime and these terms simply transport variance, and a resultant underestimation or minimum of variance would need to be present in other layers, which is not the case with THOR. Third, the turbulence time scale could be too large in the inversion layer, leading to turbulence dissipation that is too weak. While this is a possibility, it is difficult to test this hypothesis, since this quantity is seldom measured. If anything, however, it would seem that turbulence dissipation is too strong near and above the inversion since the profiles of all turbulence statistics are too short in general.

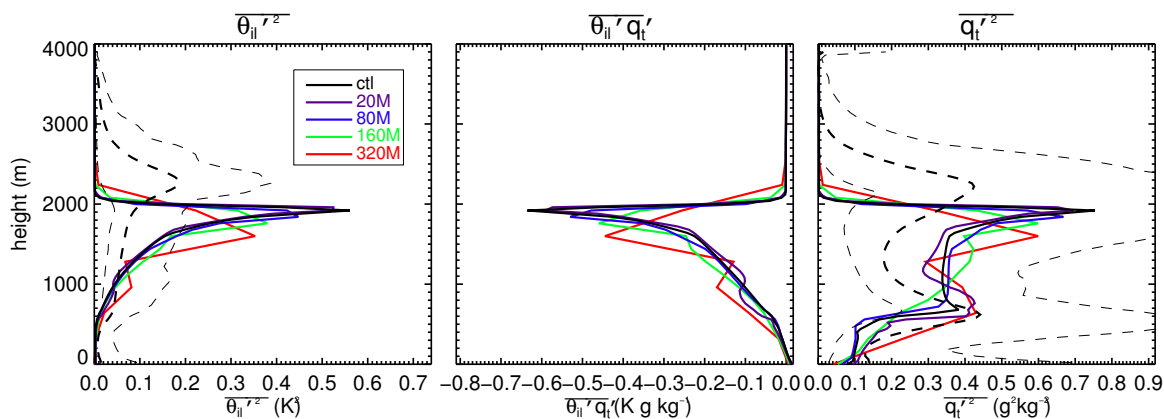


FIGURE 3.22. Mean profiles of the ice-liquid water potential temperature variance (left), ice-liquid water potential temperature-total water specific humidity covariance (center) and total water specific humidity variance for the control and grid spacing sensitivity runs. Lines are as in figure 3.15.

As with the BOMEX case, additional sensitivity tests were performed to determine THOR’s sensitivity to different model formulations. Two of the sensitivity tests that seemed to have the largest impact for the BOMEX case are repeated for the RICO case: the turbulence length scale entrainment sensitivity test and the third-order moment diagnostic versus prognostic sensitivity test. Given the similarities of the simulated atmospheres between the BOMEX and RICO cases, one would expect similar sensitivities for these tests, and this is

largely the case, so less detail is included in the analysis of these sensitivity tests. Pertinent plots are included for the interested reader as verification for the sensitivities discussed in the previous section.

Figures 3.23 and 3.24 show the vertical structure and evolution of the cloud fields produced from the length scale entrainment sensitivity runs. As with the BOMEX case, runs that used lower entrainment rates produced deeper and thinner clouds with more realistic profiles. Although the liquid water path for the lower entrainment runs are underestimated compared to the LES mean, this is mostly an artifact of too-shallow cloud depths. The higher entrainment rate run using the stochastic algorithm produced a liquid water path with better agreement to the LES mean, although the profiles show that both cloud fraction and liquid water are considerably overestimated in the mid and upper portions of the cloud field.

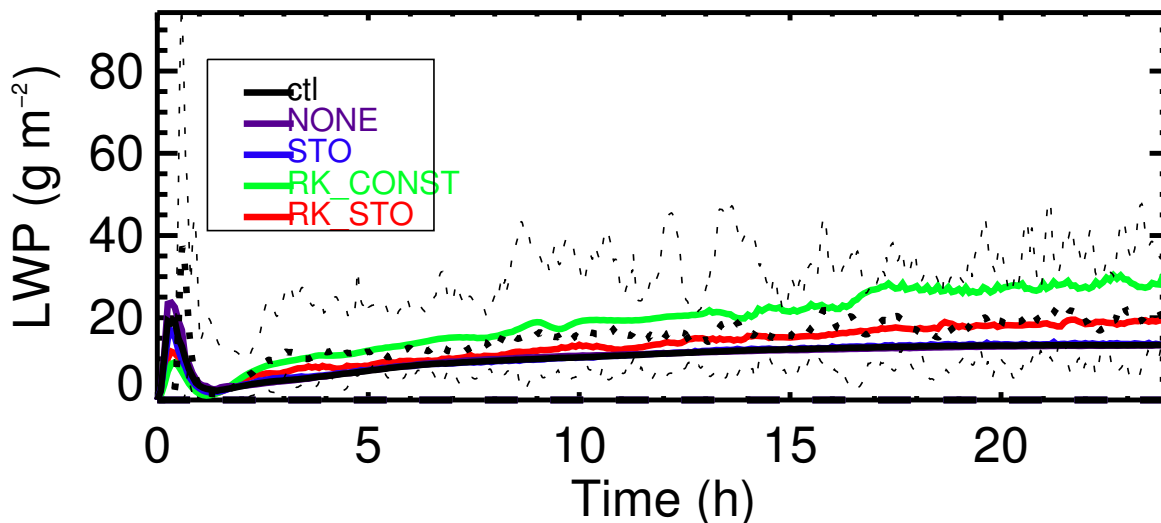


FIGURE 3.23. Time-series of liquid water path for the length scale entrainment sensitivity runs. Lines are as in figure 3.15.

Next, the profiles and time evolution of the cloud field for the diagnostic versus prognostic third-order moment sensitivity test are include in figures 3.25 and 3.26. The cloud fraction

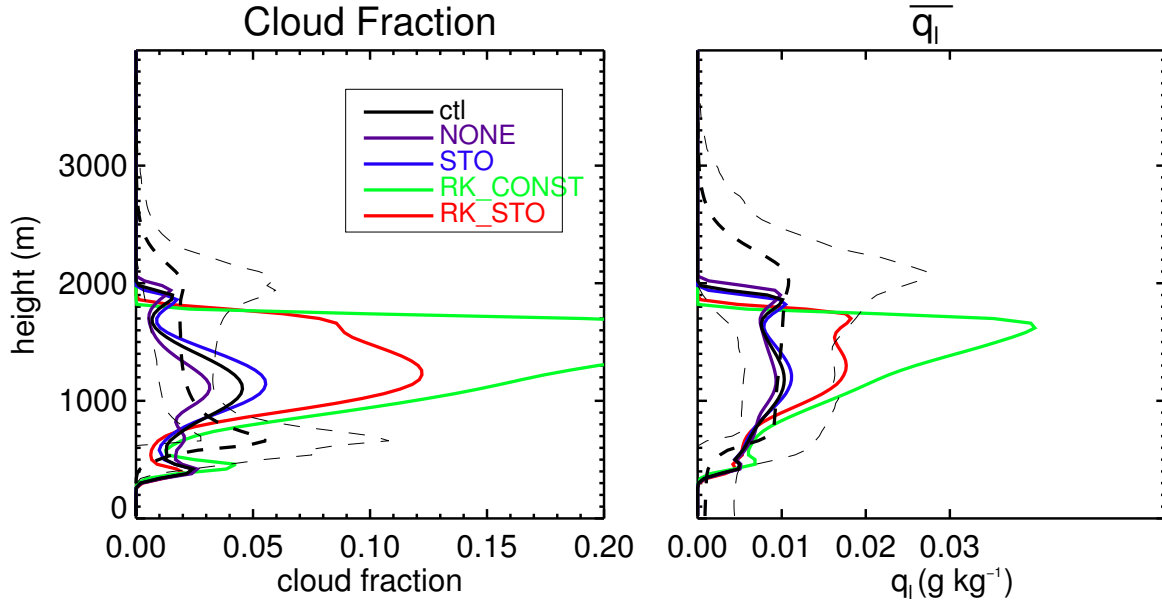


FIGURE 3.24. As in figure 3.16, but for the length scale entrainment sensitivity test.

time-height cross-section in figure 3.25 shows the evolution of the cloud field for the fully prognostic third-order moments run. As with the BOMEX case, it features an oscillation, but with a longer period, on the order of 20 minutes (compared to about 15 for the BOMEX case). Also confirming the sensitivities discussed in the previous section, the more third-order moments are predicted, the higher the liquid water content of the clouds and the higher the erroneous mid-cloud peaks in cloud fraction and cloud water content.

One sensitivity test not included for the BOMEX case is the elimination of the latin hypercube sampling algorithm for driving the microphysics parameterization since microphysical processes were excluded from that case. Since microphysics is a main thrust of the LES intercomparison of vanZanten et al. (2011), it is prudent to include microphysics for the RICO case and, further, to determine the effect of not using a sampling algorithm to drive the microphysics scheme. In the plots that follow, the run that uses grid cell mean values to drive the microphysics scheme is labeled NO-LH (for no latin hypercube sampling).

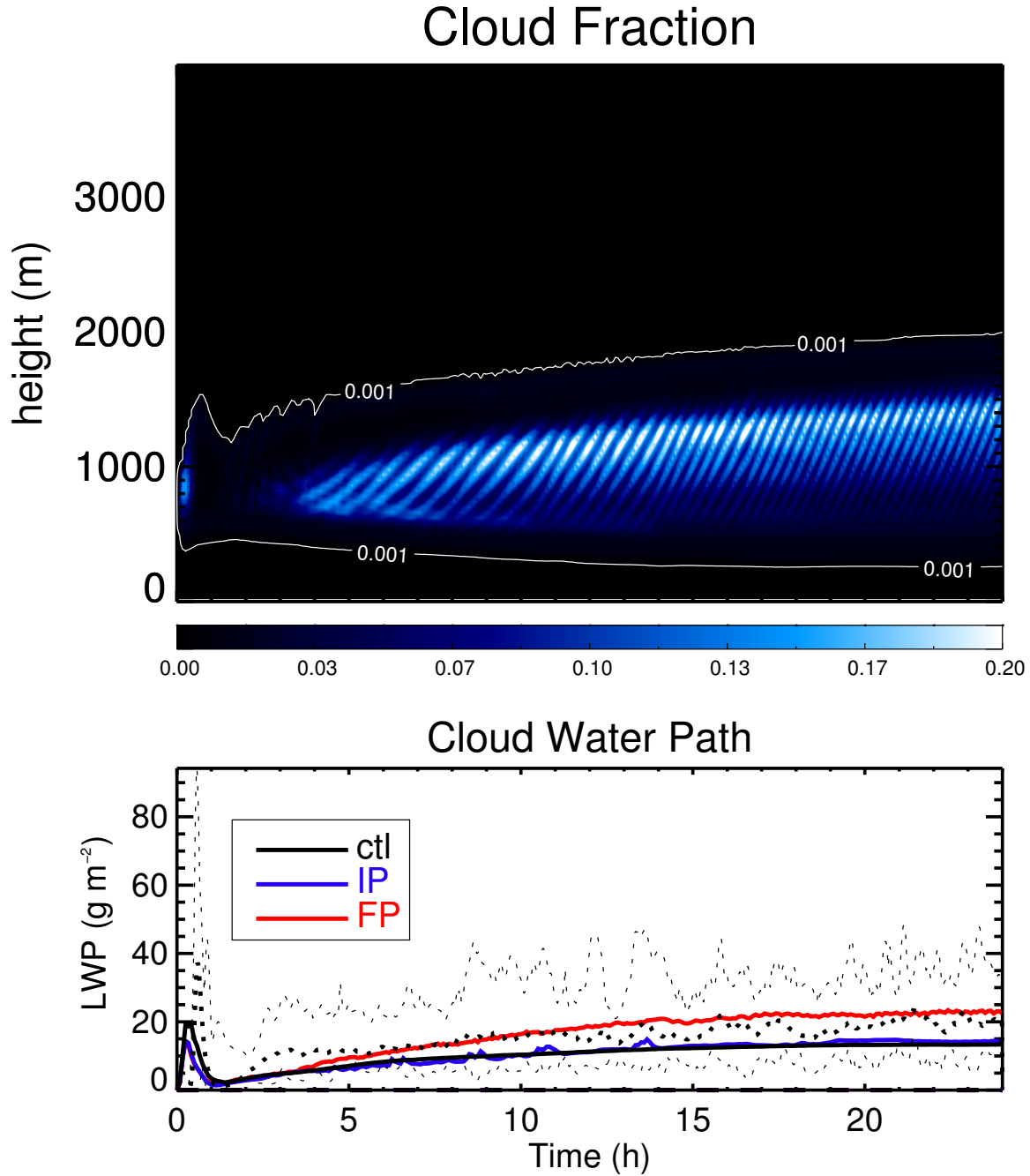


FIGURE 3.25. As in figure 3.17, but for the third-order moment calculation sensitivity test.

Figure 3.27 shows the surface precipitation rate for the control case versus the NO-LH test. The control simulation produces a surface precipitation rate that agrees well with the LES ensemble mean, and the surface precipitation rate seems to level out near the end of the

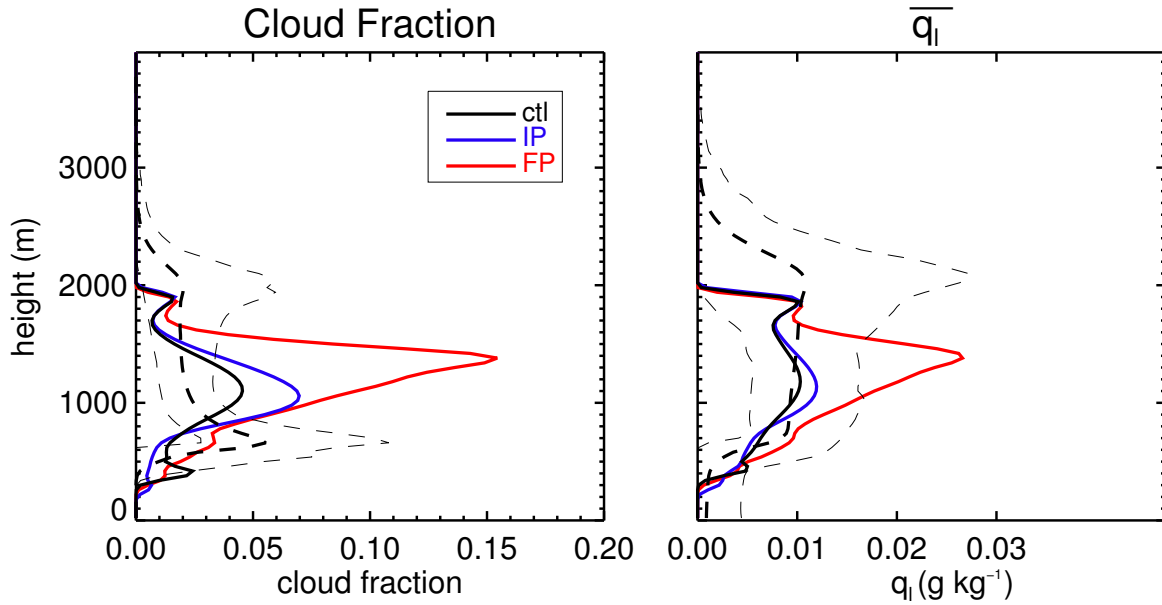


FIGURE 3.26. As in figure 3.16, but for the third-order moment calculation sensitivity test.

simulation around 0.4 mm day^{-1} . The NO-LH simulation shows that when PDF sampling is turned off, THOR produces no precipitation whatsoever. The reason for this is straightforward. In the RICO case, all precipitation is generated by the so-called “warm rain” process, meaning that precipitation is only generated in the microphysics parameterization through the rain autoconversion process. This term generates rain when cloud water exceeds a certain threshold. For the shallow cumulus clouds generated in the RICO case, there is never enough cloud water to trigger this process. Of course, the microphysics parameterization could be “tuned” to include a lower autoconversion threshold, but such a tuning would likely introduce a systematic overestimation bias for clouds with higher water contents. The rain autoconversion term for the control simulation with the latin hypercube sampling active is shown in figure 3.28, and demonstrates the random nature of the sampling process nicely. Although in the grid cell mean sense there is not enough cloud water content to create rain (according to the NO-LH test), there are presumably pockets in the cloud where local water

contents are high enough to have larger droplets that end up falling as rain. The sampling process seems to mimic nature satisfactorily by randomly selecting areas of the PDF where cloud water contents are high enough to produce rain. The time-height cross-section shows that the highest autoconversion rates are scattered in the middle part of the cloud and lighter rates are generated more consistently near cloud top and cloud base.

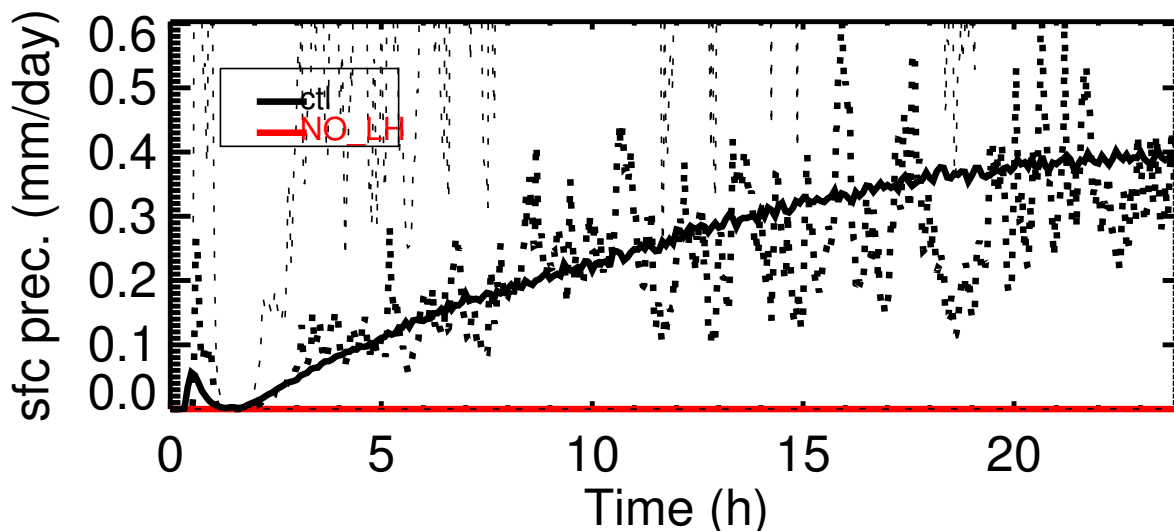


FIGURE 3.27. Time-series of surface precipitation rate for the control and NO-LH sensitivity run. Lines are as in figure 3.15, although the red line is along the abscissa axis.

Since the disabling of the PDF sampling feature in the NO-LH run effectively shut off all precipitation, what effect will this have on other atmospheric variables? The mean thermodynamic profiles are shown in figure 3.29 for both runs. There are a couple of differences that bear discussion. The first is that the subsidence inversion is higher for the NO-LH test and the second is that there is more total moisture higher in the column and less in the sub-cloud layer for the NO-LH test. This is consistent with the absence of precipitation because the cloud water stays suspended higher in the column and there is no precipitation to evaporate in the sub-cloud layer to moisten it.

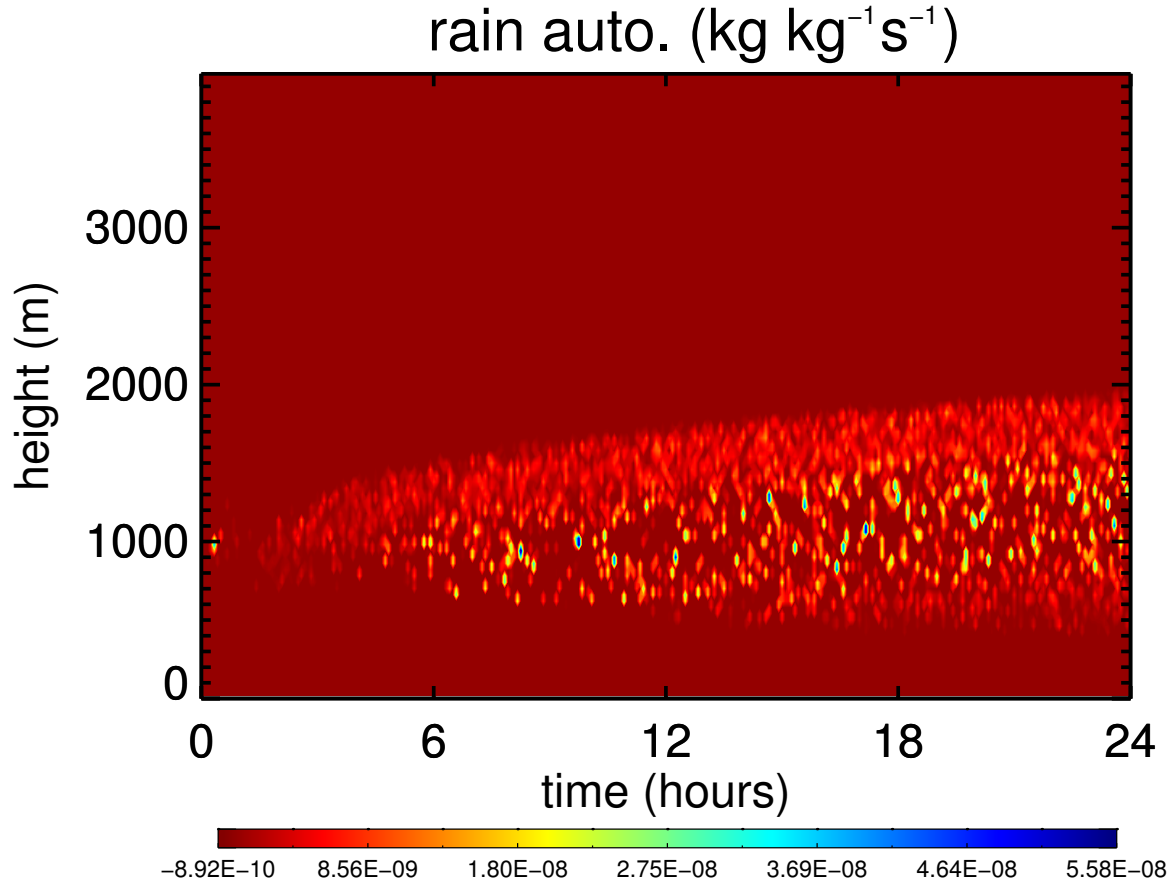


FIGURE 3.28. Time-height cross-section of the rain autoconversion rate calculated in THOR for the control simulation.

The cloud fraction difference time-height cross-section is shown in figure 3.30. Not surprisingly, the cloud fraction increases substantially when precipitation is effectively shut down. In addition, the cloud top and cloud base both rise. Without precipitation robbing the cloud of moisture, loading the updrafts with falling mass, and moistening the sub-cloud layer through evaporation, the simulated cloud is slightly more energetic, reaching a higher altitude, and cloud base is raised a tad without the extra sub-cloud moisture to bring it downward. With a cloud layer that is slightly deeper and moister, the liquid water path for the NO-LH test is increased compared to the control simulation (figure 3.31).

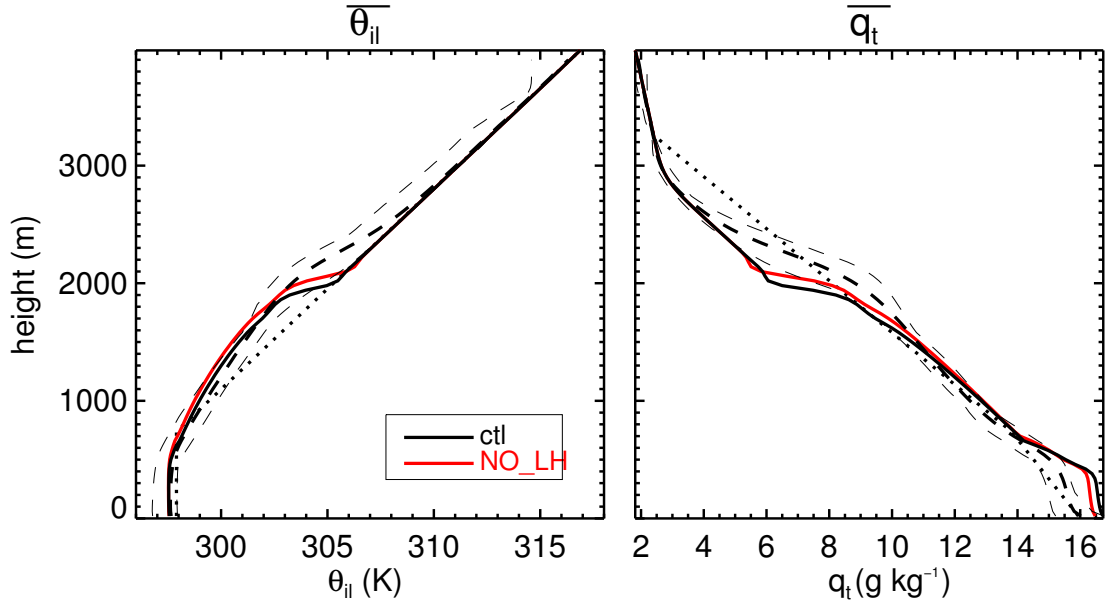


FIGURE 3.29. As in figure 3.15, but for the no-latin-hypercube-sampling sensitivity test.

Lastly, the turbulent flux and TKE profiles are shown in figure 3.32 for the no-PDF-sampling sensitivity test. From examining the mean thermodynamic profiles, it was determined that the simulation without PDF sampling produced slightly more energetic clouds, and the figure 3.32 confirms this. Both the vertical velocity variance and the TKE were increased substantially throughout the cloud layer. In addition, the turbulent fluxes of θ_{il} and q_t are significantly stronger throughout much of the column and especially in the cloud layer. The reasons for this are that the mechanical production and buoyancy terms in the $\overline{w'\theta'_{il}}$ and $\overline{w'q'_t}$ equations were increased in the absence of precipitation.

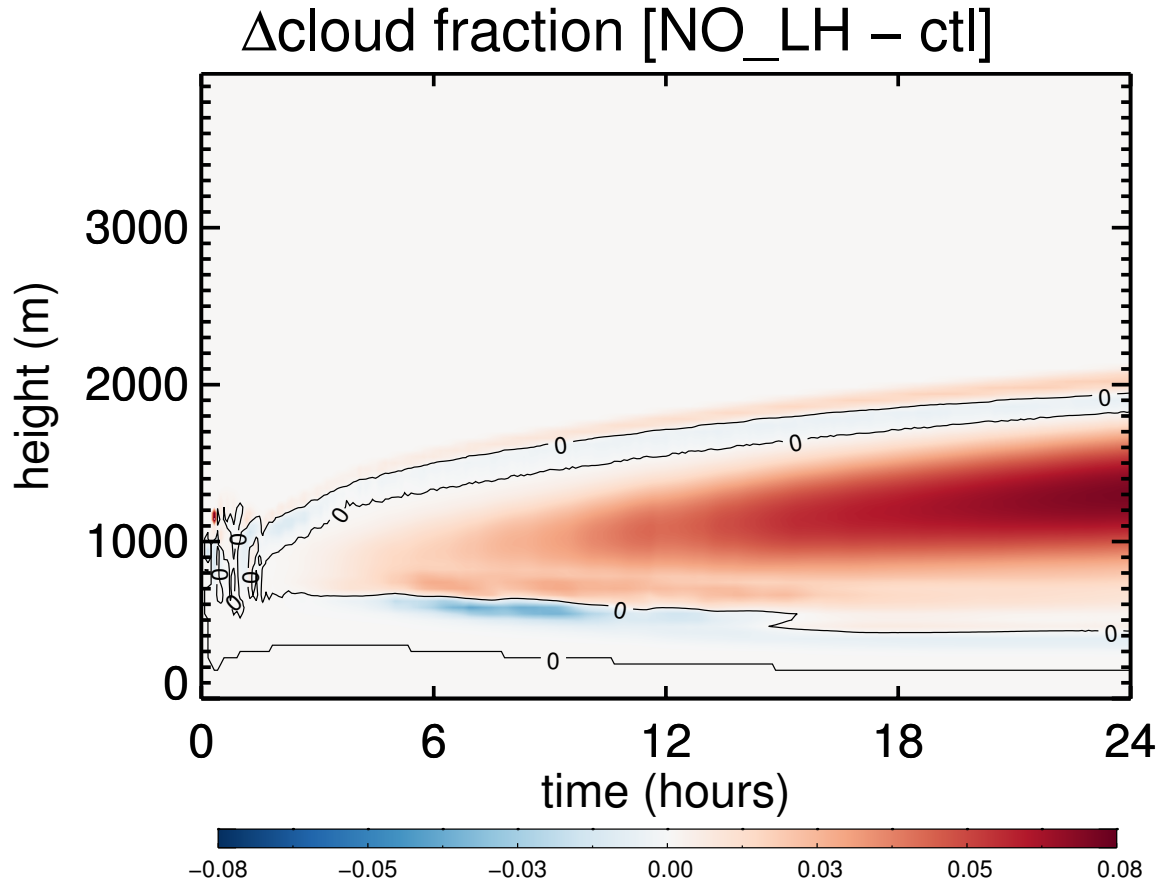


FIGURE 3.30. Time-height cross-section of the difference in cloud fraction between the NO-LH run and the control.

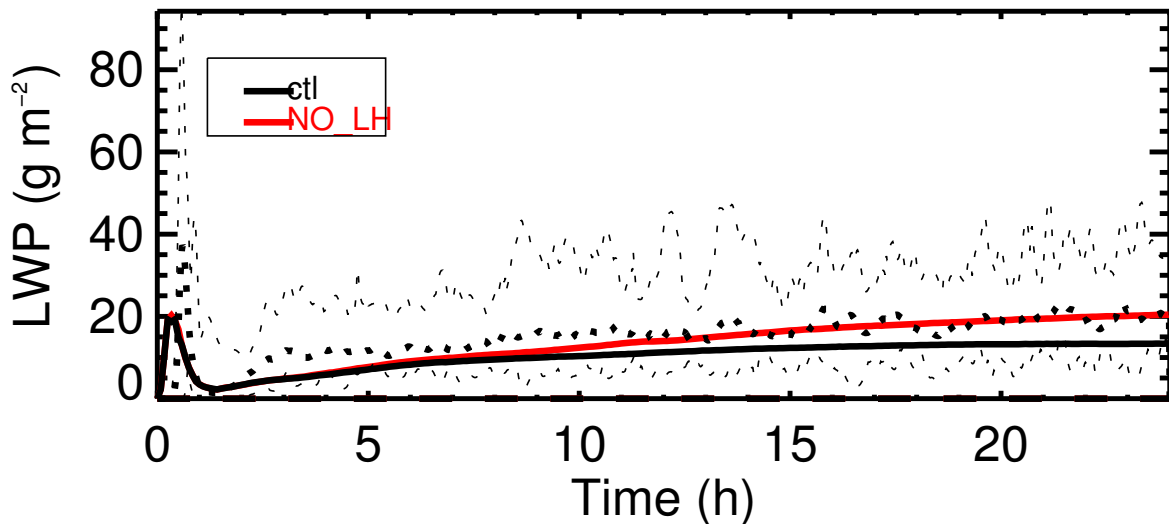


FIGURE 3.31. Time-series of the liquid water path for the no-latin-hypercube-sampling sensitivity test. Lines are as in figure 3.15.

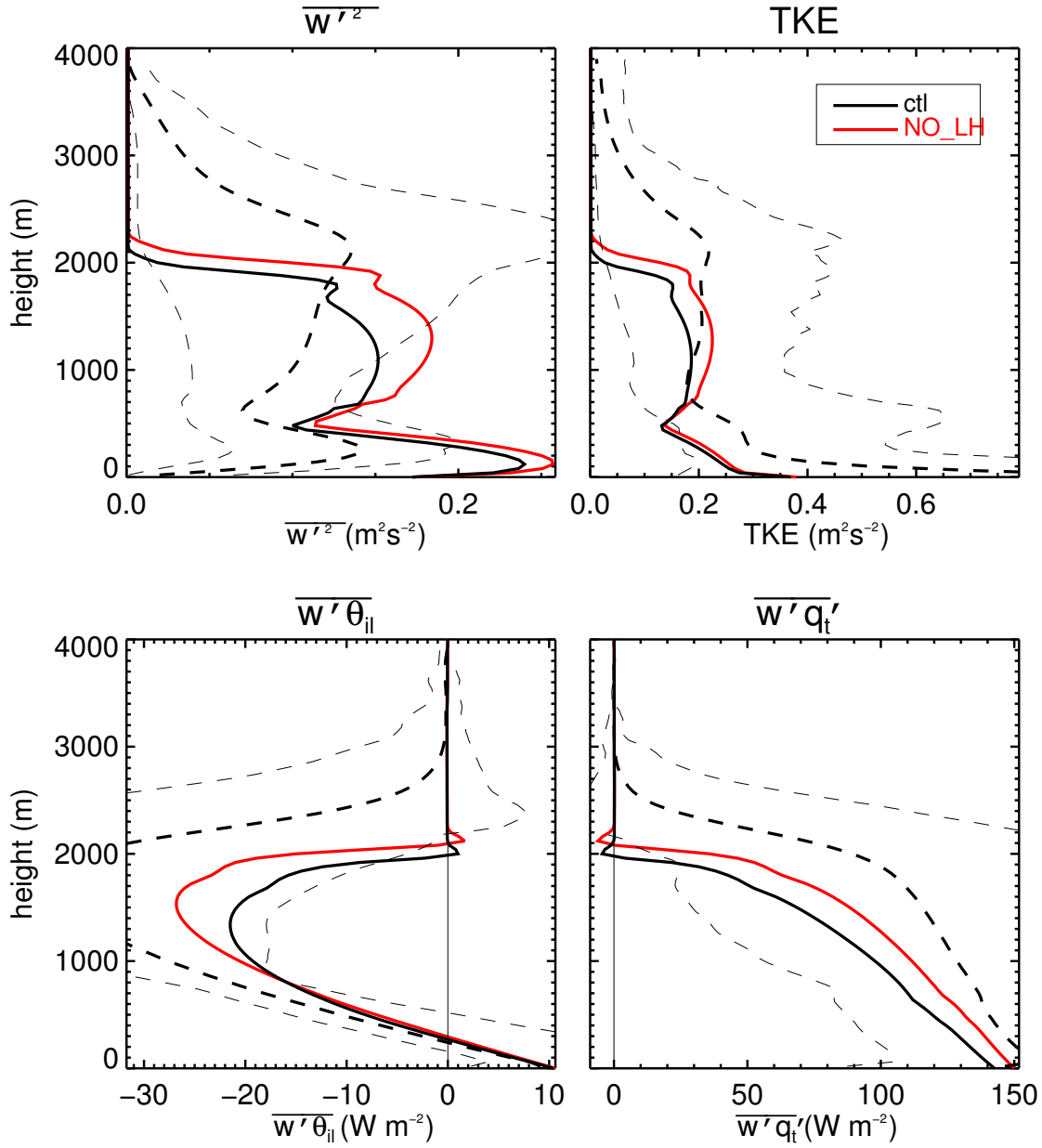


FIGURE 3.32. As in figure 3.21, but for the no-latin-hypercube-sampling sensitivity test.

3.2. STRATOCUMULUS CASES

The challenge in simulating stratocumulus stems from the finely balanced nature of these cloud systems. The synoptic conditions under which these clouds usually form consist of strong, deep anticyclonic subsidence over a relatively cool ocean surface. The sea provides

a constant supply of moisture and energy to the boundary layer in the form of moderately strong latent heat fluxes and relatively weak sensible heat fluxes. The warming and drying caused by the subsidence aloft tends to create a distinct boundary between the warm, dry free tropospheric air aloft and the cool, moist boundary layer air below. Thus, the first form of balance is between the strength of the subsidence and the magnitude of the surface heat fluxes. Tip the balance in favor of the surface heat fluxes, and the boundary layer deepens. Tip the balance in the other direction, and the subsidence drags the the temperature inversion lower.

Between the trapped boundary layer moisture and the cool temperatures, it is relatively easy to reach the condensation threshold and stratocumulus clouds readily form. As the vapor condenses, it releases latent heat that adds buoyancy and helps to generate TKE. Since the TKE is simply a measure of the strength of the individual turbulent eddies, higher TKE air contains individual eddies with sufficient energy to overcome the strong stability associated with the temperature inversion. These eddies participate in entrainment, mixing cool, moist air out of the boundary layer but also bringing in warmer and drier air into the boundary layer. The warm, dry air is then mixed well by other turbulent eddies in the boundary layer, and in this way the mean boundary layer properties are modified. Thus, a second balance is recognized. Latent heating generated by the stratocumulus clouds helps to generate TKE. The strength of the in-cloud TKE influences how much dry air is introduced into the boundary layer. Such entrainment adds mass to the boundary layer and deepens it. However, when enough dry air is entrained, it can thin or dissipate the clouds, cutting off the supply of TKE, decreasing entrainment, and lowering the inversion once again.

The balance is further complicated by radiative transfer, drizzle, and cloud top evaporation. The presence of thick cloud cover generates strong cloud-top radiative cooling and much weaker radiative warming near cloud base. The strong radiative cooling at cloud top together with evaporative cooling from dry, entrained air generates TKE by the circulations induced by sinking, negatively-buoyant parcels. The weak radiative heating at cloud base enhances latent heating there, further adding to the turbulent circulations in the cloud. If drizzle is being generated by the cloud, it can serve to reduce the cloud's water content and associated cloud-top radiative and evaporative cooling. Further, drizzle serves to redistribute latent heating, depending on where the precipitation ends up. If it evaporates in the sub-cloud layer, it removes the potential evaporation in the cloud layer, effectively leaving its latent heat there, and cools the sub-cloud layer where it evaporates. The heating-over-cooling profile adds static stability to the layer where this mechanism takes place, while reducing static stability immediately above and below this layer, with heating-below and cooling-above profiles, respectively. If the drizzle reaches the surface, then only the latent heat of condensation is left in the cloud, while the potential evaporation ends up in the ocean.

The stratocumulus story is yet more complicated when one considers the role of cloud condensation nuclei (CCN) and their potential influence on drizzle and cloud albedo. In regions of high CCN, a given amount of cloud water condenses to form relatively more numerous cloud droplets. Large populations of small cloud droplets are not conducive to efficient generation of precipitation, so whatever the role that precipitation plays is reduced or muted in regions of high CCN. In addition, many small cloud droplets increase the reflectivity of stratocumulus clouds and may enhance cloud-top radiative cooling as well as

cloud-top evaporative cooling. The opposite is true if there are few CCN. The available water condenses to make fewer but larger cloud droplets, increasing precipitation efficiency, decreasing cloud albedo, and cloud-top cooling.

Despite the complex and subtle balance associated with stratocumulus clouds, it is important that atmospheric models be able to represent some of their key features given their important role in the climate system. In this study, THOR's ability to simulate these clouds and its sensitivities to several model formulations are investigated. Two challenging test cases are used toward this purpose: one based on the Second Dynamics and Chemistry of Marine Stratocumulus (DYCOMS) field campaign that took place off the coast of southern California and one based on the Mixed-Phase Arctic Cloud Experiment (MPACE) that took place off the north slope of Alaska. As with the two cumulus cases, analysis will focus on the simulated cloud structure and the turbulence statistics for each case and the results from THOR, including sensitivity tests, will be compared with results from LES models.

3.2.1. DYCOMS CASE. The DYCOMS case is based on an idealization of the second research flight, named RF02, of the DYCOMS II field campaign. The flight measured populations of both open-cell stratocumulus with significant drizzle and closed-cell stratocumulus with little precipitation. Details of the simulation setup and the LES intercomparison results can be found in Ackerman et al. (2009). The simulation is initialized with profiles of potential temperature, total water mixing ratio, and horizontal wind components that represent an average of both open and closed cell observations. Forcings include prescribed subsidence, a large-scale pressure gradient, prescribed surface fluxes, and a simple longwave radiation parameterization that depends on the liquid water path. In addition, a cloud droplet sedimentation flux parameterization is included in the forcing. The control THOR simulation

uses a uniform 25 m grid spacing and a 1 s time step. The simulation is run for 6 simulated hours and the domain is 1500 m. Note that for simplicity, the grid was assumed uniform for the THOR runs, while the LES models used in the intercomparison used a stretched grid with 5 m grid spacing near the surface and the inversion, stretched to 25 m in the interior of the boundary layer and up to 80 m above the boundary layer.

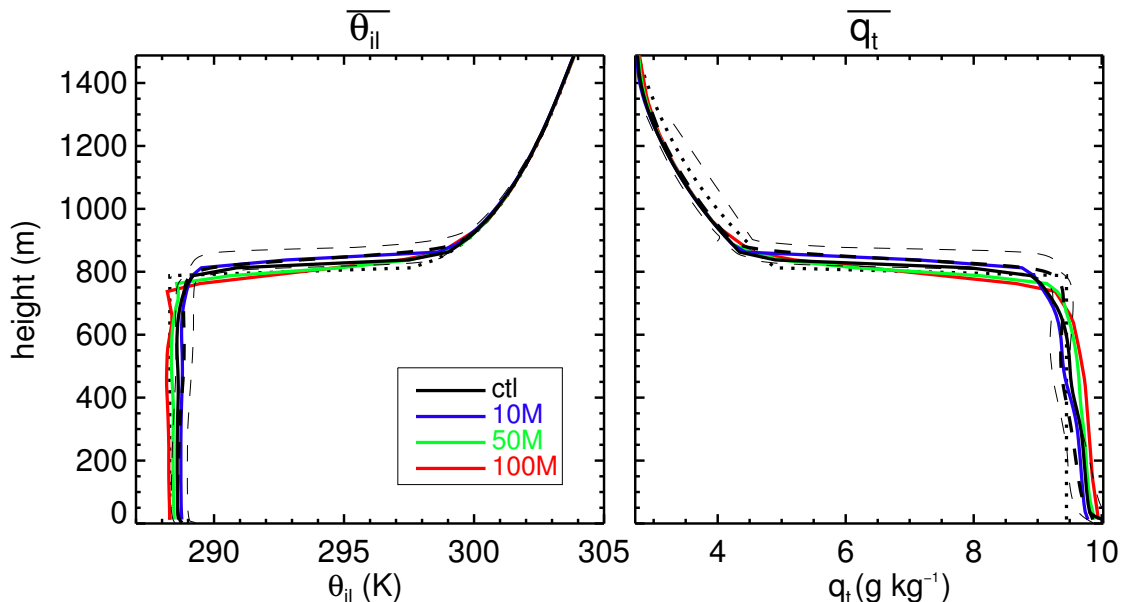


FIGURE 3.33. Mean profiles of θ_{il} and q_t for the last three hours of the control and grid spacing sensitivity test runs. As in the previous cases, solid lines represent output from THOR with the black denoting the control run and colors denoting sensitivity test runs. Black dashed lines represent the LES ensemble results, with the thick dashed line denoting the LES ensemble mean, and the thin dashed lines representing the range of LES ensemble results. The thin black dotted line represents the initial conditions.

The mean profiles of θ_{il} and q_t for the last 3 hours of the simulation are shown in figure 3.33 for the control simulation, all grid spacing sensitivity tests, and the LES models, together with the initial profiles. At first glance, it appears that all models do a reasonably good job, but there are certainly differences among the various grid spacing runs that bear discussion. First, the run that most faithfully reproduces the LES mean values is the 10 m grid spacing run. As grid spacing increases, the sharp inversion at cloud top is smoothed out

and it appears that the mixed layer becomes shallower. In addition, the mixed layer becomes moister and cooler. This could be the result of a reduced cloud-top entrainment rate. If the inversion layer is “perceived” to be 50 or 100 m thick, perhaps it becomes more difficult for the model to accurately represent the SGS entrainment process statistically. Further analysis is needed to confirm this, however.

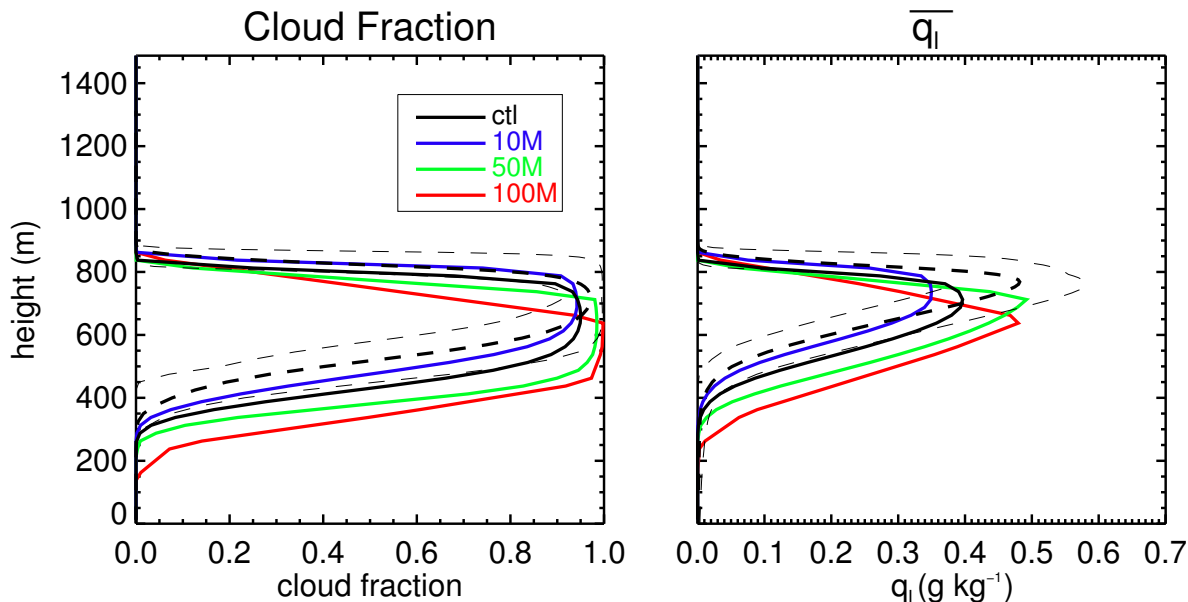


FIGURE 3.34. Mean profiles of the cloud fraction (left) and q_l (right) for the control simulation and grid spacing sensitivity tests. Lines are as in figure 3.33.

The time mean and temporal evolution of the cloud structure is presented in figure 3.34 and 3.35. As with the mean thermodynamic profiles, the smallest grid spacing seems to represent the cloud structure best, although even at 10 m, the simulation is not in perfect agreement with the LES ensemble mean. The cloud base is perhaps 50 m too low and the maximum cloud water content is underestimated by about 0.1 g kg^{-1} . Coarser resolutions have better agreement with the maximum liquid water content, but the cloud base becomes lower with increasing grid spacing along with the smoothed out cloud-top inversion. Looking at the time-series of the cloud liquid water path, the deeper simulated stratocumulus deck

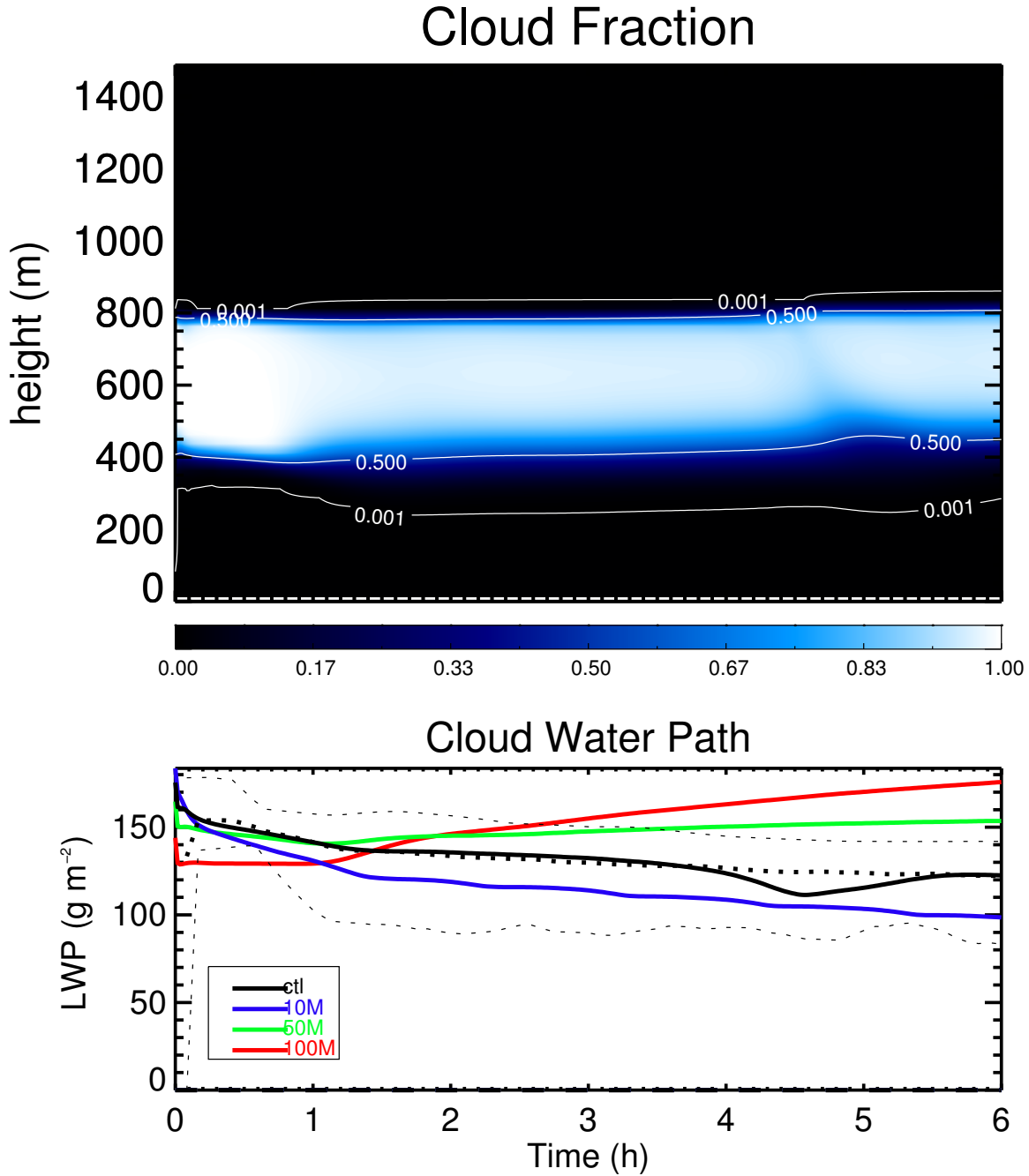


FIGURE 3.35. Time-height cross-section of the cloud fraction (top) and time-series of the cloud liquid water path (bottom) for the control and grid spacing sensitivity test runs. Lines are as in figure 3.33.

in the coarser resolutions leads to a significant overestimation, whereas the underestimated cloud liquid water content of the finest resolution run leads to an underestimation of the liquid water path, although still within the range of LES results. Another significant aspect

of the error introduced for the coarser resolution runs is the fact that the liquid water path is still increasing at the end of the simulation while it is decreasing for the finer resolution runs and for the LES models. The control simulation’s liquid water path matches the LES results the best, although it appears to be due to compensating errors, as the cloud is both too deep and too low on liquid water content compared to the LES mean.

Profiles of selected second- and third-order moments are shown in figures 3.36 - 3.39. The two finest resolution THOR runs seem to produce the correct magnitude of vertical velocity variance in the cloud layer, but all tests overestimate this quantity in the sub-cloud layer. Interestingly, although $\overline{w'^2}$ is in good agreement or slightly overestimated, the TKE profiles from THOR all show a significant underestimate of TKE throughout the boundary layer. Perhaps the single-column model framework is to blame for the underestimations of the horizontal TKE components. The profiles of the fluxes of $\overline{w'\theta'_{il}}$ and $\overline{w'q'_t}$ are particularly interesting. Although the LES models can most likely explicitly resolve the turbulent eddies that participate in the cloud-top entrainment process, a higher-order closure model like THOR most certainly cannot. Such models can only describe the statistics of what is happening at cloud top, and how well the cloud-top entrainment process is represented can be gleaned from examining these profiles. The entrainment process consists of eddies bringing warm, dry air downward and cool, moist air upwards, contributing to a negative value of $\overline{w'\theta'_{il}}$ and positive $\overline{w'q'_t}$. With figure 3.36, analysis is a little muddled by the fact that these quantities were supplied from the LES model intercomparison as “total” fluxes of θ_{il} and q_t , which includes things like the radiative fluxes and the precipitation fluxes. Regardless, one can get a reasonable idea as to how well the higher-order closure scheme is representing cloud-top entrainment by comparing these quantities with LES. For both quantities, the 10

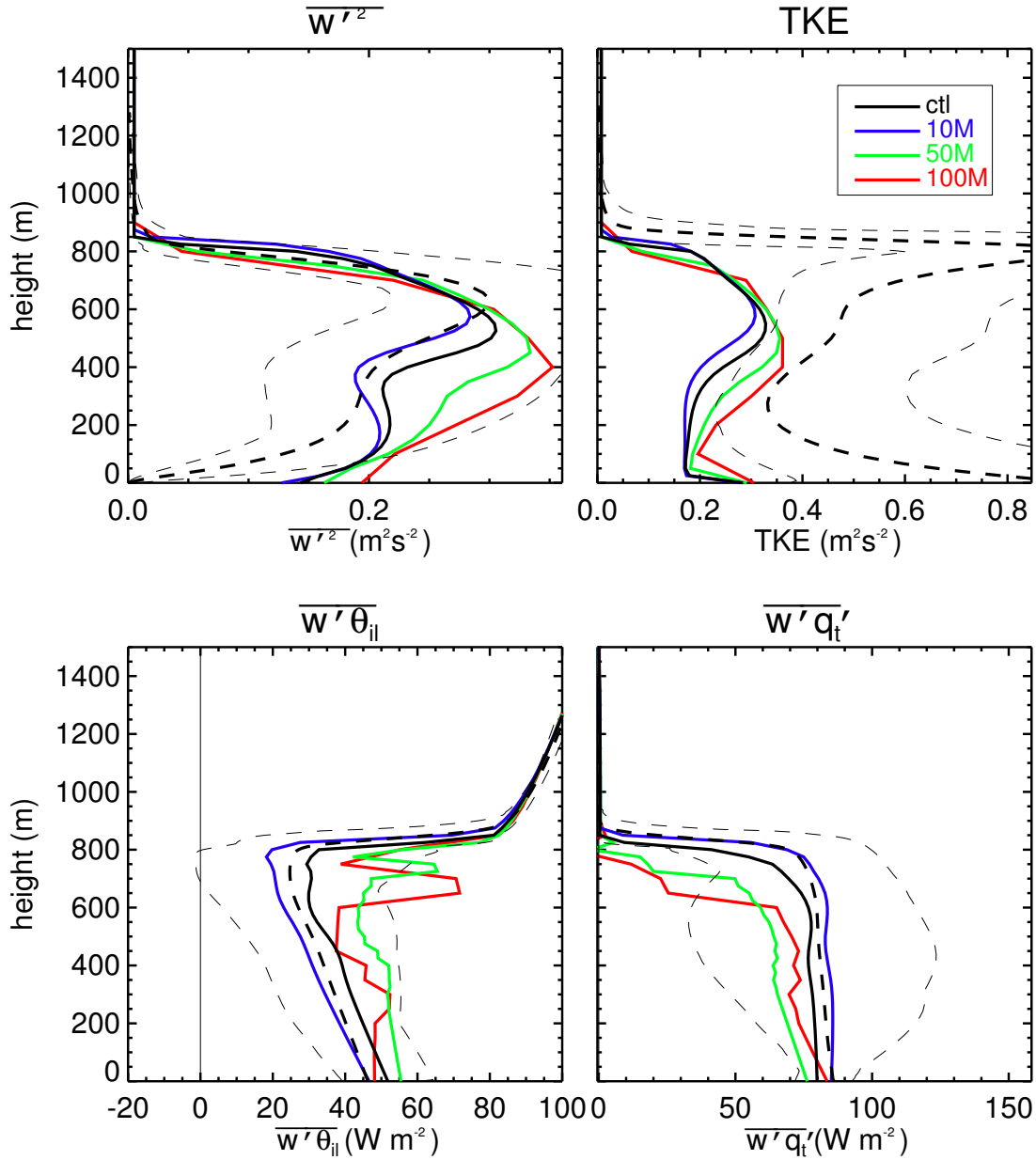


FIGURE 3.36. Mean profiles of vertical velocity variance (top left), TKE (top right), sensible heat flux (bottom left), and latent heat flux (bottom right) for the control and grid spacing sensitivity test runs. Lines are as in figure 3.33.

m and 25 m grid spacing runs seem to be doing a good job, as their profiles straddle the LES ensemble mean values. For coarser resolutions, the agreement is considerably worse, although still mostly within the range of LES models. Another measure of cloud-top entrainment is the depth of the boundary layer. For this case, the boundary layer top is defined as

the height at which the total water mixing ratio crosses 8 g kg^{-1} . Figure 3.37 shows that the boundary layer depth for the control case and for the 10 m grid spacing case rises monotonically, the 10 m case rising somewhat faster than the LES ensemble mean and the control simulation rising slightly slower than the LES ensemble mean. Both of these are consistent with the flux profiles. The coarser grid spacing test cases show little or no boundary layer deepening, suggesting the cloud top entrainment is too weak in these runs.

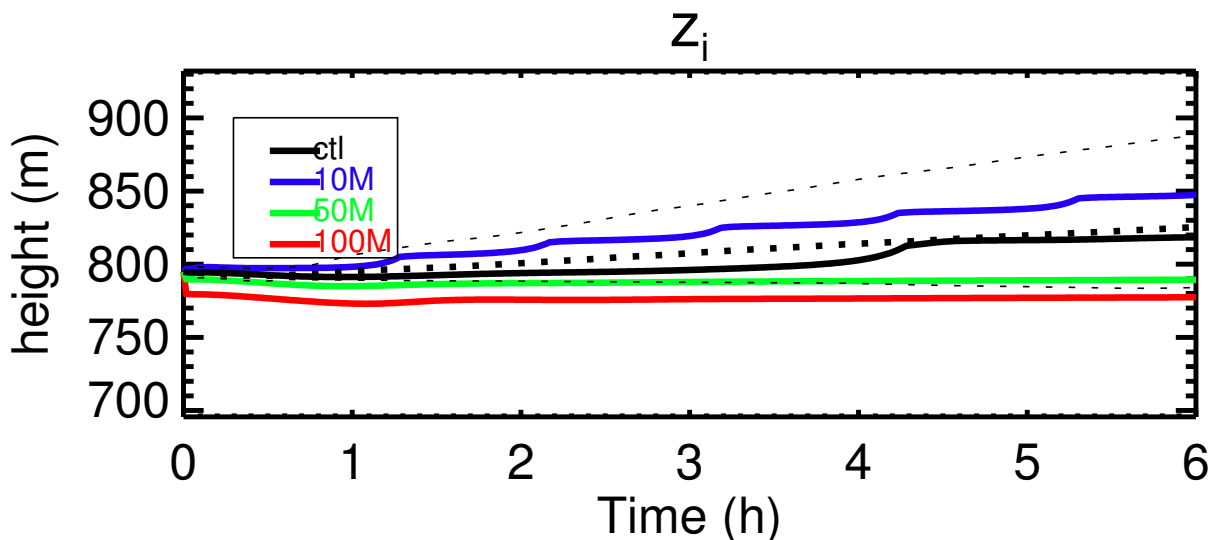


FIGURE 3.37. Time-series of boundary layer top height for the control and grid spacing sensitivity test runs. Lines are as in figure 3.33.

For the thermodynamic variances, the maximum values are underestimated compared to LES mean values. This results contrasts with the cumulus cases, where these quantities were overestimated, especially near the inversion layer. The rest of these profiles are somewhat unremarkable, although as with other turbulence quantities, the coarser resolution test runs show worse agreement. This is not surprising, however, given that the mechanical production terms for these quantities are the main producers of the variance, and these terms contain gradients of the mean quantities, which are smoothed out for coarser resolutions. The only third-order moment reported from the LES intercomparison was the vertical velocity

skewness. Interestingly, THOR underestimates this quantity through most of the boundary layer except near cloud top. In fact, THOR calculates low values of skewness for all variables throughout the column except for near cloud top. As with the second-order variances, the coarser resolutions produce reduced third-order moments compared to the finer resolutions.

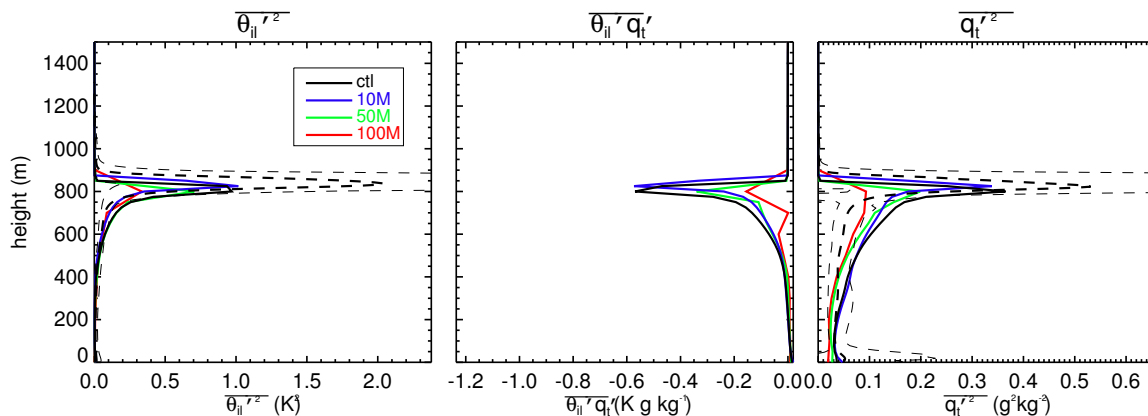


FIGURE 3.38. Mean profiles of the ice-liquid water potential temperature variance (left), ice-liquid water potential temperature-total water specific humidity covariance (center) and total water specific humidity variance for the control and grid spacing sensitivity runs. Lines are as in figure 3.33.

The diagnosed trivariate double Gaussian PDFs for mid-cloud and cloud-top points are given in figures 3.40 and 3.41, respectively. At mid-cloud, Gaussian plumes 1 and 2 are of nearly equal weight, and, with little skewness for any variable, the means of each plume are very close to the grid-cell mean for each variable. The similarity between the “updraft” and the “environmental” or “downdraft” plumes is what one would expect in a stratocumulus cloud since they are considerably more homogeneous than, say, a cumulus cloud field. The bivariate θ_{il} - q_t PDF shows that most of the diagnosed PDF is above the saturation line, and the samples chosen for the microphysics scheme are tightly packed near the mean (θ_{il}, q_t) pair, as expected. Near cloud top, recall from figure 3.39 that there is a thin strip of higher skewness values. This changes the diagnosed PDF considerably. Near the inversion layer, the thermodynamic variances are near their maximum, and the weight of plume 2 is significantly

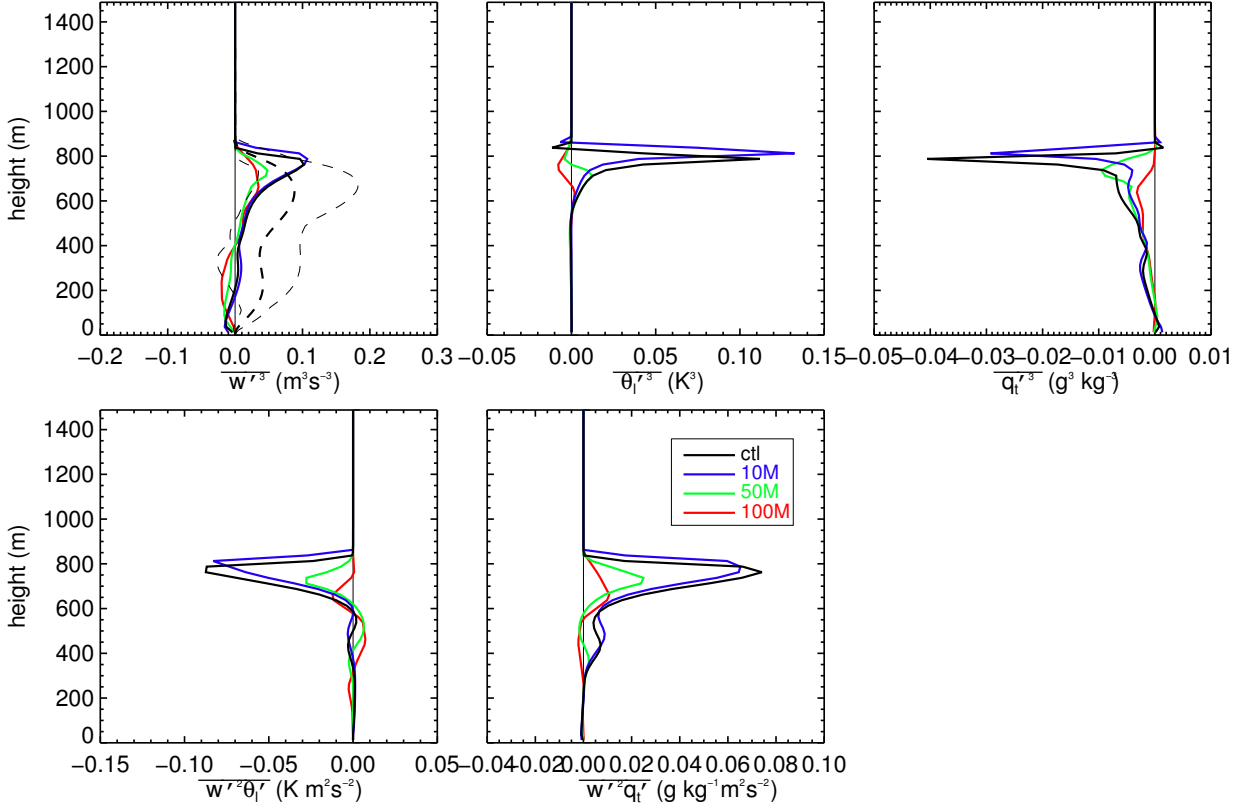


FIGURE 3.39. Mean profiles of selected third-order moments for the control and grid spacing sensitivity test runs. Lines are as in figure 3.33.

lower than the weight of plume 1 due to the higher skewness values. Although most of the bivariate θ_{il} - q_t PDF is still above the saturation line at this point, the increased variance of θ_{il} and q_t together with the covariance $\overline{\theta'_{il}q'_t}$ cause a growing fraction of the PDF to be below the saturation line. One interpretation of this is the inclusion of the above-inversion dry, warm air into the mostly cloud-filled boundary layer – a peek into the representation of the entrainment process in THOR.

Although all of the sensitivity tests run for the cumulus cases were run for this case, the simulated stratocumulus fields were almost entirely insensitive to the turbulence length scale entrainment rate and whether the third-order moments were diagnosed or prognosed. The only remaining sensitivity was to the inclusion of the latin hypercube PDF sampling

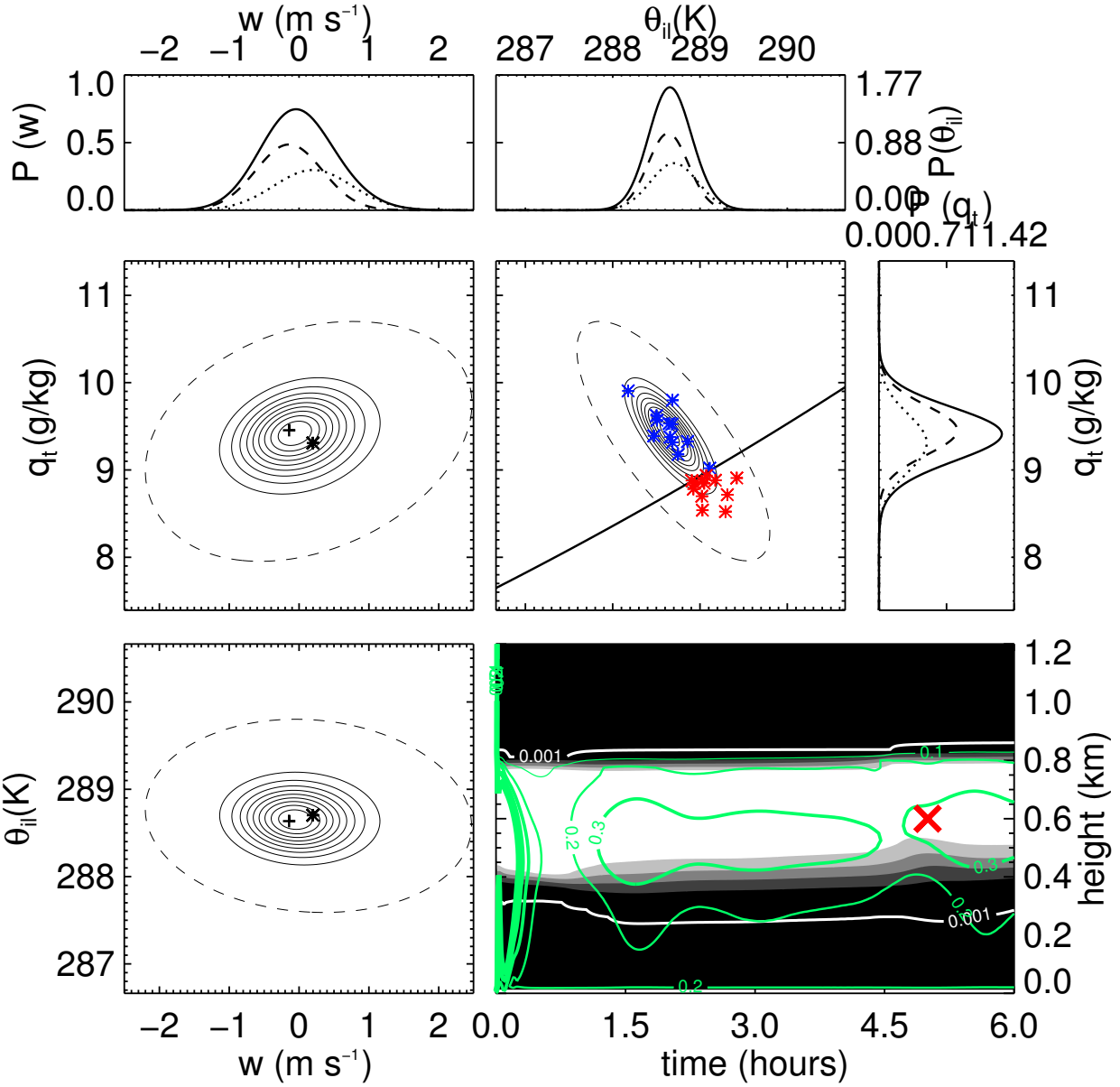


FIGURE 3.40. As in figure 3.18, but for mid-cloud for the DYCOMS control run.

algorithm. Figures 3.42 - 3.47 show results for this sensitivity test, starting with the surface precipitation rate. While the LES ensemble mean surface precipitation hovers around 5 W m^{-2} , the control simulation of THOR has considerably heavier drizzle reaching the surface, about 15 W m^{-2} . Most of the difference in these surface precipitation rates is a result of

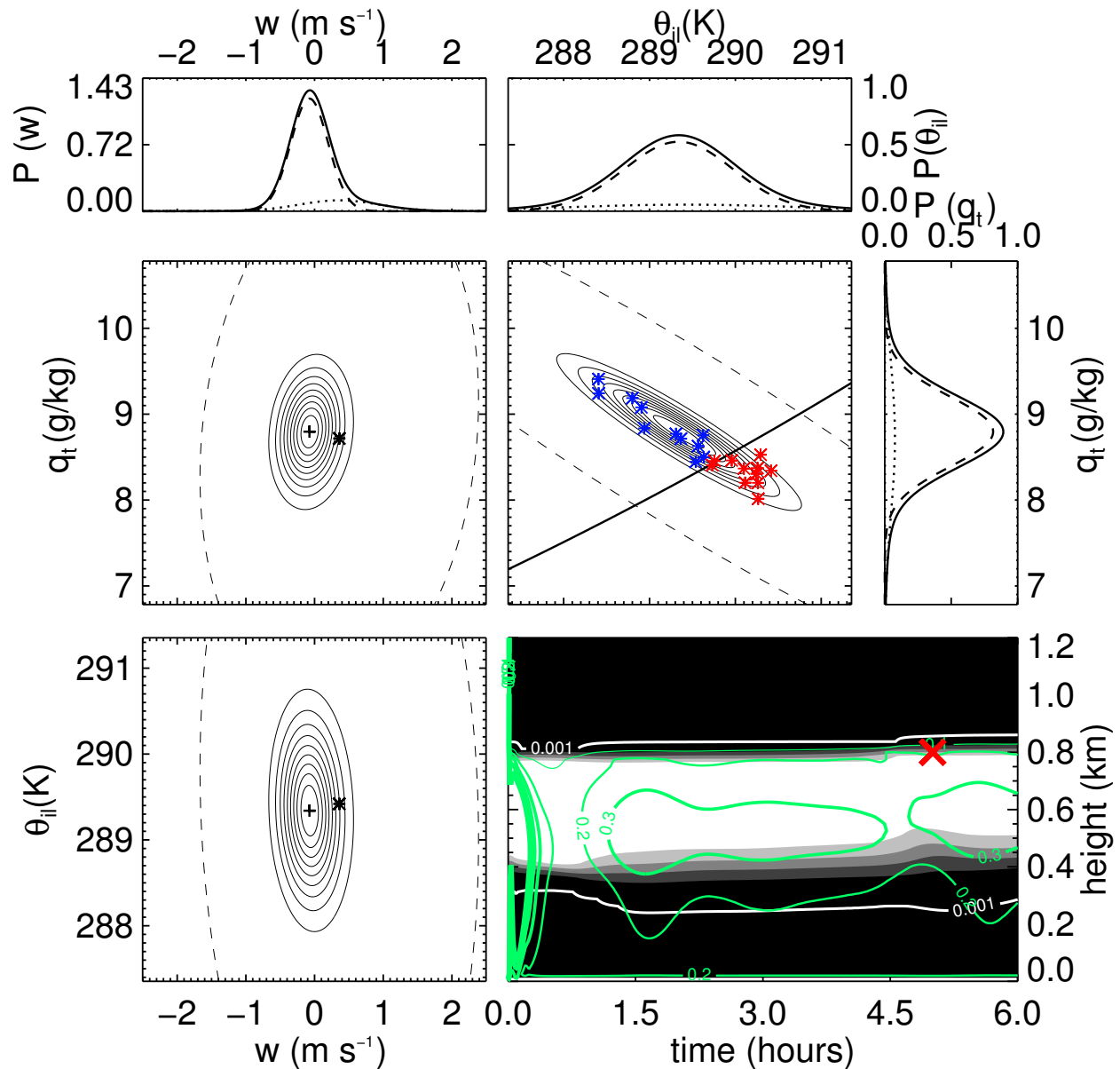


FIGURE 3.41. As in figure 3.18, but for cloud top for the DYCOMS control run.

decreased sub-cloud evaporation in the THOR simulations due to the slightly higher sub-cloud relative humidity (not shown). As with the RICO case, turning off the PDF sampling algorithm results in a complete loss of precipitation for that simulation, so this sensitivity test can be interpreted as the difference between a non-precipitating and lightly precipitating stratocumulus cloud field.

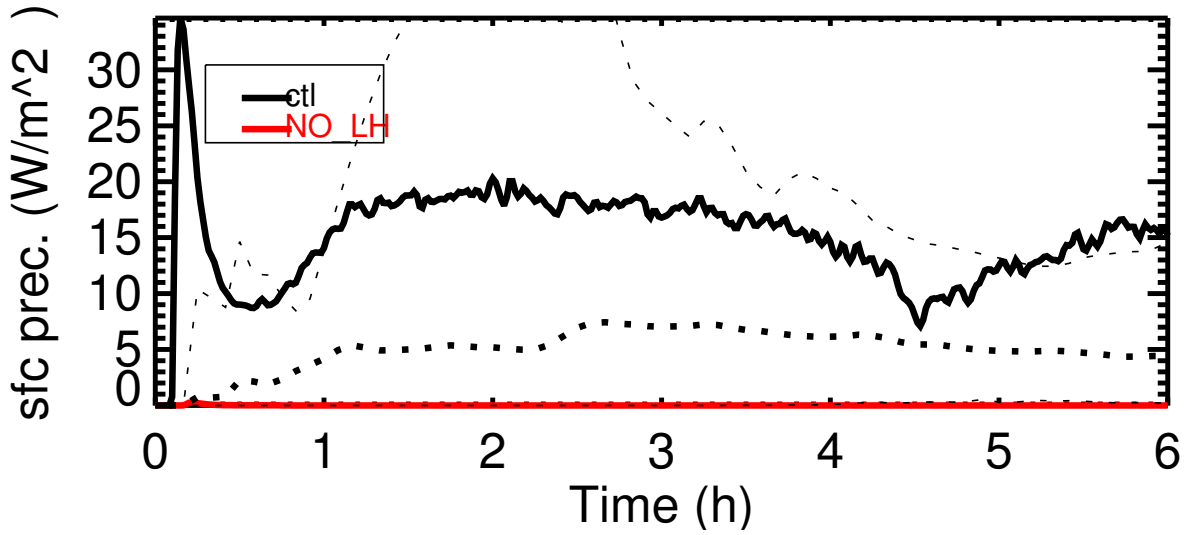


FIGURE 3.42. Time-series of the surface precipitation rate for the control and NO-LH sensitivity runs. Note that the curve for the NO-LH run is along the abscissa axis.

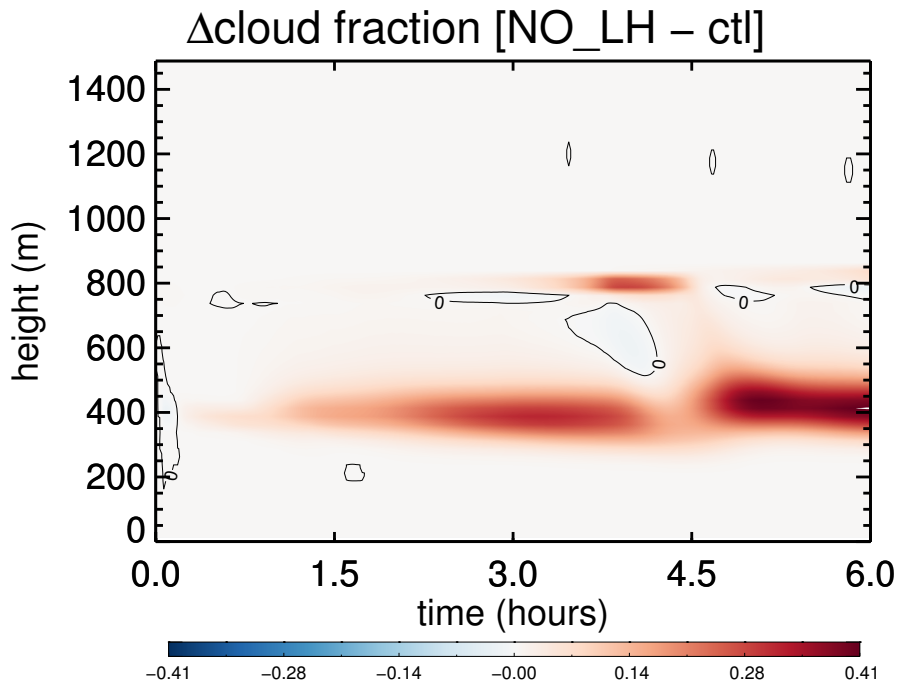


FIGURE 3.43. Time-height cross-section of the difference between the cloud fraction in the NO-LH and control simulations for the DYCOMS case.

Without precipitation to remove cloud water from the column, the cloud fraction and cloud water contents are unsurprisingly greater for the NO-LH case. Figures 3.43 and 3.44

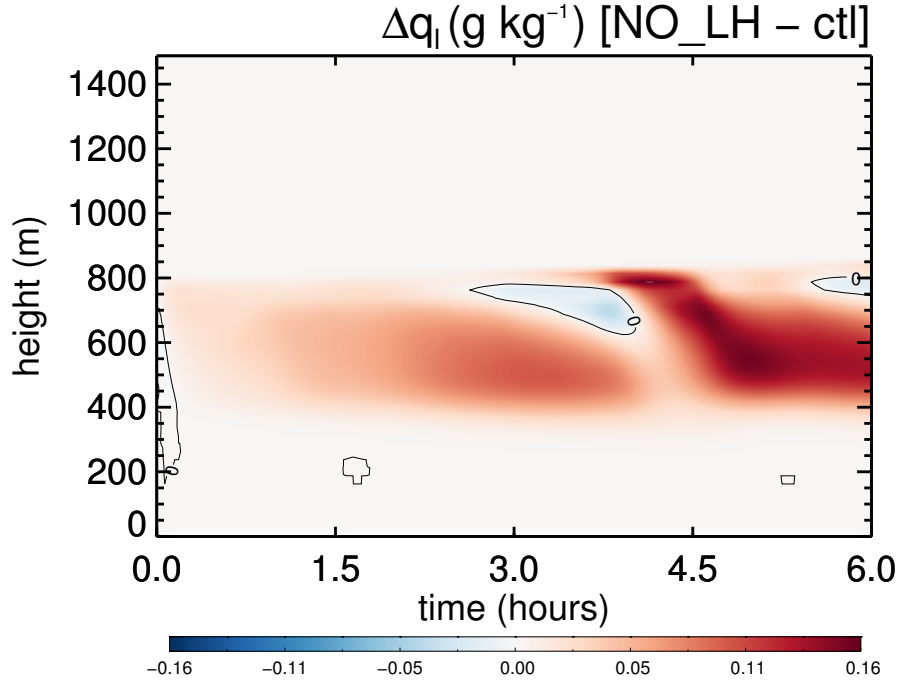


FIGURE 3.44. Time-height cross-section of the difference between the cloud water content in the NO-LH and control simulations for the DYCOMS case.

show the difference between the cloud fraction and cloud water content between the NO-LH and control simulations. The figures show that there is increased cloud water content throughout the depth of the cloud, but especially in the middle and low portions of the cloud. In addition, the lack of drizzle creates a deeper cloud, with most of the increased cloud fraction showing up at cloud base. The deeper and thicker clouds without precipitation obviously have a large effect on the cloud liquid water path, increasing it to values above the range of the LES results.

With the increased liquid water content throughout the cloud depth, one might guess that the additional latent heating would generate higher values of TKE throughout the cloud depth. According to figure 3.47, this is not the case. Instead the higher values of $\overline{w'^2}$ and TKE appear in the lower half of the cloud and sub-cloud zones. Perhaps one reason for this is that for the NO-LH case, there is no cooling caused by evaporating drizzle in the lower

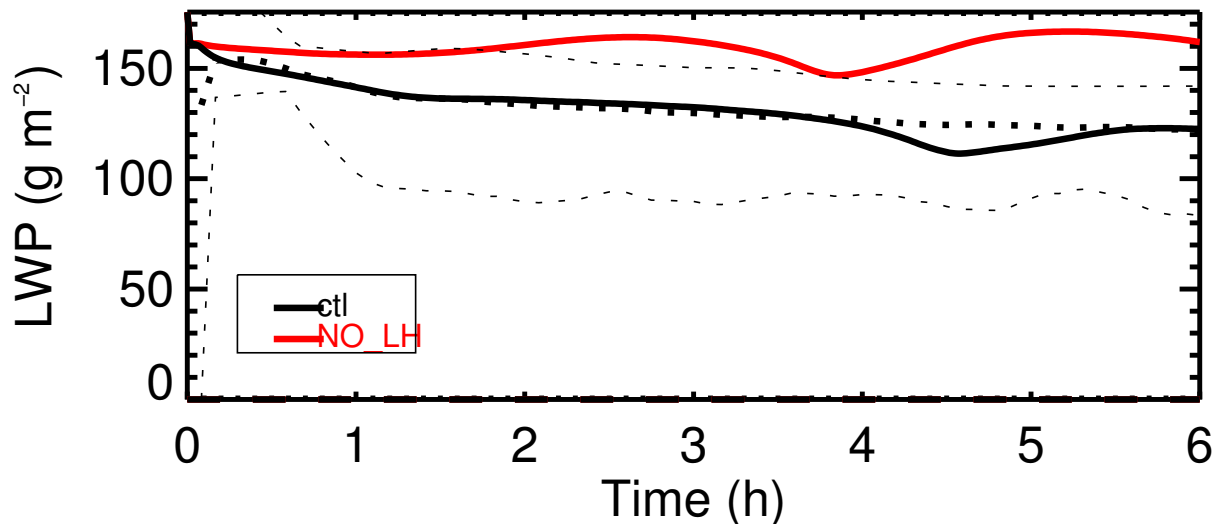


FIGURE 3.45. Time-series of the liquid water path for the control and no-latin-hypercube-sampling sensitivity test.

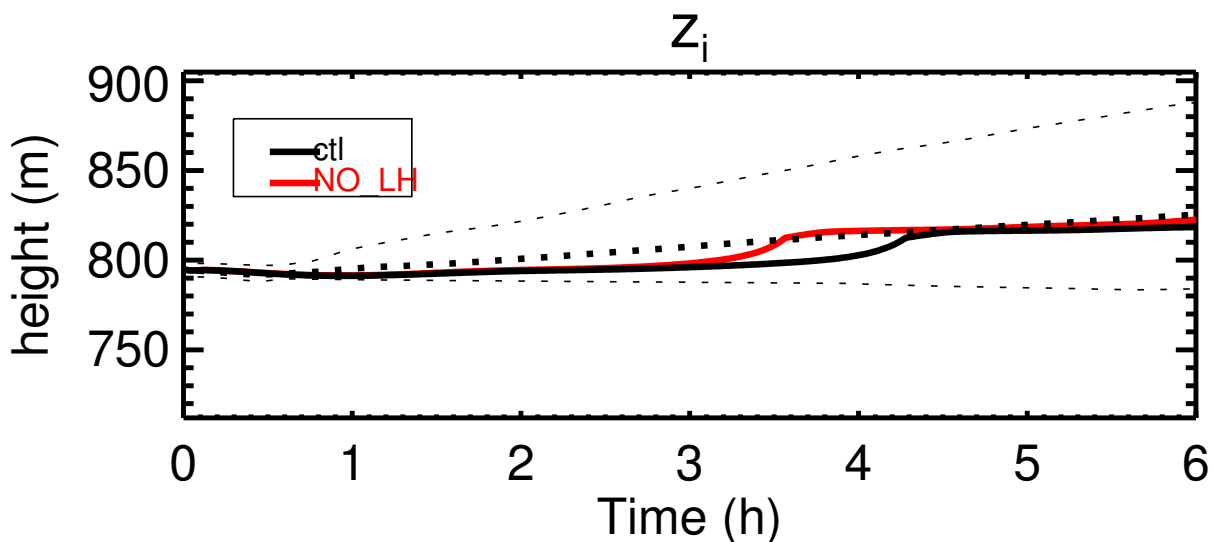


FIGURE 3.46. As in figure 3.37, but for the no-latin-hypercube-sampling sensitivity test.

cloud and sub-cloud layers, slightly decreasing the static stability there in comparison to the control case, and leading to higher-energy turbulent eddies. Although the thermodynamic flux profiles show increased magnitudes for the NO-LH run, the cloud-top entrainment as gauged by the boundary layer depth only increases slightly. This is likely the result of the

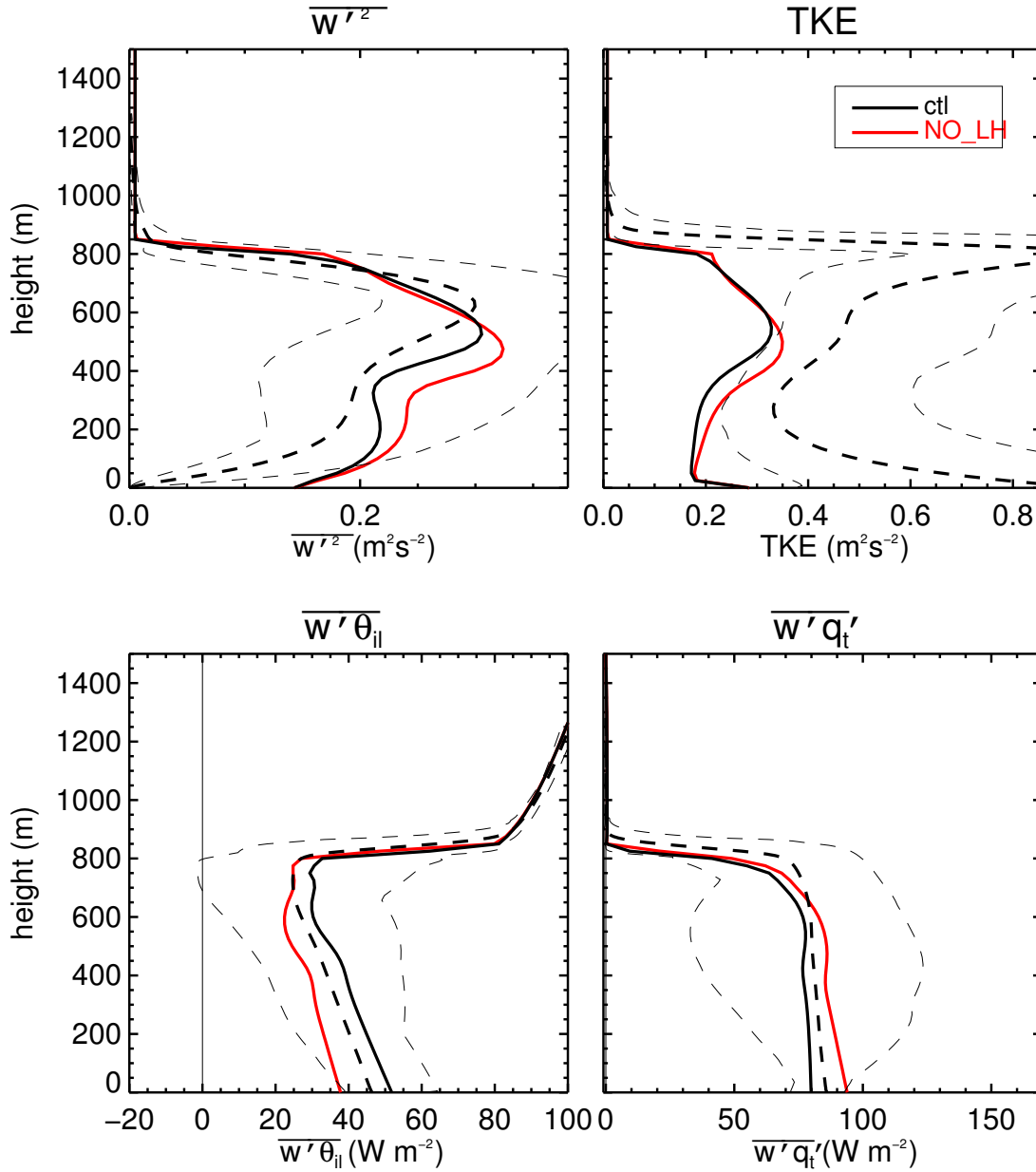


FIGURE 3.47. As in figure 3.36, but for the no-latin-hypercube-sampling sensitivity test.

fact that the increased turbulence generated by the increased latent heating occurs away from the cloud-top inversion.

3.2.2. MPACE CASE. While the MPACE test case features stratocumulus clouds, the simulated atmosphere that generates the clouds is drastically different than for the DYCOMS

case. The MPACE field campaign took place in the Beaufort Sea, between a region of sea ice to the north and the north slope of Alaska to the south. Synoptic conditions featured cold northeasterly winds under a high pressure system blowing over the open ocean. The observed stratocumulus clouds were organized in “cloud streets,” and the boundary layer was well-mixed by vigorous turbulence generated both by high surface fluxes and strong cloud-top radiative cooling. Although the temperature at cloud top was considerably below freezing (around -15°C), the observed clouds contained more supercooled water than ice and generated significant quantities of precipitation, mainly in the form of snow. As mentioned in the model intercomparison paper written by Klein et al. (2009), this case was particularly challenging for most models to simulate with accuracy due to the fact that the partitioning between cloud water and ice in arctic stratocumulus clouds is extremely complex. The amount of ice in the cloud is only a weak function of temperature and depends more on the number, size, and chemical composition of ice nuclei present.

The case simulated here is based on the observational period that featured a single layer of stratocumulus clouds, known as the “B” period within the MPACE study. As with previous cases, the model is initialized with given profiles of θ_u , q_t , u , and v and is forced with prescribed surface fluxes, large scale horizontal advection tendencies, and constant prescribed subsidence. Rather than using a large-scale pressure gradient, winds are relaxed back to the initial profile. A major difference between this case and the others discussed so far is that this case uses an active radiation scheme rather than prescribed radiation or radiative heating rates. The control simulation uses a 1 s time step and a 50 m grid spacing. The simulation is run for 12 simulated hours with a domain of 3000 m. Although both single column models and three-dimensional models participated in the MPACE study,

THOR's results are only compared with the LES models in the following plots, and each plot represents averages over the last 3 hours of the simulation. The only sensitivity tests discussed for this case are the grid-spacing, omission of PDF sampling for the radiation scheme, and the omission of ice processes tests, since the other tests demonstrated little or no sensitivity.

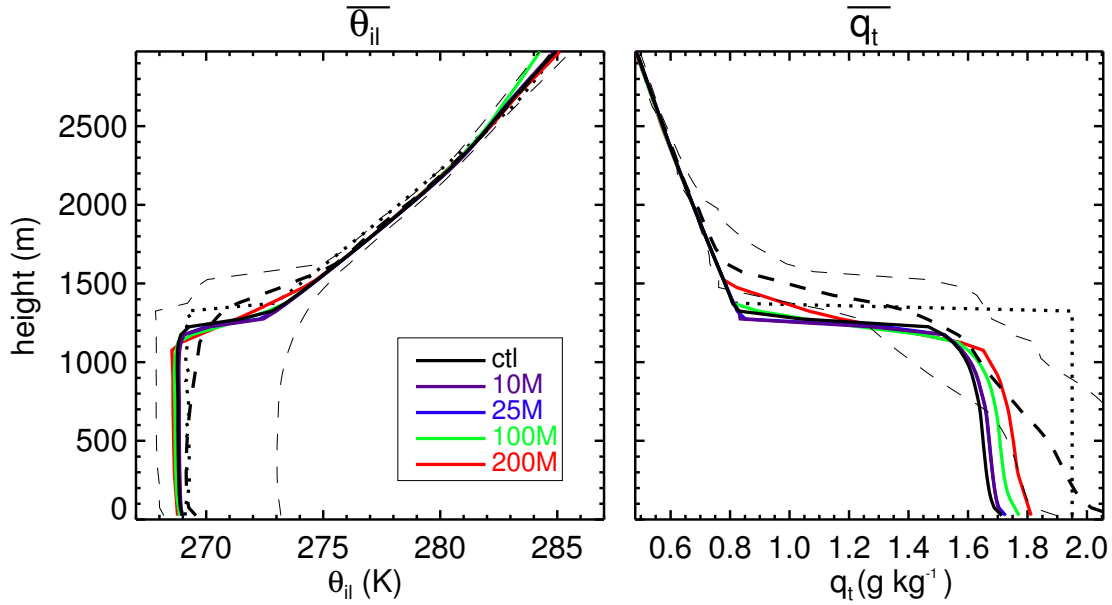


FIGURE 3.48. Mean profiles of θ_{il} and q_t for the last three hours of the control and grid sensitivity test runs. As in the previous cases, solid lines represent output from THOR with the black denoting the control run and colors denoting sensitivity test runs. Black dashed lines represent the LES ensemble results, with the thick dashed line denoting the LES ensemble mean, and the thin dashed lines representing the range of LES ensemble results. The thin black dotted line represents the initial conditions.

The initial and steady-state thermodynamic profiles are shown in figure 3.48. They are initially perfectly well-mixed up to the inversion. By the end of the simulation, the LES models diffuse the initially sharp inversion and develop significant gradients in the boundary layer, especially in the moisture field. THOR, by comparison, tends to keep a sharper cloud-top inversion and keeps the profiles more well-mixed. The fact that the moisture profiles from the THOR model are better mixed probably means that there is stronger turbulence in

the mixed-layer in this model compared to the LESs, although turbulence statistics are not included in the LES model output for this case for comparison. In addition, THOR predicts a slightly drier boundary layer than the LES models, by about 0.3 g kg^{-1} in the sub-cloud layer and by a significant amount in the inversion layer. Since the surface latent heat fluxes, subsidence, and horizontal advection terms are the same for all models, this suggests that THOR must be entraining dry air at a higher rate or perhaps precipitating at a higher rate.

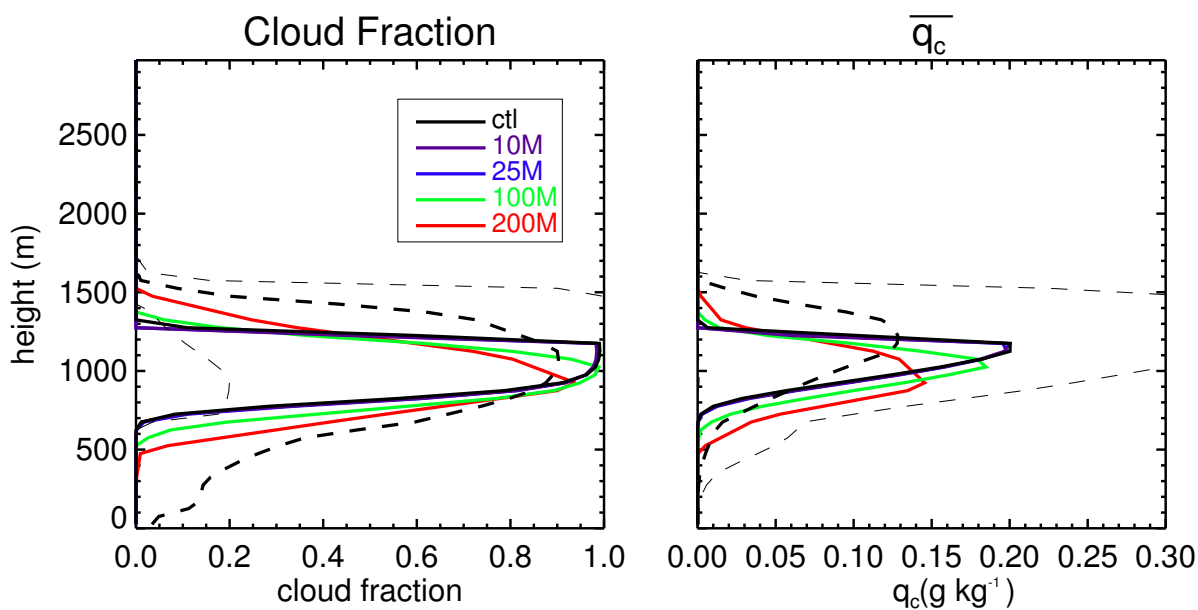


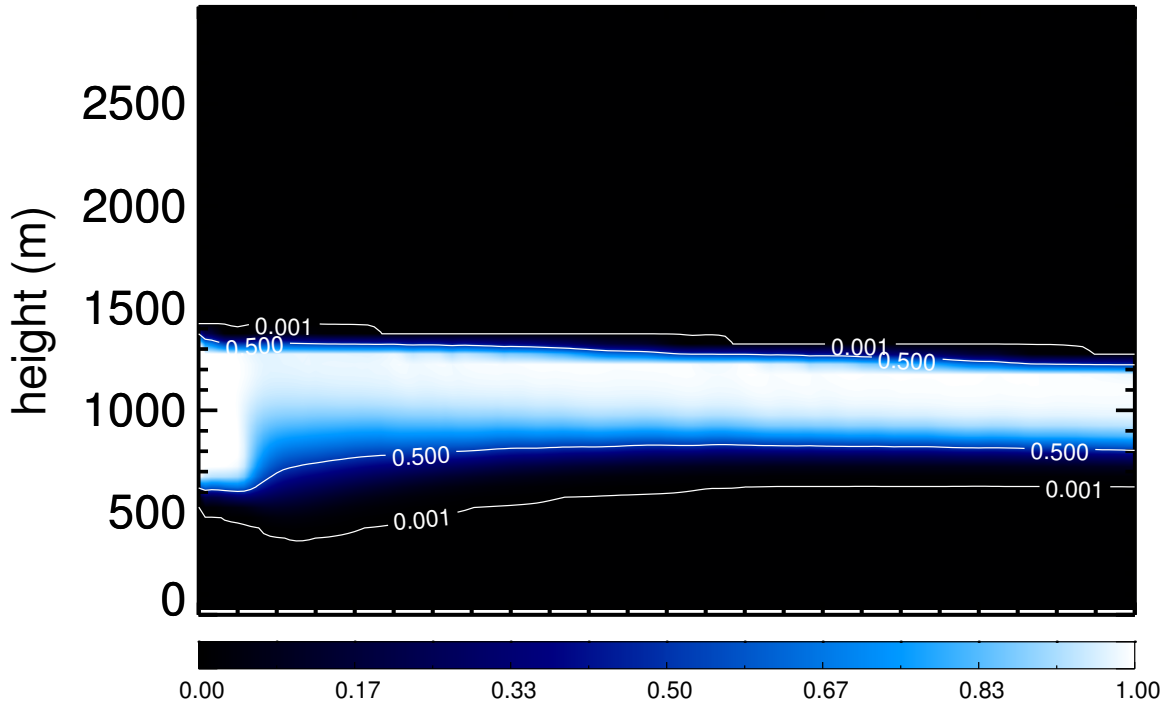
FIGURE 3.49. Mean profiles of cloud fraction (left) and q_l for the control and grid spacing sensitivity test runs for the MPACE case. Lines are as in figure 3.48.

The cloud structure for the control and grid-spacing sensitivity tests are shown in figures 3.49 and 3.50. There is virtually no difference among runs with grid-spacing 50 m and below with all of these models simulating a roughly 600 m thick stratocumulus cloud with a maximum cloud water content of about 0.2 g kg^{-1} . Coarser grid spacing runs simulate slightly deeper clouds with a lower peak water content. Interestingly, the LES ensemble mean produces some cloud fraction all the way to the surface. Unlike the DYCOMS case,

the LES models produce deeper clouds than THOR, a consequence of the LES models predicting a much moister sub-cloud and inversion layer.

The cloud liquid and ice water paths in figure 3.50 paint an interesting picture. The colored solid and dashed lines denote the liquid and ice water paths from the THOR runs, respectively. The red and blue dotted lines denote the liquid and ice water paths for LES models, respectively. The proportion of the simulated cloud that is ice in THOR's simulations is about 70% versus less than 10% in the LES models (which agree better with the available observations). This highlights a key weakness of THOR's microphysics scheme. Klein et al. (2009) explain that there are four basic types of microphysics schemes in the models that participated in this case. The first category is representative of THOR's scheme (which is identical to the SAM LES model), called a "single-moment with T-dependent partitioning" scheme. Recall that THOR diagnoses the total cloud condensate mass and partitions the cloud water into liquid and ice with a function only dependent on temperature. The other three categorizes of microphysics schemes include the so-called "single-moment with independent liquid and ice," "double-moment" that predicts both liquid and ice mass and droplet number concentrations, and "bin microphysics" that predict the evolution of different size classes of droplets. All three of these types of schemes are more complex and are capable of partitioning cloud liquid water and ice in a more realistic way that takes ice nuclei into account. The fact that THOR predicts an ice-dominated cloud instead of a supercooled liquid-dominated cloud has important repercussions. First, the ratio of ice to liquid in clouds plays a key role in determining their albedo and therefore processes like cloud-top radiative cooling and the net cloud radiative forcing that is so important for the climate. Second, precipitation processes are significantly different in ice clouds versus liquid clouds. Precipitation

Cloud Fraction



Cloud Water Path

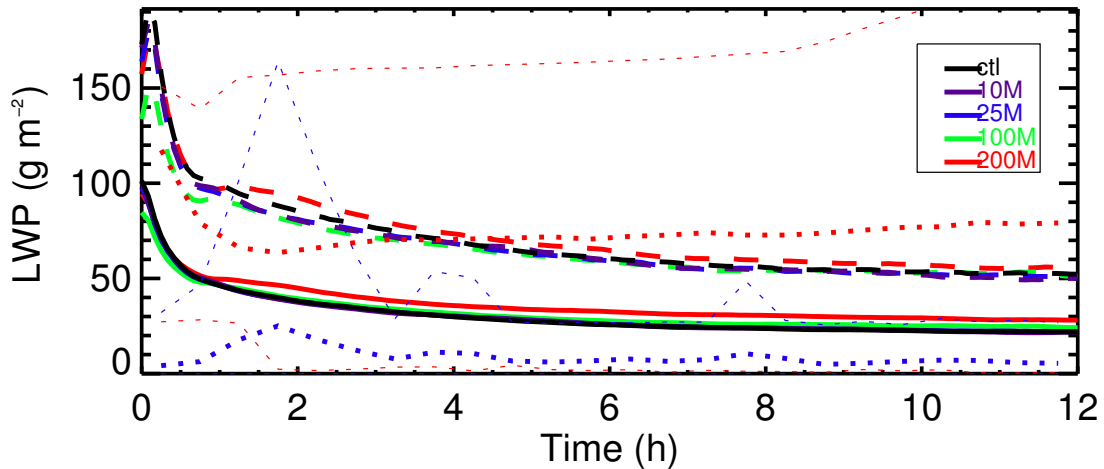


FIGURE 3.50. Time-height cross-section of the cloud fraction for the control run (top) and the time-series of cloud water path (bottom) for the control and grid spacing sensitivity runs. Solid black and colored lines denote THOR's liquid water path output, whereas black and colored dashed lines denote the ice water path output from THOR. The red dotted lines represent the liquid water path values of the LES ensemble, with the thicker dots denoting the mean and the thinner dots denoting the range. The blue dotted lines are for the ice water path for the LES ensemble.

tends to be generated more readily and in higher amounts in ice clouds versus liquid clouds. In fact, the differences in THORs simulations compared to the LES models can largely be explained by the fact that THOR produces precipitation-heavy ice-dominated clouds that end up drying out the boundary layer (in a relative sense) and producing a thinner cloud deck.

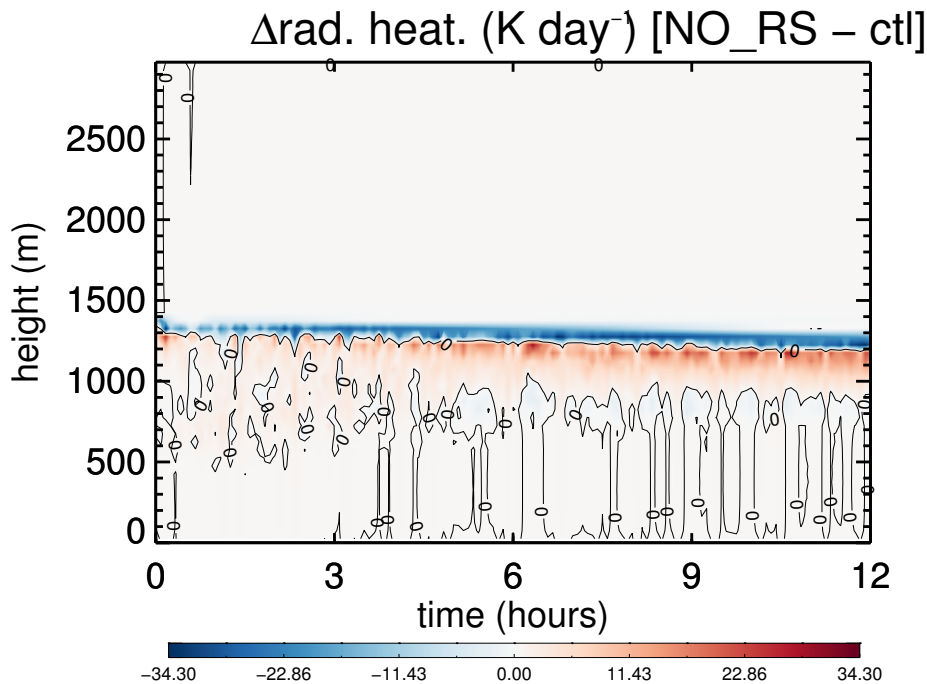


FIGURE 3.51. Time-height cross-section of the difference between radiative heating rates for the no radiation PDF sampling (NO-RS) and control simulations.

Next, THOR’s sensitivity to omitting the PDF sampling procedure (denoted NO-RS) for the radiation scheme will be discussed. The difference between radiative heating rates calculated with and without the PDF sampling is shown in figure 3.51. The major difference is that in the absence of PDF sampling, the cloud top radiative cooling is more temporally consistent and slightly higher in the column. The PDF sampling scheme allows for occasional random temporary “gaps” in the stratocumulus cloud where cloud-top radiative cooling is

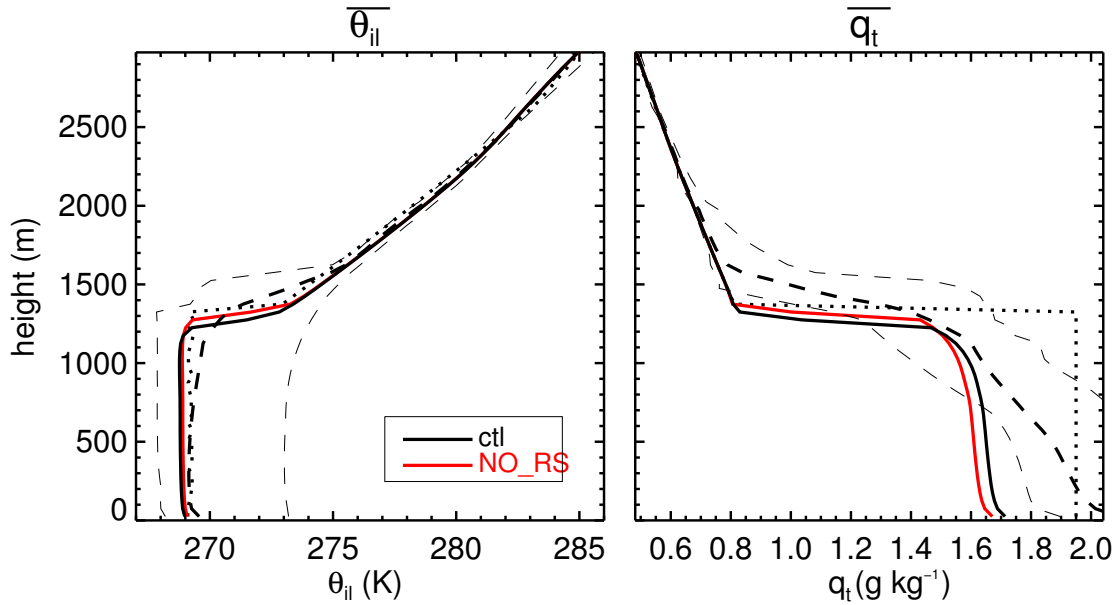


FIGURE 3.52. As in figure 3.48, but for the no-radiation-sampling sensitivity test.

reduced, weak low- and sub-cloud heating is weaker, and weak radiative cooling is allowed further down in the boundary layer. Such gaps in stratocumulus clouds that alter their radiative properties are present in nature as well. The combined effect of using the PDF sampling algorithm is to slightly weaken the cloud radiative forcing and radiatively-driven turbulence. As a consequence, in the NO-RS simulation where radiative forcing is stronger, cloud-top entrainment is slightly stronger, creating a slightly warmer and drier boundary layer, and a stratocumulus cloud that is slightly higher in the column that maintains its peak liquid water content and cloud fraction (figures 3.52 and 3.53).

The last sensitivity test to be discussed in conjunction with this case is the omission of ice processes. Figures 3.54 - 3.57 show that the simulated atmosphere with ice processes neglected is considerably different than the control case that includes ice processes. Without ice processes, the simulated cloud is almost twice as deep with over twice the amount of cloud water content (all liquid, of course). The much thicker cloud creates a strong response

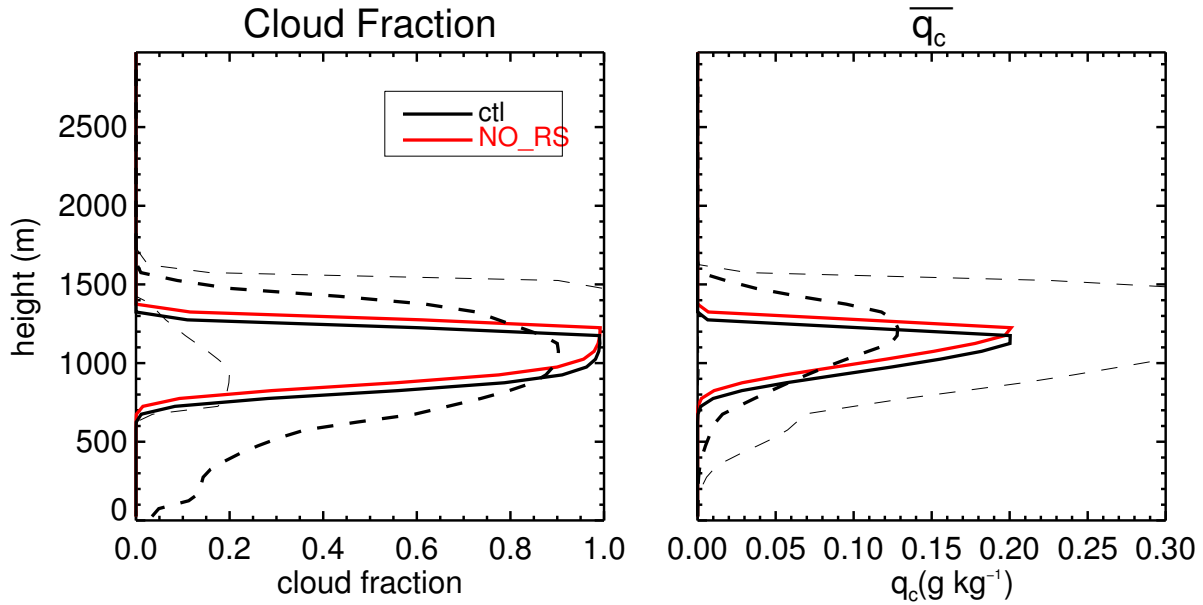


FIGURE 3.53. As in figure 3.49, but for the no-radiation-sampling sensitivity test.

in the radiative cooling, modifying the well-mixed θ_{il} profile by over 1 K. The boundary layer moisture is nearly 0.5 g kg^{-1} higher, especially near the surface, and the profile is less well-mixed in the cloud layer. The liquid water path in figure 3.56 continues to monotonically increase throughout the simulation and is about four times the cloud water path in the control case by the end of the simulation.

How does the omission of ice account for such a large difference in the simulated atmospheres? Recall from previous paragraphs that the control THOR simulation generates an ice-dominated cloud where precipitation is generated in relative copious amounts by the Bergeron-Findeisen process. Without ice, this relatively prolific production of precipitation is shut off and the relatively inefficient warm rain process produces very little precipitation in comparison (see figure 3.57). With continued strong surface latent heat fluxes, moisture continues to build up in the boundary layer, producing thick, all-liquid clouds. The same sensitivity test was performed with the participant models in the intercomparison project

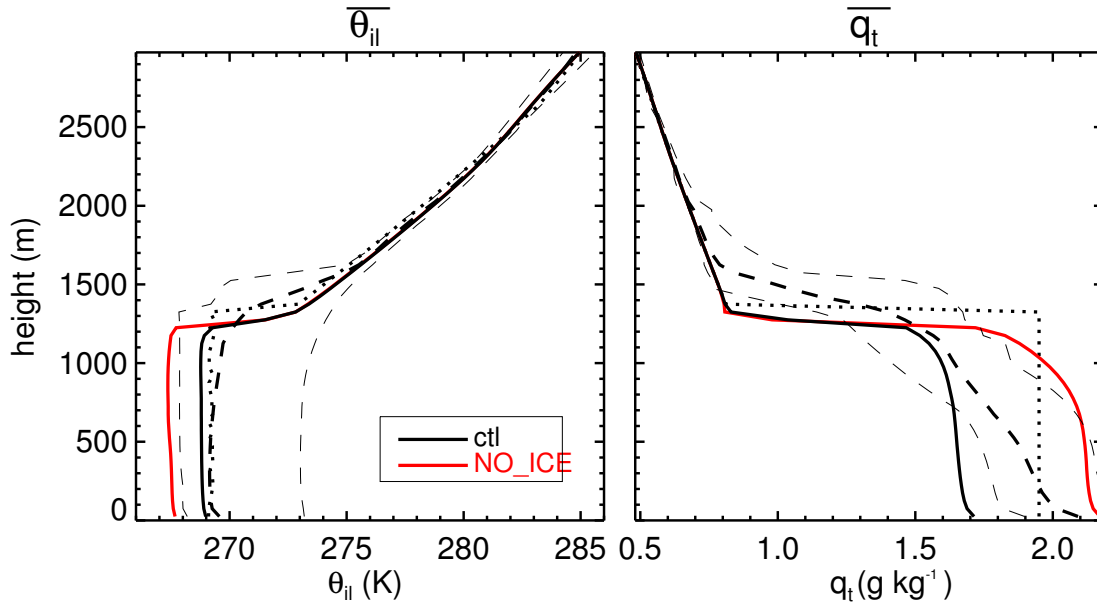


FIGURE 3.54. As in figure 3.48, but for the no-ice sensitivity test.

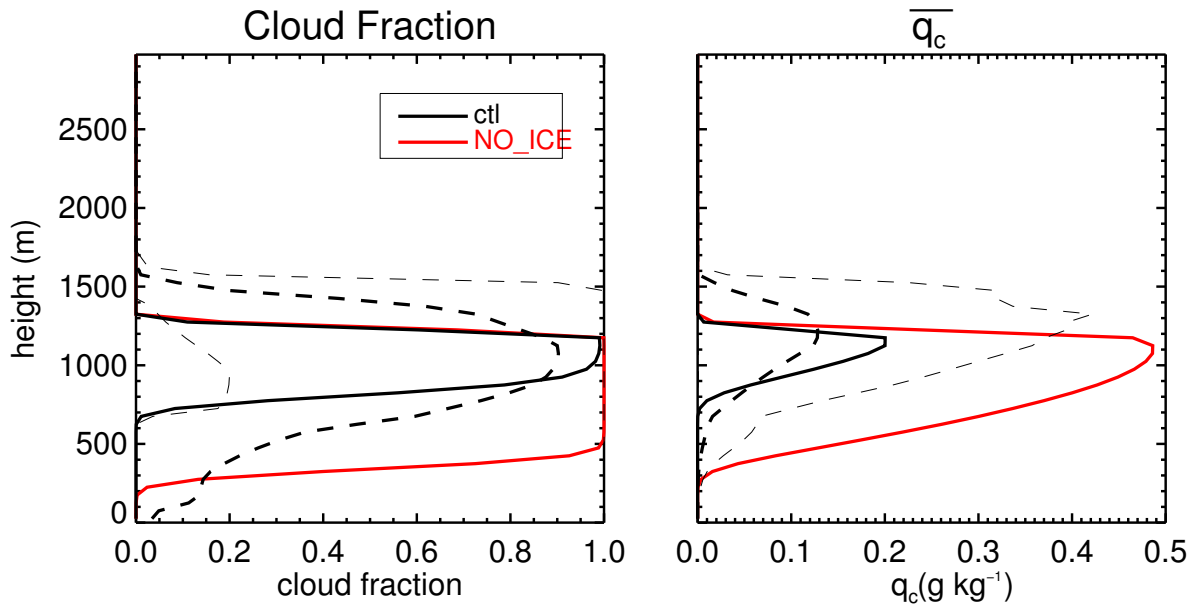


FIGURE 3.55. As in figure 3.49, but for the no-ice sensitivity test.

of Klein et al. (2009). They note that the same mechanism produces high sensitivity to the omission of ice processes, especially in models that produced ice-dominant clouds in the control simulation.

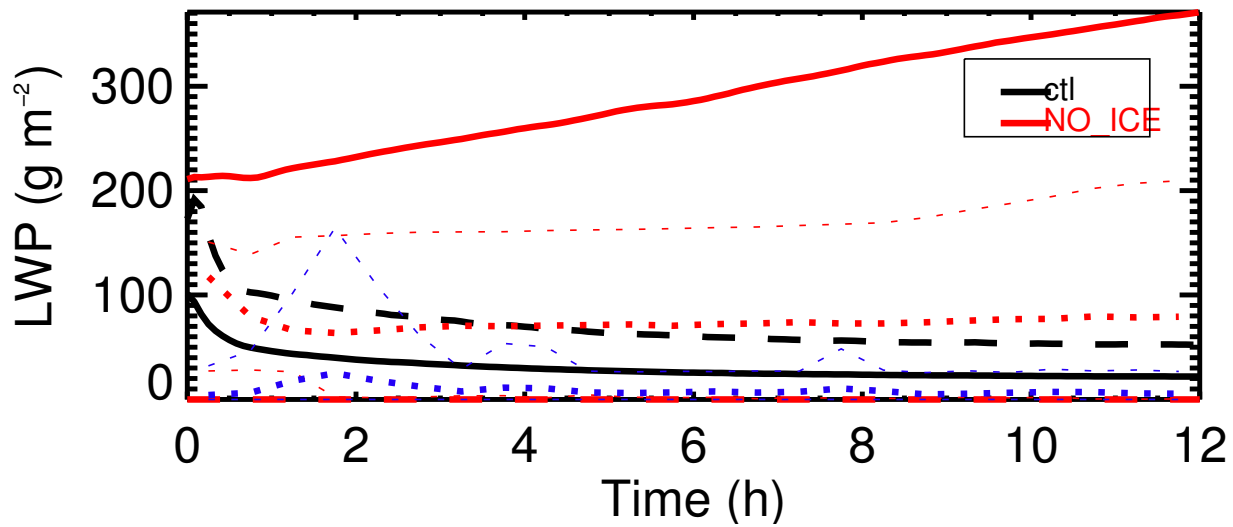


FIGURE 3.56. Time-series of the cloud water path for the control and no-ice sensitivity test. Lines are as in figure 3.50.

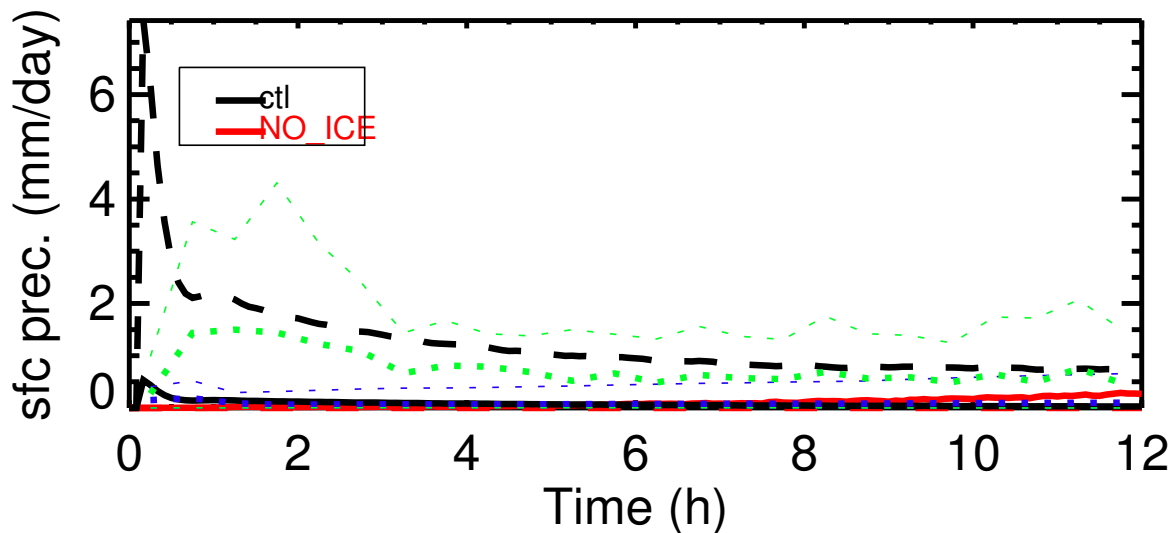


FIGURE 3.57. Time-series of surface precipitation rate for the control and no-ice sensitivity test. In this plot, solid lines denote surface rain and dashed lines denote combined surface snow and graupel. The green dotted lines denote LES ensemble surface rain and blue dotted lines denote LES ensemble surface snow, with the thickest dotted lines representing the LES ensemble means.

3.3. TRANSITIONAL CASE

The maritime subtropical high pressure systems off of the western coasts of continents are a prominent feature of the Earth's climate system. These expansive regions of subsidence

compose the sinking arm of a planetary-scale direct thermal circulation, known as the Hadley cell, that is driven by the maximum in solar heating and subsequent deep convection near the equator. As the air descends it turns equatorward to complete the direct circulation and is turned to the west by the Coriolis force to create the trade winds. In a Lagrangian sense (following the air motion), the entire air mass that makes up the massive stratocumulus fields is advected westward and equatorward by these trade winds. As the air mass moves, it is constantly modified by the sea surface below and the weakening subsidence as it heads equatorward. Eventually, the air mass is no longer conducive to producing stratocumulus clouds. The cloud cover undergoes a complicated transition to the much sparser cloud arrangement of shallow cumuli. The precise placement and timing of this transition is of critical importance for the climate system. If the transition takes place sooner (in a Lagrangian sense), the relative area of the much thicker and reflective stratocumulus clouds is reduced, eliminating area that had previously contributed to a strongly negative cloud radiative forcing. Of course, the converse is true as well. From a climate modeling standpoint, it is thought that the lack of skill in simulating this transition contributes to one of the greatest sources of error in climate simulations. The work of Teixeira et al. (2011) demonstrates that there is a substantial spread in the ability of current state-of-the-art climate models to predict this all-important transition with accuracy.

The physical mechanisms responsible for the transition are still an active area of research, but a good review of the current state of knowledge can be found in chapter six of Cotton et al. (2011). The two main drivers of the transition from stratocumulus to cumulus are thought to be decreasing subsidence and increasing SSTs. All things being equal, decreasing subsidence allows the boundary layer to deepen, and, in conjunction with rising SSTs, the boundary

layer eddies become more buoyant and energetic. The higher-energy eddies, combined with a weakening cloud-top inversion due to decreased subsidence, entrain more warm, dry free tropospheric air into boundary layer, eventually creating a minimum in the buoyancy flux below cloud base and a layer of slightly higher static stability there as well. This layer of higher stability decouples the boundary layer, effectively dividing it into two dominant areas of eddy activity with limited transfer between: the cloud layer and the surface-based layer. The decoupling effectively cuts off the supply of moisture to the stratocumulus deck, and the cloud-top radiative and evaporative cooling driven circulation within the cloud continues to entrain dry air from above, evaporating its liquid water. All the while, the surface-based eddies are capped by the stable layer. Periodically, driven by surface fluxes, some surface-based eddies garner enough energy to break through the stable layer, condensing as they go, creating a cumulus-under-stratocumulus boundary layer. The strong eddies found in the cumulus clouds reach from the surface to the boundary layer top, depositing episodic injections of moisture into the stratocumulus deck, but also penetrating the inversion layer, increasing the rate of dry air entrainment. Between the surface moisture supply being diminished and the increased entrainment of dry air into the stratocumulus deck, the cloud thins and the stratocumulus circulation is further weakened by the reduction in cloud-top radiative and evaporative cooling. Eventually, the combined processes have evaporated the entire stratocumulus deck, leaving nothing but the shallow cumulus layer.

It is with this background that the ASTEX (Atlantic Stratocumulus Transition Experiment) Lagrangian stratocumulus-to-cumulus test case was developed. Although previous model intercomparisons have also used data from ASTEX, the current case is the first time

that it has been done with large-domain LES models as participants for a 40-hour simulation that spans several of the research flight observational periods. The goal of the joint GASS/EUCLIPSE² project was to be able to study the transition in detail with state-of-the-art LES models and single-column model (SCM) versions of current operational numerical weather prediction and climate models. To that end, the case setup follows the previous ASTEX cases to a large extent, featuring a Lagrangian framework where large-scale horizontal advection can be neglected and the subsidence rate and SST are allowed to change relatively quickly. Initial profiles of θ_{il} , q_t , and u and v are supplied and are representative of a well-mixed stratocumulus boundary layer. The surface fluxes are calculated by the individual models with a SST that rises 4 K in the 40 hour simulation as shown in figure 3.58. Other forcings include subsidence that weakens linearly throughout the simulation and geostrophic winds representative of a large-scale pressure gradient. The diurnal cycle is included, and models are expected to use their own radiation schemes to calculate radiative transfer. Full details can be found in the LES intercomparison paper (van der Dussen et al. 2013). The control simulation of THOR uses 25 m grid spacing, a 1 s time step, and a 3000 m domain.

The time series of the EIS is shown in figure 3.58 and the time-height cross-section of the cloud fraction for the control simulation together with the time-series of liquid water path for the grid-spacing sensitivity test is shown in figure 3.59 to give the reader a quick idea of how the simulation evolves. The EIS goes from a high of about 4 K at the beginning of the simulation to a low of about 0.5 K by the end of the simulation, moving almost in lock-step with the increasing SST. Given this decrease in EIS, one would expect via the cloud amount

²GASS stands for the Global Atmospheric Systems Study and EUCLIPSE stands for European Union Cloud Intercomparison, Process Study and Evaluation

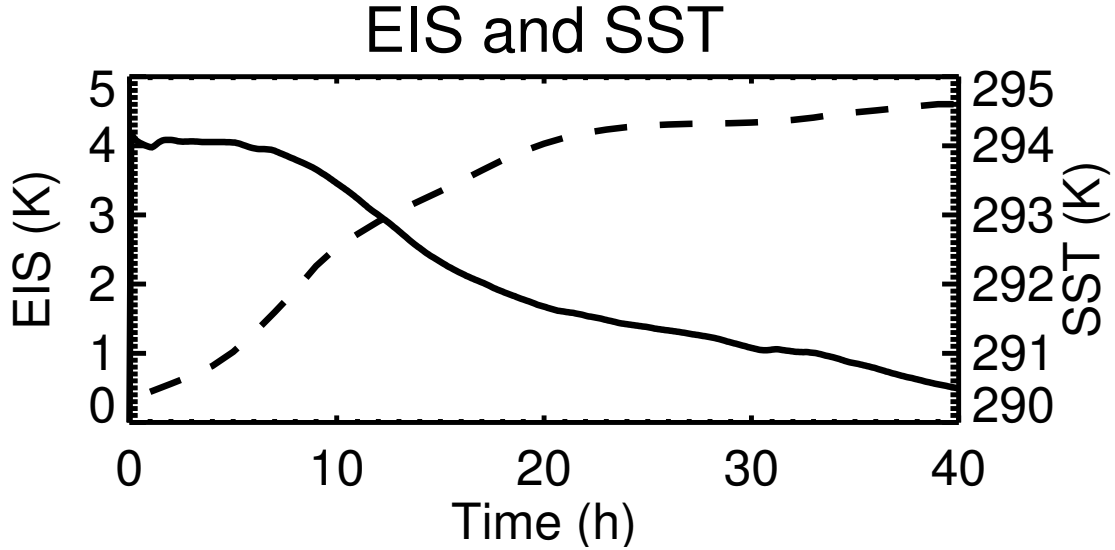
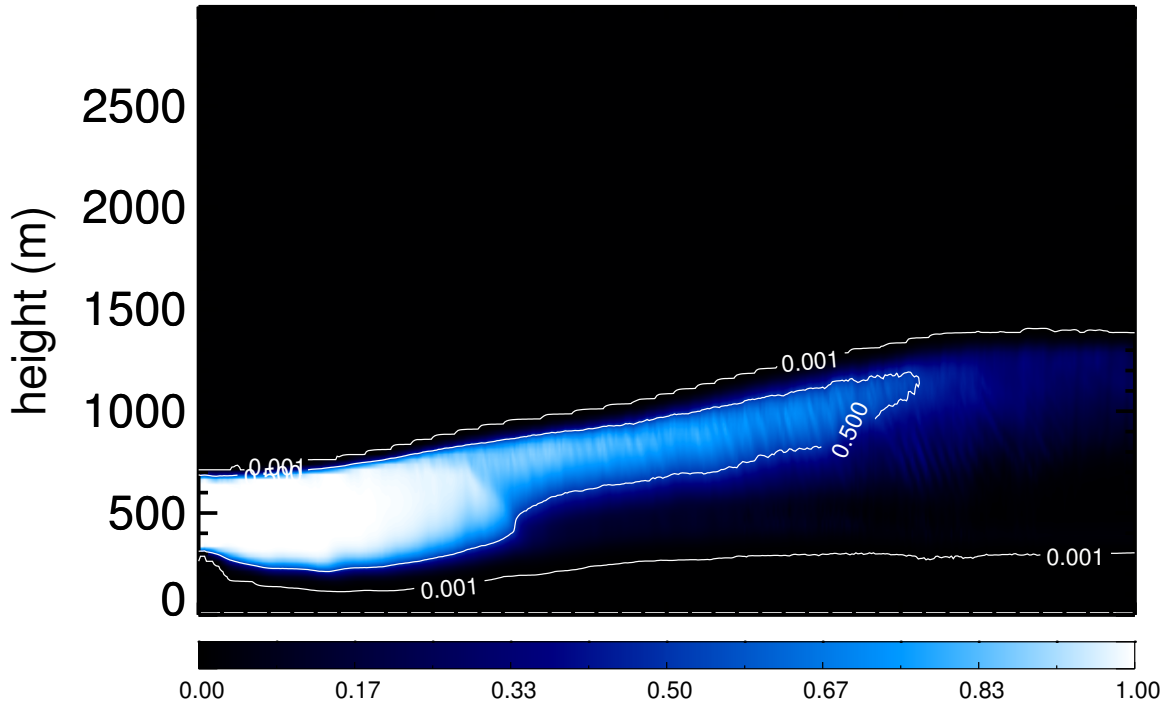


FIGURE 3.58. Time-series of estimated inversion strength (solid) and sea surface temperature (dashed) for the ASTEX control simulation.

relationship discovered in Wood and Bretherton (2006) and repeated in equation (13), that the cloud fraction should decrease considerably throughout the simulation.

Figure 3.59 shows how the cloud cover evolves throughout the simulation. For reference, the sun comes up around hours 6 and 30, sets around hour 21, and local noon is at hours 13 and 37. Cloud fraction and liquid water path reach their peak at the first sunrise and decrease precipitously throughout the first day, leveling off in the THOR simulations and slightly increasing in the LES models in the late afternoon. The second night features a steadily deepening boundary layer with the stratocumulus deck remaining fairly steady, if not decreasing in amount somewhat. After sunrise on the second day, the stratocumulus cloud continues to break up and by the end of the simulation, the boundary layer resembles a cumulus-under-thin-stratocumulus regime, not having transitioned to a strictly cumulus layer yet by this point. There is significant spread in the liquid water paths both in the LES models and in the grid-spacing sensitivity results of THOR. The 50 m run seems to match the LES results best, although the finer grid spacing runs do a good job too despite

Cloud Fraction



Cloud Water Path

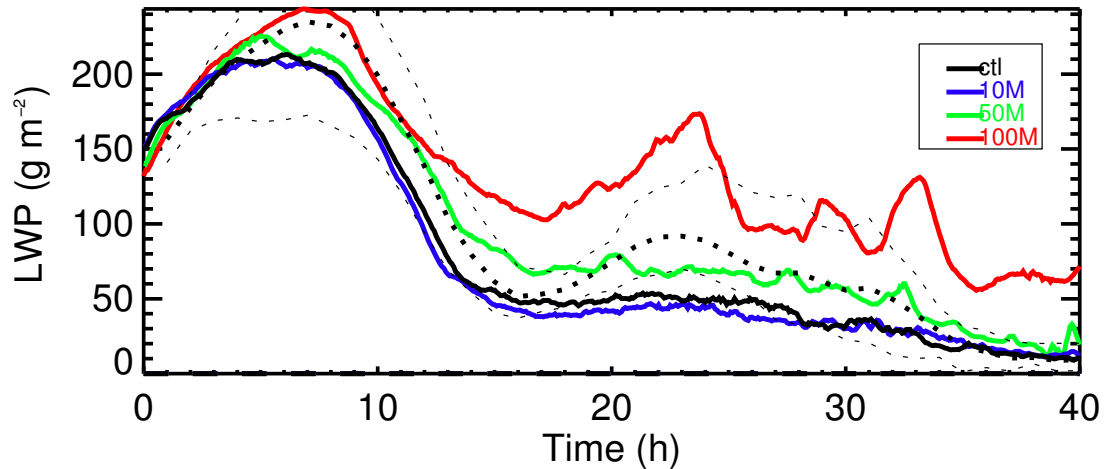


FIGURE 3.59. Time-height cross-section of cloud fraction for the control simulation (top) and time-series of liquid water path (bottom) for the grid spacing sensitivity test. As in the previous cases, solid lines represent output from THOR with the black denoting the control run and colors denoting sensitivity test runs. Black dashed lines represent the LES ensemble results, with the thick dashed line denoting the LES ensemble mean, and the thin dashed lines representing the range of LES ensemble results.

coming in on the low end of the LES range. The 100 m run is significantly different than the others and falls above the range of LES results, suggesting that 100 m might be too coarse of a vertical grid spacing to capture the processes necessary to simulate the transition successfully.

Unlike the previous test cases included in this study, the ASTEX case is not run to a steady state, so examining only the final mean state profiles would have limited utility. Instead, mean profiles are shown for three times throughout the simulation, with each profile representing the mean over the previous hour. The times chosen coincide with those used in van der Dussen et al. (2013), hours 8, 19, and 36. These times are representative of the near-maximum liquid water path stratocumulus phase, the end of the first day after significant cloud stratocumulus rising and thinning, and the second day noon hour after the boundary layer has reached its highest height, there are significant holes in the stratocumulus deck and cumulus towers begin to dominate. Figure 3.60 shows the mean profiles for the thermodynamic variables for the specified times, together with the initial profiles in the first row. For every time, the inversion height calculated in THOR is too low compared to the LES ensemble mean, but the bulk characteristics of the evolving boundary are well-simulated: the initially well-mixed layer in hour 8, the development of slightly stable layer and moisture gradient near cloud base at hour 19, and the continued increasing depth of the stable layer and drying out of the cloud layer by hour 36. As with the previous cases, however, by the time the boundary layer is cumulus dominated in hour 36, the sub-cloud layer is too moist compared to LES. Of the grid spacings tested in THOR, the 50 m run tends to produce the closest results to LES and the 100 m run tends to produce the worst simulation, significantly smoothing out gradients.

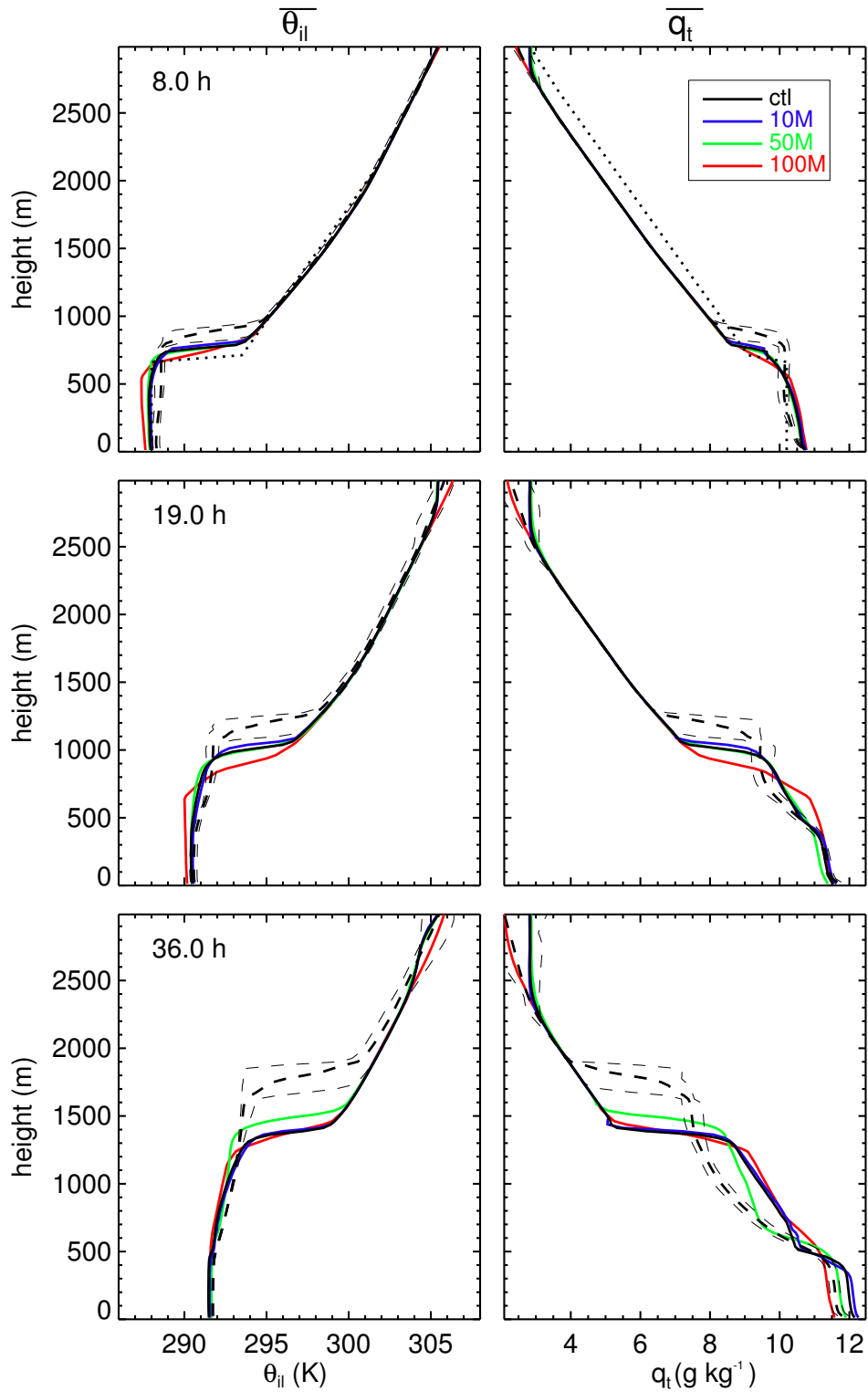


FIGURE 3.60. Mean hourly-averaged profiles of θ_{il} (left) and q_t (right) for hours 8 (top), 19 (center), and 36 (bottom) for the control and grid spacing sensitivity test runs. Lines are as in figure 3.59.

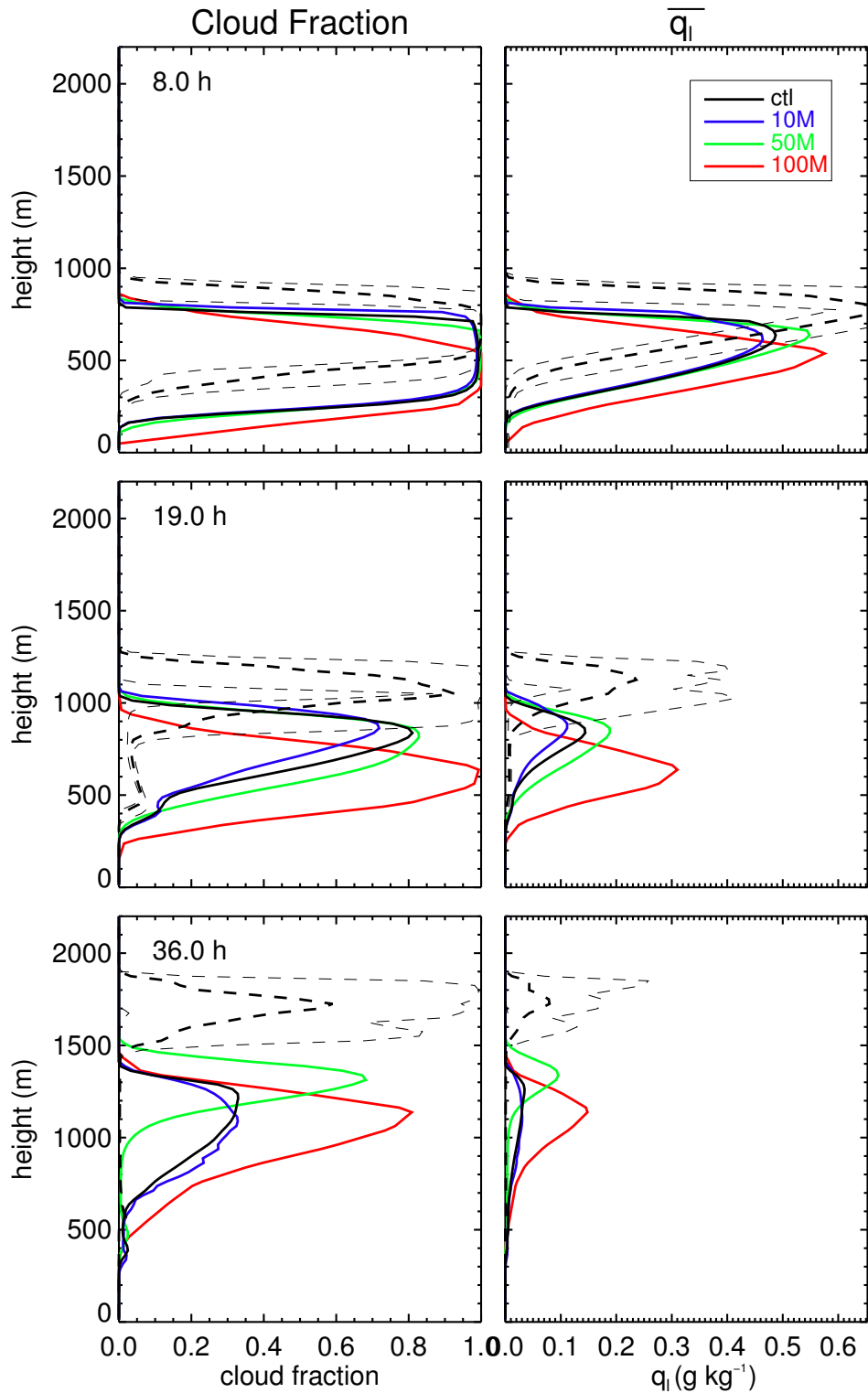


FIGURE 3.61. Mean hourly-averaged profiles of cloud fraction (left) and q_l (right) for hours 8 (top), 19 (center), and 36 (bottom) for the control and grid spacing sensitivity test runs. Lines are as in figure 3.59.

The evolution of the cloud structure is shown in figure 3.61. Although the underestimation of the boundary layer top is obvious, the shapes of the profiles are promising. During the stratocumulus phase at hour 8, THOR's cloud field is too deep with a particularly low cloud base while simultaneously underestimating the peak liquid water content, matching biases discovered for the previous stratocumulus cases. By hour 19, two prominent features begin to show up. The first is the thinning of the stratocumulus deck. Cloud fractions decrease from near 100% at hour 8 to around 80% at hour 19. The second is the development of a secondary cloud base around 500 m, indicative of a budding cumulus zone. These features are more distinct in the LES by this point in the simulation and are separated by a greater distance due to the faster rising inversion in the LES models. By hour 36, near noon on the second day, the stratocumulus has thinned to the point that it covers half or less of the area at its thickest point, while the cloud base of the cumulus deck is still evident. Liquid water contents have decreased considerably as dry air envelops the boundary layer from above and the layer becomes more cumulus-like.

Turbulence statistics profiles are shown in figures 3.62 - 3.64 in order to help determine why THOR's simulated cloud field differs from the LES models. First, the vertical velocity variance profiles show that initially, the turbulent eddies extend through the entire boundary layer, signaling that the stratocumulus top is coupled with the surface. By hour 19, a bi-model structure develops. This is indicative of a decoupled boundary layer, where the two peaks in $\overline{w'^2}$ show the centers of the two zones of convective turbulent eddies. These structures at both 8 and 19 hours are shared by the LES models. By hour 36, the boundary layer remains decoupled with two distinct maxima. The LES models simulate a sub-cloud maximum below an approximately 1000 m deep layer of very low $\overline{w'^2}$ associated with the

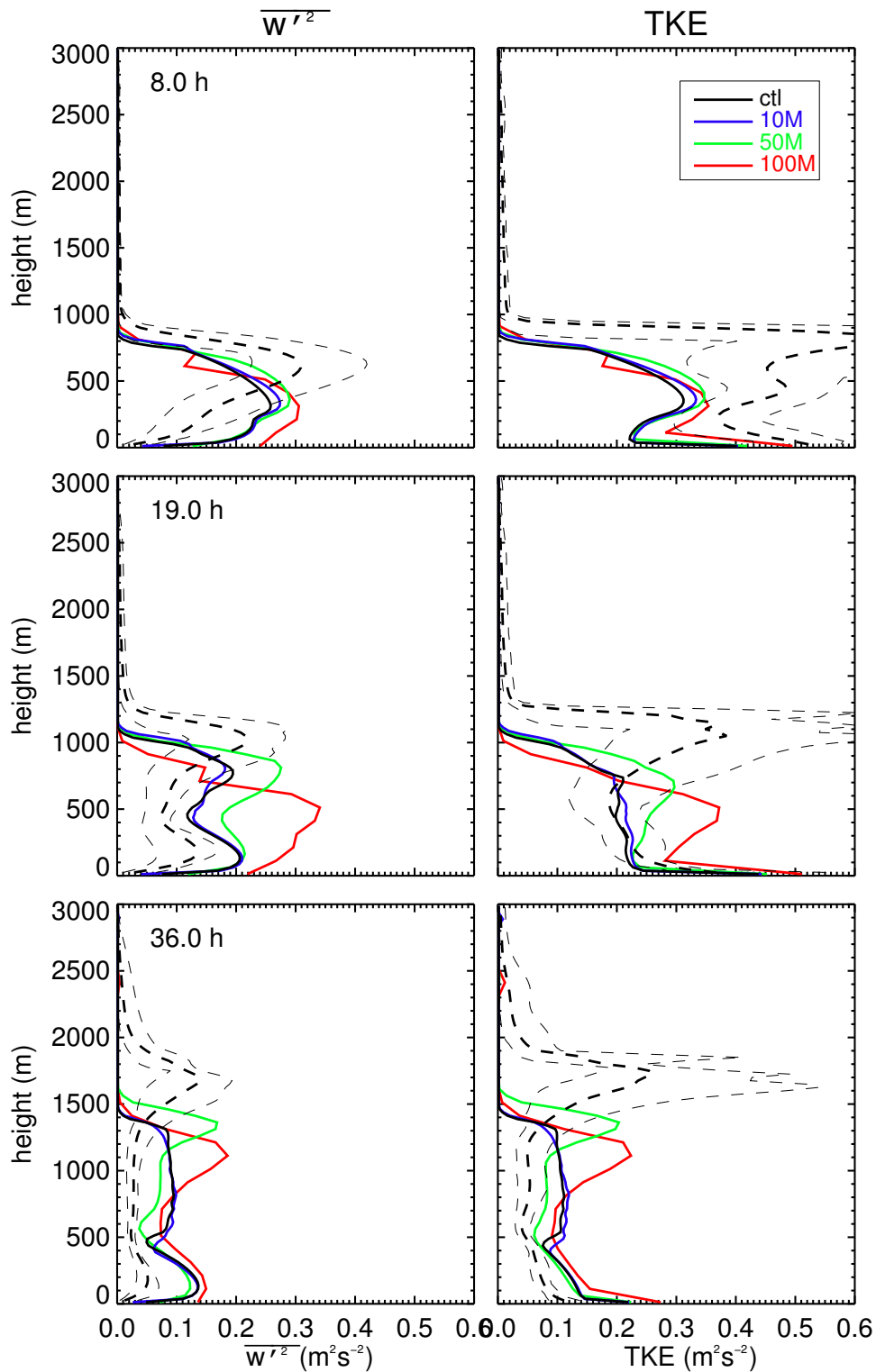


FIGURE 3.62. Mean hourly-averaged profiles of $\overline{w'^2}$ (left) and TKE (right) for hours 8 (top), 19 (center), and 36 (bottom) for the control and grid spacing sensitivity test runs. Lines are as in figure 3.59.

simulated cumulus deck, topped by a maximum at cloud top associated with the thinning stratocumulus clouds. The 50 m THOR run is able to simulate a structure like this, but the 10 m and control 25 m simulations have a broad maximum throughout much of the cumulus layer. The TKE magnitude is generally underestimated compared with LES in hour 8, simulated well in hour 19 and overestimated in hour 36, although both the underestimation in hour 8 and the overestimation in hour 36 is more in line with the observations plotted in van der Dussen et al. (2013).

The thermodynamic flux profiles in figure 3.63 show relatively poor agreement with LES in hour 8, improved agreement in hour 19, and worse agreement again by hour 36. In hour 8, the weaker fluxes of both θ_{il} and q_t help to explain the relatively slow growth of the boundary layer during this time compared to the LES models. Since these quantities are a proxy for the entrainment rate, the fact that these are underpredicted in THOR suggest that cloud-top entrainment is too weak. The differences between the LES and THOR moisture flux profiles explains why the mean moisture profiles are different in figure 3.60. In the LES moisture flux profiles for hours 19 and 36, there is a distinct minimum below the stratocumulus cloud base. This creates a positive gradient with height up to the stratocumulus cloud top. A negative gradient with height implies moisture is being deposited in these layers, whereas a positive gradient with height implies moisture is being taken from these layers. The negative gradient under a positive gradient in the LES models implies moisture is being added to the sub-cloud layers (from the surface), and it is being taken from the layers below the stratocumulus cloud top to supply the top of the boundary layer with moisture. This is consistent with the concept of cumulus-under-stratocumulus. The fact that all THOR runs (with the exception of the 50 m run) have a more-or-less monotonically decreasing moisture flux throughout the

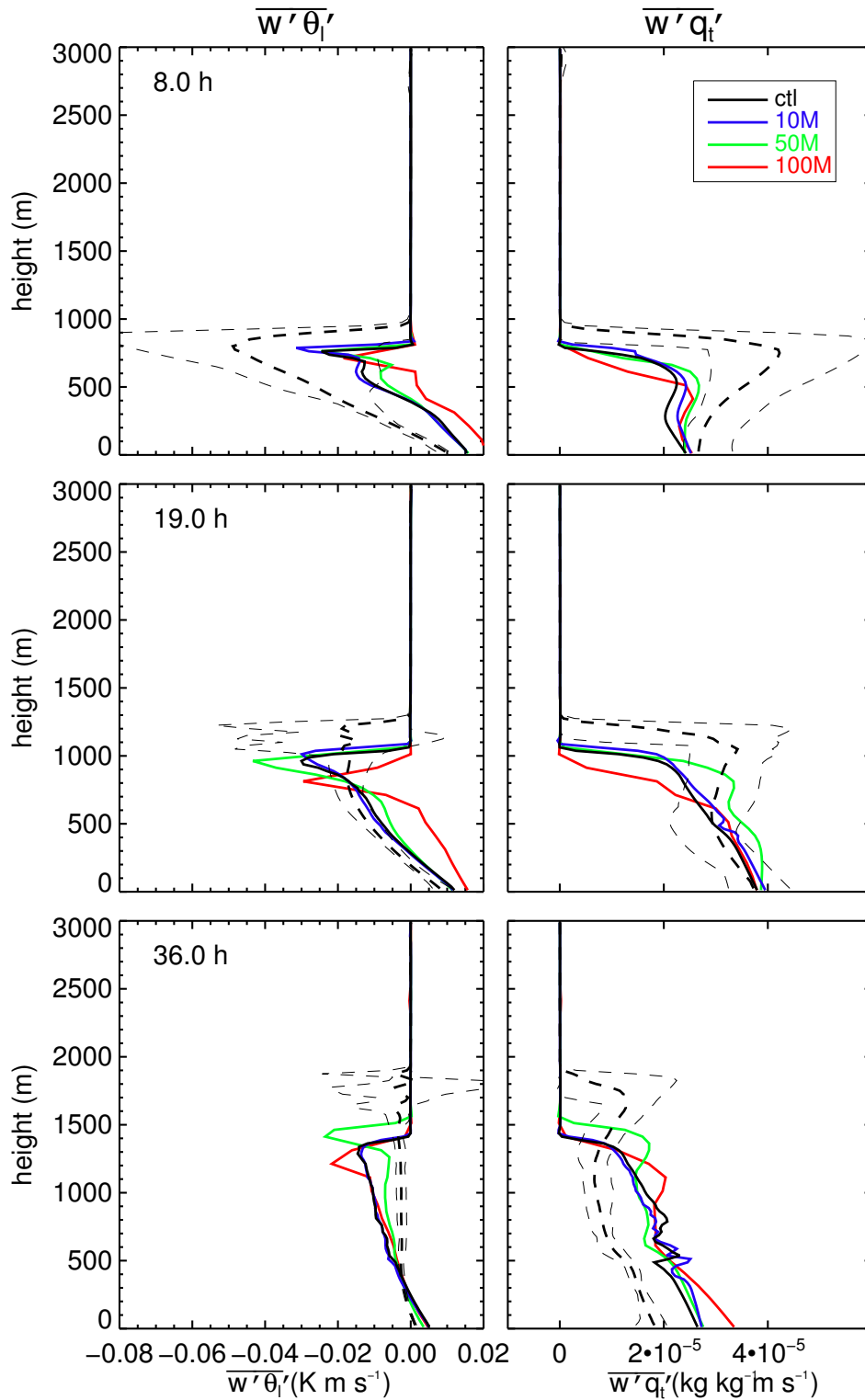


FIGURE 3.63. Mean hourly-averaged profiles of $\overline{w'\theta'_i}$ (left) and $\overline{w'q'_t}$ (right) for hours 8 (top), 19 (center), and 36 (bottom) for the control and grid spacing sensitivity test runs. Lines are as in figure 3.59.

boundary layer in hours 19 and 36 suggest that cumulus-under-stratocumulus in THOR are not transporting enough moisture upward. The lack of moisture transport by cumulus in THOR seems to be an issue that needs to be addressed for future improvement.

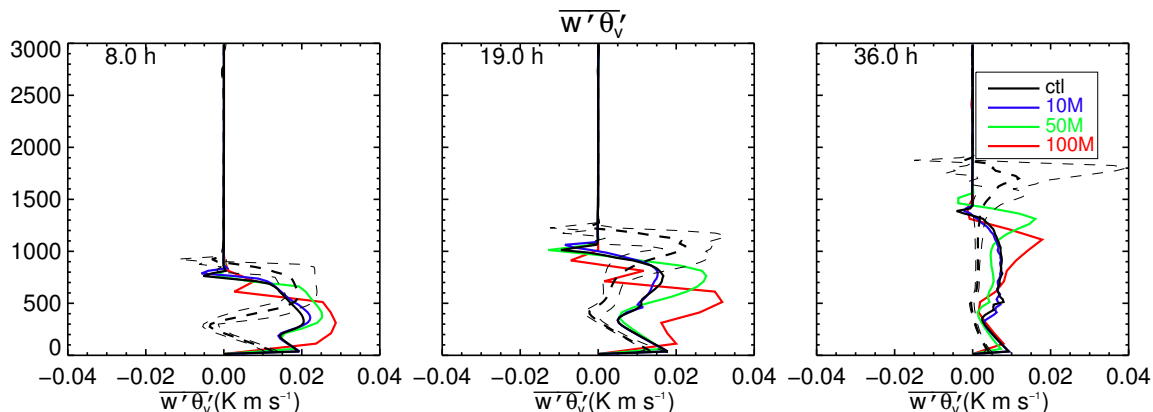


FIGURE 3.64. Mean hourly-averaged profiles of $\overline{w'\theta'_v}$ for hours 8 (left), 19 (center), and 36 (right) for the control and grid spacing sensitivity test runs. Lines are as in figure 3.59.

One of the keystones of the decoupling concept is a minimum in the buoyancy flux below cloud base. Figure 3.64 shows that THOR does generated a minimum in the buoyancy flux below cloud base, but unlike the LES models, the buoyancy flux does not go negative at any point below the cloud top. Despite this fact, other metrics do point to the fact that a type of decoupling has taken place in THOR. The fact that there are two peaks in the vertical velocity variance profiles in figure 3.62 and the fact that the master length scale is reduced above cloud base (figure 3.65). The master length scale is a good indicator of boundary layer coupling since it is based on the mean free path of a parcel originating at each level. Before hour 12 or so, the maximum in the length scale appears roughly in the middle of the boundary layer, signifying that parcels originating at cloud top reach all the way to the surface and surface parcels reach all the way to cloud top. After hour 12, the parcels originating at the surface may have enough energy to reach the boundary layer top, but

parcels originating in the stratocumulus layer are blocked from reaching the surface. This creates a maximum in the master length scale on top of the sub-cloud layer but produces reduced length scales above this layer.

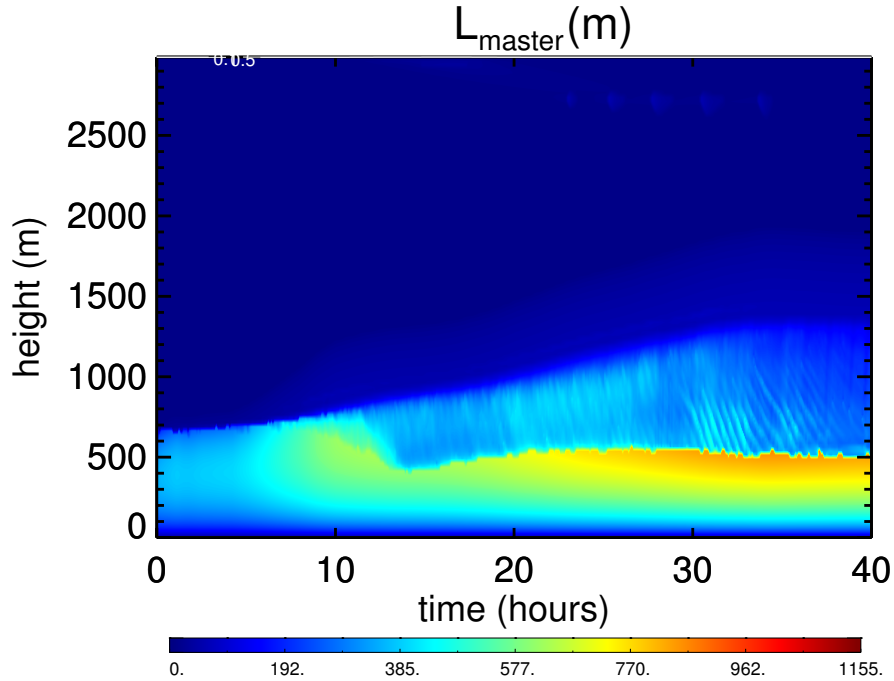


FIGURE 3.65. Time-height cross-section of the master turbulence length scale for the control ASTEX simulation.

Next, the results of the other sensitivity tests will be discussed. Results from the third-order moment diagnostic versus prognostic sensitivity test are not shown because there is very little difference in the simulated clouds or the timing of the transition. When the entrainment rate in the turbulence length scale is altered, the simulation changes as one would expect, given the response to this alteration in previous test cases. It should be noted at this time that the term entrainment is being used for two different things. For this sensitivity test, the entrainment rate refers to the rate at which a rising (or falling) parcel in the parcel model mixes with its environment as it ascends (or descends). This is different than the stratocumulus cloud-top entrainment that brings warm, dry free tropospheric air into

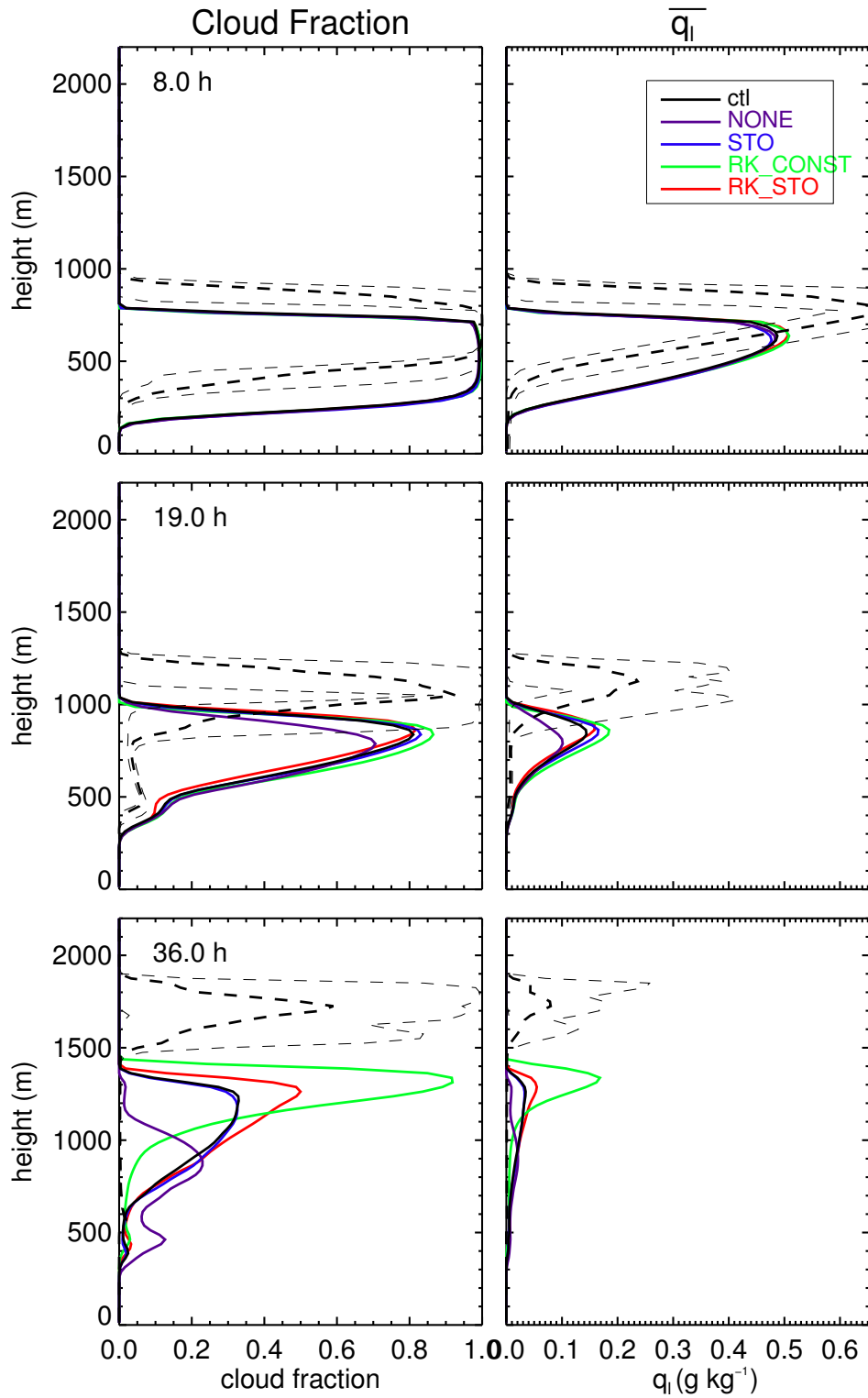


FIGURE 3.66. As in figure 3.61, but for the length scale entrainment sensitivity test.

the boundary layer. Both are mixing processes, but are in different spatial contexts. For a stratocumulus-topped boundary layer, the entrainment rate in the length scale calculation seemingly has no effect on the simulation. As the boundary layer transitions into cumulus, however, the length scale entrainment rate can have a big difference. For the higher entrainment rates (denoted with the prefix RK), turbulence is damped more in the cloud layer, leading to thicker stratocumulus clouds. With the higher length scale entrainment rate, the stochastic parcel process tends to somewhat cancel out the effects of the higher rate. If no parcel entrainment is assumed, turbulence is strongest in the cloud layer, resulting in more cloud top entrainment and a drier boundary layer. Given these profiles, the cloud liquid water path shows that stratocumulus breakup is somewhat sped up when no length scale parcel entrainment is used, and is slowed down when a constant higher parcel entrainment rate is assumed.

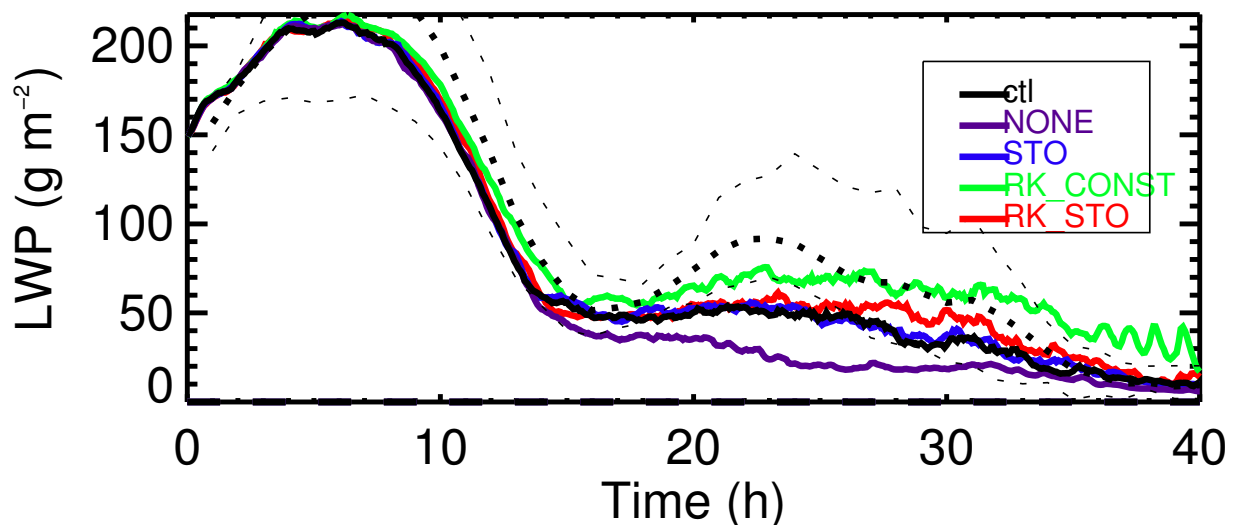


FIGURE 3.67. Time-series of liquid water path for the length scale sensitivity test. Lines are as in figure 3.59.

If grid-cell mean values are used to drive the microphysics scheme instead of the PDF sampling scheme, the surface precipitation rate is greatly reduced (figure 3.68). Precipitation

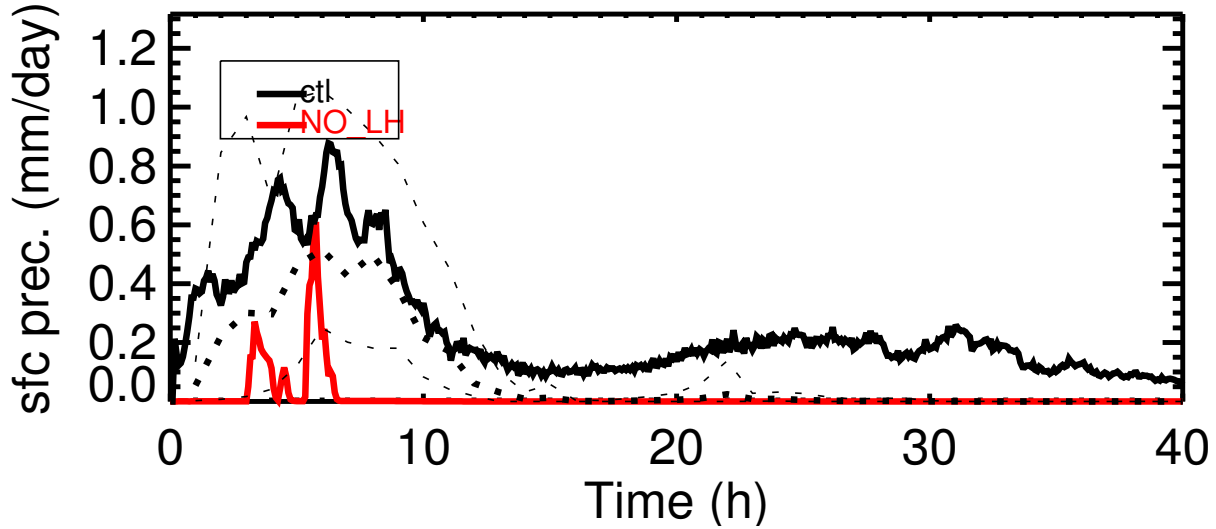


FIGURE 3.68. Time-series of the surface precipitation rate for the control and no-latin-hypercube-sampling sensitivity test. Lines are as in figure 3.59.

only occurs near the maximum of liquid water path right before sunrise on the first day. The impact on the cloud field is as one would expect from the previous test cases. Without PDF sampling, the cloud produced is deeper with more available water content and a lower cloud base (see figure 3.69). The difference is greatest during the stratocumulus stage, but remains throughout the transition. During hour 19, the extra cloud water and associated latent heating generates more turbulence and cloud-top entrainment, raising the height of the boundary layer top. This process continues as the transition enters the cumulus-dominated phase, represented by the hour 36 plots. The liquid water path time series in figure 3.70 shows a much higher peak during the stratocumulus phase, but is actually in much better agreement with the LES after noon on the first day when precipitation is overestimated compared to the LES in the control case.

Perhaps the most interesting sensitivity test performed for the ASTEX case is the test where PDF sampling is omitted for driving the radiation scheme, denoted as NO-RS. The time-height cross-sections of the radiative heating rates for the control simulation and the

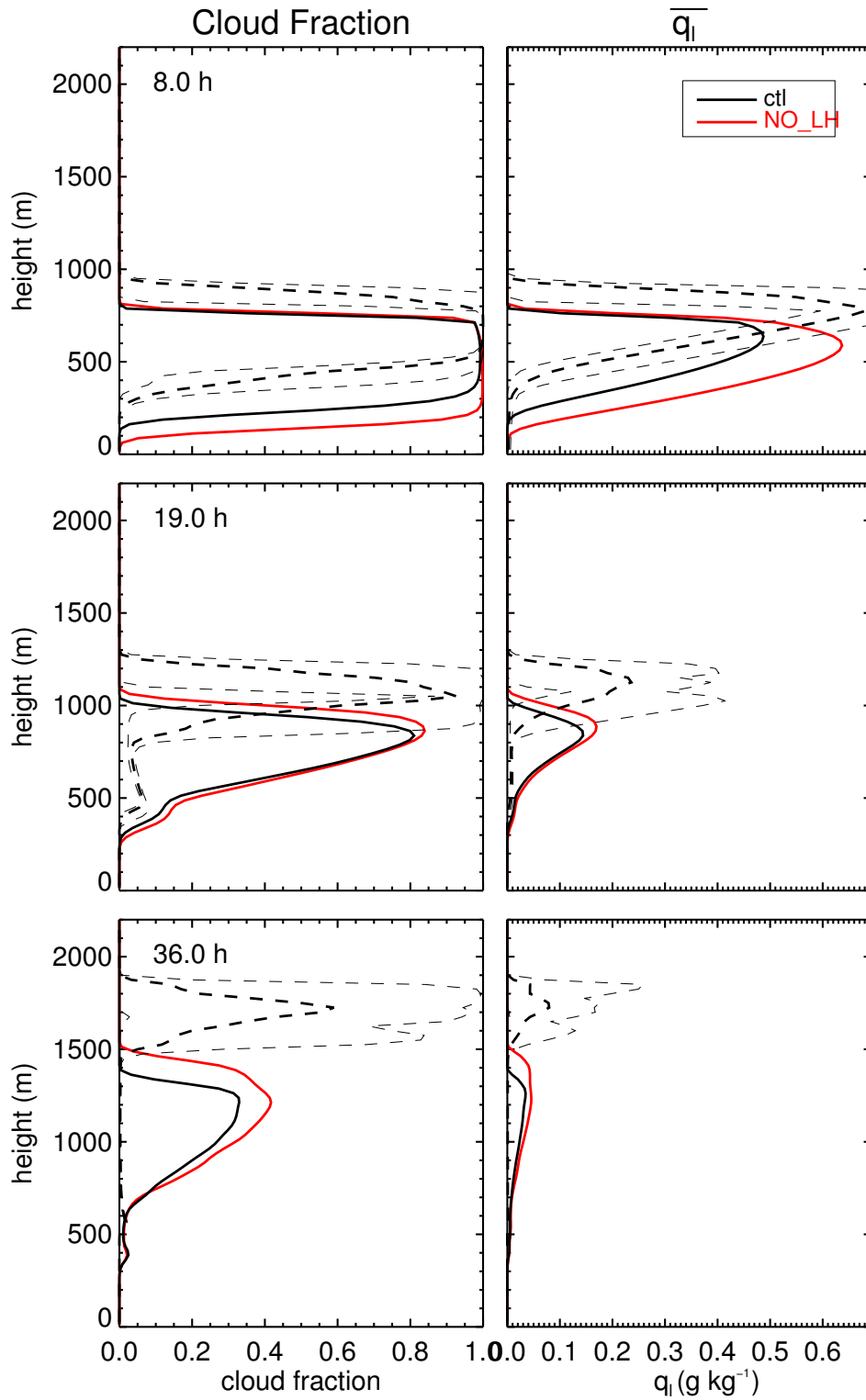


FIGURE 3.69. As in figure 3.61, but for the no-latin-hypercube-sampling sensitivity test.

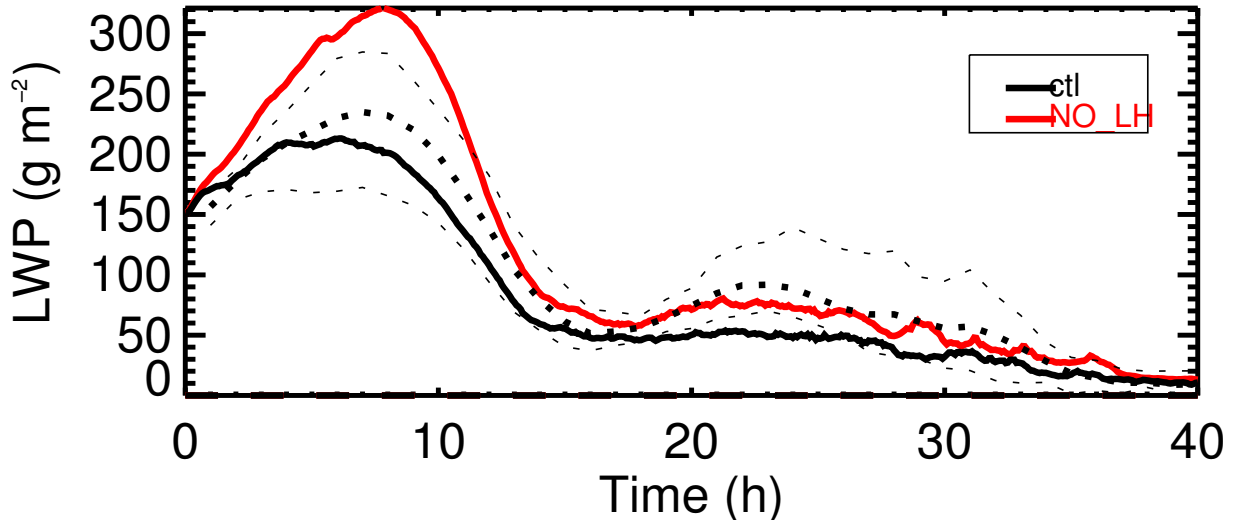


FIGURE 3.70. As in figure 3.67, but for the no-latin-hypercube-sampling sensitivity test.

sensitivity test without PDF sampling for radiation are shown in figures 3.71 and 3.72, respectively. When PDF sampling is enabled, a few differences are noted. First, significant noise is introduced into the solution. Second, cloud top radiative cooling is not as constant as in the NO-RS test, since the sampling algorithm occasionally samples “gaps” in the relatively homogeneous cloud field where more shortwave radiation is allowed into the boundary layer and more longwave radiation out. The difference in the two simulations becomes greater as the stratocumulus cloud fraction decreases, allowing more and more gaps in the stratocumulus to be sampled. The radiative heating rates during the second night are particularly different. The NO-RS simulation produces strong and constant cloud-top cooling throughout the second night, helping to drive the in-cloud turbulence and cloud-top entrainment, creating a considerably deeper boundary layer.

Interestingly, the NO-RS sensitivity test compares most favorably to the mean of the LES ensemble out of all of the THOR simulations. Profiles of the mean thermodynamic variables along with the cloud structure and TKE are shown in figures 3.73 - 3.75. For all three

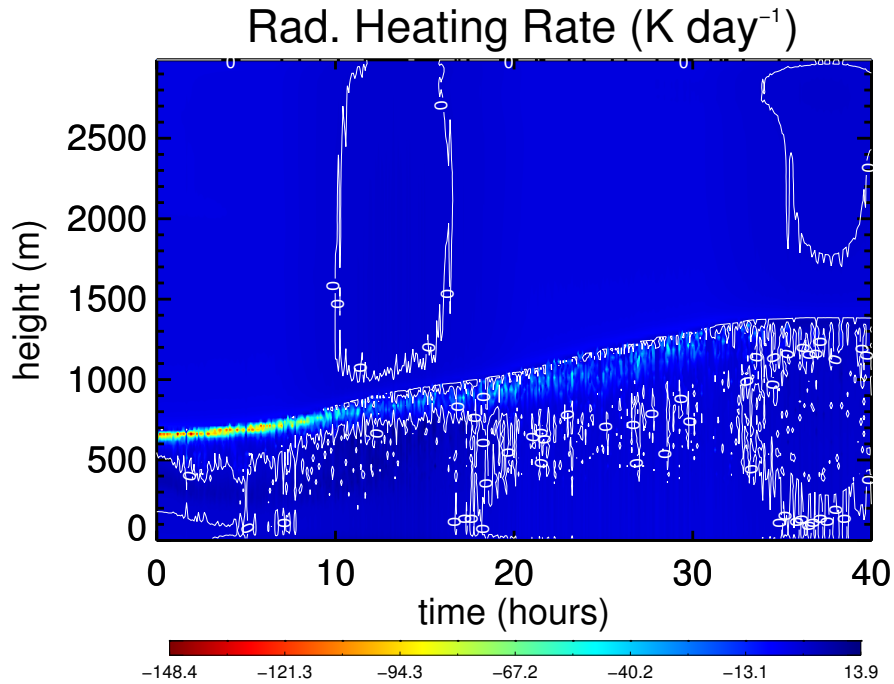


FIGURE 3.71. Time-height cross-section of the radiative heating rate for the control ASTEX simulation.

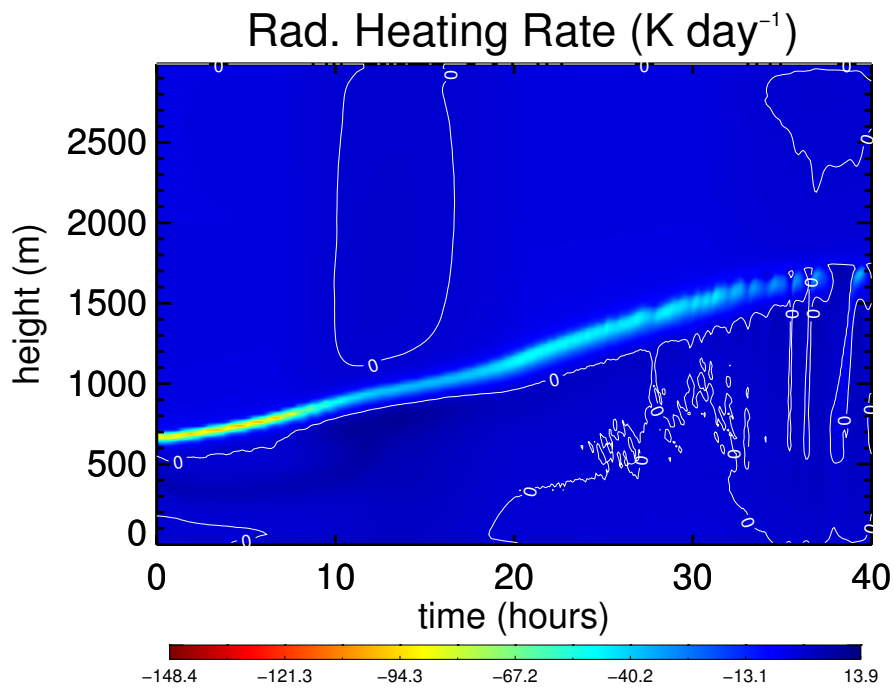


FIGURE 3.72. Time-height cross-section of the radiative heating rate for the no-radiation-sampling sensitivity test run.

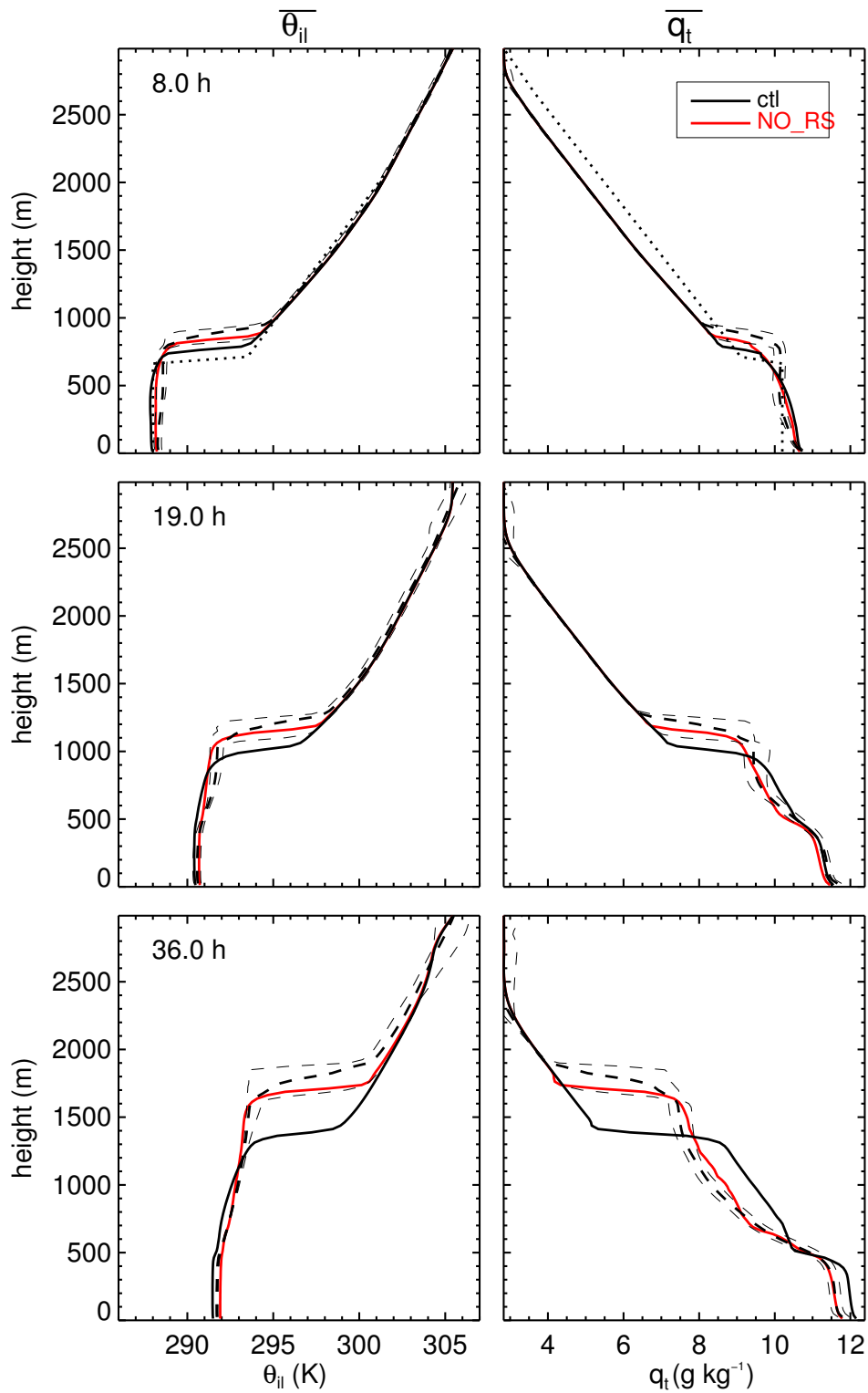


FIGURE 3.73. As in figure 3.60, but for the no-radiation-sampling sensitivity test.

times, the profiles of the thermodynamic variables look better for the NO-RS simulation. The boundary layer height is within the range of LES results, the stable layer depth and strength is nearly perfectly simulated along with the near neutral sub-cloud and cloud-top layers at 19 and 36 hours. In addition, the sub-cloud moisture is almost in perfect agreement with the LES results, and the drier air in the cumulus layer at hour 36 is much better versus the control. The fact that the mean profiles are in such good agreement suggests that the stronger cloud-top radiative cooling calculated using the mean grid-cell quantities in the radiation scheme is more realistic for this case, leading to better representation of the turbulence and cloud-top entrainment processes.

Not surprisingly, the cloud structure in the NO-RS test is in better agreement with the LES results as well (figure 3.74). While the cloud base height is still lower than LES at every time, the cloud top height is in much better agreement. For hours 8 and 19, the change in how radiation is calculated does not seem to affect either the magnitude of the peaks in cloud fraction or liquid water content, but it certainly affects their vertical placement. By hour 36, however, the stratocumulus layer in the NO-RS test remains more “filled-in” yet not as deep as the control case, which is also in better agreement with the LES. Despite the better vertical arrangement of the cloud cover in the NO-RS run, the liquid water path remains virtually the same, generally underestimated after the first sunrise (not shown). In addition, the vertical profiles of $\overline{w'^2}$ and TKE are improved in the NO-RS case by maintaining higher magnitude peaks higher up in the column while reducing overestimations in the cumulus and sub-cloud layers. This improvement is associated with the increased cloud-top radiative cooling which drives more energetic turbulence at cloud top and the stronger cooling under

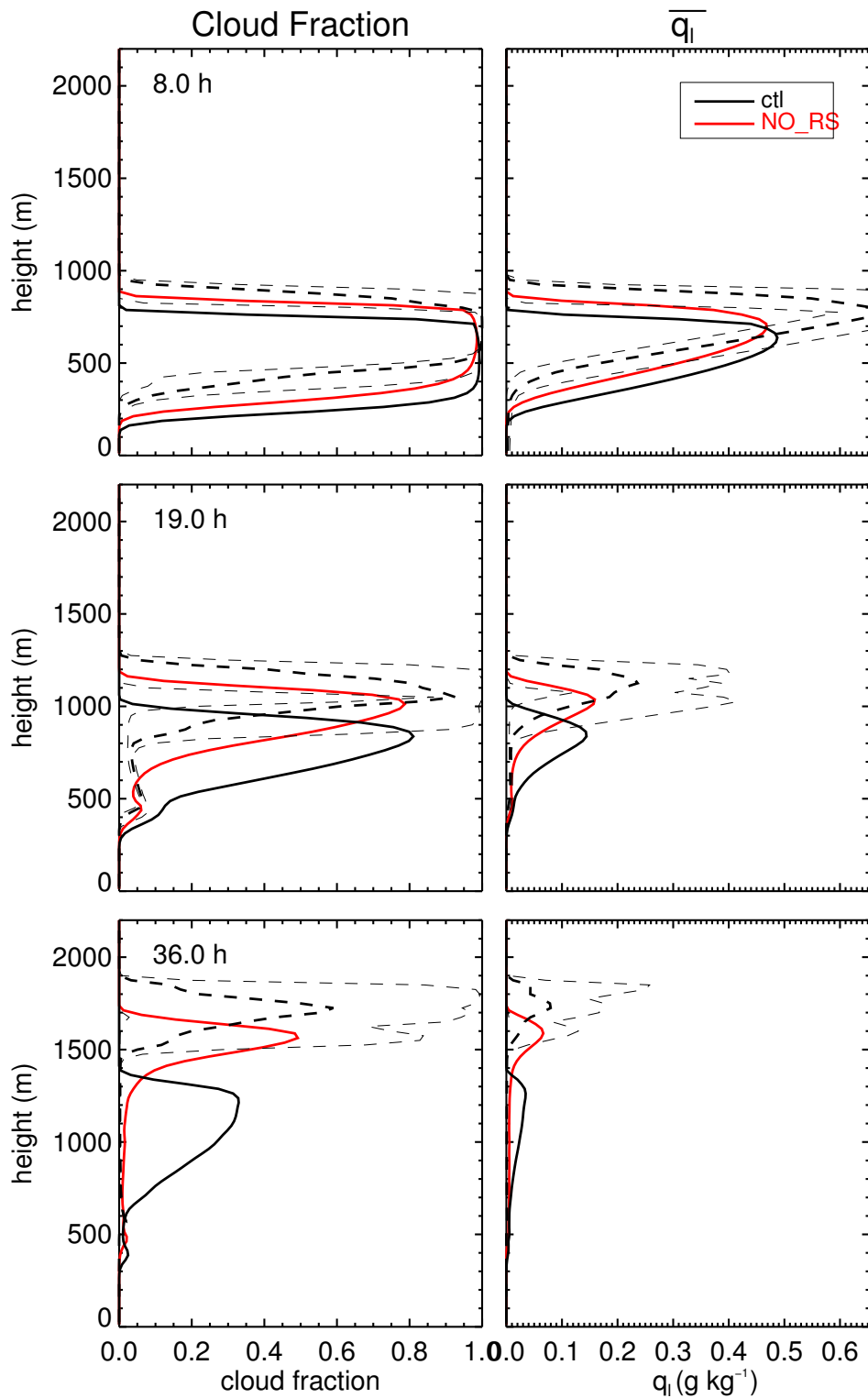


FIGURE 3.74. As in figure 3.61, but for the no-radiation-sampling sensitivity test.

heating signature below cloud top (especially during the second night) that increases static stability and hinders turbulence somewhat there.

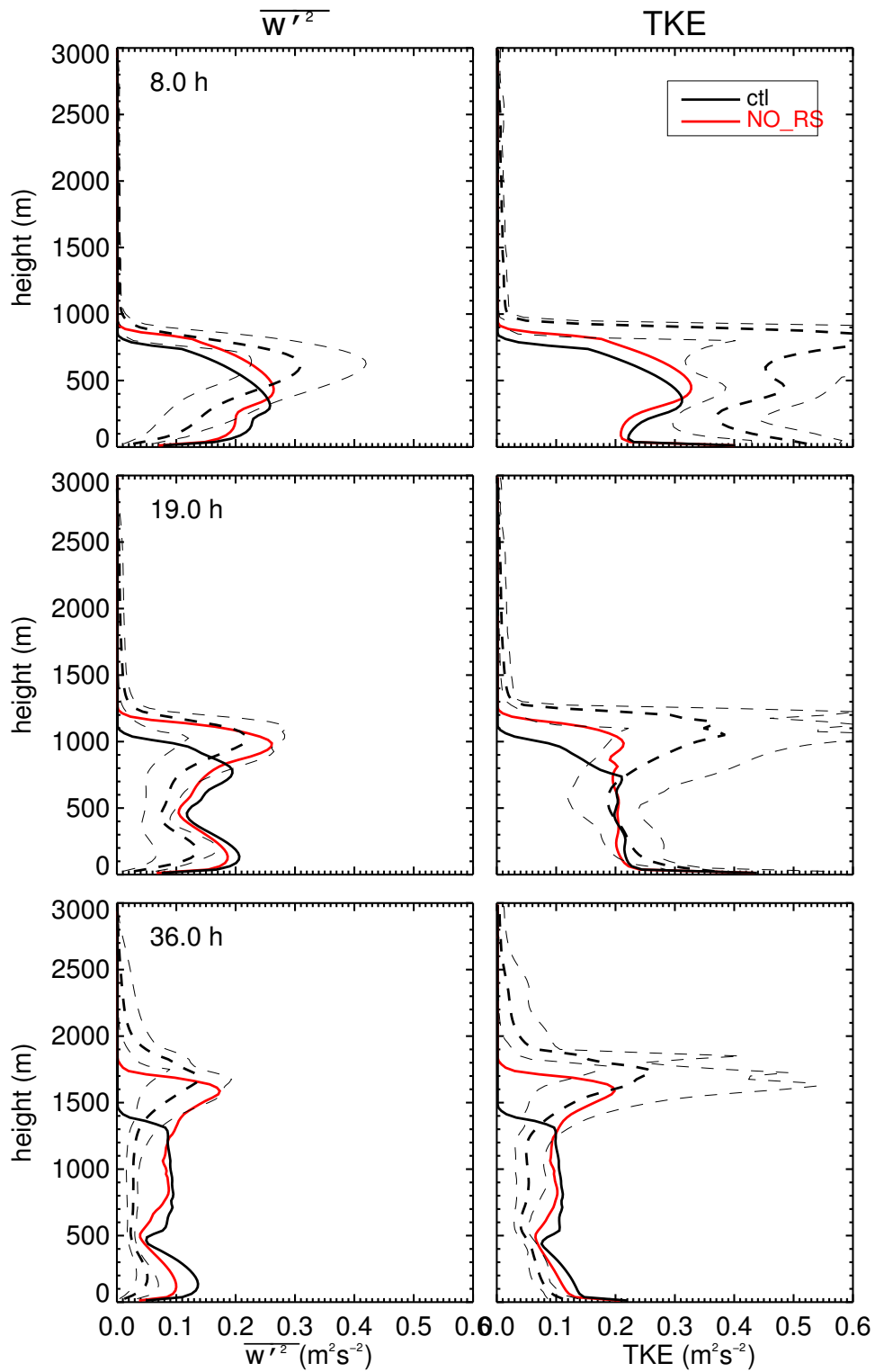


FIGURE 3.75. As in figure 3.62, but for the no-radiation-sampling sensitivity test.

CHAPTER 4

LOW CLOUD FEEDBACK EXPERIMENTS

Although it is a well-recognized problem that low cloud feedbacks are one of the main drivers of variability in future climate simulations, the AGCMs used to draw this conclusion may not be the best tool for studying and rectifying this problem. The reason for this is the inherent inability of such models to sufficiently resolve the processes that are important for modulating low cloud cover or even the low clouds themselves. Unfortunately, models capable of resolving low clouds and their intricately balanced processes, such as cloud-resolving models (CRMs) and LESs, are incapable of running over the entire globe for centuries-long simulations due to the massive computational expense. An intermediate approach could therefore be useful to illuminate physical mechanisms responsible for low cloud feedbacks, provide a better estimate of the sign and magnitude of low cloud feedbacks, and to perhaps inform modelers to generate new parameterizations that adequately capture the salient processes with low computational expense so that they may be included in the centuries-long AGCM simulations.

The framework espoused by the CGILS¹ intercomparison project seems like a step toward this intermediate approach. The general idea of the CGILS project is to develop initial profiles and large-scale forcings for the present day climate and for a warmed climate in order to use them to drive low-cloud-resolving large eddy and single column models. By simulating low clouds in detail in the same locations for the current climate and a warmed climate scenario, one can straightforwardly compare the cloud structure between the two

¹CGILS is a multiple-nested acronym that stands for the CFMIP-GASS Intercomparison of LES and SCMs where the GASS acronym has been discussed previously and CFMIP stands for the Cloud Feedback Model Intercomparison.

atmospheric states and potentially extrapolate the calculated cloud feedbacks to other areas of the Earth with similar changing conditions. While this approach could theoretically be used anywhere on the planet, the creators of the project derived forcing only for a strategic area of the world where particular insights may be gained about low cloud feedbacks. The strategic area consists of the GPCI² cross-section shown in figure 4.1, reproduced from figure 1 of Teixeira et al. (2011). This cross-section is particularly strategic because it transects areas of coastal stratocumulus, shallow cumulus, deep convection and transitions in between. By studying and simulating this cross-section, one can sample the regions most important for low cloud feedbacks and any understanding gained about them should be representative of similar areas around the world.

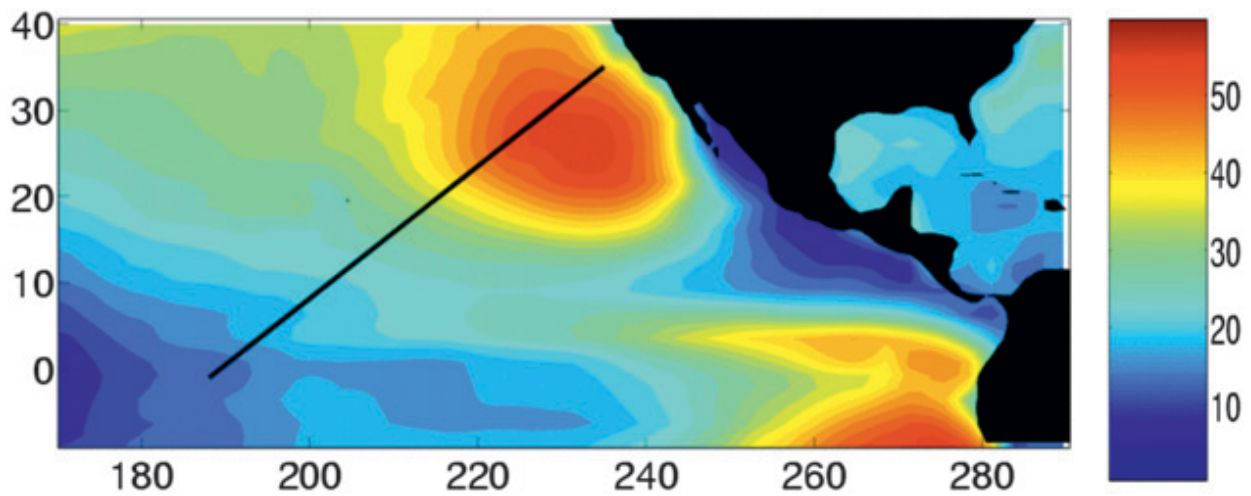


FIGURE 4.1. Figure 1 from Teixeira et al. (2011); contours denote low cloud cover percentage from the ISCCP climatology for JJA. The black line is the location of the GPCI cross-section.

In the following sections, a brief description of the experimental setup for the CGILS cases will be included, followed by results from THOR for the three locations along the GPCI

²GPCI stands for the GCSS/WGNE Pacific Cross-section Intercomparison where GCSS/WGNE stands for GEWEX Cloud Systems Study/Working Group on Numerical Experimentation.

cross-section used in the CGILS study representing shallow cumulus (location S6), cumulus-under-stratocumulus (location S11) and coastal stratocumulus (location S12). The results will focus on the change in simulated states between the current and idealized perturbed climates as well as a comparison of the implied feedbacks calculated in the THOR model with those calculated in the CGILS LES intercomparison. In addition to the discussion of results from points S6, S11, and S12, the final section will explore the simulated low cloud changes in THOR along the majority of the GPCI cross-section, from point S5 poleward.

4.1. CGILS

Full details of the CGILS model setup are found in Zhang et al. (2012), and a brief summary is included here. For the idealized setup for the current climate run, data from the Interim ECMWF Re-analysis (ERA-Interim) along the GPCI for July of 2003 is used for the initial profiles of θ_{il} , q_t , u , and v (see figure 4.2). Although only points S6, S11, and S12 are used in the CGILS study, corresponding to latitude 17°N, 32°N, and 35°N, initial profiles and forcings for the entire cross section are calculated and included in the following plots. The cross-section captures many prominent features, including the relatively large surface temperature gradient going poleward and the associated water vapor gradient, the weak temperature gradient aloft, the strong subsidence inversion north of about 22°N, the very dry air just above the inversion north of about 26°N, and the lower tropospheric northerly and easterly winds in the subtropical latitudes. Figure 4.3 is a plot of the SST and surface pressure as a function of latitude, and clearly shows the 10+ K gradient from the ITCZ to 35°N (evenly raised by 2K in the warmed climate run), the surface low associated with the ITCZ and the surface subtropical high pressure maxing around 30°N.

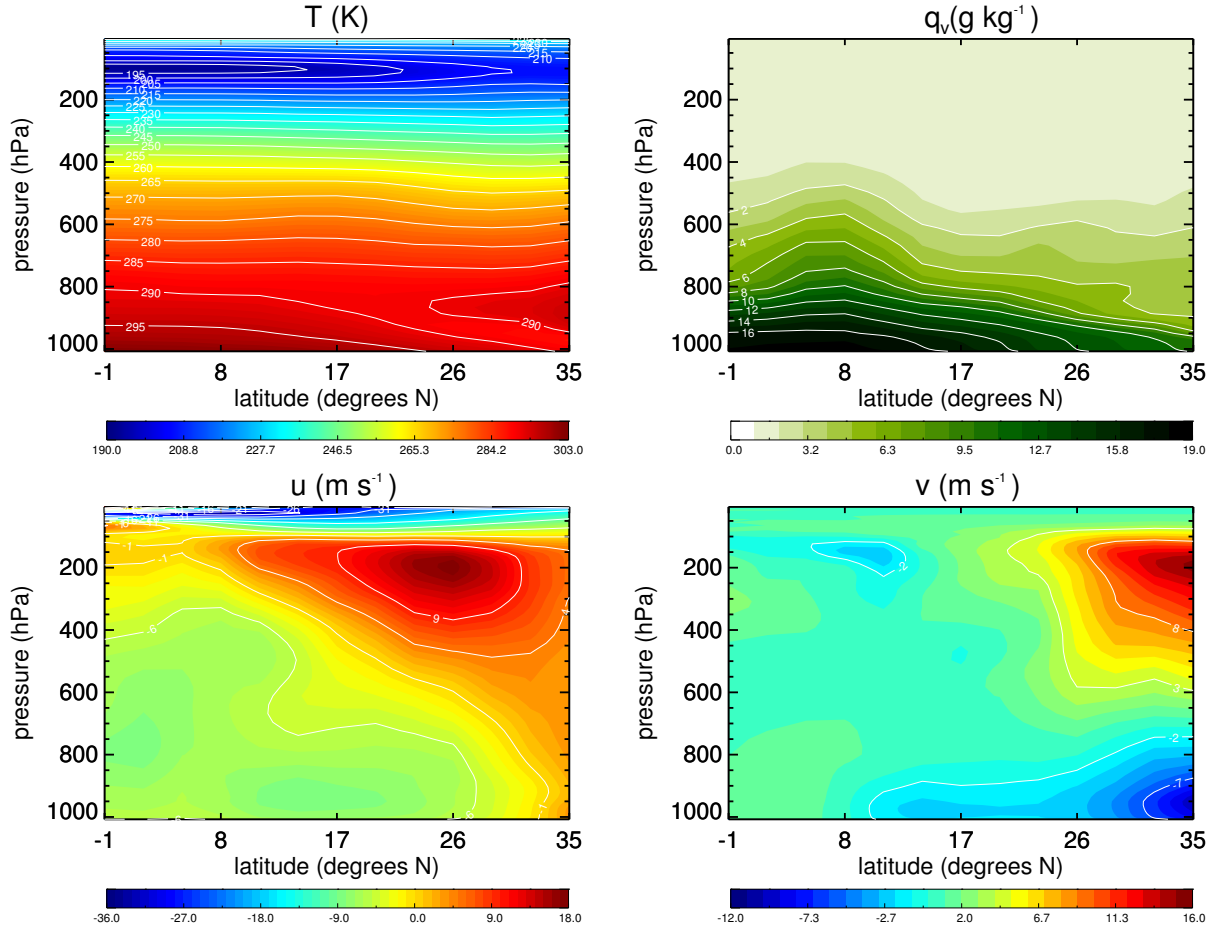


FIGURE 4.2. Plots show the initial conditions of T (top left), q_v (top right), u (bottom left) and v (bottom right) as a function of latitude and pressure along the GPCI cross-section.

Other large-scale forcings such as the subsidence rate and horizontal advection of temperature and moisture are more complicated. First, the profiles of subsidence rate are calculated using the steady-state balance in the free troposphere between large-scale horizontal advection of temperature, subsidence warming, and the net clear-sky radiative cooling. A representative profile shape with a maximum at 750 hPa is assumed for the subsidence rate, with the magnitude of the profile governed by the balance of the forces mentioned previously from the ERA-Interim data from 900 to 300 hPa at point S12. For other points along the

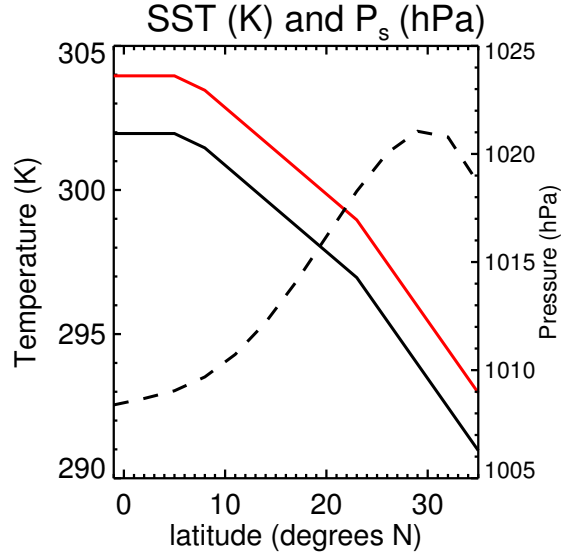


FIGURE 4.3. The sea surface temperature (solid lines) for the control (black) and perturbed climate (red) and the surface pressure (dashed) along the GPCI cross-section.

cross-section, the shape of the profile is the same as that at S12, but the magnitude is modulated by the ratio of the ERA-Interim subsidence rate to that calculated at S12. Zhang et al. (2012) point out that this procedure is used since it is relatively straightforward to apply for the current climate and for the perturbed climate and its simplicity aids in interpreting model results. The horizontal advection terms are calculated using winds and temperature and moisture gradients from the ERA-Interim data from the surface to 900 hPa. Above 800 hPa, these terms are calculated as residuals using the balance of forces discussed above since the subsidence has been specified and the radiative cooling rate can be readily calculated with the state variables from ERA-Interim. In between 800 and 900 hPa, the horizontal advective terms are calculated from simple linear interpolation. These large-scale forcings for the current climate are shown in figure 4.4. Prominent features include cooling and drying in the boundary layer due to horizontal advection and generally warming and moistening

above. The subsidence rate has a maximum magnitude at the northernmost point, S12, decreases to a local minimum at 26°N, point S9, and increases slightly again between latitudes 14°N and 23°N. The ITCZ is evident in this plot as the region of rising motion (negative ω) between 0°N and 11°N.

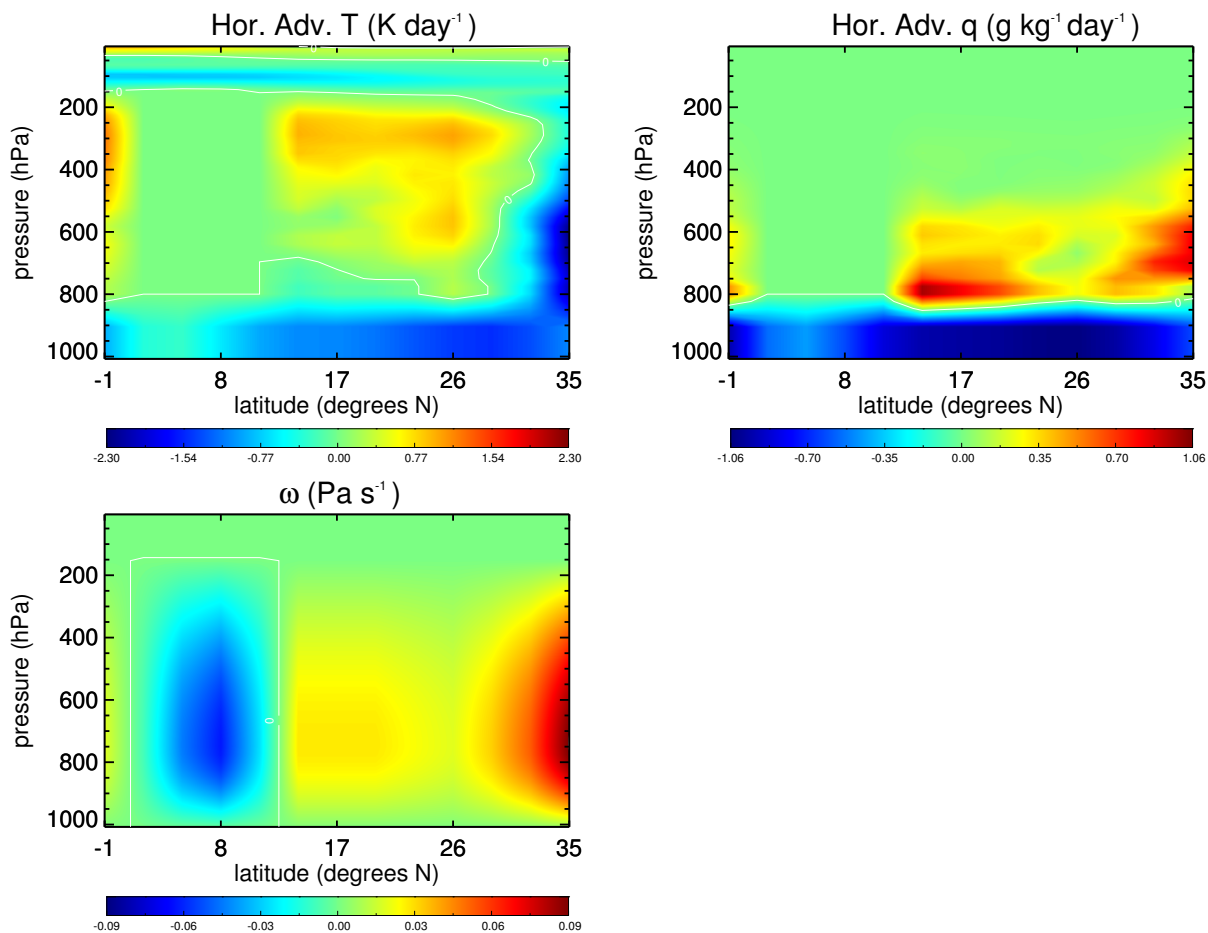


FIGURE 4.4. The horizontal advection of temperature (top left) and moisture (top right) and the large-scale pressure velocity (bottom left) for the control climate as a function of latitude and pressure along the GPCI cross-section.

For the perturbed, warmed climate simulations, the driver of the change is a +2 K change in SST. The temperature change for the troposphere is calculated using a surface parcel at 10°N with 80% relative humidity rising pseudo-adiabatically to the tropopause. The temperature change for the rest of the cross-section is calculated using the weak temperature

gradient hypothesis. The change in water vapor is calculated assuming that relative humidity remains constant from the control simulation using the perturbed climate temperature. Both horizontal wind components are assumed to be the same as for the control climate. The perturbed climate subsidence rate is calculated using the same method as for the control climate using the radiative heating rate for the perturbed climate and assuming the vertical integral of the horizontal advection of temperature remains the same as for the control case at point S12. Subsidence profiles at other points are calculated as in the control case using the same scaling factors from the ERA-Interim data used in the control climate. Finally, horizontal advection terms are again calculated as residuals using the perturbed case radiative transfer and subsidence rates. The change in tropospheric temperature and water vapor are shown in figure 4.5 together with the change in large scale forcings for the perturbed case in figure 4.6. The change in temperature gradually changes from 2 K near the surface to a little over 5 K aloft using the adiabatic parcel method, and the change in water vapor follows the change in temperature via the Clausius-Clapeyron relationship. Subsidence is weakened approximately 10% in the perturbed climate, consistent with the hypothesis of a slowed Hadley cell in a warmed world. The change in horizontal advection terms includes increased boundary layer drying and very slightly decreased boundary layer cooling. In Zhang et al. (2012), the forcings calculated for the CGILS experiment are broadly consistent with the control and warmed climate states in the CAM, GFDL AM2, and SPCAM climate models used for comparison in that paper, but without biases and influences from individual climate models, a major goal satisfied by the CGILS experiment organizers.

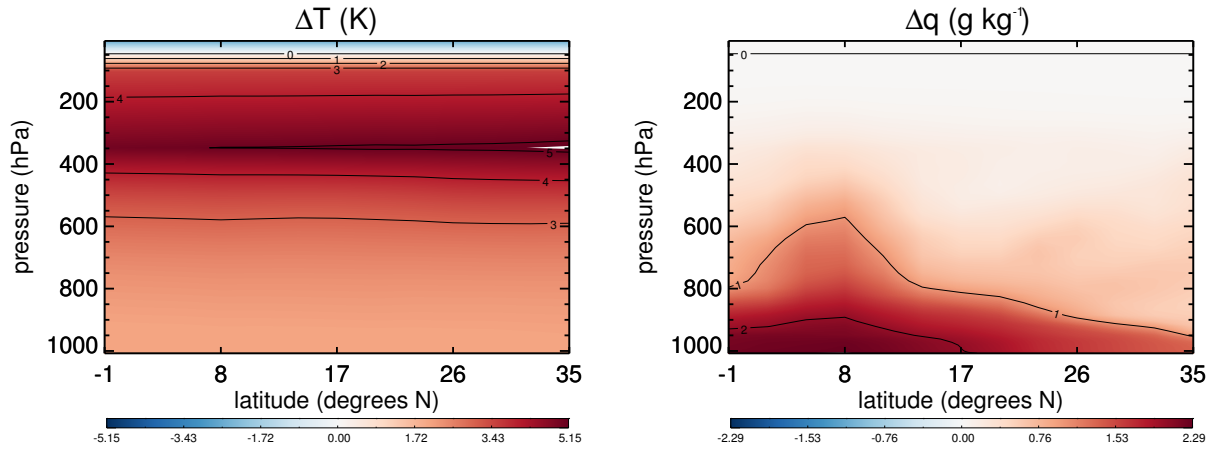


FIGURE 4.5. The change in the temperature (left) and moisture (right) in the perturbed climate scenario compared to the control climate as a function of latitude and pressure along the GPCI cross-section.

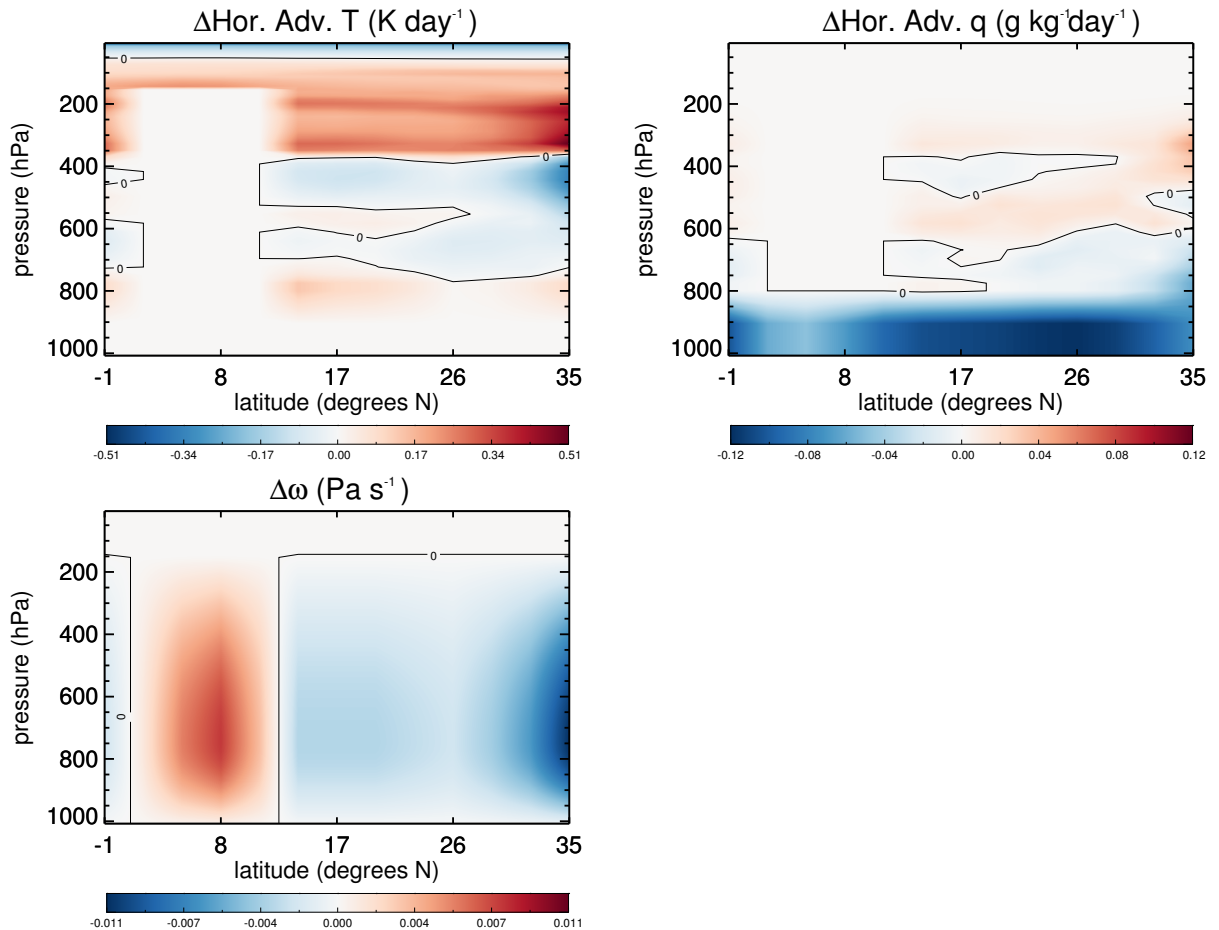


FIGURE 4.6. The change in large-scale horizontal advection (top) and pressure velocity (bottom) in the perturbed climate compared to the control climate as a function of latitude and pressure along the GPCI cross-section.

For THOR and the other models participating in the intercomparison, in order to reduce inter-model differences, the radiation schemes are configured to use constant diurnally-averaged insolation and all models are asked to use a common cloud droplet number concentration and effective cloud droplet radius calculation. In addition, all models use a common surface flux scheme and strong nudging of the horizontal winds to the initial profiles. Additional case specifications for LES model participants are included in Blossey et al. (2013) and are followed by THOR. These are generally minor modifications to the existing setup, like adding a moisture floor where spurious dry layers tend to develop above cloud top, nudging thermodynamic variables aloft, and slightly reduced subsidence rates at point S12 to eliminate erroneous stratocumulus breakup. For all CGILS simulations, THOR is run for 100 simulated days with 30 m grid spacing at point S6 and 15 m grid spacing at S11 and S12 with timesteps of 1 s and half a second, respectively. Model domains differ depending on the expected depth of the simulated clouds. For all mean profiles presented in this chapter, values were averaged over the last 50 days of the solution.

4.2. LOCATION S6

At location S6, corresponding to latitude 17°N and representing the shallow cumulus regime, the initial and steady-state profiles of θ_{it} and q_t for the control case and the steady-state solution for the perturbed climate case (denoted as P2K from here on) are shown in figure 4.7. Aside from the obvious shifts to higher temperature and moisture values, the profile shapes are remarkably similar. As with previous shallow cumulus cases, four layers are present: the sub-cloud layer (below about 350 m), the cloud layer (from about 350 m to 2800 m or 3050 m), the inversion layer (about 2800 m or 3050 m), and the free troposphere above the inversion layer. The most striking difference between the control (hereafter CTL)

and P2K simulations is the rise in inversion height. According to table 4.1, the inversion height (defined as the height where the relative humidity first crosses the 50% threshold) increases by 270 m while cloud base remains unchanged.

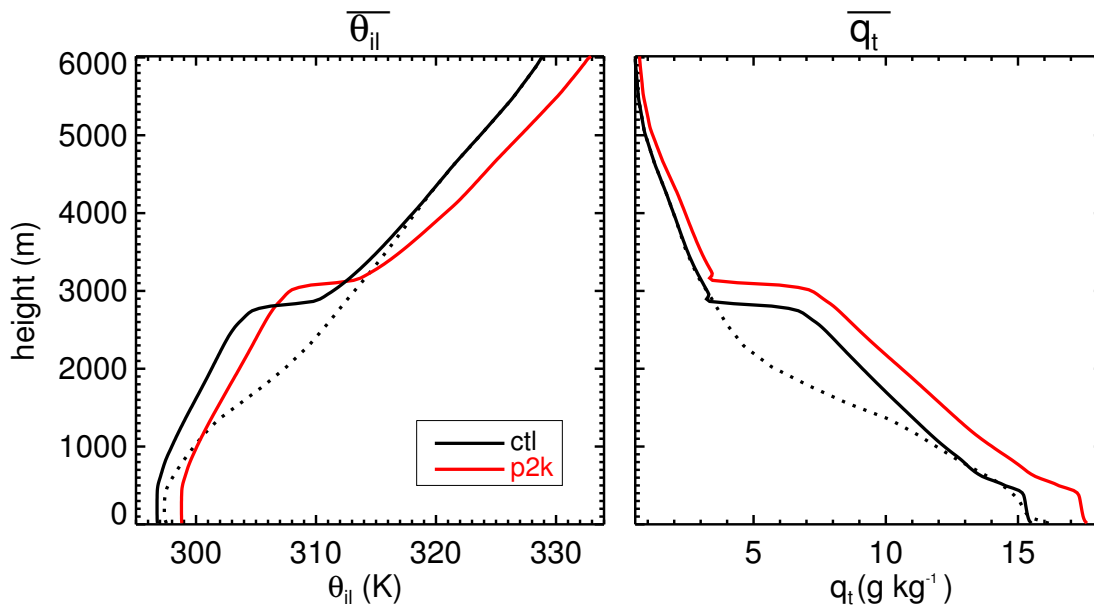


FIGURE 4.7. Steady-state profiles of θ_{il} (left) and q_t (right) for the control (black) and perturbed climate (red). The initial conditions for the control case are shown with the black dotted lines.

TABLE 4.1. Steady-state values for location S6; the included values are inversion height (z_i), cloud base height (z_{cb}), surface sensible heat flux (shf), surface latent heat flux (lhf), liquid water path (lwp), maximum cloud fraction (cld cvr), surface precipitation (src precip), shortwave cloud radiative forcing (sw crf), longwave cloud radiative forcing (lw crf), and net cloud radiative forcing (net crf).

Run	z_i [m]	z_{cb} [m]	shf [W m ⁻²]	lhf [W m ⁻²]	lwp [g m ⁻²]	cld cvr	sfc precip [mm day ⁻¹]	sw crf [W m ⁻²]	lw crf [W m ⁻²]	net crf [W m ⁻²]
ctl	2788	337	8.63	122.67	36.54	0.196	0.684	-52.32	6.02	-46.30
p2k	3057	336	8.12	133.64	37.49	0.177	0.809	-50.24	5.63	-44.60
Δ	270	-1	-0.51	10.97	0.95	-0.018	0.124	2.08	-0.39	1.69

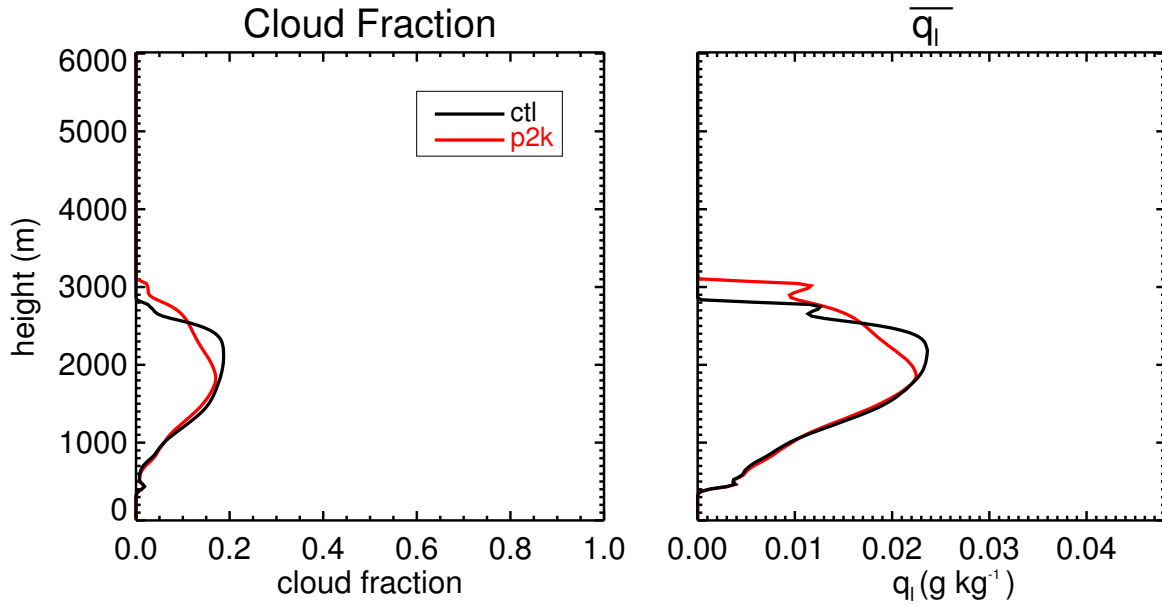


FIGURE 4.8. Steady-state profiles of cloud fraction (left) and q_l (right) for the control (black) and perturbed climate (red).

The vertical cloud structure and time evolution are shown in figures 4.8 and 4.9. While the liquid water path seems to reach an equilibrium value after a couple of days, the cloud depth continues to increase until about 16 days into the simulation when a steady-state is reached. For both simulations, cloud fraction maxes out less than 20% toward the upper middle of the cloud layer with only a small secondary maximum at cloud base. In the P2K run, the cloud top height is extended with the inversion by about 270 m, although it seems to grow in height at the expense of cloud water slightly lower in the column. The increased depth of the cloud is almost completely compensated by the decrease in cloud liquid water further down in the column so that the liquid water path of the P2K run is increased by less than 1 g m^{-2} , or about 2.5%. The cloud cover, defined as the maximum cloud fraction in the column, is decreased by about 10% of the CTL value in the P2K run.

The increase in surface temperature increases the surface latent heat flux by about 11 W m^{-2} , or about 9%, from the control simulation while the surface sensible heat flux decreases

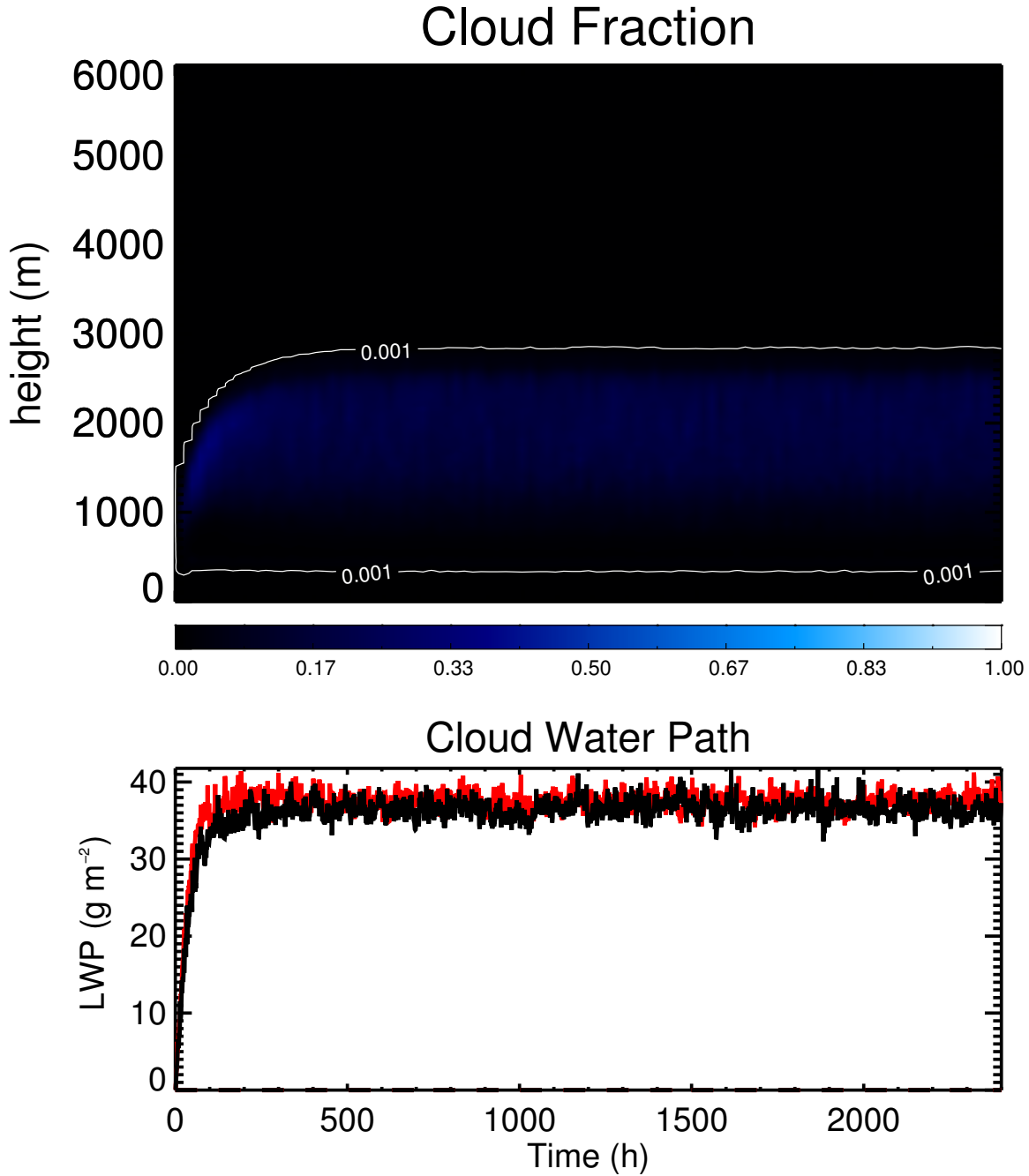


FIGURE 4.9. Time-height cross-section of cloud fraction for the control climate (top) and the time-series of liquid water path for the control (black) and the perturbed climates (red).

by about 6%, or about a half $W \text{ m}^{-2}$. Between the increased inversion height and increased buoyancy flux throughout the cloud layer driven by the increased moisture flux, the turbulent eddies within the cloud layer are slightly more energetic with higher values of $\overline{w'^2}$ and TKE.

The third-order moments of w , θ_{il} , and q_t are increased by between 15 and 50% in the cloud layer (not shown), indicating that transport by the turbulent eddies in the shallow cumulus cloud layer is considerably stronger in a warmed climate.

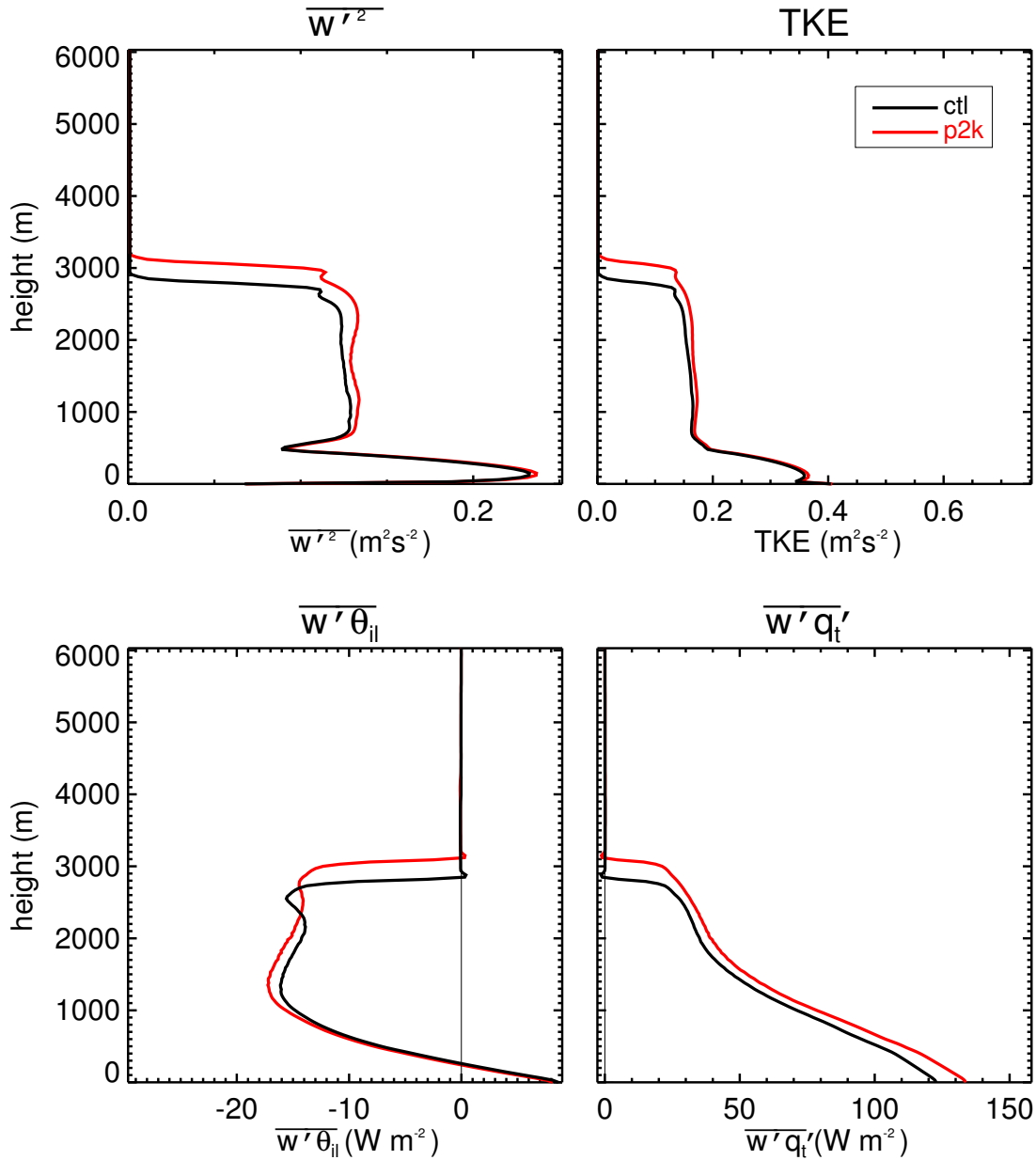


FIGURE 4.10. Steady-state profiles of vertical velocity variance (top left), TKE (top right), sensible heat flux (bottom left) and latent heat flux (bottom right) for the control (black) and perturbed climates (red).

Blossey et al. (2013) compare results from six LES models running the CGILS case. The LES simulations evolve similarly to the THOR simulation. Most LES models simulated a cumulus-under-stratocumulus regime for the first several days, but the stratocumulus top thinned and was dissipated in half the models by the end of their 10 day simulation. THOR does not seem to produce a stratocumulus-topped layer at any time, although the first 10 days do feature a higher cloud fraction near the boundary layer top. Blossey et al. (2013) point out that the simulated cloud layer is considerably deeper than observed by between 1 and 2 km. They blame the deeper cloud layer on errors in the CGILS forcing, particularly the horizontal advection of moisture. They argue that this term is supposed to offset drying due to subsidence, but it ends up moistening the upper portions of the cloud layer. This may also explain the top-heavy shape of the cloud profile simulated by THOR, which does not match general observations for shallow cumulus layers that have a distinct maximum cloud fraction at cloud base.

The authors of the LES intercomparison study claim that precipitation plays a central role in modulating the cloud field at point S6. They argue that cloud deepening (and therefore boundary layer deepening) halts when precipitation begins to be generated efficiently, and that increased precipitation in the P2K run reduces cloud top entrainment so that the increase in the boundary layer height is stunted. In the LES models, surface precipitation is increased by between 8 and 40% and boundary layer heights only increase by between 0 and 170 m, or generally less than 5%. In THOR, surface precipitation is increased by about 18% and the boundary layer depth increased by about 10% in the P2K run, so it seems that precipitation is less successful at modulating cloud-top entrainment in THOR. Surface precipitation rates range between 0.4 and 1.5 mm day⁻¹ in the LES models according to

Blossey et al. (2013) with the majority of models producing rain rates greater than 1 mm day⁻¹. THOR produces slightly lighter precipitation rates in the 0.7-0.8 mm day⁻¹ range, so the reduced precipitation in THOR might account for some of the greater entrainment rate. In addition, the increase in transport by the third-order moments and turbulence intensity in THOR's P2K run that leads to stronger cloud-top entrainment is also influenced by the radiative cooling. The shortwave cloud forcing is about -50 W m⁻² in THOR compared with -15 to -31 W m⁻² in the LES models. Shortwave cooling is stronger in THOR due to its slightly greater liquid water path and cloud fractions as compared to the LES models.

Despite the differences between THOR and the participating LES models in Blossey et al. (2013), all models produce the same magnitude of cloud feedback. The cloud feedback, as diagnosed from the change in net cloud radiative forcing, is very small and positive at 1.69 W m⁻². The small positive feedback in THOR appears to be driven by slightly stronger cloud-top entrainment that brings more dry air into the boundary layer near the cloud top. This reduces cloud fraction and liquid water there compared to the control simulation, so although the cloud is deeper with a slightly higher liquid water path in the warmed climate run, the reduction in cloud coverage near cloud top reduces shortwave reflection by a small amount, leading to a small positive feedback.

4.3. LOCATION S11

Location S11 is located at 32°N and features a cumulus-under-stratocumulus regime. The mean profiles of the thermodynamic variables for the CTL and P2K for the last 50 days of the simulations are shown in figure 4.11 together with the initial conditions for the CTL case. Although initial profiles from the ERA-Interim are only well-mixed up to about 500 m, THOR develops a boundary layer at steady-state that is about 1150 m deep in the

CTL simulation and about 1300 m deep in the P2K simulation. There is some evidence of stratocumulus decoupling, as one would expect in a cumulus-under-stratocumulus boundary layer. Both simulations have a sub-cloud well-mixed layer below about 600 m. Above this layer is a subtle, shallow layer of slightly increased stability with a weak moisture gradient, most prominent in the P2K run but also evident in the CTL run. The top of the boundary layer is once again well-mixed and neutral. The steady-state inversion height in the CTL case reaches 1146 m versus 1278 m for the P2K case, a difference of 132 m.

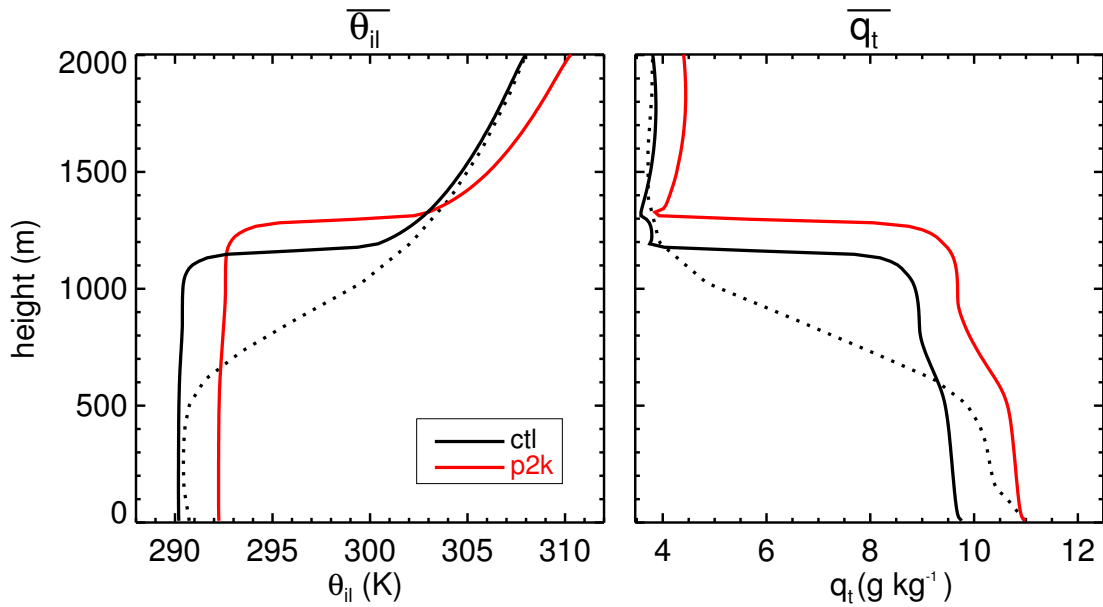


FIGURE 4.11. As in figure 4.7, but for location S11.

TABLE 4.2. Steady-state values for location S11; as in table 4.1, but with the addition of the stratocumulus base height (z_b).

Run	z_i [m]	z_b [m]	z_{cb} [m]	shf [W m ⁻²]	lhf [W m ⁻²]	lwp [g m ⁻²]	cld cvr	sfc precip [mm day ⁻¹]	sw crf [W m ⁻²]	lw crf [W m ⁻²]	net crf [W m ⁻²]
ctl	1146	787	495	5.62	94.99	92.68	0.976	0.132	-168.42	9.92	-158.50
p2k	1278	921	491	4.96	108.93	91.68	0.976	0.129	-165.90	10.70	-155.20
Δ	132	134	-4	-0.67	13.94	-0.99	0.000	-0.003	2.52	0.78	3.30

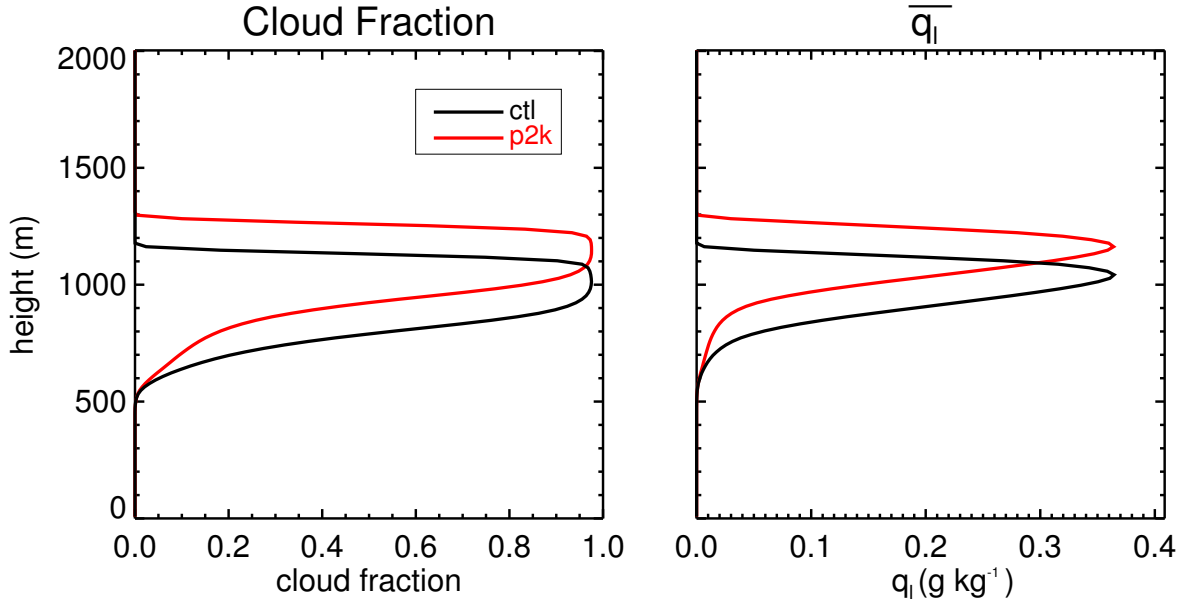


FIGURE 4.12. As in figure 4.8, but for location S11.

The vertical cloud structure and evolution are shown in figures 4.12 and 4.13. A steady state is achieved after about 10 days of simulation, and the simulated clouds cover a maximum of 97.6% of the area in both simulations. The maximum liquid water content is about the same in both cases, but the P2K run features a smoother gradient below cloud base, suggesting a more decoupled layer with more cumulus underneath the stratocumulus layer. From table 4.2, one can calculate the thicknesses of the stratocumulus and underlying cumulus layers using the inversion height, z_i , stratocumulus cloud base (defined as the height below the height of maximum cloud fraction where the cloud fraction is equal to 50% of the maximum), z_b , and cloud base (defined as the height at which cloud fraction is equal to 0.1%), z_{cb} . For the CTL case, the stratocumulus deck is 359 m thick and the cumulus layer is 292 m deep. For the P2K case, the stratocumulus layer is approximately the same depth, 357 m, but the cumulus layer is significantly deeper at 430 m. Despite a deeper cumulus layer and an identical stratocumulus water content, there is an approximately 1% decrease

in liquid water path in the P2K run versus the control. Since the cumulus layer is deeper in the P2K case, the slight reduction in liquid water path for this case must come from a slightly thinner stratocumulus cloud.

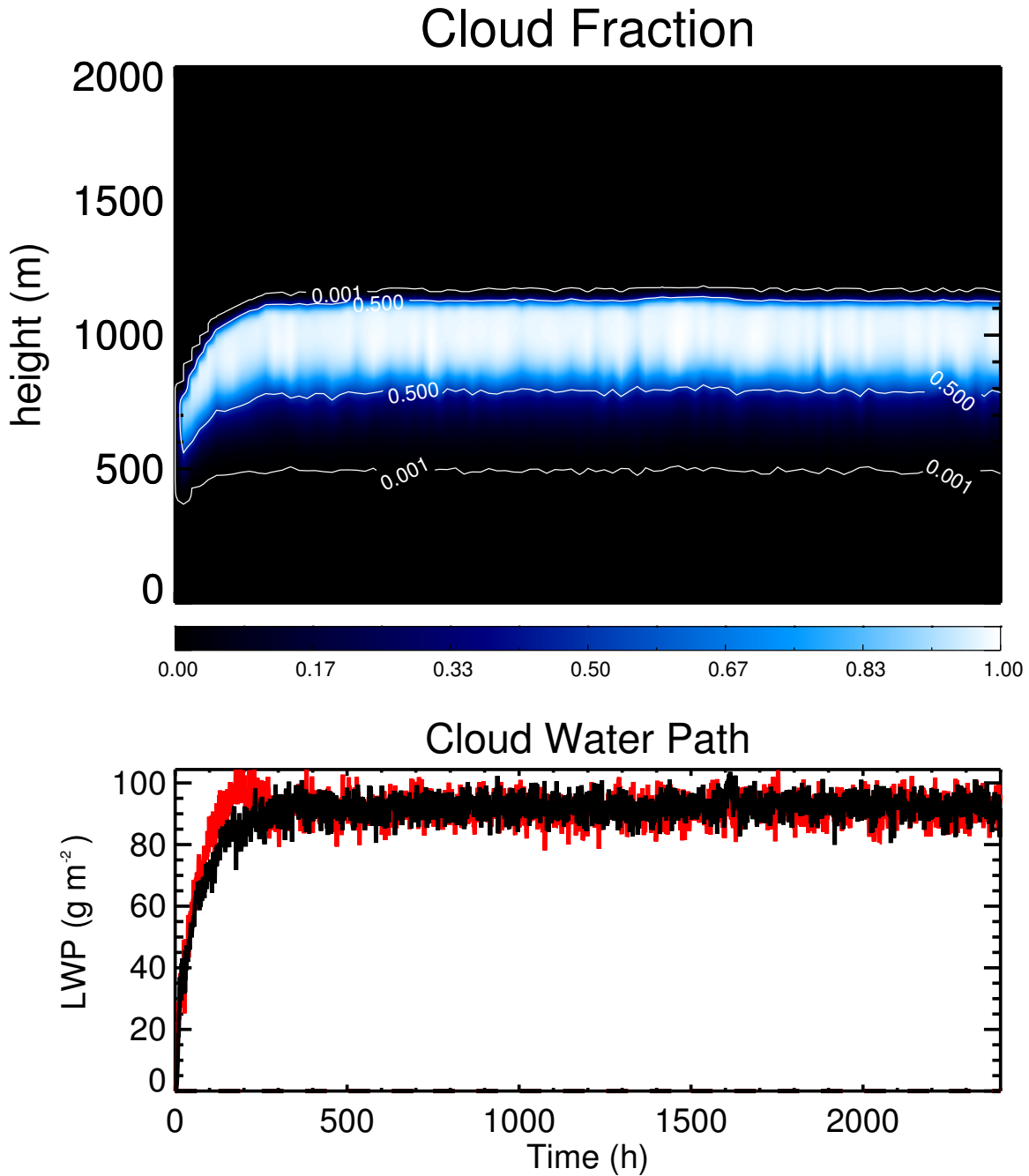


FIGURE 4.13. As in figure 4.9, but for location S11.

Further evidence of the increased decoupling of the stratocumulus layer from the sub-cloud layer is found in figure 4.14. The profiles of $\overline{w'^2}$ and TKE show that the minimum values near the stratocumulus cloud base are significantly lower in the P2K case, indicating that the eddies driven by surface forces and those driven by cloud-top radiative cooling are more separated in that run. Interestingly, the magnitudes of the maximum values of $\overline{w'^2}$, TKE, $\overline{w'\theta'_{il}}$, $\overline{w'q'_t}$, and $\overline{w'\theta'_v}$ in the stratocumulus layer are all the same or slightly greater in the P2K run versus the CTL run, indicating that although decoupling is greater in the P2K simulation, the layer is receiving enough moisture from the sub-cloud layer to thicken and deepen the stratocumulus layer and the increased cloud-top radiative and evaporative cooling is sufficient to sustain the “healthy” stratocumulus deck.

The evolution of the cloud deck simulated at point S11 by the CGILS LES models as discussed in Blossey et al. (2013) is similar to that of THOR, featuring a stratocumulus cloud rising to an equilibrium level with cumulus underneath. The LES models simulate a deeper stratocumulus cloud that reaches up to 1400-1500 m, but this overshoots the observations at this latitude by quite a margin, and THOR’s results are more in-line with observations. In the LES results, the deeper boundary layer is evidence of stronger cloud-top entrainment. In the warmed LES climate simulations, the strong entrainment warming and drying of the boundary layer together with strong decoupling below the stratocumulus layer overcomes the increased surface moisture flux, and the cloud layer thins. For all LES models, the change in net cloud radiative forcing is weak but positive, leading to a weakly positive feedback at this point. It appears the same mechanism is operating in THOR, as the very slight decrease in liquid water path leads to reduced shortwave cloud forcing and weak, positive feedback of 3.3 W m^{-2} .

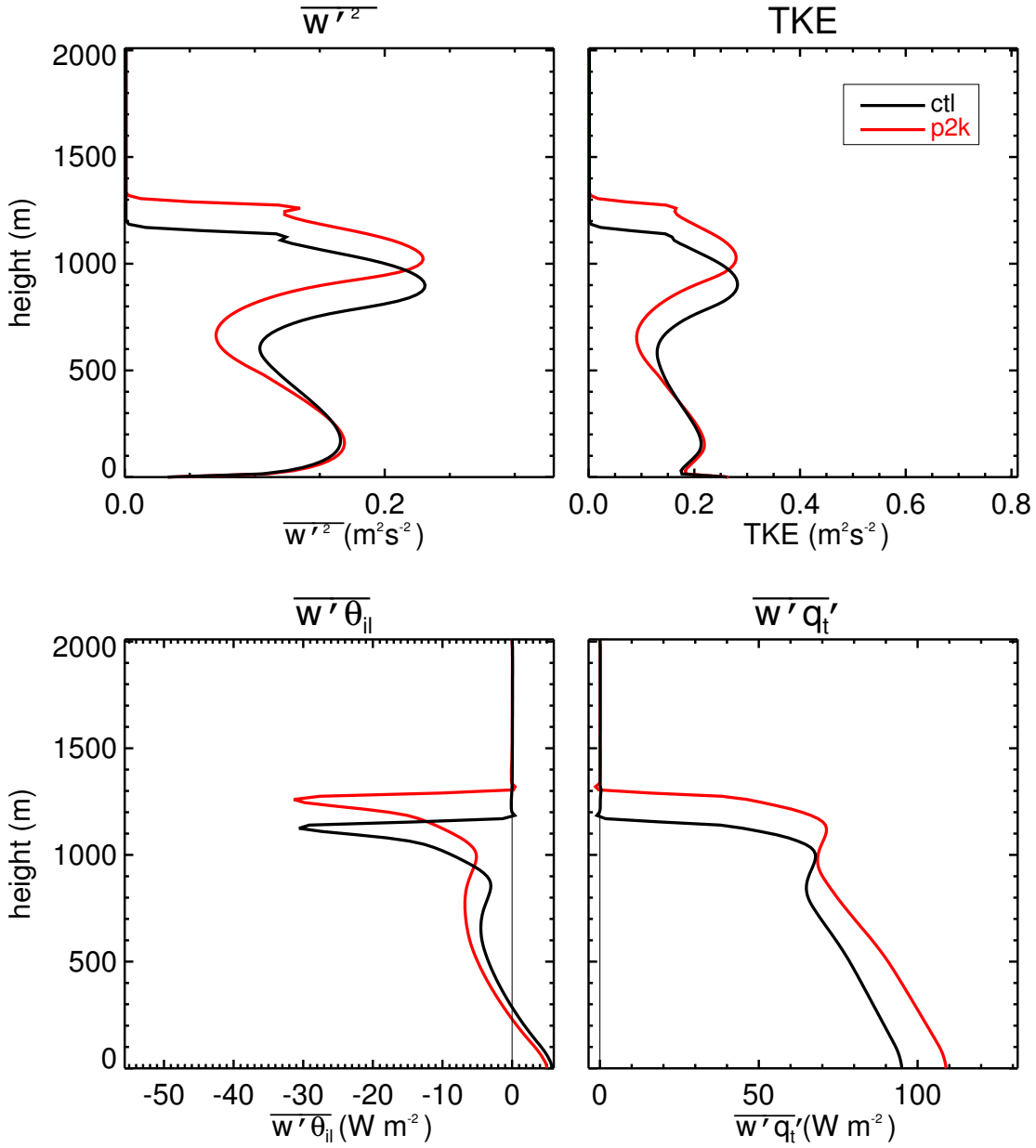


FIGURE 4.14. As in figure 4.10, but for location S11.

4.4. LOCATION S12

Location S12 is the northernmost point simulated in the GPCI cross-section and it is closest to the coast of California. It features the strongest subsidence and the strongest inversion. The mean steady-state thermodynamic profiles for this location for both climate states are shown in figure 4.15 along with the initial profiles for the control case. Of note

are the extremely sharp inversions that develop in the steady state and the constant moisture profile above the inversion. The constant moisture profile above the inversion is the result of the “quick fix” moisture floor as part of the CGILS setup for the S12 location to fix the overactive combined subsidence and advection drying above the boundary layer top. Without the moisture floor above the inversion, excessive drying above cloud top affects the clouds simulated through excessive entrainment drying. Although artificial-looking, the case coordinators maintain that the simulations produced with these modified forcings are representative of the stratocumulus regime at this location. Both the CTL and P2K simulations develop well-mixed layers with very little evidence of decoupling. In the P2K simulation, the boundary layer height increases by about 100 m from 476 m to 575 m, due to the decreased subsidence and the increased latent heat flux.

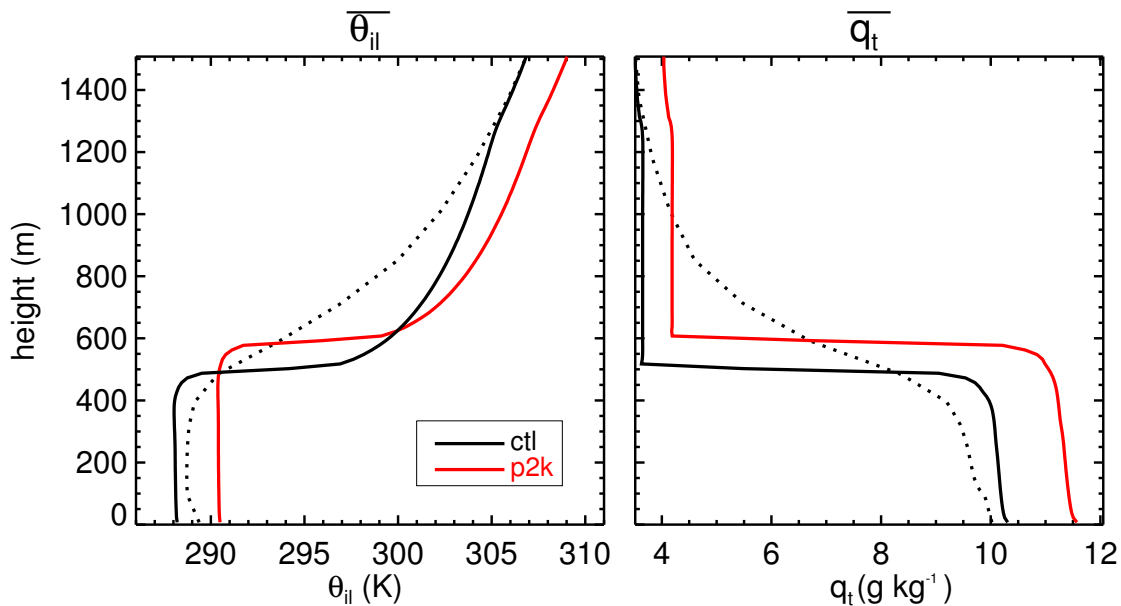


FIGURE 4.15. As in figure 4.7, but for location S12.

The steady-state vertical cloud structure and time evolution are shown in figures 4.16 and 4.17. At first glance, the changes between the CTL and P2K simulations seem minor.

TABLE 4.3. Steady-state values for location S12; as in table 4.2.

Run	z_i [m]	z_b [m]	z_{cb} [m]	shf [W m ⁻²]	lhf [W m ⁻²]	lwp [g m ⁻²]	cld cvr	sfc precip [mm day ⁻¹]	sw crf [W m ⁻²]	lw crf [W m ⁻²]	net crf [W m ⁻²]
ctl	476	255	169	15.19	61.10	42.80	0.966	0.033	-110.67	3.17	-107.50
p2k	575	335	236	11.48	72.79	46.03	0.954	0.044	-109.21	3.63	-105.59
Δ	98	80	67	-3.72	11.69	3.23	-0.012	0.011	1.46	0.46	1.92

In the P2K simulation, there is a very small reduction in the maximum cloud fraction in the stratocumulus layer, from 96.6% to 95.4%, although the maximum liquid water content is increased by about 4%, consistent with the negative cloud feedback mechanism of Betts and Harshvardhan (1987) relating to the increase in available cloud water due to the Clausius-Clapeyron relationship. The depth of the stratocumulus layer calculated from z_i and z_b is 221 m for the CTL simulation versus 240 m for P2K. The combined effect of the deeper stratocumulus layer with more liquid water is an increase in liquid water path of about 7.5% in the P2K simulation.

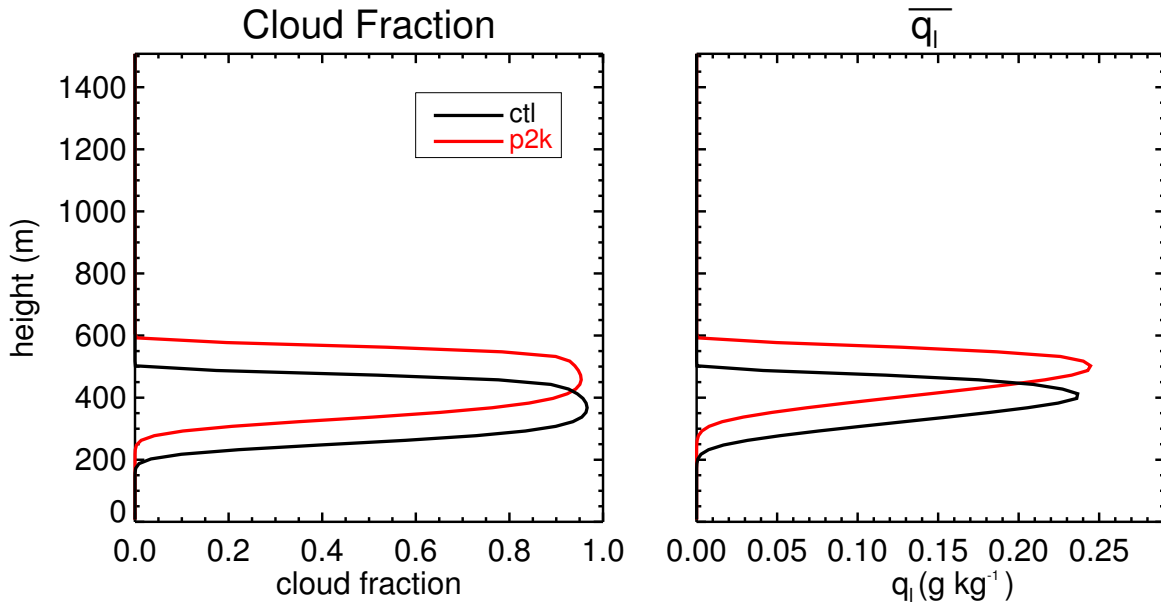


FIGURE 4.16. As in figure 4.8, but for location S12.

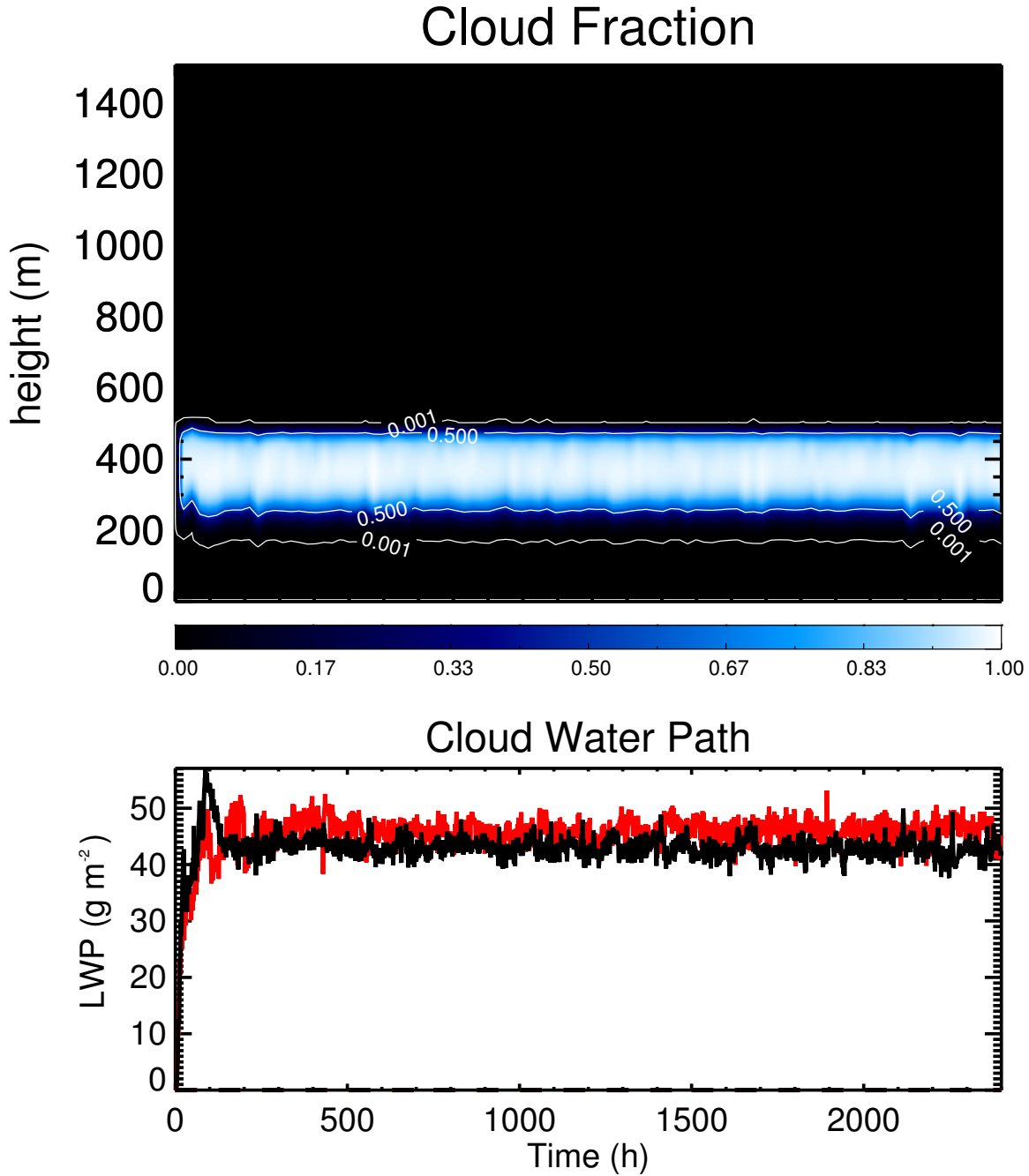


FIGURE 4.17. As in figure 4.9, but for location S12.

The mean profiles of $\overline{w'^2}$, TKE, $\overline{w'\theta'_{il}}$, and $\overline{w'q'_t}$ are shown in figure 4.18 for completeness. The reduced minimum in the $\overline{w'^2}$ profile in the P2K run together with the slightly smoothed out gradient in cloud water at cloud base indicates that the boundary layer might be trending toward a decoupled boundary layer in a warming climate, but this effect is subtle. Other

notable changes include a decrease in the surface sensible heat flux and an increase in the surface latent heat flux, but these are expected given the +2K increase in SST.

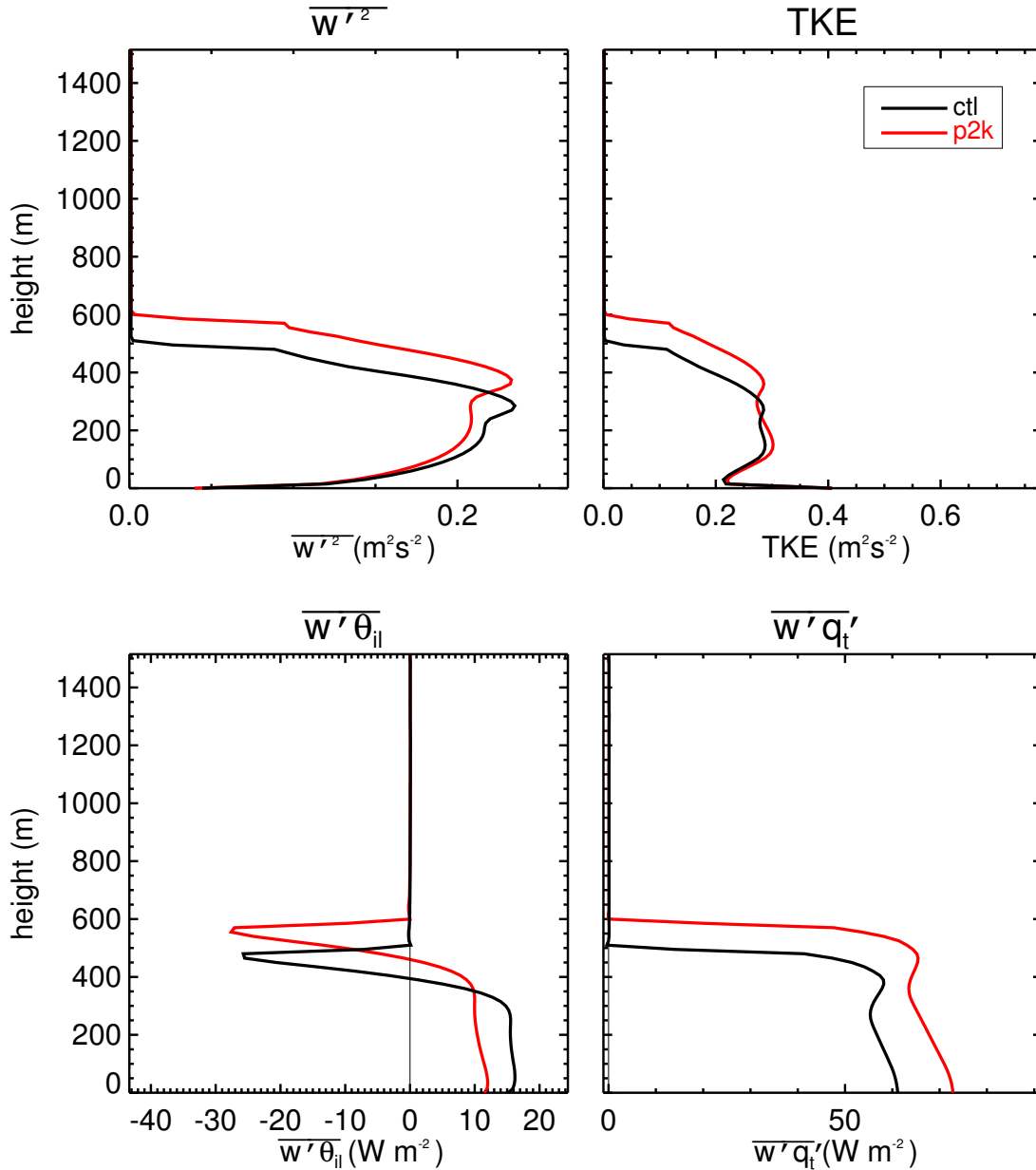


FIGURE 4.18. As in figure 4.10, but for location S12.

In the context of the simulated clouds at point S12, Blossey et al. (2013) discuss the competing thermodynamic and dynamic effects of a warmed climate on stratocumulus clouds. They complete an additional simulation at point S12 that uses all of the changes in initial

state and forcings associated with a +2K SST perturbation except for the subsidence, which they keep the same as the control case. With this additional run, the authors are able to separate the changes in stratocumulus cloud due to the increased temperature alone and the dynamics effect of reduced subsidence. Using this technique, they are able to determine that a stratocumulus deck thins due to the thermodynamic effect and thickens due to the dynamic effect. There is competition and cancellation between these two effects, and in the LES models, the dynamic effect seems to hold greater influence, as the S12 point features thicker clouds in a warmed climate and a small negative feedback. In THOR, although the liquid water path is increased in the P2K simulation, the change in net cloud radiative forcing is actually positive, at 1.92 W m^{-2} . This is likely due to the fact that the maximum cloud fraction has decreased in the P2K simulation. The mechanism that seems to be operating is that the increased entrainment rate induced by the decreased subsidence causes more dry air to evaporate larger “gaps” in the stratocumulus cloud, making them slightly less reflective for shortwave radiation, despite there being slightly higher water content where cloud does exist.

4.5. CROSS SECTION RESULTS

Although the CGILS LES intercomparison only used model runs at three points, broadly representing the shallow cumulus, stratocumulus, and transitional cloud regimes, initial conditions and large-scale forcing profiles were calculated for all points along the GPCI cross-section. It would be extremely computationally demanding to run control and perturbed climate simulations to steady state at all points along the cross-section with LES models, but it can be done with relatively little expense using THOR. In this study, results are presented from simulations of all CGILS points where subsidence exists aloft, where low clouds are

expected to form. All points north of point S5 at latitude 14°N are simulated, covering an additional five points for both the control and perturbed climate. At point S8 (23°N) and southward, THOR is run for 100 simulated days with a grid spacing of 30 m and a domain of between 4000 and 4500 m. For points north of 23°N , grid spacing is reduced to 15 m to better simulate stratocumulus-topped boundary layers and the domain is reduced to better coincide with the expected cloud top height.

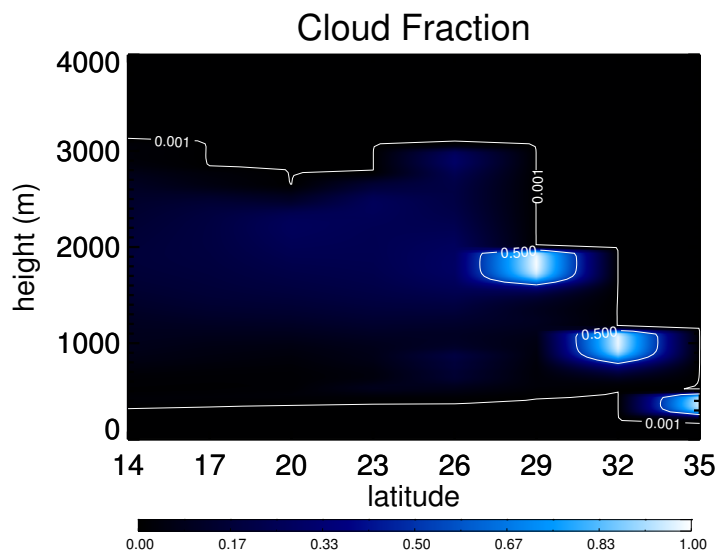


FIGURE 4.19. Cloud fraction as a function of latitude and height along the GPCI cross-section for the control climate.

The steady-state cloud fraction along the cross-section simulated for the control climate is shown in figure 4.19 along with the change in cloud fraction in the perturbed climate in figure 4.20. The analogous plots for the cloud liquid water are shown in figures 4.21 and 4.22. In the control simulation there is a relatively sharp gradient in maximum cloud fraction between latitudes 26°N and 29°N . This coincides with the transition from stratocumulus to shallow cumulus regimes. THOR is able to correctly simulate the lifting of the stratocumulus layer with weakening subsidence and warmer SSTs that occurs in nature at these locations. As discussed in the previous sections, points S12 and S11 (coinciding with latitudes 35°N

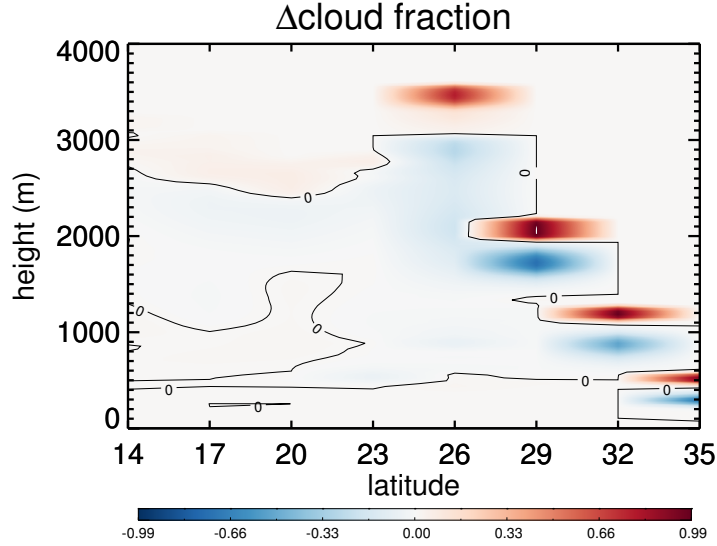


FIGURE 4.20. The change in cloud fraction from the control climate to the perturbed climate as a function latitude and height along the GPCI cross-section.

and 32°N, respectively), feature a well-mixed stratocumulus layer and an elevated stratocumulus layer with a very shallow layer of cumulus underneath, respectively. The transition from cumulus-under-stratocumulus to a purely shallow cumulus regime continues to take place from latitude 29°N all the way to latitude 23°N. At 29°N, the stratocumulus deck still provides nearly 100% coverage, even though the inversion height has risen to nearly 2000 m, and the underlying cumuli are becoming deeper and more energetic. At 26°N, the stratocumulus deck has thinned nearly completely, although the slight cloud fraction maximum at cloud top combined with the higher inversion height there due to cloud-top radiative cooling provide evidence that it remains intact to some extent. At 23°N and southward, THOR tends to predict a similar shallow cumulus cloud structure, although minor differences in inversion height and maximum cloud fraction exist.

In the perturbed climate, the most obvious change is the rise in the inversion height, indicated by the positive/negative pairs in the cloud fraction and cloud water change plots.

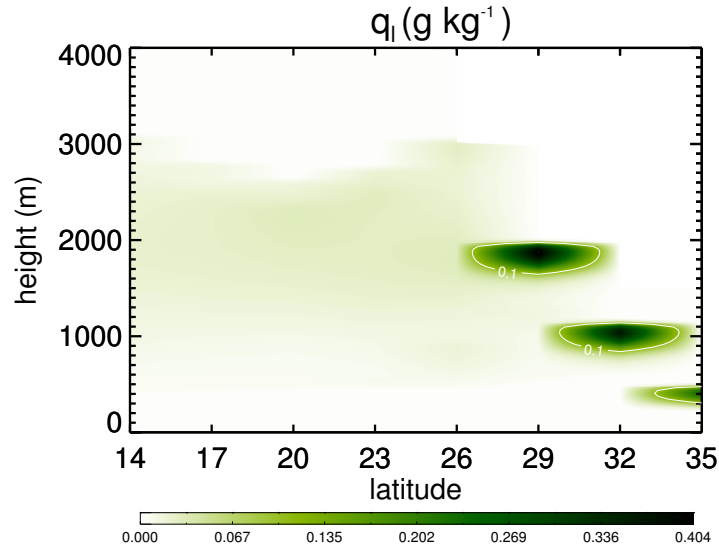


FIGURE 4.21. Cloud liquid water content as a function of latitude and height along the GPCI cross-section for the control climate.

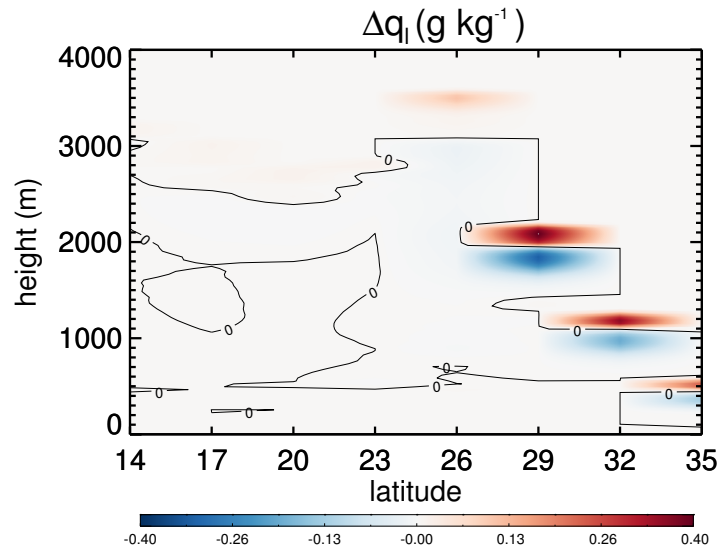


FIGURE 4.22. The change in cloud water content from the control climate to the perturbed climate as a function latitude and height along the GPCI cross-section.

The rise in inversion height increases as one goes poleward from 35°N. There is little apparent change from 23° southward, although it appears as though cloud fraction and liquid water content is reduced in the middle and upper portions of the cumulus field and is displaced upward. The biggest change happens at point S9, at 26°N. Recall that at this point in the

control simulation, a cloud field consisting mostly of cumuli was topped by a thin, broken layer of stratocumulus on the order of 30% cloud fraction. In the perturbed climate, the stratocumulus deck appears to fill in appreciably, to well over 50% areal coverage. In addition, between the increased cloud-top radiatively driven turbulence and weakened subsidence at this location, the boundary layer entrains significantly more free tropospheric air, and the boundary layer depth rises to the highest level at any point along the cross-section.

Values of many diagnostic quantities along the cross-section for both the control and perturbed climate runs are shown in figure 4.23. A common characteristic over the subtropical ocean, the Bowen ratio is quite low throughout the cross-section, and the surface latent heat flux increases as one goes southward, toward warmer SSTs. A +2K SST perturbation is translated into an approximately 10 W m^{-2} increase in the latent heat flux for all points and a very small, roughly 1 W m^{-2} decrease in the sensible heat flux. There is nearly a monotonic increase in inversion height going from 35°N southward along the cross-section except for the “bump” in inversion height near 26°N associated with a local minimum of subsidence in the forcing. Cloud base is nearly constant from north to south at around 500 m, and the stratocumulus depth increases from about 200 m near the coast at 35°N to a maximum of 400 m at 29°N . South of this point, stratocumulus depth decreases as it is thinned away. The liquid water path has a relatively low constant value from latitudes 14°N to about 23°N . Northward of this point, the shallow cumulus regime transitions to the cumulus-under-stratocumulus regime from latitudes 26° to 32°N where a maximum in liquid water path is collocated. The liquid water path decreases from this point toward the coast as the regime switches to thinner stratocumulus. The maximum cloud fraction plot shows a rather sharp transition from a low cloud cover of around 20% to nearly full coverage over

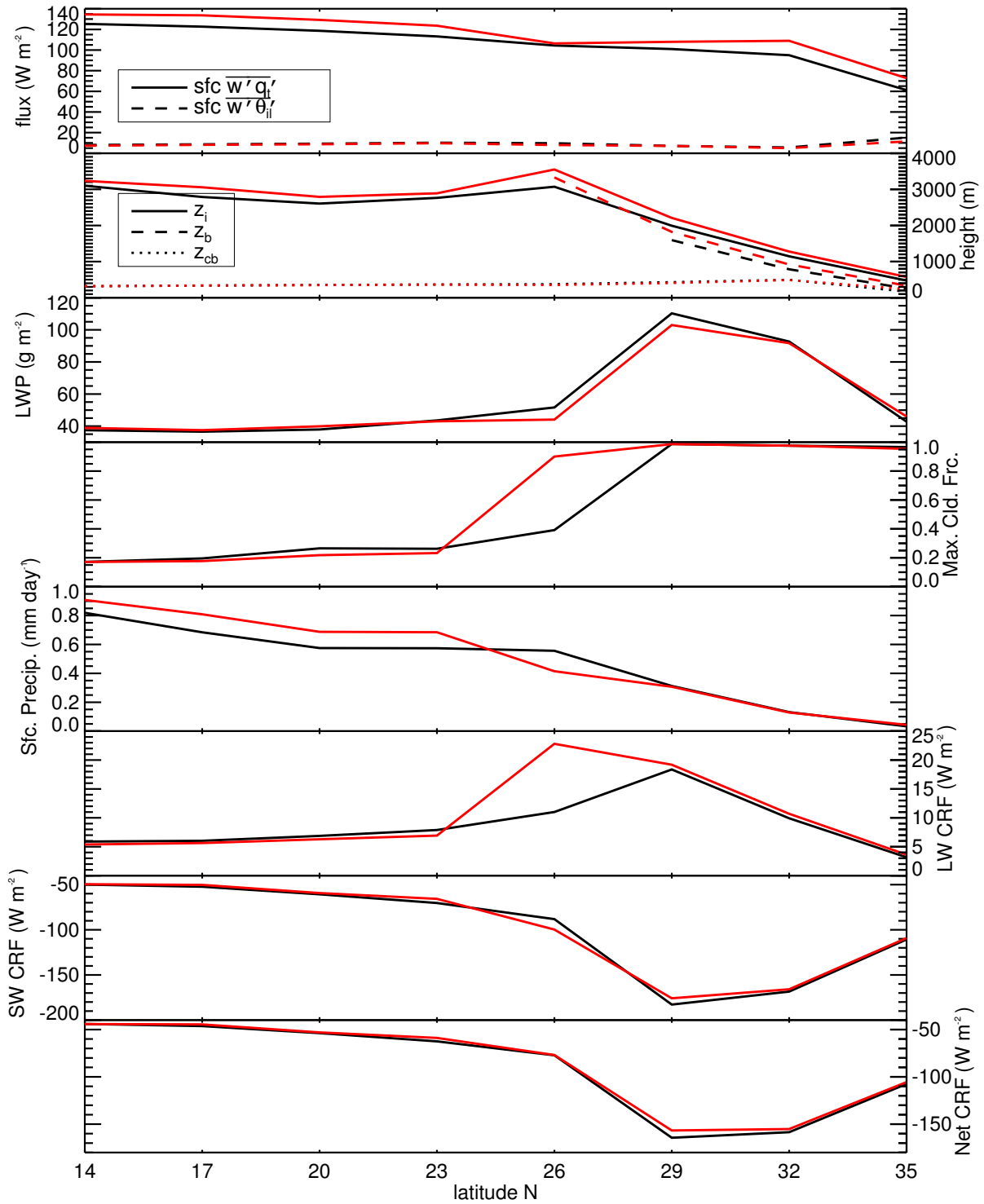


FIGURE 4.23. Sfc. fluxes (first), boundary layer height, Sc base height, and cloud base height (second), liquid water path (third), max. cloud fraction (fourth), sfc. precip. (fifth), longwave CRF (sixth), shortwave CRF (seventh), and net CRF (eighth) for the control climate (black) and the perturbed climate (red) as a function of latitude along the GPCI cross-section.

two simulation points. Surface precipitation decreases monotonically from south to north along the cross section as the more efficient precipitation processes in cumulus give way to the lighter drizzle found in stratocumulus.

The bottom three plots in figure 4.23 show the longwave, shortwave, and net cloud radiative forcing, respectively. The longwave radiative forcing is a function of cloud top temperature in relation to the SST and cloud water content, and therefore the shape of its curve is somewhat determined by a combination of those representing the inversion height, z_i , and the liquid water path. It is weakest near the coast where the cloud is very close to the ground and the cloud-top temperature and SST are very close, and increases as the boundary layer depth and liquid water path increase between latitudes 26° and 32° . The shortwave radiative forcing is determined by how much incoming solar radiation is reflected by clouds compared to reflection by the surface, and is therefore a function of both the liquid water path and the areal cloud cover. The shape of the shortwave cloud radiative forcing is nearly a mirror image of the liquid water path curve. When liquid water path is high, reflection due to clouds is also high, and shortwave cloud forcing is strongly negative. The net cloud radiative forcing is a combination of these two, and is dominated by the shortwave component.

Figure 4.24 summarizes the changes simulated by THOR between the control and perturbed climate states. The rise in inversion height is generally consistent, between 100-200 m, but is considerably higher, as discussed previously, at 26°N due to weaker subsidence, the thickening of the stratocumulus layer, and the resultant increased cloud top cooling and entrainment. The change in liquid water path in the perturbed climate has an interesting pattern. There are modest increases in liquid water path south of 20°N and at the

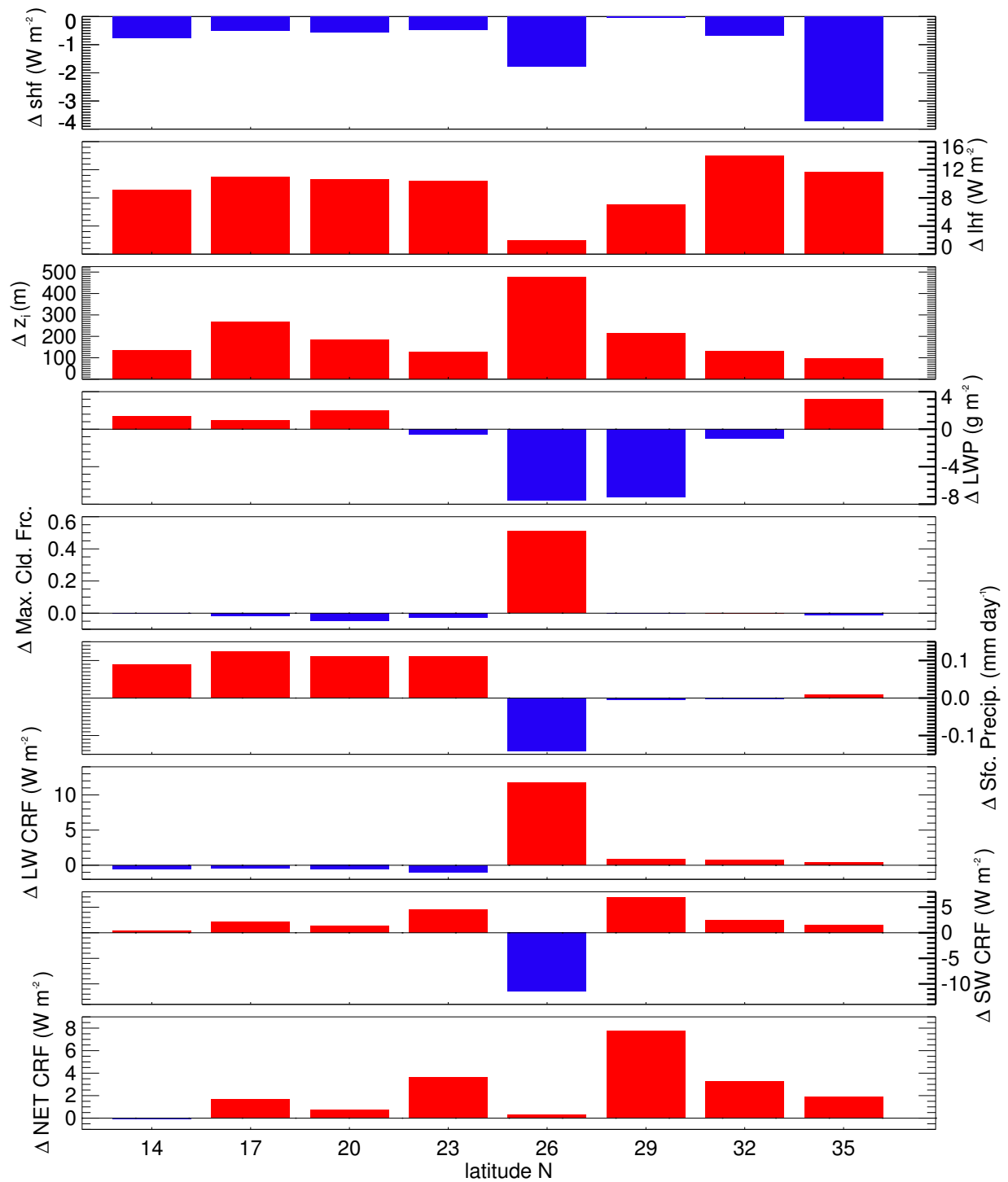


FIGURE 4.24. The change in quantities shown in figure 4.23 for the perturbed climate compared to the control climate for each latitude along the GPCI cross-section that was simulated. Blue bars represent negative change and red bars represent positive change.

northernmost point, but there is a loss of liquid water path in between, with relatively large reductions between 26° and 29°N. The reasons for the reduction in liquid water path for 32°N have been discussed, and it appears to be due to the combined effects of stronger cloud top entrainment mixing bringing in warm and dry air into the boundary layer and greater decoupling of the stratocumulus layer from the moisture-supplying surface layer. The process seems to be stronger at 29°N than at 32°N (point S11), and the associated drop in liquid water path is therefore significantly larger. The increase in liquid water path at 35°N was determined to be due to the fact that warmer air is able to have more water vapor at a given relative humidity and the fact that increased cloud-top entrainment does not quite balance out increased moisture input from surface fluxes. The small increases of liquid water path in the shallow cumulus regime is thought to be the result of slightly deeper cumuli.

There is little change in the maximum cloud fraction in a warmed climate for most latitudes, except for at 26°N. The small reduction in maximum cloud fraction in the cumulus latitudes is thought to mainly be due to increased entrainment of dry air at cloud top, slightly reducing cloud fractions in the detrainment zone. The large increase in maximum cloud fraction at S9, as discussed previously, is due to the transition from shallow cumulus to a cumulus-under-stratocumulus regime at this location in a warmed climate. This change seems to be radiatively driven in THOR. The cloud field initially evolves as cumulus with a very thin, broken stratocumulus layer on top. As the simulation progresses in the warmed climate, there is slightly more liquid water in the stratocumulus layer with slightly stronger radiative cooling. At some point, the radiative cooling seems to reach a threshold where a positive feedback between the condensation and radiation schemes develops, perpetuating the thicker stratocumulus layer, not unlike the physical process of sustaining stratocumulus

layers in nature. The switch from the cumulus to cumulus-under-stratocumulus at 26°N in the perturbed climate run ends up reducing surface precipitation since much of the cloud water that had been part of relatively deep cumulus towers is instead dispersed in thin stratocumulus at the boundary layer top where precipitation processes are less efficient. Surface precipitation for the shallow cumulus latitudes is generally increased by about 0.1 mm day⁻¹ with the slightly deeper cumulus towers and increased surface flux of moisture, and, as discussed in Blossey et al. (2013), the increase helps to modulate the growth of the boundary layer.

The change in the longwave cloud radiative forcing is negligible at every point aside from 26°N. The roughly 12 W m⁻² increase in the longwave radiative forcing (surface warming) at this location is due to the almost 500 m increase in the boundary layer height and associated drop in cloud top temperature together with the displacement of liquid water upward in the column. The increase in longwave cloud radiative forcing is almost entirely offset by the increased cooling due to the shortwave cloud radiative forcing at this location that is the result of the increased coverage of highly reflective stratocumulus clouds. At every other location along the cross-section, cooling due to the reflection of shortwave is decreased (a positive change in shortwave cloud radiative forcing, or warming). At latitudes 23°, 29°, and 32°N, the reduction in shortwave cooling is the result of decreased liquid water path, and also the decreased cloud cover at 23°N. At latitudes 17°, 20°, and 35°N, the reduction in shortwave cooling must be due to the decrease in cloud cover, since the liquid water path has increased at all of these points. The final balance between longwave and shortwave radiative forcings is the net radiative forcing, shown in the bottom plot in figure 4.24. Except for latitude 14°N, where a vanishingly small negative net cloud radiative forcing is calculated, a

positive feedback is calculated at all latitudes. This means that, according to this experiment conducted with THOR, the change in low clouds in a warmed climate is expected to enhance the original warming.

CHAPTER 5

CONCLUSION

Guided by the need to improve the simulation of low cloud cover in AGCMs in order to reduce uncertainties in the projections of future climate, a new, generalized SGS parameterization called THOR has been developed. It was designed to bridge the spatial gap between those processes that are well-represented on a large-scale climate model grid and those that occur on the micro-scale, including what is commonly referred to as turbulence, but also processes like small-scale advection that cannot be captured by larger grids. THOR uses a two-and-a-half order turbulence scheme as its base in order to calculate the statistics of SGS processes. Using the variances, covariances, and skewness values calculated from the turbulence scheme, a trivariate probability density function is diagnosed among the vertical velocity, ice-liquid water potential temperature, and total water specific humidity. The PDF describes exactly how these variables relate to one another, giving the probability of finding a particular (w, θ_{il}, q_t) triplet within a given grid cell. Using this information, one can calculate what percentage of a grid cell is covered with clouds, how much liquid and frozen water is contained in those clouds, and the statistics of how the water is being moved through the grid cell. In addition, such a PDF can be used to more accurately determine how precipitation and radiation interact with the clouds within the grid cell.

At least four novel concepts are included in THOR. The first has to do with how turbulence is dissipated in the two-and-a-half order turbulence scheme. Turbulence is dissipated, or damped, on a time scale that is related to the average time a parcel spends in the largest of the turbulent eddies. The size of these eddies is determined by calculating a quantity called the master turbulence length scale. In order to calculate this length, a parcel model is

used. Parcels are released, given a specific amount of kinetic energy and are tracked as they rise or fall. The distance that the parcels move from their original location is determined both by their initial energy and the static stability of the environment that they encounter. In addition, as the parcels move upward or downward, they are allowed to mix with their environment. The standard way of calculating how much the parcels mix with their environment is to assume that they do so at a low, constant rate. A new procedure was introduced that assumes that entrainment happens as discrete events. How much mixing takes place is determined by the likelihood that a mixing event occurs and the probability that a mixing event exchanges a certain amount of air with its environment. The sensitivity to the new way of calculating turbulence dissipation was investigated in this study.

The second novel concept that is introduced in THOR is the new way to diagnose the trivariate PDF from the turbulence statistics. Although many previous studies have assumed that the diagnosed PDF is in the double-Gaussian family, many dubious assumptions have been made in order to arrive at a particular PDF, given a set of turbulence statistics. Some have assumed that vertical velocity skewness is representative of the skewness of temperature and moisture, and therefore only require one third-order moment. Others have assumed that sub-plume variance is zero or that the sub-plume variance of one Gaussian plume is equal to that of the other Gaussian plume. THOR calculates the double Gaussian PDF parameters using the skewnesses of all variables, and it parameterizes the sub-plume variances so that the minor Gaussian plume that represents the active, or updraft portion of the cloud field, has a higher variances than the major Gaussian plume that represents the environment. In addition, although previous studies have assumed that correlations between vertical velocity and temperature and moisture are zero, THOR relaxes this assumption. Although THOR's

solution requires that a two-equation nonlinear system be solved at each grid level and time step, an efficient algorithm is developed that uses a look-up table that only depends on a variable's skewness and the Gaussian mixture variable.

The third new development included in THOR is the inclusion of a way to calculate condensation over ice in a SGS condensation scheme. Subgrid condensation schemes have existed since the late 1970's, but to the author's knowledge, they have always assumed that condensation takes place over a liquid substrate. Ice is only considered after cloud condensate has been calculated by using a microphysics scheme to freeze some of the condensate. The approach used in THOR generalizes the linearized saturation curve used to calculate what portion of the diagnosed PDF is supersaturated. The linearization approximates the Clausius-Claperyon relationship over ice for extremely cold temperatures, the Clausius-Clapeyron relationship over liquid for temperatures above freezing, and interpolates between the two relationships for temperatures conducive to supercooled cloud droplets.

The fourth novel concept introduced is the use of the diagnosed PDF to calculate radiative transfer through a partially cloudy grid cell. Perhaps the most efficient way to do this would be to use the McICA approach from Pincus et al. (2003) whereby sub-columns that sample the SGS cloudiness are generated and used for each band of a broadband radiative transfer calculation. Due to the complexities of implementing this approach with the current SGS cloudiness scheme, one would probably be tied to using one particular radiation transfer scheme with THOR. To mimic this approach without having to modify the radiation scheme, THOR generates sub-columns that sample the SGS cloudiness, but use a full broadband radiative transfer calculation with each sub-column. Depending on how many sub-columns are generated and how long the radiation time step is, this method can introduce numerical

noise into the simulation and add considerable computational cost. These drawbacks are balanced by the ability to use different radiation schemes, however.

In order to evaluate THOR, five test cases representing a wide range of marine boundary layer clouds were run. For each case, results generated by THOR are compared with an LES ensemble, the members of which participated in published intercomparison studies. Using the LES ensemble as a benchmark, THOR's results were analyzed in order to determine how well it represented various types of boundary layer clouds. Specific attention was paid to the vertical structure of turbulence statistics and simulated cloud structure. Where discrepancies or errors were noted, attempts were made to determine their cause in order to facilitate future improvement and to understand model bias.

After the two shallow cumulus cases were run, the following strengths and weaknesses were determined. In general, THOR produced cloud fields that greatly resembled those produced by LES with well-defined cloud bases and a secondary maximum in cloud fraction in the detrainment zone at cloud top. Cloud liquid water content was well within the range of LES results too. Both cumulus cases, however, developed a sub-cloud layer that was too moist and a cloud layer that was too shallow. The turbulent fluxes of θ_{il} and q_t were found to be slightly too weak, although generally still within the range of LES results. Since third-order moment transport terms were determined to generally be of the proper magnitude, it was determined that the weak turbulent fluxes are probably the result of an improper balance between the pressure correlation and buoyancy terms.

Of the two stratocumulus cases simulated, THOR had better success simulating the subtropical DYCOMS case. THOR was able to simulate and sustain a stratocumulus field of the appropriate thickness with seemingly the right cloud-top entrainment rate as judged

by the inversion rise and cloud top fluxes of θ_{il} and q_t . Profiles of $\overline{w'^2}$, $\overline{w'\theta'_{il}}$, and $\overline{w'q'_t}$ were all very close to the LES ensemble mean. The MPACE case was considerably more challenging for THOR. Although a steady-state stratocumulus cloud was simulated, it was too thin. The biggest error was in the composition of the cloud. THOR produced a cloud that was ice-dominated and relatively heavily-precipitating, whereas LES and observations feature liquid-dominated clouds and lighter precipitation. Most of the issues with the MPACE simulation can be traced back to the temperature dependence used for determining the partition between liquid and ice, copied from the SAM microphysics scheme.

The ASTEX case featured a Lagrangian-style transition from stratocumulus to cumulus as an air mass moved equatorward toward warmer SSTs and weaker subsidence. THOR simulated the gross features of the transition well with thick, precipitating stratocumulus the first night, a thinning and rising cumulus-under-stratocumulus layer during the first day and second night, and finally a cumulus layer under a thin and sparse stratocumulus layer toward the end of the simulation. Throughout the simulation, however, the boundary layer was simulated as too shallow, the result of a weak convective flux of moisture by the cumulus-under-stratocumulus, too much precipitation, and weak cloud-top entrainment.

In addition to evaluating THOR's performance relative to LES models, six sensitivity tests were conducted on the five test cases, where appropriate, to determine how sensitive THOR is to various model formulations. The effect of changing grid spacing was evaluated for all test cases. For the cumulus cases, THOR's results were relatively insensitive to the grid spacing below about 200 m. Above this level, gradients in mean quantities and turbulence statistics were smoothed out, resulting in errors of various significance. In the RICO case, the number of cloud fraction maxima was a function of grid spacing: for grid spacing finer

than 80 m, a trimodal structure developed, whereas for the 160 m run, a bimodal structure developed and a single maximum in the middle of the cloud layer developed for the 320 m case. More significant differences were evident for the stratocumulus cases, as expected. Cloud-top entrainment seemed to be strong function of grid spacing, with coarser resolutions leading to weaker entrainment and a moister and cooler boundary layer with thicker, deeper clouds. For the DYCOMS case, significant errors began to develop in the simulation at grid spacings of 50-100 m, whereas for the MPACE case, the limit seemed to be in the 100-200 m range.

Unlike the grid spacing sensitivity test where the stratocumulus cases displayed greater sensitivity, the cumulus cases show greater sensitivity to how the third-order moments are calculated (the stratocumulus cases showed no sensitivity whatsoever). In addition to the control setup where all third-order moments are diagnosed, all cases were run with the intermediately prognostic (IP) setup where only $\overline{w'^3}$, $\overline{\theta'_{il}^3}$, and $\overline{q'_t^3}$ are predicted and the fully prognostic (FP) setup where all third-order moments are predicted. In both the BOMEX and RICO cases, an oscillation on the order of 10-15 minutes developed when either the IP or FP configurations were used, with the oscillation being strongest in the FP runs. In addition, the IP and FP runs tended to reduce the cloud fraction maximum near cloud base and increase the cloud fraction in the middle and/or upper portions of the cloud. The FP runs for the cumulus cases also had the highest liquid water path of those tested.

Another sensitivity test that seemed to have little effect on the stratocumulus cases but a substantial effect on the cumulus cases was the turbulence length scale entrainment sensitivity test. Three entrainment rates and two entrainment methods were tested. The control simulations used a lower constant rate consistent with observations of shallow cumulus and

previous studies. The higher rate was tested following the work of Romps and Kuang (2010), whose study also led to the development of the stochastic parcel entrainment algorithm. It was found that the higher parcel entrainment rate significantly reduced the turbulence length scale, leading to reduced turbulence and cumulus clouds with higher cloud fractions and liquid water contents, especially near cloud top. Whether the stochastic parcel entrainment algorithm was used or not did not seem to matter much if a lower entrainment rate was assumed. If a higher entrainment rate was assumed, however, the stochastic parcel entrainment algorithm was found to lengthen the turbulence length scale somewhat and to reduce the negative effects of using the higher entrainment rate. For the ASTEX transitional case, the length scale entrainment sensitivity tests did not change the results during the thick stratocumulus phase of the runs, but did influence the simulation when cumuli were introduced below the stratocumulus deck. The higher parcel entrainment rate tended to slow the transition to cumulus, while the lower entrainment rates sped up the transition.

The efficacy of the latin hypercube PDF sampling algorithm was tested by switching the algorithm off and instead calculating microphysics terms using the grid-cell mean variables. For cases with low liquid water content, like the RICO and DYCOMS cases, turning off the PDF sampling algorithm effectively eliminated all precipitation. The grid-cell mean cloud water was not enough to trigger the autoconversion process in the microphysics parameterization. The effect of eliminating precipitation in the cumulus case was to dry out the sub-cloud layer and moisten the middle and upper cloud layers. The increased in-cloud moisture led to more latent heat release and more energetic turbulence through the buoyancy and mechanical production terms, eventually leading to increased cloud-top entrainment and a

deeper boundary layer. For the DYCOMS stratocumulus case, the elimination of precipitation increased cloud water and cloud fraction throughout the cloud layer, but especially at cloud base. The increased latent heating at cloud base did not seem to effect the strength of cloud-top entrainment for that case. Interestingly, the sensitivity test where ice processes were neglected for the MPACE mixed-phase stratocumulus case had a very similar effect. Since the control simulation produced an ice-dominated cloud, and since ice clouds tend to precipitate at a lower cloud water content, the control simulation produced relatively high precipitation. When ice processes were neglected, the cloud water was insufficient to generate precipitation, so the cloud grew increasingly thick, and significantly increased the cloud-top radiative cooling. Due to the strong subsidence however, the additional turbulence generated by latent heating and radiative cooling did not seem to increase the entrainment rate in that case.

The last sensitivity test performed tested the effect of using grid-cell mean values to calculate the radiative transfer instead of sampling the diagnosed PDF. This test was performed for the MPACE and ASTEX cases. For both cases, it was determined that using the PDF sampling scheme to drive the radiative transfer significantly reduced cloud-top radiative cooling. The effect that this had on the simulated cloud field varied. For the MPACE case, the reduced cloud-top cooling did reduce the entrainment rate leading to a cooler and moister boundary layer, but the diagnosed cloud was affected little. For the ASTEX case, it was found that turning *off* the PDF sampling scheme significantly *improved* the simulation of the transition between stratocumulus and cumulus as compared to the LES ensemble mean. It seems as though the algorithm developed for THOR to drive radiation based on the SGS variability leads to a significant underestimate of cloud-top radiative cooling, and

further work should be done to rectify this issue. However, a sensitivity test was performed for the shallow cumulus location of the CGILS experiment that tested the sampling scheme for the radiative transfer (not shown) and it was found that the sampling scheme substantially improved radiative transfer for that case. If grid-cell mean values were used in that case, strong radiative cooling persisted at cloud top, and a cumulus-under-stratocumulus regime was simulated instead of the shallow cumulus regime. It seems as though the PDF sampling scheme is useful for cumulus regimes, but detrimental for use with stratocumulus regimes. Further research is warranted in order to improve the algorithm.

In addition to running standard test cases to evaluate the new model, an additional experiment was performed to investigate low cloud feedbacks as simulated by THOR. As part of the CGILS project, idealized initial profiles and large-scale forcings largely based upon ERA-Interim data along the GPCI cross-section in the northeastern Pacific Ocean were developed. The main goal of the project was to be able to study low cloud feedbacks using LESs and SCMs in an area of the world where low clouds dominate and where transitions between different low cloud regimes can be included. Initial conditions and forcings for both the current climate and a perturbed climate with a +2K SST change were produced to drive the participating models. Three points along the cross-section were chosen to represent the shallow cumulus, cumulus-under-stratocumulus, and coastal stratocumulus regimes for the LES intercomparison. Simulations were performed using THOR for all three locations for both the control and perturbed climate states in order to compare the change in clouds simulated by THOR with those simulated by LES.

For the cumulus regime location, the simulated cloud field became deeper along with the lifting of the subsidence inversion. The slightly deeper cumulus deck ended up with slightly

lower areal coverage and lower water content, especially near cloud top. These changes combined to have little effect on the liquid water path, but shortwave cloud radiative cooling was slightly reduced owing to the slight reduction in cloud cover. The weak positive feedback was similar to the weak positive feedbacks produced by the LES ensemble. For the cumulus-under-stratocumulus point, the simulated cloud field was more decoupled in the perturbed climate with a deeper and more active cumulus layer underneath the stratocumulus layer. The increased cloud-top entrainment slightly thinned the stratocumulus layer, leading to reduced liquid water path, and less shortwave cooling. The consensus of THOR and the LES ensemble was a weak positive feedback for this point. The northernmost point was forced by the strongest subsidence and featured a well-mixed stratocumulus-topped boundary layer. In the perturbed climate, THOR simulated a boundary layer and a slightly deeper cloud layer with a higher maximum liquid water content. However, the reduced areal coverage simulated by THOR led to a very weak positive feedback, counter to the results of the LES ensemble that produced a weak negative feedback.

The CGILS project was extended in this study by simulating five additional locations along the GPCI cross-section, so that the entire subsiding portion of the cross-section was simulated (from 14°N to 35°N). THOR simulated shallow cumulus from 14-23°, cumulus-under-stratocumulus from 26-32°, and well-mixed stratocumulus at 35°N. The boundary layer depth rose nearly monotonically from the northernmost point to the southernmost point, consistent with observations. A relatively sharp transition between low cloud coverage and high cloud coverage is simulated in both climate states, with the transition occurring between 26° and 29° in the control climate and between 23° and 26° in the perturbed climate. Although this seems like an expansion of the areal coverage of the reflective stratocumulus

shield, the liquid water path was simulated to decrease in the transitional zone due to greater boundary layer decoupling and stronger cloud-top entrainment drying. There was little change in the longwave cloud radiative forcing except for at 26°N, where the increase in cloud coverage and the rise in the boundary layer height caused longwave warming to increase by a large margin. The increased shortwave radiative cooling at the same location nearly compensated for the longwave increase, but the net change in cloud radiative forcing at this location was still positive, signifying a positive feedback. At other locations along the cross section, either decreases in liquid water path or areal coverage led to a decrease in shortwave cooling and a positive net change in cloud radiative forcing. For all locations along the cross-section, a positive or neutral feedback was calculated.

Potential exists for considerable future work with THOR. First, it was determined that THOR tends to underestimate the convective moisture and heat fluxes in shallow cumulus layers. The deficiency seems to be rooted in the balance between production of fluxes by the buoyancy terms and destruction of fluxes by the pressure correlation terms. An improved parameterization of the pressure correlation terms for cloudy boundary layers should be a priority for future work. Second, improvements should be made to how cloud water is partitioned between liquid and ice. More accurate methods that include information about cloud condensation nuclei and ice nuclei have been developed and would be a logical step forward. Third, turbulence dissipation seems to be influenced more by the rate of parcel entrainment than by the particular method used to determine parcel mixing. Rather than slowing THOR down with the stochastic Poisson process entrainment, perhaps one could use a single variable entrainment rate that might be a function of parcel speed, buoyancy, and some measure of its size. Fourth, although the PDF sampling algorithm for the radiative transfer scheme

improves radiative transfer in cumulus regimes, it appears to underestimate the radiative flux divergence at cloud top in stratocumulus regimes. This algorithm should be improved to work better in such regimes. Fifth, although a few preliminary deep convective cases have been simulated using THOR (not shown), more work needs to be done to determine its efficacy for simulating these types of clouds if THOR is to be utilized in a AGCM.

The details of THOR's formulation have been discussed at length in this work, including the underlying higher-order closure scheme, the parcel method for determining the turbulence length scale, the new algorithm for determining the trivariate PDF parameters, the improved SGS condensation scheme that accounts for condensation over ice, a new surface layer scheme, and PDF sampling methods for driving any chosen microphysics and radiation parameterizations. Test cases were simulated that represent both shallow cumulus, stratocumulus, and transitional regimes and results were compared with LES ensembles. Finally, an example of the applicability for using THOR to study low cloud feedbacks was presented following the work done as part of the CGILS project along the GPCI cross-section. Despite the shortcomings discovered by simulating standard test cases and running sensitivity tests, THOR has proven to be a useful tool for understanding boundary layer clouds. It remains to be seen whether the advances put forth in this work can be successfully transferred to a AGCM and whether they will improve the representation of boundary layer clouds in climate simulations, but at the very least, they represent progress toward this goal.

BIBLIOGRAPHY

- Ackerman, A. S., et al., 2009: Large-eddy simulations of a drizzling, stratocumulus-topped marine boundary layer. *Monthly Weather Review*, **137**, 1083–1110, doi:DOI 10.1175/2008MWR2582.1.
- André, J., G. DeMoor, G. P. Lacarrère, and R. Vachat, 1976: Turbulence approximation for inhomogeneous flows: Part 2. The numerical simulation of a penetrative convection experiment. *Journal of the Atmospheric Sciences*, **33**, 482–491.
- Barker, H. W., 2008: Representing cloud overlap with an effective decorrelation length: An assessment using CLOUDSAT and CALIPSO data. *Journal of Geophysical Research-Atmospheres*, **113**, D24 205, doi:DOI 10.1029/2008JD010391.
- Beljaars, A., 1995: The parametrization of surface fluxes in large-scale models under free-convection. *Quarterly Journal of the Royal Meteorological Society*, **121** (522), 255–270.
- Benedict, J. J. and D. A. Randall, 2007: Observed characteristics of the MJO relative to maximum rainfall. *Journal of the Atmospheric Sciences*, **64**, 2332–2354, doi:DOI 10.1175/JAS3968.1.
- Betts, A. and Harshvardhan, 1987: Thermodynamic constraint on the cloud liquid water feedback in climate models. *Journal of Geophysical Research-Atmospheres*, **92**, 8483–8485.
- Blossey, P., et al., 2013: Marine low cloud sensitivity to an idealized climate change: The CGILS LES intercomparison. *Journal of Geophysical Research-Atmospheres*, (**accepted**).
- Bogenschutz, P. A., A. Gettelman, H. Morrison, V. E. Larson, D. P. Schanen, N. R. Meyer, and C. Craig, 2012: Unified parameterization of the planetary boundary layer and shallow convection with a higher-order turbulence closure in the community atmosphere model: single-column experiments. *Geoscientific Model Development*, **5**, 1407–1423, doi:DOI 10.5194/gmd-5-1407-2012.
- Bogenschutz, P. A., S. K. Krueger, and M. Khairoutdinov, 2010: Assumed probability density functions for shallow and deep convection. *Journal of Advances In Modeling Earth Systems*, **2**, 10, doi:DOI 10.3894/JAMES.2010.2.10.
- Bony, S. and J. Dufresne, 2005: Marine boundary layer clouds at the heart of tropical cloud feedback uncertainties in climate models. *Geophysical Research Letters*, **32**, L20 806, doi:DOI 10.1029/2005GL023851.
- Bony, S., K. Lau, and Y. Sud, 1997: Sea surface temperature and large-scale circulation influences on tropical greenhouse effect and cloud radiative forcing. *Journal of Climate*, **10**, 2055–2077.
- Bony, S., et al., 2006: How well do we understand and evaluate climate change feedback processes? *Journal of Climate*, **19**, 3445–3482.

- Bougeault, P. and J. C. André, 1986: On the stability of the 3rd-order turbulence closure for the modeling of the stratocumulus-topped boundary-layer. *J. Atmos. Sci.*, **43** (15), 1574–1581.
- Brutsaert, W., 1982: *Evaporation into the atmosphere: theory, history and applications*. D. Reidel Publishing Co.
- Businger, J. A., J. C. Wyngaard, Y. Izumi, and E. Bradley, 1971: Flux-profile relationships in atmospheric surface layer. *J. Atmos. Sci.*, **28** (2), 181–189.
- Canuto, V., F. Minotti, C. Ronchi, R. Ypma, and O. Zeman, 1994: 2nd-order closure PBL model with new 3rd-order moments - comparison with LES data. *Journal of the Atmospheric Sciences*, **51**, 1605–1618.
- Cess, R., et al., 1990: Intercomparison and interpretation of climate feedback processes in 19 atmospheric general-circulation models. *Journal of Geophysical Research-Atmospheres*, **95**, 16 601–16 615.
- Charnock, H., 1955: Wind stress on a water surface. *Quarterly Journal of the Royal Meteorological Society*, **81** (350), 639–640.
- Chen, J.-M., 1991: Turbulence-scale condensation parameterization. *J. Atmos. Sci.*, **48** (12), 1510–1512.
- Cheng, A. and K. Xu, 2006: Simulation of shallow cumuli and their transition to deep convective clouds by cloud-resolving models with different third-order turbulence closures. *Quarterly Journal of the Royal Meteorological Society*, **132**, 359–382, doi:DOI 10.1256/qj.05.29.
- Cheng, A., K. Xu, and J. Golaz, 2004: The liquid water oscillation in modeling boundary layer cumuli with third-order turbulence closure models. *Journal of the Atmospheric Sciences*, **61**, 1621–1629.
- Cheng, A. and K.-M. Xu, 2011: Improved low-cloud simulation from a multiscale modeling framework with a third-order turbulence closure in its cloud-resolving model component. *Journal of Geophysical Research-Atmospheres*, **116**, D14 101, doi:DOI 10.1029/2010JD015362.
- Cheng, Y., V. Canuto, and A. Howard, 2005: Nonlocal convective PBL model based on new third- and fourth-order moments. *J. Atmos. Sci.*, **62** (7), 2189–2204.
- Clement, A. C., R. Burgman, and J. R. Norris, 2009: Observational and model evidence for positive low-level cloud feedback. *Science*, **325**, 460–464, doi:DOI 10.1126/science.1171255.
- Cotton, W., G. Bryan, and S. van den Heever, 2011: *Storm and Cloud Dynamics*, International Geophysics Series, Vol. 99. 2d ed., Academic Press, USA.
- Eitzen, Z. A., K.-M. Xu, and T. Wong, 2011: An estimate of low-cloud feedbacks from variations of cloud radiative and physical properties with sea surface temperature on interannual

- time scales. *Journal of Climate*, **24**, 1106–1121, doi:DOI 10.1175/2010JCLI3670.1.
- Firl, G., 2009: Development of a third-order closure turbulence model with subgrid-scale condensation. M.S. thesis, Colorado State University, Department of Atmospheric Science.
- Golaz, J., V. Larson, and W. Cotton, 2002: A PDF-based model for boundary layer clouds: Part 1. Method and model description. *J. Atmos. Sci.*, **59** (24), 3540–3551.
- Golaz, J.-C., V. E. Larson, J. A. Hansen, D. P. Schanen, and B. M. Griffin, 2007: Elucidating model inadequacies in a cloud parameterization by use of an ensemble-based calibration framework. *Monthly Weather Review*, **135**, 4077–4096.
- Grell, G. A., J. Dudhia, and D. R. Stauffer, 1994: A description of the fifth-generation Penn State/NCAR mesoscale model (MM5). Tech. Rep. NCAR TN-398-1-STR, NCAR Tech. Note.
- Hartmann, D., M. Ockertbell, and M. Michelsen, 1992: The effect of cloud type on Earth’s energy balance: Global analysis. *Journal of Climate*, **5**, 1281–1304.
- Jimenez, P. A., J. Dudhia, J. F. Gonzalez-Rouco, J. Navarro, J. P. Montavez, and E. Garcia-Bustamante, 2012: A revised scheme for the WRF surface layer formulation. *Monthly Weather Review*, **140** (3), 898–918, doi:DOI 10.1175/MWR-D-11-00056.1.
- Khairoutdinov, M. and D. Randall, 2003: Cloud resolving modeling of the ARM summer 1997 IOP: Model formulation, results, uncertainties, and sensitivities. *J. Atmos. Sci.*, **60** (4), 607–625.
- Klein, S. and D. Hartmann, 1993: The seasonal cycle of low stratiform clouds. *Journal of Climate*, **6**, 1587–1606.
- Klein, S. and C. Jakob, 1999: Validation and sensitivities of frontal clouds simulated by the ECMWF model. *Monthly Weather Review*, **127**, 2514–2531.
- Klein, S. A., et al., 2009: Intercomparison of model simulations of mixed-phase clouds observed during the ARM mixed-phase arctic cloud experiment: 1. Single-layer cloud. *Quarterly Journal of the Royal Meteorological Society*, **135**, 979–1002, doi:DOI 10.1002/qj.416.
- Krueger, S., 1988: Numerical-simulation of tropical cumulus clouds and their interaction with the subcloud layer. *Journal of the Atmospheric Sciences*, **45**, 2221–2250.
- Lappen, C. and D. Randall, 2001: Toward a unified parameterization of the boundary layer and moist convection: Part 1. A new type of mass-flux model. *Journal of the Atmospheric Sciences*, **58**, 2021–2036.
- Larson, V. and J. Golaz, 2005: Using probability density functions to derive consistent closure relationships among higher-order moments. *Monthly Weather Review*, **133** (4), 1023–1042.

- Larson, V., J. Golaz, and W. Cotton, 2002: Small-scale and mesoscale variability in cloudy boundary layers: Joint probability density functions. *J. Atmos. Sci.*, **59** (24), 3519–3539.
- Larson, V., J. Golaz, H. Jiang, and W. Cotton, 2005: Supplying local microphysics parameterizations with information about subgrid variability: Latin hypercube sampling. *J. Atmos. Sci.*, **62** (11), 4010–4026.
- Larson, V., R. Wood, P. Field, J. Golaz, T. Haar, and W. Cotton, 2001a: Small-scale and mesoscale variability of scalars in cloudy boundary layers: One-dimensional probability density functions. *Journal of the Atmospheric Sciences*, **58**, 1978–1994.
- Larson, V., R. Wood, P. Field, J. Golaz, T. Vonder Haar, and W. Cotton, 2001b: Systematic biases in the microphysics and thermodynamics of numerical models that ignore subgrid-scale variability. *J. Atmos. Sci.*, **58** (9), 1117–1128.
- Lawrence, M., 2005: The relationship between relative humidity and the dewpoint temperature in moist air - a simple conversion and applications. *Bulletin of the American Meteorological Society*, **86**, 225–+, doi:DOI 10.1175/BAMS-86-2-225.
- Lewellen, W. S. and S. Yoh, 1993: Binormal model of ensemble partial cloudiness. *J. Atmos. Sci.*, **50** (9), 1228–1237.
- Li, Y., Z. Gao, D. H. Lenschow, and F. Chen, 2010: An improved approach for parameterizing surface-layer turbulent transfer coefficients in numerical models. *Boundary-Layer Meteorology*, **137** (1), 153–165, doi:DOI 10.1007/s10546-010-9523-y.
- Lin, W. and M. Zhang, 2004: Evaluation of clouds and their radiative effects simulated by the NCAR community atmospheric model against satellite observations. *Journal of Climate*, **17**, 3302–3318.
- Marchand, R. and T. Ackerman, 2010: An analysis of cloud cover in multiscale modeling framework global climate model simulations using 4 and 1 km horizontal grids. *Journal of Geophysical Research-Atmospheres*, **115**, D16 207, doi:DOI 10.1029/2009JD013423.
- Marchand, R., J. Haynes, G. G. Mace, T. Ackerman, and G. Stephens, 2009: A comparison of simulated cloud radar output from the multiscale modeling framework global climate model with CLOUDSAT cloud radar observations. *Journal of Geophysical Research-Atmospheres*, **114**, D00A20, doi:DOI 10.1029/2008JD009790.
- Medeiros, B., L. Nuijens, C. Antoniazzi, and B. Stevens, 2010: Low-latitude boundary layer clouds as seen by CALIPSO. *Journal of Geophysical Research-Atmospheres*, **115**, D23 207, doi:DOI 10.1029/2010JD014437.
- Medeiros, B. and B. Stevens, 2011: Revealing differences in GCM representations of low clouds. *Climate Dynamics*, **36**, 385–399, doi:DOI 10.1007/s00382-009-0694-5.
- Mellor, G. L., 1977: Gaussian cloud model relations. *J. Atmos. Sci.*, **34** (2), 356–358.

- Miller, R., 1997: Tropical thermostats and low cloud cover. *Journal of Climate*, **10**, 409–440.
- Neggers, R. A. J., J. D. Neelin, and B. Stevens, 2007: Impact mechanisms of shallow cumulus convection on tropical climate dynamics. *Journal of Climate*, **20**, 2623–2642, doi:DOI 10.1175/JCLI4079.1.
- Noda, A. T., K. Oouchi, M. Satoh, H. Tomita, S.-i. Iga, and Y. Tsushima, 2010: Importance of the subgrid-scale turbulent moist process: Cloud distribution in global cloud-resolving simulations. *Atmospheric Research*, **96**, 208–217, doi:DOI 10.1016/j.atmosres.2009.05.007.
- Norris, J., 1998: Low cloud type over the ocean from surface observations: Part 2. Geographical and seasonal variations. *Journal of Climate*, **11**, 383–403.
- Norris, J. and C. Weaver, 2001: Improved techniques for evaluating GCM cloudiness applied to the NCAR CCM3. *Journal of Climate*, **14**, 2540–2550.
- Peters, M. E. and C. S. Bretherton, 2006: Structure of tropical variability from a vertical mode perspective. *Theoretical and Computational Fluid Dynamics*, **20**, 501–524, doi:DOI 10.1007/s00162-006-0034-x.
- Pincus, R., H. Barker, and J. Morcrette, 2003: A fast, flexible, approximate technique for computing radiative transfer in inhomogeneous cloud fields. *Journal of Geophysical Research-Atmospheres*, **108**, 4376, doi:DOI 10.1029/2002JD003322.
- Pincus, R., C. Hannay, S. Klein, K. Xu, and R. Hemler, 2005: Overlap assumptions for assumed probability distribution function cloud schemes in large-scale models. *Journal of Geophysical Research-Atmospheres*, **110**, D15S09, doi:DOI 10.1029/2004JD005100.
- Räisänen, P., H. Barker, M. Khairoutdinov, J. Li, and D. Randall, 2004: Stochastic generation of subgrid-scale cloudy columns for large-scale models. *Quarterly Journal of the Royal Meteorological Society*, **130**, 2047–2067, doi:DOI 10.1256/qj.03.99.
- Randall, D., 2012: Gaussian entrainment, QuickStudies in Atmospheric Science.
- Randall, D., Q. Shao, and C. Moeng, 1992: A 2nd-order bulk boundary-layer model. *Journal of the Atmospheric Sciences*, **49**, 1903–1923.
- Randall, D., et al., 2007: Climate models and their evaluation. *Climate Change 2007: The Physical Science Basis. Contribution of Working Group I to the Fourth Assessment Report of the Intergovernmental Panel on Climate Change*, S. Solomon, D. Qin, M. Manning, Z. Chen, M. Marquis, K. Averyt, M. Tignor, and H. Miller, Eds., Cambridge University Press, 589–682.
- Ringer, M. and R. Allan, 2004: Evaluating climate model simulations of tropical cloud. *Tellus Series A-Dynamic Meteorology and Oceanography*, **56**, 308–327.
- Romps, D. M. and Z. Kuang, 2010: Nature versus nurture in shallow convection. *J. Atmos. Sci.*, **67** (5), 1655–1666, doi:DOI 10.1175/2009JAS3307.1.

- Rossow, W. and R. Schiffer, 1999: Advances in understanding clouds from ISCCP. *Bulletin of the American Meteorological Society*, **80**, 2261–2287.
- Siebesma, A., et al., 2003: A large eddy simulation intercomparison study of shallow cumulus convection. *Journal of the Atmospheric Sciences*, **60**, 1201–1219.
- Soden, B. J. and G. A. Vecchi, 2011: The vertical distribution of cloud feedback in coupled ocean-atmosphere models. *Geophysical Research Letters*, **38**, L12704, doi:DOI 10.1029/2011GL047632.
- Sommeria, G. and J. W. Deardorff, 1977: Subgrid-scale condensation in models of nonprecipitating clouds. *J. Atmos. Sci.*, **34** (2), 344–355.
- Stephens, G., 2010: Is there a missing low cloud feedback in current climate models. *Global Energy and Water Cycle Experiment News*, **20**, 5–7.
- Stevens, B. and G. Feingold, 2009: Untangling aerosol effects on clouds and precipitation in a buffered system. *Nature*, **461**, 607–613, doi:DOI 10.1038/nature08281.
- Stevens, B., et al., 2005: Evaluation of large-eddy simulations via observations of nocturnal marine stratocumulus. *Monthly Weather Review*, **133**, 1443–1462.
- Stull, R. B., 1988: *An introduction to boundary layer meteorology*. Kluwer Academic Publishers, Dordrecht, URL <http://www.loc.gov/catdir/enhancements/fy1006/88015564-d.html>.
- Tao, W.-K., et al., 2009: A multiscale modeling system developments, applications, and critical issues. *Bulletin of the American Meteorological Society*, **90**, 515–+, doi:DOI 10.1175/2008BAMS2542.1.
- Teixeira, J., et al., 2011: Tropical and subtropical cloud transitions in weather and climate prediction models: The GCSS/WGNE Pacific cross-section intercomparison (GPCI). *Journal of Climate*, **24**, 5223–5256, doi:DOI 10.1175/2011JCLI3672.1.
- Tselioudis, G., A. DelGenio, W. Kovari, and M. Yao, 1998: Temperature dependence of low cloud optical thickness in the GISS GCM: Contributing mechanisms and climate implications. *Journal of Climate*, **11**, 3268–3281.
- Tselioudis, G. and C. Jakob, 2002: Evaluation of midlatitude cloud properties in a weather and a climate model: Dependence on dynamic regime and spatial resolution. *Journal of Geophysical Research-Atmospheres*, **107**, 4781, doi:DOI 10.1029/2002JD002259.
- Tselioudis, G. and W. Rossow, 1994: Global, multiyear variations of optical-thickness with temperature in low and cirrus clouds. *Geophysical Research Letters*, **21**, 2211–2214.
- van der Dussen, J., et al., 2013: The GASS/EUCLIPSE model intercomparison of the stratocumulus transition as observed during ASTEX: LES results. *Journal of Advances In Modeling Earth Systems*, (in press).

- vanZanten, M. C., et al., 2011: Controls on precipitation and cloudiness in simulations of trade-wind cumulus as observed during RICO. *Journal of Advances In Modeling Earth Systems*, **3**, M06 001, doi:DOI 10.1029/2011MS000056.
- Weare, B., 2004: A comparison of AMIP II model cloud layer properties with ISCCP D2 estimates. *Climate Dynamics*, **22**, 281–292, doi:DOI 10.1007/s00382-003-0374-9.
- Webb, M., C. Senior, S. Bony, and J. Morcrette, 2001: Combining ERBE and ISCCP data to assess clouds in the Hadley Centre, ECMWF and LMD atmospheric climate models. *Climate Dynamics*, **17**, 905–922.
- Webb, M. J., et al., 2006: On the contribution of local feedback mechanisms to the range of climate sensitivity in two GCM ensembles. *Climate Dynamics*, **27**, 17–38, doi:DOI 10.1007/s00382-006-0111-2.
- Wood, R. and C. S. Bretherton, 2006: On the relationship between stratiform low cloud cover and lower-tropospheric stability. *Journal of Climate*, **19**, 6425–6432.
- Zeman, O. and J. Lumley, 1976: Modeling buoyancy driven mixed layers. *Journal of the Atmospheric Sciences*, **33**, 1974–1988.
- Zhang, C. and S. M. Hagos, 2009: Bi-modal structure and variability of large-scale diabatic heating in the tropics. *Journal of the Atmospheric Sciences*, **66**, 3621–3640, doi:DOI 10.1175/2009JAS3089.1.
- Zhang, M., C. S. Bretherton, P. N. Blossey, S. Bony, F. Brient, and J.-C. Golaz, 2012: The CGILS experimental design to investigate low cloud feedbacks in general circulation models by using single-column and large-eddy simulation models. *Journal of Advances In Modeling Earth Systems*, **4**, M12 001, doi:DOI 10.1029/2012MS000182.
- Zhang, M., et al., 2005: Comparing clouds and their seasonal variations in 10 atmospheric general circulation models with satellite measurements. *Journal of Geophysical Research-Atmospheres*, **110**, D15S02, doi:DOI 10.1029/2004JD005021.

APPENDIX A

ESTIMATED INVERSION STRENGTH CALCULATION

Wood and Bretherton (2006) define the EIS as

$$\text{EIS} = \text{LTS} - \Gamma_m^{850} (z_{700} - \text{LCL}) \quad (137)$$

where LTS is the lower tropospheric stability defined as

$$\text{LTS} = \theta_{700} - \theta_{sfc} \quad (138)$$

and Γ_m^{850} is the moist adiabatic lapse rate at 850 hPa, LCL is the lifted condensation level, and z_{700} is the height of the 700 hPa surface. The moist adiabatic lapse rate can be calculated with

$$\Gamma_m(T, p) = \frac{g}{c_p} \left[1 - \frac{1 + \frac{L_v q_s(T, p)}{R_a T}}{1 + \frac{L_v^2 q_s(T, p)}{c_p R_v T^2}} \right] \quad (139)$$

where g is the gravitational acceleration, c_p is the specific heat of dry air at constant pressure, L_v is the latent heat of vaporization, R_a is the dry air gas constant, R_v is the water vapor gas constant, and q_s is the saturation specific humidity. The LCL may readily be estimated by the Epsy formula (Lawrence 2005)

$$\text{LCL} = 125 (T_{sfc} - T_{d_{sfc}}) \quad (140)$$

The dewpoint temperature can be calculated by solving Tetens's saturation formula for T :

$$T_d = \frac{35.86 * \ln\left(\frac{e}{6.1078}\right) - 17.2693882 * 273.16}{\ln\left(\frac{e}{6.1078}\right) - 17.2693882} \quad (141)$$

where e is the water vapor partial pressure, easily calculable from the specific humidity with a standard formula.

Of course, this formula is only applicable for model domains that extend up to 700 hPa. Using a shallower domain can be warranted for study of low clouds. In such a case, EIS is

approximated by the formula

$$EIS_{\text{approx}} = (\theta_{\text{model top}} - \theta_{sfc}) - \Gamma_m^{\text{model midpoint}} (z_{\text{model top}} - LCL) \quad (142)$$

APPENDIX B

PARCEL CONDENSATION

It is assumed that the values of θ_{il} , q_t , and p are known from the parcel model. First, calculate the parcel ice-liquid temperature since the parcel pressure is known.

$$T_{il_{\text{parcel}}} = \left(\frac{p_{\text{parcel}}}{p_0} \right)^\kappa \theta_{il_{\text{parcel}}} \quad (143)$$

If, $T_{il_{\text{parcel}}} > 273.16$, then there is only the potential for liquid condensate, and the saturation specific humidity using the liquid water temperature is calculated with

$$q_{s_{il}} = \frac{\varepsilon e_s}{p_{\text{parcel}} - (1 - \varepsilon)e_s} \quad (144)$$

where e_s is given by Tetens's formula

$$e_s = 6.1078e^{\frac{17.2693882(T_{il_{\text{parcel}}} - 273.16)}{T_{il_{\text{parcel}}} - 35.86}}. \quad (145)$$

The quantity s is calculated using

$$s_{\text{parcel}} = c_{qt} \left(q_{t_{\text{parcel}}} - q_{s_{il}} \right) \quad (146)$$

where

$$c_{qt} = \frac{1}{1 + \frac{\varepsilon L_v^2 q_{s_{il}}}{c_p R_d T_{il_{\text{parcel}}}^2}} \quad (147)$$

Finally, the parcel liquid water content is given by

$$q_{l_{\text{parcel}}} = \text{MAX}(s_{\text{parcel}}, 0) \quad (148)$$

If, $T_{il_{\text{parcel}}} \leq 273.16$, then the parcel condensate will contain at least some ice. The amount of ice depends only on the parcel temperature as determined in the SAM model microphysics. Since the parcel temperature depends on the parcel liquid and ice condensate, a simple iterative procedure is used:

- (1) Calculate the saturation specific humidities over liquid and ice using (144) and (149).
- (2) Calculate the first guess w_n assuming no cloud condensate ($T = T_{il}$) using equation (85).
- (3) Calculate c_{qt} according to (151) and s according to (152).
- (4) Using values calculated in step 3, calculate new values of parcel water and ice using equations (153) and (154).
- (5) Calculate a new estimate of temperature using the definition of T_{il} (68).
- (6) Calculate a new estimate for w_n using (85).
- (7) Repeat steps 3 - 6 until the change in temperature estimates is below some threshold, currently 0.001 K.

The following equations are used in the iterative procedure:

$$q_{s_{iil}} = \frac{\varepsilon e_{s_i}}{p_{parcel} - (1 - \varepsilon)e_{s_i}} \quad (149)$$

$$e_{s_i} = 6.112e^{\frac{22.46(T_{il_{parcel}} - 273.15)}{272.62 + (T_{il_{parcel}} - 273.15)}}. \quad (150)$$

$$c_{qt} = \frac{1}{1 + \frac{\varepsilon}{c_p R_d T_{il_{parcel}}^2} \left\{ [w_n L_v + (1 - w_n) L_s] [w_n L_v q_{s_{iil}} + (1 - w_n) L_s q_{s_{iil}}] \right\}} \quad (151)$$

$$s_{parcel} = c_{qt} \left\{ q_{t_{parcel}} - [w_n q_{s_{iil}} + (1 - w_n) q_{s_{iil}}] \right\} \quad (152)$$

$$q_{l_{parcel}} = w_n \text{MAX}(s_{parcel}, 0) \quad (153)$$

$$q_{i_{parcel}} = (1 - w_n) \text{MAX}(s_{parcel}, 0) \quad (154)$$

APPENDIX C

NOTES ON SOLVING THE NONLINEAR SYSTEM

Let $p = (\bar{x}_2 - \bar{x}_1)$ and $q = \sigma_x$. Then the system (55), (57) becomes

$$\begin{aligned} 2q^2 + a(1-a)p^2 - \left(\bar{x}'^2 - \bar{x}'^2_{thresh}\right) &= 0 \\ (1-2a)p \left[q^2 + \left(\bar{x}'^2 - \bar{x}'^2_{thresh}\right) \right] - \bar{x}'^3 &= 0 \end{aligned} \tag{155}$$

Many methods exist for solving a system of nonlinear equations, including Newton's method, Broyden's method, and Powell's method. One popular FORTRAN package that uses Powell's method is MINPACK, and it is used here. Powell's method requires the Jacobian of the system, and although MINPACK contains routines to calculate the Jacobian numerically, it is easy enough to calculate the Jacobian analytically for this system:

$$J = \begin{Bmatrix} 2a(1-a)p & 4q \\ (1-2a) \left[q^2 + \left(\bar{x}'^2 - \bar{x}'^2_{thresh}\right) \right] & 2(1-2a)pq \end{Bmatrix} \tag{156}$$

Figure C.1 shows the solution to the system as a function of skewness with assumed variance of unity for different values of a . Solid lines denote the bias whereas dashed lines denote σ_x^2 . Note that there is a maximum value of skewness below which a valid solution to the system exists for each a . Regardless of the value of a , for zero skewness the bias is zero (as expected) and the value of σ_x^2 is at a maximum, namely $\frac{\bar{x}'^2 - \bar{x}'^2_{thresh}}{2}$. As skewness increases, the bias increases and the sub-plume variance decreases regardless of a , although the higher a is, steeper the increase in the bias and the decrease in the sub-plume variance. Interestingly, the sub-plume variance tends to stay near its maximum through much of the range of permissible skewness values, and only drops off appreciably as the skewness approaches its maximum value for a given a . Likewise, the bias seems to increase linearly with skewness until its growth accelerates as the skewness approaches its maximum value.

Unfortunately, solving this simple nonlinear system at every level in the model domain every time step using MINPACK is very expensive. Compared to using a purely analytical

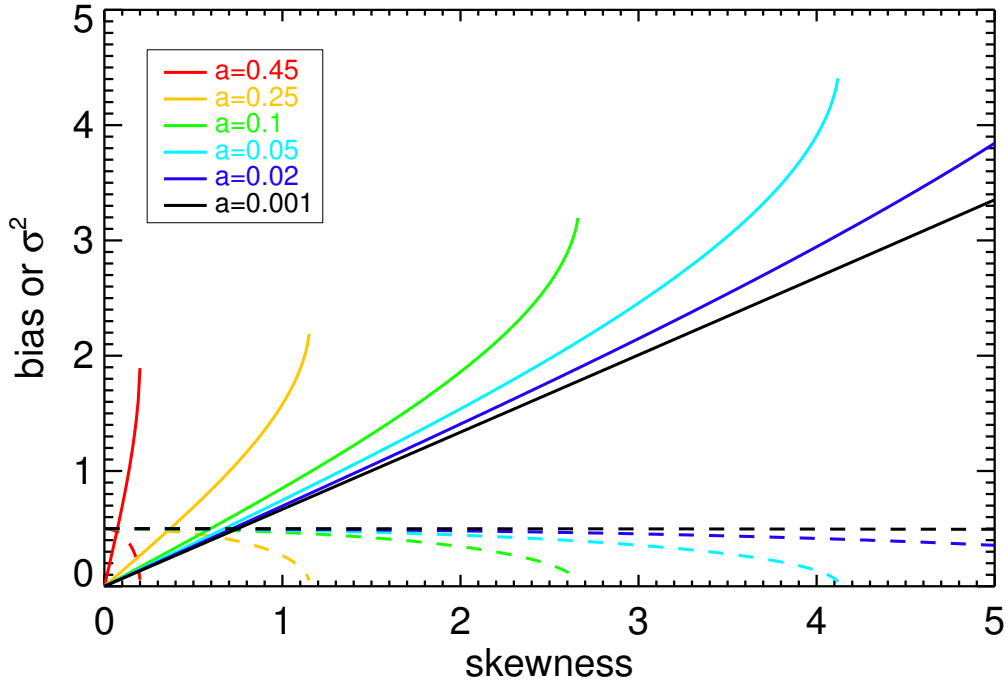


FIGURE C.1. The solution to the nonlinear system (55),(57) for various values of a as a function of skewness. The input variance is 1. Solid lines are the bias. Dashed lines are σ_x^2 .

scheme as in Larson et al. (2002), using this method is nearly an order of magnitude slower. A significant improvement in algorithm efficiency can be achieved by making use of a lookup table for solving the nonlinear system. The lookup table is constructed as a function of skewness and a . The domain of skewness is $[0, 3]$ and the domain of a is $[0, 0.49]$. The system is solved at one million points in the two-dimensional domain using MINPACK and an assumed value of variance of 10. The lookup table needs only to be generated once and requires about 8 MB of computer storage/memory with double precision floating point values. Since the actual magnitudes of the variances among w , θ_{il} , and q_t varies by several orders of magnitude (from $0-10 \text{ m}^2\text{s}^{-2}$ for w variance to $0-1 \times 10^{-4} \text{ kg}^2\text{kg}^{-2}$ for q_t variance), it is necessary to scale the lookup table output to the appropriate variance at each point in space-time. Exchanging the nonlinear system solver in the model for the simple interpolation required for the lookup table increases the efficiency of the algorithm about an order of magnitude so that this parameterization is comparable in speed to a purely analytical one.

Figures C.2 and C.3 display the calculated lookup table for a skewness domain of $[0, 5]$. The dotted lines in both plots denote the maximum value of a where a solution exists for each value of skewness.

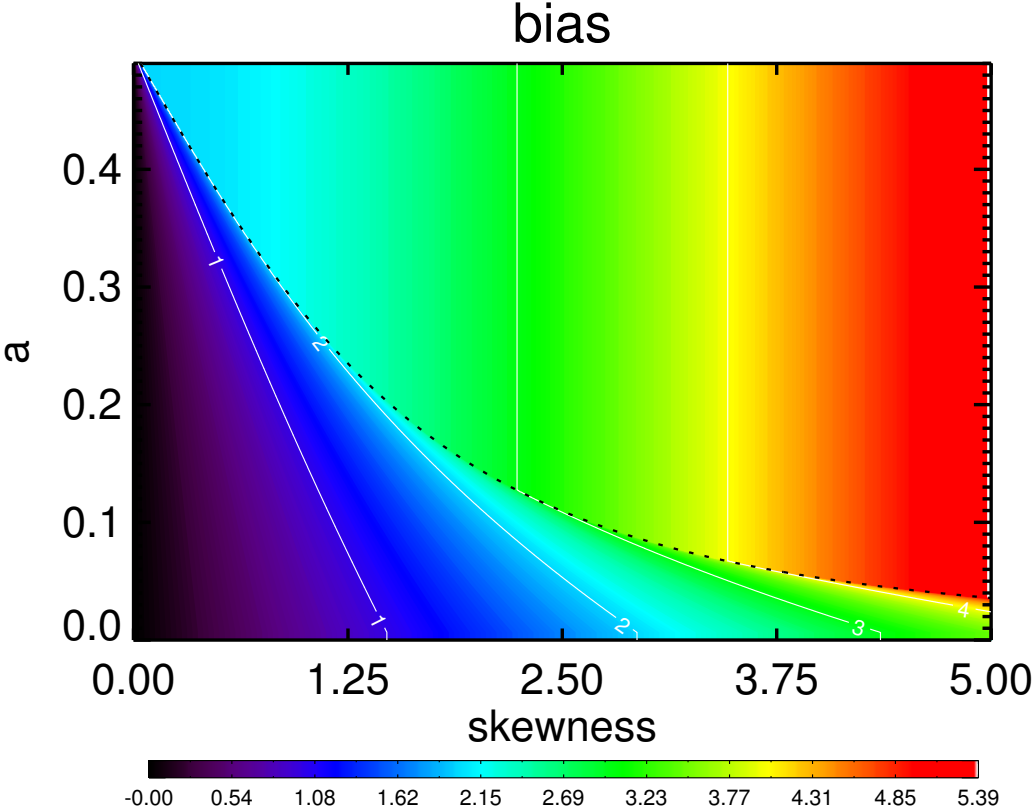


FIGURE C.2. The bias calculated for all values of interest as a function of a and skewness with an assumed variance of 1. The dotted line denotes the maximum value of a for which a solution exists at a given skewness.

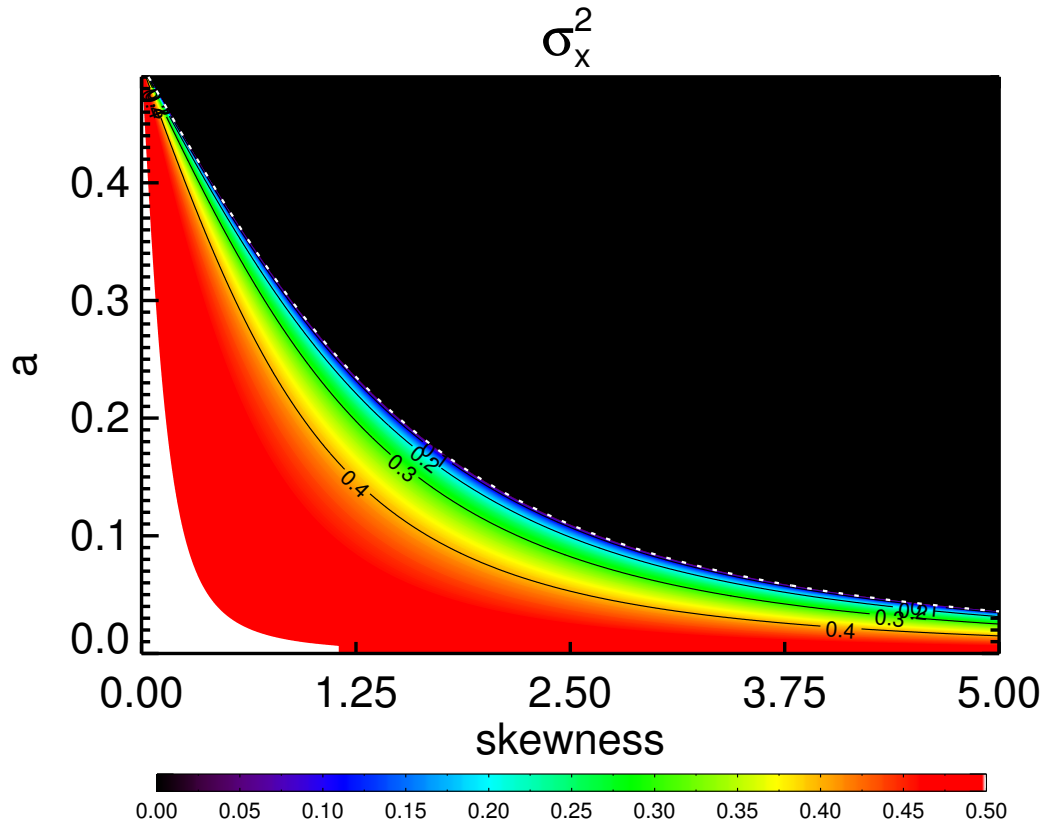


FIGURE C.3. The parameter σ_x^2 calculated for all values of interest as a function of a and skewness with an assumed variance of 1. The dotted line denotes the maximum value of a for which a solution exists at a given skewness.

APPENDIX D

MICROPHYSICS SCHEME

Rain Autoconversion:¹

$$\left(\frac{\partial q_p}{\partial t}\right)_{auto} = \max [0, \alpha (q_{i_{sample}} - q_{c0})] \quad (157)$$

Ice Aggregation:

$$\left(\frac{\partial q_p}{\partial t}\right)_{aggr} = \max \left[0, \beta e^{0.025(T_{sample}-273.16)} (q_{i_{sample}} - q_{i0})\right] \quad (158)$$

Accretion of Cloud Water and Ice:

$$\left(\frac{\partial q_m}{\partial t}\right)_{accr,l} = A_{am} q_{i_{sample}} q_m^{(3+b_m)/4} \quad (159)$$

where A_{am} is given by

$$A_{am} = \frac{\pi}{4} a_m N_{0m} E_{ml} \Gamma(3 + b_m) \left(\frac{\rho_0}{\rho}\right)^{0.5} \left(\frac{\rho}{\pi \rho_m N_{0m}}\right)^{(3+b_m)/4} \quad (160)$$

and the subscript m represents rain, snow, or graupel precipitation species. Accretion of cloud ice is a similar formula but with an additional temperature dependence.

$$\left(\frac{\partial q_m}{\partial t}\right)_{accr,i} = A_{am} q_{i_{sample}} q_m^{(3+b_m)/4} \quad (161)$$

$$A_{am} = \frac{\pi}{4} a_m N_{0m} E_{mi} \Gamma(3 + b_m) \left(\frac{\rho_0}{\rho}\right)^{0.5} \left(\frac{\rho}{\pi \rho_m N_{0m}}\right)^{(3+b_m)/4} e^{0.025(T_{sample}-273.16)} \quad (162)$$

Evaporation:

$$\left(\frac{\partial q_m}{\partial t}\right)_{evap} = \frac{2\pi C_m N_{0m}}{\rho(A+B)} \left[A_{em} q_m^{0.5} + B_{em} q_m^{\frac{5+b_m}{8}} \right] (S-1) \quad (163)$$

¹All unexplained constants and symbols are described in detail in the “List of Contents” table in Appendix B of Khairoutdinov and Randall (2003).

where A_{em} and B_{em} are

$$\begin{aligned}
A_{em} &= a_{fm} \left(\frac{\rho}{\pi \rho_m N_{0m}} \right)^{0.5} \\
B_{em} &= b_{fm} \left(\frac{\rho a_m}{\mu} \right)^{0.5} \Gamma \left(\frac{5 + b_m}{2} \right) \left(\frac{\rho_0}{\rho} \right)^{0.25} \left(\frac{\rho}{\pi \rho_m N_{0m}} \right)^{(5+b_m)/8}
\end{aligned} \tag{164}$$

The quantities A , B , and S differ based on whether evaporation of liquid or ice is being calculated. For liquid,

$$\begin{aligned}
A &= \frac{L_v}{K_a T_{sample}} \left(\frac{L_v}{R_v T_{sample}} - 1 \right) \\
B &= \frac{R_v R}{D_a e_{sat_l}} \\
S &= \frac{q_{t_{sample}}}{q_{sat_l}}
\end{aligned} \tag{165}$$

where e_{sat_l} is the saturation vapor pressure over liquid and q_{sat_l} is the saturation mixing ratio over liquid. For evaporation of ice hydrometeors,

$$\begin{aligned}
A &= \frac{L_s}{K_a T_{sample}} \left(\frac{L_s}{R_v T_{sample}} - 1 \right) \\
B &= \frac{R_v R}{D_a e_{sat_i}} \\
S &= \frac{q_{t_{sample}}}{q_{sat_i}}
\end{aligned} \tag{166}$$

where e_{sat_i} is the saturation vapor pressure over ice and q_{sat_i} is the saturation mixing ratio over ice.

Precipitation Fluxes:

Precipitation fluxes are calculated exactly as in Khairoutdinov and Randall (2003) with grid-cell mean precipitation mixing ratios:

$$P_m = \frac{a_m \Gamma(4 + b_m)}{6} (\pi \rho_m N_{0m})^{-b_m/4} \left(\frac{\rho_0}{\rho} \right)^{0.5} (\rho q_m)^{1+b_m/4} \tag{167}$$

LIST OF ACRONYMS

- AGCM:** atmospheric general circulation model
- AMIP:** Atmospheric Model Intercomparison Project
- AR4:** Fourth Assessment Report
- ASTEX:** Atlantic Stratocumulus Transition Experiment
- BOMEX:** Barbados Oceanographic and Meteorological Experiment
- CALIPSO:** Cloud-Aerosol Lidar and Infrared Pathfinder Satellite Observations
- CAM:** Community Atmosphere Model
- CAPE:** convective available potential energy
- CCM3:** NCAR Community Climate Model
- CCN:** cloud condensation nuclei
- CFMIP:** Cloud Feedback Model Intercomparison
- CGILS:** CFMIP-GASS Intercomparison of LES and SCMs
- CIN:** convective inhibition
- CLUBB:** Cloud Layers Unified By Binormals
- CRM:** cloud-resolving model
- CTL:** control simulation
- DYCOMS:** Dynamics and Chemistry of Marine Stratocumulus
- ECMWF:** European Centre for Medium-Range Weather Forecasts
- EIS:** estimated inversion strength
- ERA-Interim:** Interim ECMWF Re-analysis
- ERBE:** Earth Radiation Budget Experiment
- FP:** fully prognostic

GASS: Global Atmospheric Systems Study

GCSS: GEWEX Cloud Systems Study

GEWEX: Global Energy and Water Exchanges Project

GISS: Goddard Institute for Space Studies

GFDL AM2: Geophysical Fluid Dynamics Laboratory Atmospheric Model V.2

GPCI: GCSS/WGNE Pacific Cross-section Intercomparison

IP: intermediately prognostic

IPCC: Inter-governmental Panel on Climate Change

ISCCP: International Satellite Cloud Climatology Project

ITCZ: intertropical convergence zone

LES: large eddy simulation

LMD: Laboratoire de Météorologie Dynamique

McICA: Monte Carlo Independent Column Approximation

MPACE: Mixed-Phase Arctic Cloud Experiment

NCAR: National Center for Atmospheric Research

NO-LH: no latin hypercube sampling

NO-RS: no radiation PDF sampling

P2K: +2K SST simulation

PDF: probability density function

RAMS: Regional Atmospheric Modeling System

RICO: Rain In Cumulus over the Ocean

RRTMG: Rapid Radiative Transfer Model for GCMs

SAM: System for Atmospheric Modeling

SCM: single-column model

SGS: subgrid scale

SPCAM: Super-parameterized Community Atmosphere Model

SST: sea surface temperature

TKE: turbulence kinetic energy